frontiers | Research Topics

# Biomarkers and therapeutic strategies in acute lymphoblastic leukemia

**Edited by**
Ki-Young Lee, Maristella Maggi and Claudia Scotti

**Published in**
Frontiers in Cell and Developmental Biology
Frontiers in Oncology
Frontiers in Immunology

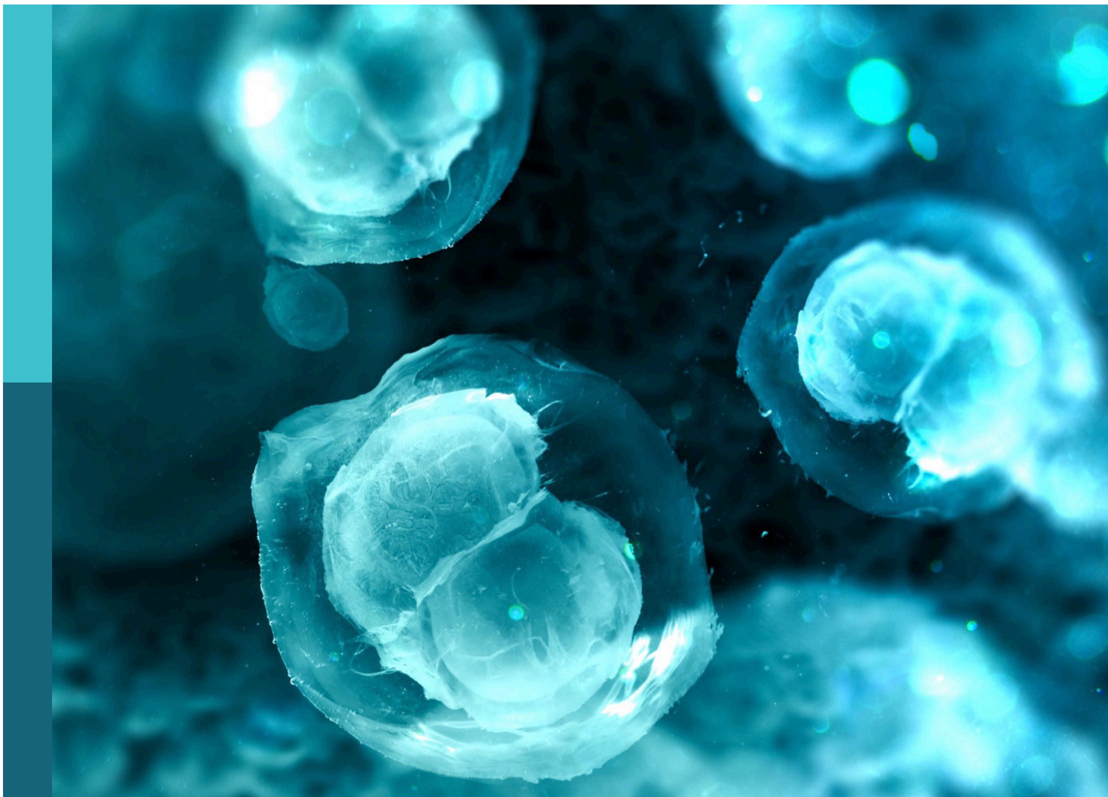

ISSN 1664-8714
ISBN 978-2-8325-2603-3
DOI 10.3389/978-2-8325-2603-3

## About Frontiers

Frontiers is more than just an open access publisher of scholarly articles: it is a pioneering approach to the world of academia, radically improving the way scholarly research is managed. The grand vision of Frontiers is a world where all people have an equal opportunity to seek, share and generate knowledge. Frontiers provides immediate and permanent online open access to all its publications, but this alone is not enough to realize our grand goals.

## Frontiers journal series

The Frontiers journal series is a multi-tier and interdisciplinary set of open-access, online journals, promising a paradigm shift from the current review, selection and dissemination processes in academic publishing. All Frontiers journals are driven by researchers for researchers; therefore, they constitute a service to the scholarly community. At the same time, the *Frontiers journal series* operates on a revolutionary invention, the tiered publishing system, initially addressing specific communities of scholars, and gradually climbing up to broader public understanding, thus serving the interests of the lay society, too.

## Dedication to quality

Each Frontiers article is a landmark of the highest quality, thanks to genuinely collaborative interactions between authors and review editors, who include some of the world's best academicians. Research must be certified by peers before entering a stream of knowledge that may eventually reach the public - and shape society; therefore, Frontiers only applies the most rigorous and unbiased reviews. Frontiers revolutionizes research publishing by freely delivering the most outstanding research, evaluated with no bias from both the academic and social point of view. By applying the most advanced information technologies, Frontiers is catapulting scholarly publishing into a new generation.

## What are Frontiers Research Topics?

Frontiers Research Topics are very popular trademarks of the *Frontiers journals series*: they are collections of at least ten articles, all centered on a particular subject. With their unique mix of varied contributions from Original Research to Review Articles, Frontiers Research Topics unify the most influential researchers, the latest key findings and historical advances in a hot research area.

Find out more on how to host your own Frontiers Research Topic or contribute to one as an author by contacting the Frontiers editorial office: frontiersin.org/about/contact

# Biomarkers and therapeutic strategies in acute lymphoblastic leukemia

**Topic editors**
Ki-Young Lee — University of Calgary, Canada
Maristella Maggi — University of Pavia, Italy
Claudia Scotti — University of Pavia, Italy

**Citation**
Lee, K.-Y., Maggi, M., Scotti, C., eds. (2023). *Biomarkers and therapeutic strategies in acute lymphoblastic leukemia*. Lausanne: Frontiers Media SA.
doi: 10.3389/978-2-8325-2603-3

# Table of contents

frontiers | Frontiers in Cell and Developmental Biology

TYPE Editorial
PUBLISHED 17 May 2023
DOI 10.3389/fcell.2023.1211569

Check for updates

OPEN ACCESS

EDITED AND REVIEWED BY
Ramani Ramchandran,
Medical College of Wisconsin,
United States

*CORRESPONDENCE
Ki-Young Lee,
kylee@ucalgary.ca

RECEIVED 24 April 2023
ACCEPTED 09 May 2023
PUBLISHED 17 May 2023

CITATION
Lee K-Y, Maggi M and Scotti C (2023), Editorial: Biomarkers and therapeutic strategies in acute lymphoblastic leukemia.
*Front. Cell Dev. Biol.* 11:1211569.
doi: 10.3389/fcell.2023.1211569



# Editorial: Biomarkers and therapeutic strategies in acute lymphoblastic leukemia

Ki-Young Lee[1]*, Maristella Maggi[2] and Claudia Scotti[2]

[1]Department of Cell Biology and Anatomy, Arnie Charbonneau Cancer and Alberta Children's Hospital Research Institutes, University of Calgary, Calgary, AB, Canada, [2]Unit of Immunology and General Pathology, Department of Molecular Medicine, University of Pavia, Pavia, Italy

KEYWORDS

**acute lymphoblastic leukemia, biomarkers, chemotherapy, blood-related disorders, leukemia**

Editorial on the Research Topic
Biomarkers and therapeutic strategies in acute lymphoblastic leukemia

Acute lymphoblastic leukemia (aLL) is a malignancy characterized by an expeditious increase in immature B- (in ~85% of cases) and T-(in ~15% of cases) lymphocytes in the blood and bone marrow. It is the most prevalent cancer in children and the primary cause of death from pediatric cancer (Hunger and Mullighan, 2015). Chemotherapy continues to be the main treatment for aLL (Lee et al., 2019). There is considerable evidence for superior outcome from multiple rounds of highly intensive chemotherapy (Pui and Evans, 2006). However, the risk of acquiring resistance and toxicity from chemotherapy could be fatal. Although novel therapies such as monoclonal antibodies have been developed, their effectiveness is greatly enhanced when used in combination with chemotherapy. Thus, there is continued interest in chemotherapy. However, some of these combinations are effective in certain patients but have no clinical benefit to others, and their non-specific effects make them intolerable to many. Thus, unnecessary toxicity- and resistance-induced patient suffering or mortality occurs frequently, and relapsed and refractory aLL continue to be a major concern. A growing number of resistance biomarkers for aLL drugs have been identified (Kang et al., 2017; Lee et al., 2019), increasing the current understanding of the molecular mechanisms by which chemotherapy resistance develops. On the other hand, the extensive genetic heterogeneity in B- and T-acute lymphoblastic leukemia precursor cells indicates a range of biomarkers that promote disease development and recurrence.

The objective of this Research Topic is to bring forth recent advances in biomarkers and potential therapeutic strategies in aLL as well as their implications in managing the disease. The ultimate goal is to foster exploitation of these discoveries and provide insight into the development of more innovative and effective therapeutic approaches for aLL.

## 1 Novel biomarkers and therapeutics

Utilizing novel innovative tools such as high throughput small molecular drug screening and gene expression analyses/datasets, a number of new biomarkers and potential therapeutics have been identified. For example, a large-scale screening of small molecule drugs for aLL performed by (Nevado et al.) led to the identification of synthetic oleanane

10.3389/fcell.2023.1211569

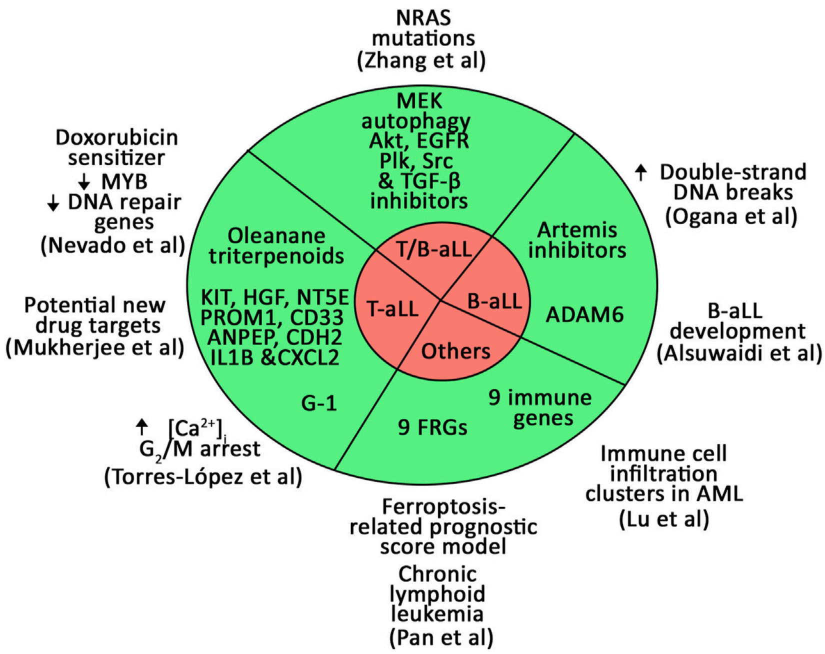


FIGURE 1
Novel biomarkers and prognostic models for B- and T-aLL and other types of leukemias identified in the current Research Topic.

triterpenoids (OTs) as sensitizers of T-aLL cells to doxorubicin, a common component of aLL chemotherapy regimens. OTs attenuate the *MYB* transcription factor and its downstream targets, and downregulate the expression of DNA repair genes. The authors proposed that OTs may be utilized in the treatment of aggressive T-aLL with poor prognosis.

Through gene expression analyses of 207 children with high-risk pre-B-aLL, (Ogana et al.) found that upregulation of Artemis, an endonuclease in V(D)J recombination and non-homologous end joining (NHEJ) of DNA double-strand break (DSB) repair, is correlated with poor prognosis. Artemis inhibition sensitizes RAG-expressing T- and B-aLL cells by causing DSBs. Through a large Artemis targeted drug screen, the authors identified four compounds (8,27,171, 8,27,032, 8,26,941, and 8,25,226) that markedly reduce proliferation of B-aLL cells, while sparing normal B Cells. This provides a basis for the authors to suggest that Artemis inhibition as a therapeutic strategy for B-aLL.

Alsuwaidi et al. analyzed datasets to identify genetic biomarkers for early detection, risk stratification, and prognosis in childhood B-aLL. The authors found that *ADAM6* is a novel biomarker for B-aLL development and progression.

Torres-López et al. demonstrate that T-aLL cells express G-protein–coupled estrogen receptor (GPER), which is stimulated by the non-steroidal agonist, G-1. The authors show that G-1 kills T-aLL cells by causing a premature rise in intracellular $Ca^{2+}$ and arresting cells in $G_2/M$, resulting in apoptosis. They suggest that G-1 is a promising T-aLL therapeutic drug.

Mukherjee et al. tackled early T precursor-aLL (ETP-aLL), which still exhibits poor clinical outcome. Gene expression of ETP-aLL blasts was compared to non-ETP-aLL blasts and nine genes (KIT, HGF, NT5E, PROM1, CD33, ANPEP, CDH2, IL1B, and CXCL2) were validated as possible diagnostic ETP-aLL markers using another gene expression dataset (GSE78132) with 17 ETP-aLL and 27 non-ETP-aLL samples. B-lineage-skewed markers were also identified, with distinct functionality and possible druggability in ETP-aLL. These data could help identifying the dominant lineage specification programmes in the ETP-aLL blasts on a personalized level, thus providing new drug targets.

Zhang et al. studied NRAS mutations, which affect relapse susceptibility in the ~15% of aLL cases with negative outcomes. About one-third of the NRAS mutations significantly transformed Ba/F3 cells as measured by IL3-independent growth and, through a high-throughput drug screening method, the authors uncovered that leukemogenic-NRAS mutations might respond to MEK, autophagy, Akt, EGFR signaling, Polo–like kinase, Src signaling, and TGF-β receptor inhibition depending on the mutation profile.

## 2 Novel tools for assessing prognosis

Lu et al. studied the role of immune genes in the prognosis and microenvironment of acute myeloid leukaemia (AML) by single-cell analysis. Comparison of the gene expression between high and low immune cell infiltration clusters identified nine prognostic immune genes. The authors validated a constructed model that can serve as a new method to assess the prognosis of AML patients.

Pan et al. built a novel prognostic model to improve risk stratification in chronic lymphoid leukaemia patients based on ferroptosis, a lipid peroxidation–induced cell death. Using the ferroptosis-related prognostic score (FPS) model, which was based on nine ferroptosis-related genes (FRGs: AKR1C3, BECN1, CAV1, CDKN2A, CXCL2, JDP2, SIRT1, SLC1A5, and SP1), they showed that patients with high FPS correlated with worse overall and treatment free survival.

## 3 Allogeneic hematopoietic stem cell transplantation (allo-HSCT) and anti-CD19 chimeric antigen receptor (CAR) T Cell therapy

Cao et al. focus their work on an uncommon complication from allogeneic hematopoietic stem cell transplantation (allo-HSCT) and anti-CD19 chimeric antigen receptor (CAR) T Cell therapy for B Cell lymphoblastic lymphoma/aLL. The authors discussed the development of a cardiac mass and myocardial infiltration, which are associated with increased cytokine levels following allo-HSCT and CAR T Cell therapy. They indicated that monitoring of cardiac functions in B Cell lymphoblastic lymphoma/aLL patients undergoing allo-HSCT and CAR T Cell therapy is of paramount importance.

The current Research Topic highlights new biomarkers and prognostic models for aLL and other types of leukemias (Figure 1). They have the advantage of expanding the potential targets for personalized medicine, which, as it is emerging from clinical practice, paves the way for improved therapy outcome, reducing off-target side effects, and preventing relapse (Rosen et al., 2022).

## Author contributions

K-YL wrote the initial draft of the editorial. MM and CS provided constructive comments and revision to the editorial. K-YL edited the final version of the editorial. All authors contributed to the editorial and approved it for publication.

## Funding

This work was supported by a grant from CIHR (PJT-174983) to K-YL. This research was funded by: "Associazione Un sorriso alla vita—ONLUS" and a grant from the Italian Ministry of Education, University and Research (MIUR) to the Department of Molecular Medicine, University of Pavia, under the initiative "Dipartimento di Eccellenza (2023-2027)".

## Conflict of interest

CS and MM are coinventors of a patent on L-asparaginase.

The remaining authors declare that the research was conducted in the absence of any commercial or financial relationships that could be construed as a potential conflict of interest.

## Publisher's note



## References

Hunger, S. .P, and Mullighan, C. .G (2015). Acute lymphoblastic leukemia in children. *N. Engl. J. Med.* 373 (16), 1541–1552. doi:10.1056/NEJMra1400972

Kang, S. .M, Rosales, J. .L, Meier-Stephenson, V, Kim, S, Lee, K. .Y, and Narendran, A (2017). Genome-wide loss-of-function genetic screening identifies opioid receptor μ1 as a key regulator of L-asparaginase resistance in pediatric acute lymphoblastic leukemia. *Oncogene* 36 (42), 5910–5913. doi:10.1038/onc.2017.211

Lee, J. .K, Kang, S, Wang, X, Rosales, J. L., Gao, X., Byun, H. G., et al. (2019). HAP1 loss confers l-asparaginase resistance in ALL by downregulating the calpain-1-Bid-caspase-3/12 pathway. *Blood* 133 (20), 2222–2232. doi:10.1182/blood-2018-12-890236

Pui, C. .H, and Evans, W. .E (2006). Treatment of acute lymphoblastic leukemia. *N. Engl. J. Med.* 354 (2), 166–178. doi:10.1056/NEJMra052603

Rosen, E, Drilon, A, and Chakravarty, D (2022). Precision oncology: 2022 in review. *Cancer Discov.* 12 (12), 2747–2753. doi:10.1158/2159-8290.CD-22-1154

frontiers in Cell and Developmental Biology

HYPOTHESIS AND THEORY
published: 25 June 2021
doi: 10.3389/fcell.2021.706129

# Novel Markers in Pediatric Acute Lymphoid Leukemia: The Role of ADAM6 in B Cell Leukemia

*Laila Alsuwaidi[1], Mahmood Hachim[1,2]* and Abiola Senok[1]*

[1] College of Medicine, Mohammed Bin Rashid University of Medicine and Health Sciences, Dubai, United Arab Emirates, [2] Center for Genomic Discovery, Mohammed Bin Rashid University of Medicine and Health Sciences, Dubai, United Arab Emirates

**Background:** The extensive genetic heterogeneity found in the B cell precursor acute lymphoblastic leukemia (BCP-ALL) subtype of childhood ALL represents a potential repository of biomarkers. To explore this potential, we have carried out *in silico* analysis of publicly available ALL datasets to identify genetic biomarkers for childhood BCP-ALL, which could be used either individually or in combination as markers for early detection, risk stratification, and prognosis.

**Methods:** To explore novel genes that show promising clinical and molecular signatures, we examined the cBioPortal online tool for publicly available datasets on lymphoid cancers. Three studies on lymphoblastic and lymphoid leukemia with 1706 patients and 2144 samples of which were identified. Only B-Lymphoblastic Leukemia/Lymphoma samples ($n$ = 1978) were selected for further analysis. Chromosomal changes were assessed to determine novel genomic loci to analyze clinical and molecular profiles for the leukemia of lymphoid origin using cBioPortal tool.

**Results:** ADAM6 gene homozygous deletions (HOM:DEL) were present in 59.60% of the profiled patients and were associated with poor ten years of overall patients' survival. Moreover, patients with ADAM6 HOM:DEL showed a distinguished clinical and molecular profile with higher Central Nervous System (CNS) sites of relapse. In addition, ADAM6 HOM:DEL was significantly associated with unique microRNAs gene expression patterns.

**Conclusion:** ADAM6 has the potential to be a novel biomarker for the development and progress of BCP- ALL.

**Keywords: ADAM6, acute lymphoid leukemia, bioinformactics analysis, biomarkers, pediatric leukemia**

OPEN ACCESS

***Edited by:***
*Maristella Maggi,*
*University of Pavia, Italy*

***Reviewed by:***
*Carlo Ganini,*
*University of Rome Tor Vergata, Italy*
*Jan Styczynski,*
*University of Bydgoszcz, Poland*

***Correspondence:**
*Mahmood Hachim*
*Mahmood.AlMashhadani@mbru.ac.ae*

***Specialty section:***
*This article was submitted to Molecular Medicine, a section of the journal Frontiers in Cell and Developmental Biology*

***Received:*** *06 May 2021*
***Accepted:*** *03 June 2021*
***Published:*** *25 June 2021*

***Citation:***
*Alsuwaidi L, Hachim M and Senok A (2021) Novel Markers in Pediatric Acute Lymphoid Leukemia: The Role of ADAM6 in B Cell Leukemia. Front. Cell Dev. Biol. 9:706129. doi: 10.3389/fcell.2021.706129*

## BACKGROUND

Acute lymphoblastic leukemia (ALL) is a clonal expansion of abnormal lymphoid progenitors of B cell or T cell origin, eventually invading the bone marrow and peripheral blood (Pastorczak et al., 2021). ALL is the most common malignancy in the pediatric age group accounting for 26% of childhood and adolescent cancers (Ward et al., 2014). Although ALL develops in children and adults, the peak incidence is in those aged 1–4 years (Malard and Mohty, 2020).

Some cases of pediatric acute leukemias that can be diagnosed in children under one year of age are characterized by unique and aggressive biology (Ibrahimova et al., 2021). On the other hand, 60% of ALL are diagnosed before the age of 20 years (Giddings et al., 2016; Howlader et al., 2021). It represents a significant health concern globally as a major cause of childhood cancer-related mortality affecting children and young adults in their prime age (Starý and Hrušák, 2016; Zapata-Tarrés et al., 2021). From 1975-2012, ALL incidence increased by 0.8% per year in the United States to reach 15.7 cases for every $10^6$ persons, with approximately 5,970 new cases and 1,440 deaths in 2017 (Siegel et al., 2016).

The B cell precursor ALL (BCP-ALL) is a subtype of childhood ALL with a suggested multi-factorial etiology of a mixed inherited and infectious exposure (Greaves, 2018). Notably, BCP-ALL includes many genetic subtypes characterized by significant chromosomal alterations that result in the upregulation of genes by juxtaposition or dysregulation of proteins through the formation of chimeric genes (Malard and Mohty, 2020). These genes include hematopoietic transcription factors, epigenetic modifiers, cytokine receptors, and tyrosine kinases (Malard and Mohty, 2020). BCP-ALL cases usually carry a chromosome translocation as a primary genetic event, plus acquired secondary genetic alterations commonly affect cellular mechanisms that control B-cell differentiation and proliferation(Zhou et al., 2012).

The extensive genetic heterogeneity found within ALL in general, and BCP-ALL specifically represents a potential repository of biomarkers that could be harnessed for the

**TABLE 1A |** Cancer Type Detailed and numbers for lymphoid cancers and specifically the studies with lymphoblastic and Lymphoid leukemia [Acute Lymphoblastic Leukemia (St Jude, Nat Genet 2015), Acute Lymphoblastic Leukemia (St Jude, Nat Genet 2016), and Pediatric Acute Lymphoid Leukemia - Phase II (TARGET, 2018)] used in our study.

| Cancer type detailed | Number | Percentage |
|---|---|---|
| B-Lymphoblastic leukemia/lymphoma | 1978 | 92.26% |
| B-Cell acute lymphoid leukemia | 70 | 3.26% |
| T-Cell acute lymphoid leukemia | 8 | 0.37% |
| Acute lymphoblastic leukemia | 3 | 0.14% |
| Leukemia | 1 | 0.05% |
| Acute undifferentiated leukemia | 1 | 0.05% |
| Acute myeloid leukemia | 10 | 0.47% |
| Acute lymphoid leukemia | 73 | 3.40% |
| Total samples | 2144 | 100.00% |
| Total patients | 1706 | |

**TABLE 1B |** Pediatric Acute Lymphoid Leukemia - Phase II (TARGET, 2018)] used in our study classified according to their cell of origin.

| Category | Number of samples | Percentage of samples |
|---|---|---|
| B-precursor | 943 | 47.7% |
| B cell all | 726 | 36.7% |
| T cell all | 300 | 15.2% |
| NA | 9 | 0.5% |

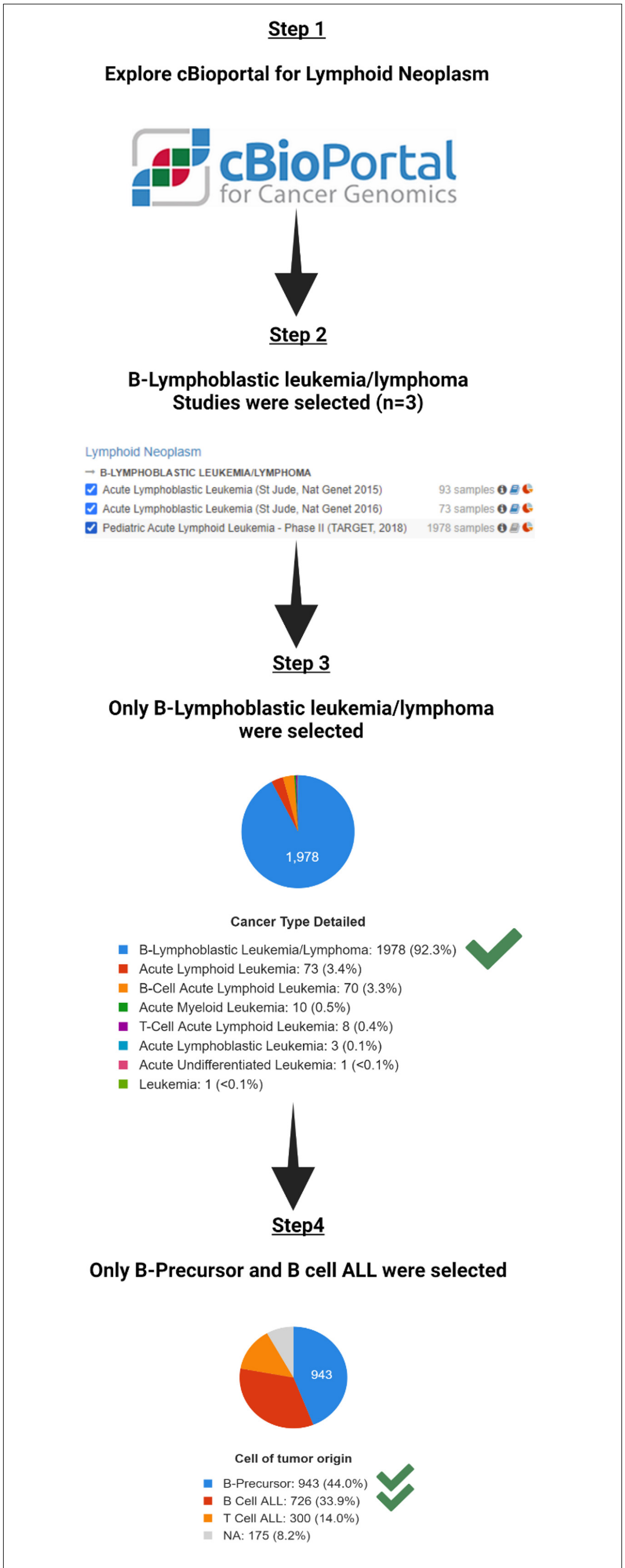


**FIGURE 1 |** The flowchart for the studies and samples selected for the analysis.

**TABLE 2 |** Distribution of genes with the highest percentage of chromosomal changes in the profiled samples.

| Gene | Cytoband | CNA | Samples with the given CNA | Profiled samples | Percentage | Is cancer gene (source: OncoKB) |
|---|---|---|---|---|---|---|
| ADAM6 | *14q32.33* | HOMDEL | 455 | 764 | 59.60% | No |
| LINC00226 | *14q32.33* | HOMDEL | 355 | 764 | 46.50% | No |
| FAM30A | *14q32.33* | HOMDEL | 340 | 764 | 44.50% | No |
| LINC00221 | *14q32.33* | HOMDEL | 307 | 764 | 40.20% | No |
| CDKN2A | 9p21.3 | HOMDEL | 276 | 764 | 36.10% | ***Yes*** |
| CDKN2B | 9p21.3 | HOMDEL | 257 | 764 | 33.60% | ***Yes*** |
| CDKN2B-AS1 | 9p21.3 | HOMDEL | 236 | 764 | 30.90% | No |
| MTAP | 9p21.3 | HOMDEL | 203 | 764 | 26.60% | ***Yes*** |
| PRSS1 | 7q34 | HOMDEL | 193 | 764 | 25.30% | ***Yes*** |

*CNA, copy number aberration.*

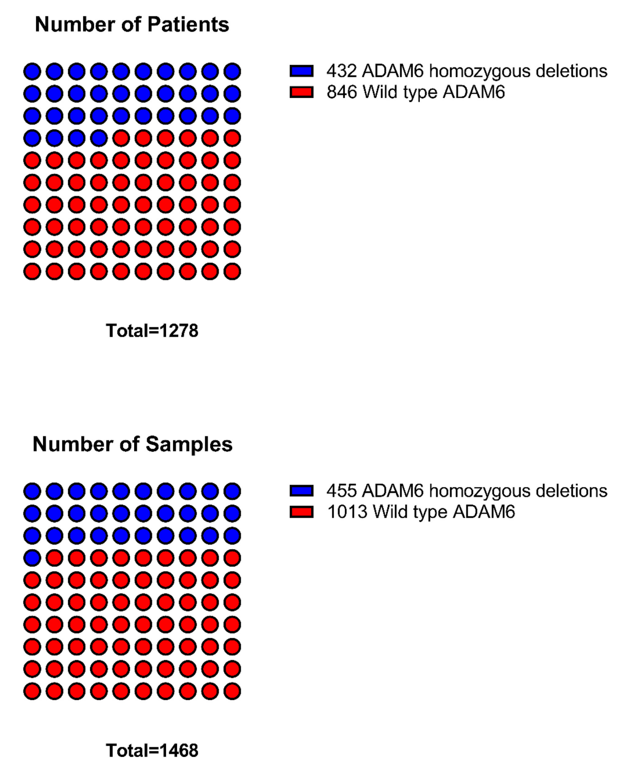


**FIGURE 2 |** Distribution of samples and patients with ADAM6 homozygous deletions compared to the rest with wild-type ADAM6.

development of early diagnostic and monitoring tools as well as novel chemotherapeutic targets. This is pertinent as cytogenetics plays a significant role in patients' diagnosis and risk stratification for treatment in childhood BCP-ALL (Schwab et al., 2013). The application of bioinformatics tools enables rapid screening for novel biomarkers, which can be further investigated for prognostic and predictive use to enhance personalized precision treatment. To facilitate this, we have carried out *in silico* analysis of publicly available ALL datasets to identify genetic biomarkers for childhood BCP-ALL, which could be used either individually or in combination as markers for early detection, risk stratification, and prognosis.

## MATERIALS AND METHODS

### Explore Publicly Available Patients Clinical and Molecular Databases

To explore the novel or less studied genes that show promising clinical and molecular signatures, we examined the cBioPortal online tool for publicly available datasets (Cerami et al., 2012). We searched for lymphoid cancers, and selected the three studies with lymphoblastic and lymphoid leukemia [Acute Lymphoblastic Leukemia (St Jude, Nat Genet 2015), Acute Lymphoblastic Leukemia (St Jude, Nat Genet 2016), and Pediatric Acute Lymphoid Leukemia - Phase II (TARGET, 2018)]. These are based in whole or part based upon data generated by the Therapeutically Applicable Research to Generate Effective Treatments[1] initiative, phs000218. The data used for this analysis are available at https://portal.gdc.cancer.gov/projects.

In total, the three studies included 1706 total patients with 2144 samples. B-Lymphoblastic Leukemia/Lymphoma was the largest in the three studies with 1978 samples (**Table 1A**). To decrease heterogeneity of sample sources, only these 1978 B-Lymphoblastic Leukemia/Lymphoma samples were selected for further analysis. Pediatric Acute Lymphoid Leukemia - Phase II (TARGET, 2018) contains those 1978 samples, so we restricted

[1] https://ocg.cancer.gov/programs/target

**TABLE 3 |** Comparison of clinical attributes of ADAM6 homozygous deletion (ADAM6:HOMDEL) versus ADAM6 wild-type (WT:ADAM6) patients.

| Clinical attribute | Attribute type | Statistical test | *p*-Value | *q*-Value |
|---|---|---|---|---|
| Diagnosis age | Patient | Wilcoxon test | 5.85E−07 | 2.39E−06 |
| Diagnosis age (days) | Patient | Wilcoxon test | 1.06E−06 | 3.99E−06 |
| WBC | Patient | Wilcoxon test | 7.42E−05 | 2.57E−04 |
| Alternative therapy given | Patient | Chi-squared test | 9.64E−04 | 3.10E−03 |
| CNS status | Patient | Chi-squared test | 5.54E−08 | 2.49E−07 |
| First event | Patient | Chi-squared test | 0.0157 | 0.0353 |
| MRD Percentage day 8 | Patient | Wilcoxon test | 0.0231 | 0.0472 |
| MRD Percentage day 29 sensitivity | Patient | Wilcoxon test | 5.94E−10 | 5.35E−09 |

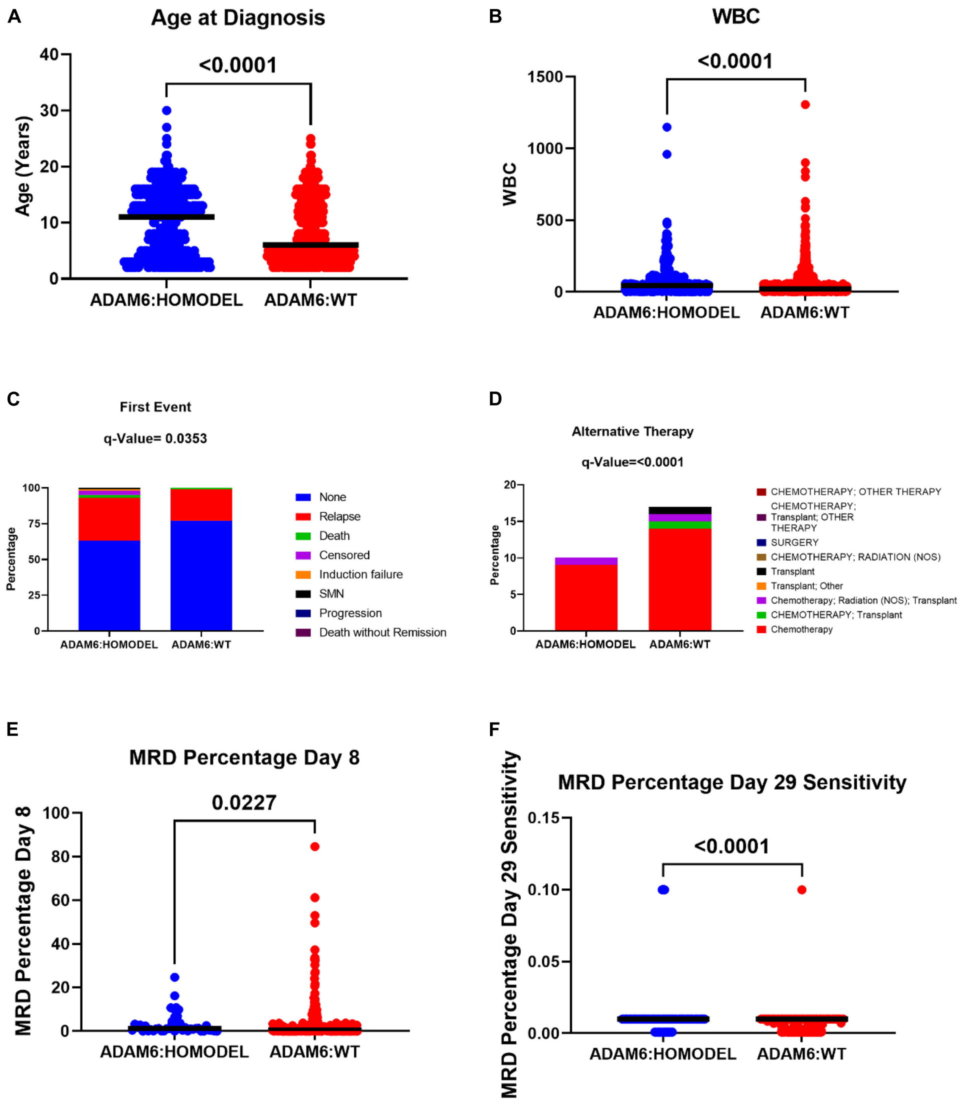


**FIGURE 3 |** The difference in the clinical attributes between ADAM6:HOMDEL versus WT:ADAM6 patients.

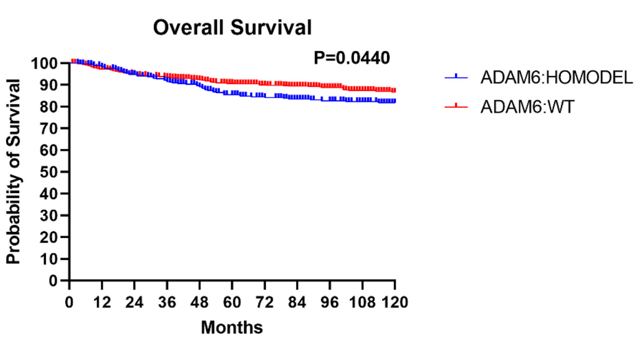


| | | |
|---|---|---|
| Comparison of Survival Curves | | |
| | | |
| Log-rank (Mantel-Cox) test | | |
| Chi square | 4.056 | |
| df | 1 | |
| P value | 0.0440 | |
| P value summary | * | |
| Are the survival curves sig different? | Yes | |
| | | |
| Gehan-Breslow-Wilcoxon test | | |
| Chi square | 4.685 | |
| df | 1 | |
| P value | 0.0304 | |
| P value summary | * | |
| Are the survival curves sig different? | Yes | |
| | | |
| Median survival | | |
| ADAM6:HOMODEL | Undefined | |
| ADAM6:WT | Undefined | |
| | | |
| Hazard Ratio (Mantel-Haenszel) | A/B | B/A |
| Ratio (and its reciprocal) | 1.431 | 0.6990 |
| 95% CI of ratio | 1.010 to 2.027 | 0.4933 to 0.9905 |
| | | |
| Hazard Ratio (logrank) | A/B | B/A |
| Ratio (and its reciprocal) | 1.403 | 0.7130 |
| 95% CI of ratio | 0.9905 to 1.986 | 0.5035 to 1.010 |

**FIGURE 4 |** Overall survival showing the ADAM6:HOMDEL versus WT:ADAM6.

the further analysis according to the cell of origin in the study, so we excluded those from T cell ALL ($n$ = 300) and kept only B-Precursor and B Cell ALL (**Table 1B**). The flowchart for the studies and samples selected for the analysis is shown in **Figure 1**.

## Molecular Differences Between the Identified Groups

For downstream work, we used the cBioPortal tool to analyze the clinical and molecular profiles of patients. Chromosomal changes in the selected samples were assessed to determine if any novel genomic loci for the leukemia of lymphoid origin were identifiable. The subsequent analysis focused on distinguishing the profiles of patients who had the predominant novel genomic loci compared to those with intact or wild counterparts.

## miRNA Targets

To determine the common targets of the identified miRNA, we used miRDB online database for miRNA target prediction and functional annotations[2]. The identified differentially expressed miRNA targets between the groups were intersected with the target of the rest of miRNA, and common targets among at least 4 out of the six miRNAs were selected. TargetScan[3] was used to predict biological targets of miRNAs by searching for the presence of conserved 8mer, 7mer, and 6mer sites that match the seed region of each miRNA(Agarwal et al., 2015).

# RESULTS

## Identification of the Novel Genomic Loci Significant in Leukemia of Lymphoid Origin

Interestingly we identified nine genes (ADAM6, LINC00226, FAM30A, LINC00221, CDKN2A, CDKN2B, CDKN2B-AS1, MTAP, and PRSS1) which had homozygous deletions present in more than 25% of profiled cases (**Table 2**). Additionally, most of these genes were found in two common loci where (ADAM6, LINC00226, FAM30A, and LINC00221 in 14q32.33 cytoband) and (CDKN2A, CDKN2B, CDKN2B-AS1, and MTAP in 9p21.3 cytoband). Of these nine genes, only four are known Cancer Genes in OncoKB (CDKN2A, CDKN2B, MTAP, and PRSS1), as shown in **Table 2**.

The frequency of ADAM6 homozygous deletion (ADAM6 HOM: DEL) was the highest among the nine genes (455 out of 764; 59.60%); therefore, further analysis was carried out to examine the difference between patients with this deletion ($n$ = 455 samples from 432 patients) and the patients without the deletion ($n$ = 846 samples from 1013 patients) as shown in **Figure 2**.

[2]http://mirdb.org/mirdb/

[3]http://www.targetscan.org/vert_72/

## Patients With ADAM6 HOM:DEL Showed a Distinct Clinical Profile

To determine if there were clinical differences between patients with the ADAM6 HOM: DEL and those with intact ADAM6 (wild-type ADAM6 [WT:ADAM6]), the cBioPortal clinical comparison tools was used to compare the two groups. Compared to patients with WT:ADAM6, those with ADAM6 HOM:DEL presented at a later age, higher total WBC count, needed chemotherapy, radiation, and transplant as an alternative therapy, more relapse rate as the first event with higher minimal residual disease (MRD) at day 8 and 29 as shown in **Table 3** and **Figure 3**.

Additionally, we found that patients with the ADAM6 HOM:DEL showed poor ten-year survival compared to those with intact ADAM6 (**Figure 4**).

## ADAM6 HOM:DEL Patients Showed Distinct Molecular Profile

Samples from patients with ADAM6 HOM:DEL had B precursor predominantly as a cell of origin with specific molecular subtypes like higher frequencies of TCF3-PBX1, ETV6-RUNX1 Fusion, and less Trisomy 4_10 status. Furthermore, although ADAM6 HOM:DEL was associated with higher mutation counts and a less altered fraction of the genome, as shown in **Table 4** and **Figure 5**.

## ADAM6 HOM:DEL Patients Showed Specific Deletion of Other Key Genes

In patients with ADAM6 HOM:DEL, we identified other genes which were also deleted. The top genes with the highest deletion were (FAM30A, LINC00226, LINC00221, VPREB1, PRSS1, PRSS2, BCL2L14, LRP6, and ETV6). Of note, 3 of these genes (FAM30A, LINC00226, and LINC00221) are present in the same cytoband, while the other three genes (BCL2L14, LRP6, and ETV6) are located in the 12p13.2 cytoband. Two genes

**TABLE 4 |** Comparison of Molecular attributes of ADAM6 homozygous deletion (ADAM6:HOMDEL) versus ADAM6 wild-type (WT:ADAM6) patients.

| Clinical attribute | Attribute type | Statistical test | *p*-Value | *q*-Value |
|---|---|---|---|---|
| Cell of tumor origin | Sample | Chi-squared test | 0 | 0 |
| TCF3-PBX1 status | Sample | Chi-squared test | 8.62E-03 | 0.0215 |
| Mutation count | Sample | Wilcoxon test | 0.0151 | 0.0353 |
| Fraction genome altered | Sample | Wilcoxon test | 0.0221 | 0.0472 |
| ETV6-RUNX1 fusion status | Sample | Chi-squared test | 1.67E−15 | 1.87E−14 |
| Molecular subtype | Sample | Chi-squared test | 3.92E−08 | 1.96E−07 |
| Trisomy 4_10 | Sample | Chi-squared test | 6.52E−09 | 4.19E−08 |
| DNA index | Sample | Chi-squared test | 2.05E−03 | 6.16E−03 |
| MLL status | Sample | Chi-squared test | 1.33E−08 | 7.49E−08 |

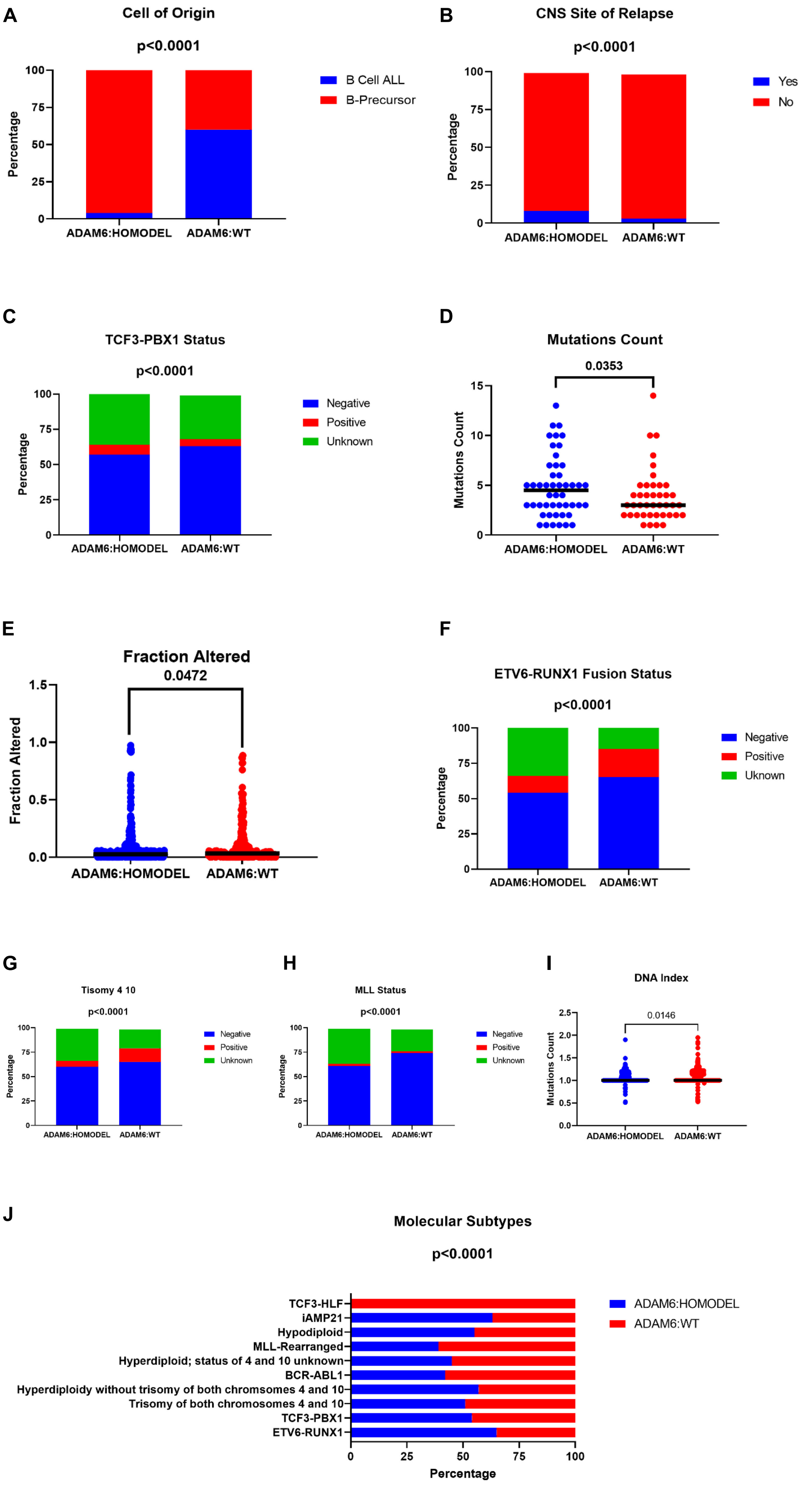


**FIGURE 5 |** Comparison of Molecular attributes of ADAM6 homozygous deletion (ADAM6:HOMDEL) versus ADAM6 wild-type (WT:ADAM6) patients.

**TABLE 5 |** Most frequently deleted genes in ADAM6 homozygous deletion (ADAM6:HOMDEL) versus ADAM6 wild-type (WT:ADAM6) patients.

| Gene | Cytoband | (A) ADAM6:HOMDEL | (B) WT:ADAM6 | Log Ratio | *p*-Value | *q*-Value |
|---|---|---|---|---|---|---|
| ADAM6 | 14q32.33 | 432 (100.00%) | 0 (0.00%) | > 10 | 7.45E−194 | 1.24E−189 |
| FAM30A | 14q32.33 | 309 (71.53%) | 19 (7.60%) | 3.23 | 2.06E−65 | 1.72E−61 |
| LINC00226 | 14q32.33 | 301 (69.68%) | 36 (14.40%) | 2.27 | 4.06E−47 | 2. 26E−43 |
| LINC00221 | 14q32.33 | 249 (57.64%) | 48 (19.20%) | 1.59 | 1.29E−23 | 5.36E−20 |
| VPREB1 | 22q11.22 | 128 (29.63%) | 20 (8.00%) | 1.89 | 2.90E−12 | 9.68E−09 |
| PRSS1 | 7q34 | 151 (34.95%) | 36 (14.40%) | 1.28 | 1.87E−09 | 5.21E−06 |
| PRSS2 | 7q34 | 104 (24.07%) | 19 (7.60%) | 1.66 | 1.32E−08 | 3.14E−05 |
| BCL2L14 | 12p13.2 | 57 (13.19%) | 5 (2.00%) | 2.72 | 8.57E−08 | 1.59E−04 |
| LRP6 | 12p13.2 | 57 (13.19%) | 5 (2.00%) | 2.72 | 8.57E−08 | 1.59E−04 |
| ETV6 | 12p13.2 | 70 (16.20%) | 9 (3.60%) | 2.17 | 1.02E−07 | 1.70E−04 |

**q-Value < 0.05 significant, ADAM6:HOMDEL, ADAM6 homozygous deletion; WT:ADAM6, ADAM6 wild-type.*

**TABLE 6 |** Specific microRNA changes between the ADAM6 HOM:DEL group and the rest of the patients.

| Gene | Mean Log2 expression ADAM6:HOMDEL | The standard deviation of lo2 expression ADAM6:HOMDEL | Mean Log2 expression WT:ADAM6 | The standard deviation of lo2 expression WT:ADAM6 | Log Ratio | *p*-Value | *q*-Value | Higher expression in |
|---|---|---|---|---|---|---|---|---|
| MIR-6735/3P | 1.7 | 2.35 | 0.61 | 0.74 | 1.09 | 1.09E−04 | 0.0452 | ADAM6:HOMDEL |
| MIR-6735/5P | 1.7 | 2.35 | 0.61 | 0.74 | 1.09 | 1.09E−04 | 0.0452 | ADAM6:HOMDEL |
| MIR-6734/3P | 2.32 | 2.76 | 0.92 | 1.34 | 1.4 | 9.21E−05 | 0.0452 | ADAM6:HOMDEL |
| MIR-6734/5P | 2.32 | 2.76 | 0.92 | 1.34 | 1.4 | 9.21E−05 | 0.0452 | ADAM6:HOMDEL |
| MIR-574/3P | 78.95 | 89.45 | 33.81 | 44.55 | > 10 | 1.04E−04 | 0.0452 | ADAM6:HOMDEL |
| MIR-574/574 | 78.95 | 89.45 | 33.81 | 44.55 | > 10 | 1.04E−04 | 0.0452 | ADAM6:HOMDEL |
| MIR-574/5P | 78.95 | 89.45 | 33.81 | 44.55 | > 10 | 1.04E−04 | 0.0452 | ADAM6:HOMDEL |

**q-Value < 0.05 significant, ADAM6:HOMDEL, ADAM6 homozygous deletion; WT:ADAM6, ADAM6 wild-type.*

(PRSS1and PRSS2) are present on 12p13.2, while VPREB1 was the only gene on 22q11.22 as listed in the **Table 5**.

## ADAM6 HOM:DEL Is Associated With Unique mRNA and microRNA Genes Expression

To examine if there are specific mRNA changes between patients with ADAM6 HOM:DEL and those without ADAM6 deletion, the mRNA expression (microarray) comparison tool of cBioPortal was used. Our findings showed specific significant differential expression of 1080 genes between the two groups. To examine if there are specific microRNA changes between patients with ADAM6 HOM:DEL and those without ADAM6 deletion, the miRNA comparison tool of cBioPortal was used. Our findings showed specific significant differential expression of 3 pairs of miRNA targets (MIR-574/3P MIR-574/574, MIR-574/5P, MIR-6734/3P, MIR-6734/5P, MIR-6735/3P, and MIR-6735/5P) as shown in **Table 6** and **Figure 6**.

MicroRNAs (miRNAs) are small non-coding RNAs that act as master regulators of the expression of their gene targets, so predicting miRNA targets is a vital step in the characterization of miRNA functions (Chen and Wang, 2019). We surmised that if the miRNA target the same genes, we might identify a novel mechanism that controls the Differentially expressed genes (DEGs) between the two groups. Therefore, to determine the common targets of the identified miRNA, we used miRDB online database for miRNA target prediction and functional annotations[2] for analysis. The target of each miRNA was intersected with the target of the rest miRNA and common targets among at least 4 out of the six miRNAs were selected (**Table 7**).

Our findings show that myocyte-enhancer factor 2 C (MEF2C) was common between 5 miRNA targets. In order to identify the putative binding sequence of the target gene (MEF2C) and binding scores, we used targetscan online tool[3] to search for MEF2C-miRNA interactions. The identifier MEF2C corresponds to 2 transcripts. One is the representative (most prevalent) transcript for MEF2C (ENST00000340208.5) and The second is the less prevalent transcript for MEF2C (ENST00000506554.1). The MEF2C-miRNA interactions, binding sites, and scores are shown in **Table 8**.

In order to understand the correlation between MEF2C and different leukemias, we explored BloodSpot[4] "a database of gene expression profiles and transcriptional programs for healthy and malignant hematopoiesis"(Bagger et al., 2015) looking for MEF2C expression. MEF2C expression showed its specificity to ALL, as shown in **Figure 7**.

## PRSS1, ACOT11, NTRK2, NOVA2, and SEMA7A Might Be the Novel Players in ADAM6 HOM:DEL ALL

Finally, to determine if common players link genomics, transcriptomics, and miRNA together, we intersected the

[4]http://servers.binf.ku.dk/bloodspot/

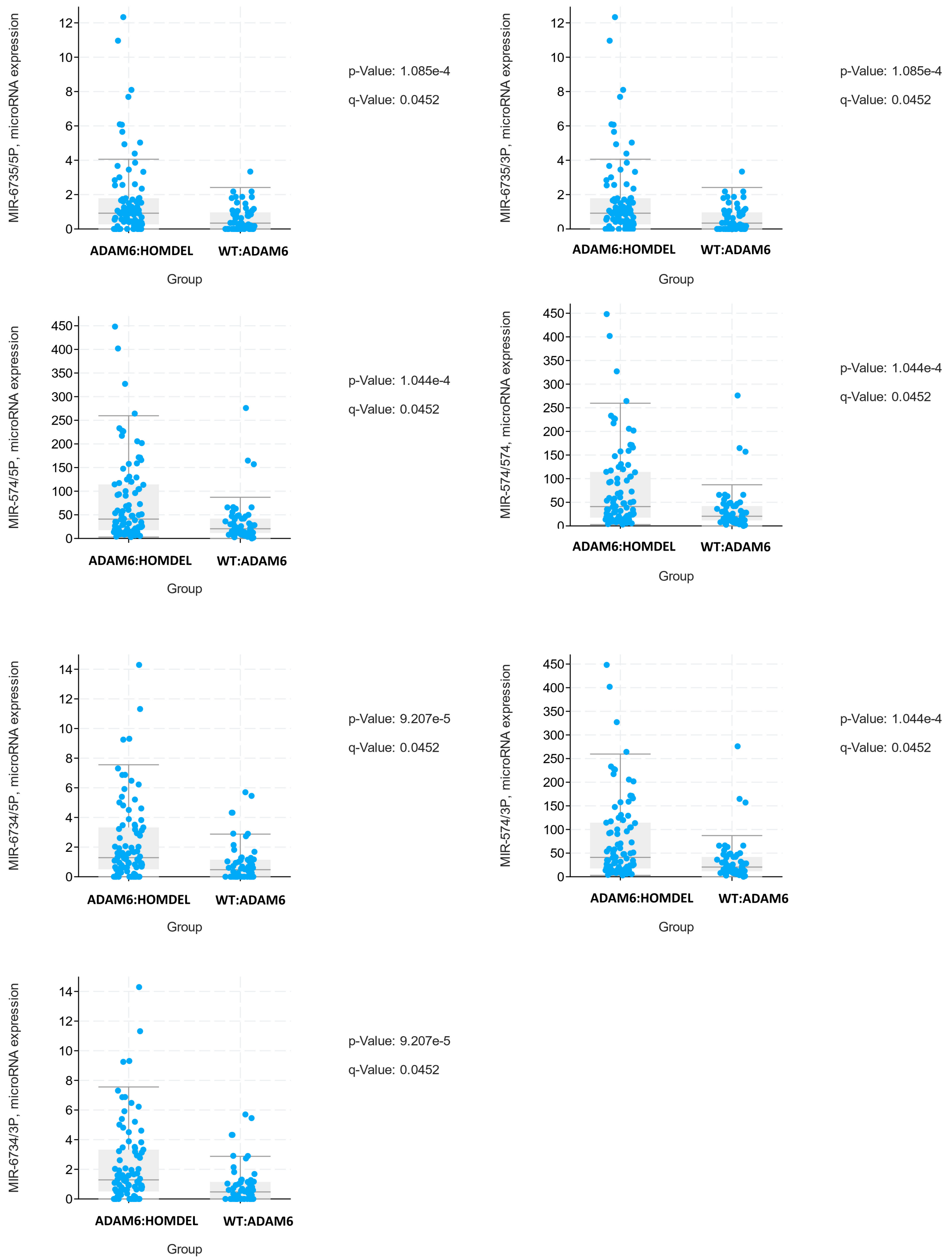


**FIGURE 6 |** The top statistically different miRNA between ADAM6:HOMDEL versus WT:ADAM6 patients.

commonly deleted genes, the DEGs, and the shared miRNA targets. Our findings identified the common genes as *PRSS1*, *ACOT11*, *NTRK2*, *NOVA2*, and *SEMA7A*, suggesting that they might be the novel players in ADAM6 HOM:DEL ALL as shown in **Figure 8**.

## DISCUSSION

Our findings demonstrate that patients with ADAM6 HOM:DEL had a distinct clinical profile compared to those with intact ADAM6. These findings suggest a possible role for ADAM6

**TABLE 7 |** Shared targets by the specific microRNA changed between the ADAM6 HOM:DEL group and the rest of the patients.

| | |
|---|---|
| [hsa-miR-6735-3p] and [hsa-miR-6735-5] and [hsa-miR-6734-3] and [hsa-miR-6734-5p] | CCDC85C, ACVR2B, NOVA2, TBC1D16, FKTN, STIM1, HLA-DQA1, C6orf106 |
| [hsa-miR-6735-3p] and [hsa-miR-6735-5] and [hsa-miR-574-5p] and [hsa-miR-6734-3] | KIAA0513, TMEM106A, DCAF8, SEMA7A |
| [hsa-miR-6735-3p] and [hsa-miR-6735-5] and [hsa-miR-574-5p] and [hsa-miR-6734-5p] | NOS1, NTRK2, FOXN3, MASP1 |
| [hsa-miR-6735-3p] and [hsa-miR-6735-5] and [hsa-miR-574-5p] and [hsa-miR-6734-3] and [hsa-miR-6734-5p] | MEF2C |

**TABLE 8 |** The MEF2C-miRNA interactions, binding sites and scores as per Targetscan tools.

| TargetScan_7.2 ENST00000340208.5 | Position in the UTR | seed match | context + + score | context + + score percentile | weighted context + + score | conserved branch length |
|---|---|---|---|---|---|---|
| hsa-miR-6734-3p | 65–71 | 7mer-m8 | −0.12 | 79 | −0.12 | 0 |
| hsa-miR-574-5p | 2370–2377 | 8mer | −0.27 | 90 | −0.02 | 0 |
| hsa-miR-6734-3p | 2814–2820 | 7mer-m8 | −0.2 | 89 | −0.02 | 0 |
| hsa-miR-6735-5p | 3427–3433 | 7mer-m8 | −0.1 | 69 | −0.01 | 0.322 |
| hsa-miR-6734-5p | 3595–3601 | 7mer-1A | −0.11 | 67 | −0.01 | 0.159 |
| **TargetScan_7.2 ENST00000506554.1** | **Position in the UTR** | **seed match** | **context + + score** | **context + + score percentile** | **weighted context + + score** | **conserved branch length** |
| hsa-miR-6734-3p | 214–220 | 7mer-m8 | −0.11 | 76 | −0.11 | 0 |
| hsa-miR-574-5p | 2519–2526 | 8mer | −0.28 | 91 | 0 | 0 |
| hsa-miR-6735-5p | 3576–3582 | 7mer-m8 | −0.11 | 71 | 0 | 0.322 |
| hsa-miR-6734-5p | 3744-3750 | 7mer-1A | −0.11 | 68 | 0 | 0.159 |

in disease pathogenesis, progression, and patient survival. The finding of significant differences in the 10-year survival rate between patients with ADAM6 HOM:DEL *versus* those with intact ADAM6 is of interest as this could potentially be used as a novel biomarker for monitoring the development and progression of BCP-ALL. ADAM6 is a member of a disintegrin and metalloproteinases (ADAMs) gene family of proteins which display a common domain organization featuring a pro-domain, a metalloprotease, a disintegrin, a cysteine-rich, an epidermal growth factor-like, and a transmembrane domain, as well as a C-terminal cytoplasmic tail (Wolfsberg et al., 1995; Brocker et al., 2009). ADAM members are multifunctional proteins involved in the proteolytic processing of other transmembrane proteins, cell adhesion, and cell signaling events (Weber and Saftig, 2012). Several reports have shown that members of the ADAM family are overexpressed in human cancers such as ADAM8 in human renal cell carcinomas, ADAM15 in lung carcinoma, and ADAM17 in breast cancers (Mochizuki and Okada, 2007). Differences in the active site sequence of the metalloproteinase domain indicate that 60% of ADAM members are pseudogenes and non—proteolytic molecules; as a result, several members of the ADAM family, including ADAM6, a pseudogene located in chromosome 14 (14q32.33), have hitherto not been well studied or reported on in the literature (Mochizuki and Okada, 2007). Indeed, the function of ADAM6 in disease or normal physiological scenarios is yet to be fully elucidated and our findings are an essential contribution to the paucity of data on ADAM6.

Interestingly, our study noted specific microRNA changes in patients with ADAM6 HOM:DEL where the expression of *MIR-574/3P* gene was observed in most ADAM6 HOM:DEL suggesting an association between ADAM6 deletion and the overexpression of the gene. Since *MIR-574/3P* gene is known to suppress proliferation and induces apoptosis of chronic myeloid leukemia (CML) cells via targeting IL6/JAK/STAT3 pathway (Yang et al., 2018), the findings of this study provide novel insights into the association of ADAM6 with miR-574-3p signaling pathway in leukemia. Furthermore, the findings demonstrate that the deletion of ADAM6 is associated with unique microRNA genes expression with significant differential expression of 3 pairs of miRNA targets. The *MEF2C* gene was the one most linked showing an association with 5 of these *miRNA* targets. *MEF2C* is necessary for the proper development of megakaryocytes and platelets and bone marrow B-lymphopoiesis. Moreover, *MEF2C* is required for B-cell survival and proliferation in response to B cell receptor (BCR) stimulation, efficient IgG1 antibody responses to T-cell-dependent antigens, and normal germinal center induction B-cells. This gene is a selectively expressed transcription factor that, if ectopically expressed due to chromosomal rearrangements, can lead to mixed-lineage leukemia-rearranged acute myeloid leukemia and immature T-cell acute lymphoblastic leukemia (Canté-Barrett et al., 2014). Phosphorylation of *MEF2C* has been reported in the majority of primary chemotherapy-resistant AML (Brown et al., 2018). Its high expression is linked with a subset of AML patients with adverse-risk disease features and poor outcomes, with confirmation that high MEF2C mRNA expression leads to overexpression of MEF2C protein (Laszlo et al., 2015). These findings provided the rationale for the therapeutic targeting of MEF2C transcriptional activation in AML. The finding of *MEF2C* as a common link among the miRNA targets in *ADAM6 HOM:DEL* patients suggests the potential role for this gene in disease progression, which warrants further investigation of its use as a biomarker.

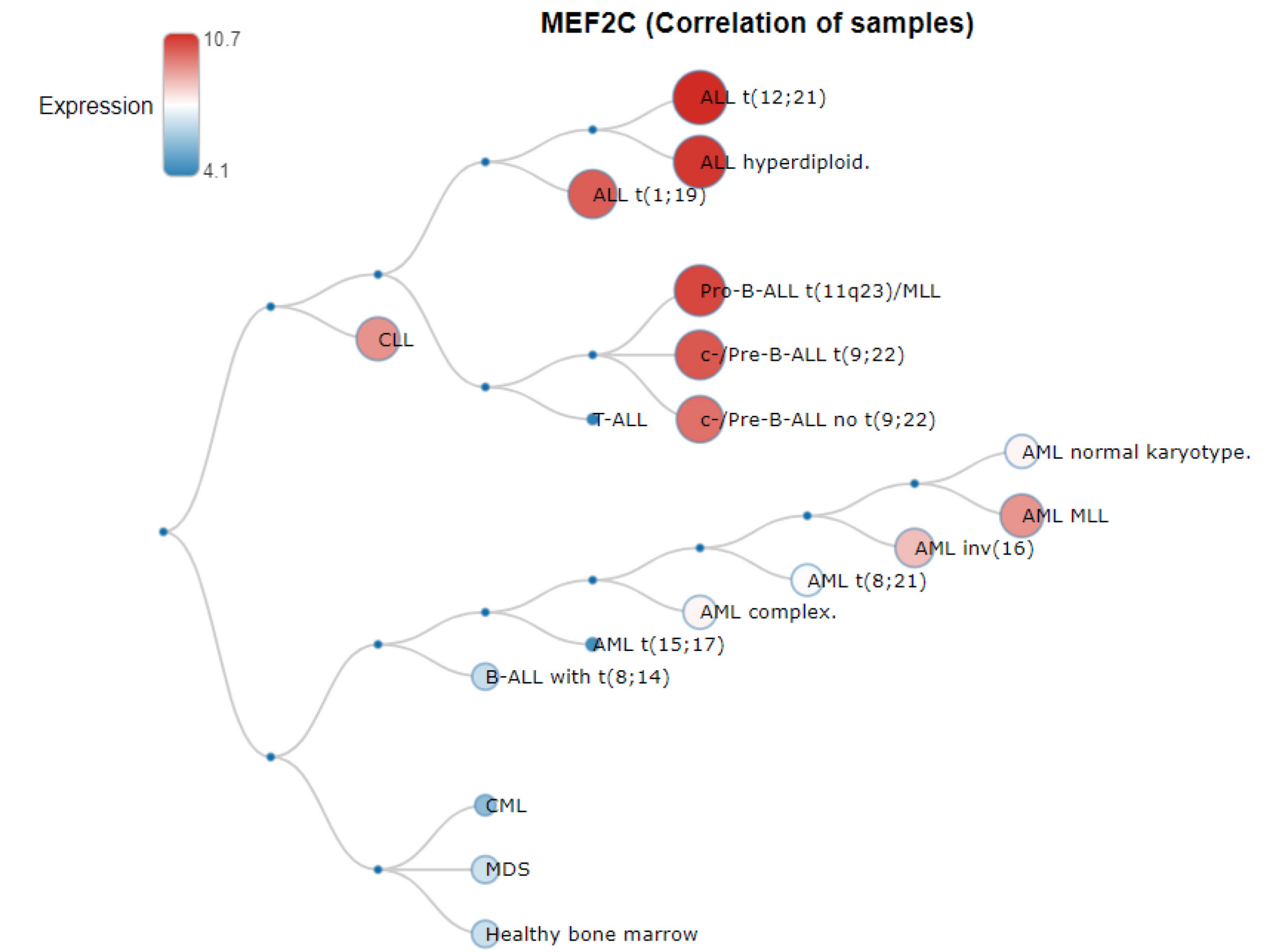


| Short | Abbreviation |
|---|---|
| ALL hyperdiploid | ALL with hyperdiploid karyotype |
| ALL t(12;21) | ALL with t(12;21) |
| ALL t(1;19) | ALL with t(1;19) |
| AML complex. | AML complex aberrant karyotype |
| AML inv(16) | AML with inv(16)/t(16;16) |
| AML normal karyotype | AML with normal karyotype + other abnormalities |
| AML MLL | AML with t(11q23)/MLL |
| AML t(15;17) | AML with t(15;17) |
| AML t(8;21) | AML with t(8;21) |
| CLL | CLL |
| CML | CML |
| MDS | MDS |
| Healthy bone marrow | Non-leukemia and healthy bone marrow |
| Pro-B-ALL t(11q23)/MLL | Pro-B-ALL with t(11q23)/MLL |
| T-ALL | T-ALL |
| c-/Pre-B-ALL t(9;22) | c-ALL/Pre-B-ALL with t(9;22) |
| c-/Pre-B-ALL no t(9;22) | c-ALL/Pre-B-ALL without t(9;22) |
| B-ALL with t(8;14) | mature B-ALL with t(8;14) |

**FIGURE 7 |** MEF2C (Correlation of samples) in Human AML, ALL and preleukemic stages cells are from GSE13159.


| Gene Symbol | Description | Biological Process (GO) |
|---|---|---|
| **PRSS1** | serine protease 1 | GO:0009235 cobalamin metabolic process;GO:0033013 tetrapyrrole metabolic process;GO:0022617 extracellular matrix disassembly |
| **ACOT11** | acyl-CoA thioesterase 11 | GO:0009409 response to cold;GO:0120163 negative regulation of cold-induced thermogenesis;GO:0006637 acyl-CoA metabolic process |
| **NTRK2** | neurotrophic receptor tyrosine kinase 2 | GO:0099183 trans-synaptic signaling by BDNF, modulating synaptic transmission;GO:0099191 trans-synaptic signaling by BDNF;GO:0099540 trans-synaptic signaling by neuropeptide |
| **NOVA2** | NOVA alternative splicing regulator 2 | GO:0120163 negative regulation of cold-induced thermogenesis;GO:0000381 regulation of alternative mRNA splicing, via spliceosome;GO:0000380 alternative mRNA splicing, via spliceosome |
| **SEMA7A** | semaphorin 7A (John Milton Hagen blood group) | GO:0060907 positive regulation of macrophage cytokine production;GO:0010935 regulation of macrophage cytokine production;GO:0010934 macrophage cytokine production |

**FIGURE 8 |** Shared genes between the commonly deleted genes, upregulated mRNA genes, and common targets of the altered miRNA.

Our findings also demonstrate that the *PRSS1*, *ACOT11*, *NTRK2*, *NOVA2*, and *SEMA7A* genes were common denominators linking the unique genomic, transcriptomic, and miRNA profiles identified in the ADAM6 HOM:DEL ALL patients. This is pertinent as *PRSS1*, *ACOT11*, *NTRK2* have been shown individually to play a role in other hematopoietic and solid organ malignancies but have hitherto not been previously reported in the context of BCP-ALL. Trypsin-encoding *PRSS1-PRSS2* variations influence the risk of asparaginase-associated pancreatitis in children with acute lymphoblastic leukemia (Wolthers et al., 2019). Recent genome-wide association studies have found different candidate single-nucleotide polymorphisms associated with pancreatitis in patients with ALL (Rank et al., 2019). Acyl-CoA Thioesterase 11 (ACOT11) is a protein-coding gene, and its high expression in patients with lung adenocarcinoma was associated with cell proliferation and poor prognosis (Hung et al., 2017). In AML, high ACOT11 expression was associated with poor overall survival (Luo et al., 2016). In clear (ccRCC), ACOT11 has been identified as a diagnostic marker wherein mRNA level of *ACOT11* was decreased compared to those in normal kidneys (Luo et al., 2016). Neurotrophic receptor tyrosine kinase 2 (NTRK2) is a kinase target for differentially expressed glutathione peroxidases (GPX-8) in AML (Wei et al., 2020). NTRK2 has been implicated in several types of cancers, including neuroblastoma, medulloblastoma, Wilm's tumor, and adenocarcinomas of the lung, prostate, and pancreas as well as multiple myeloma (Yuzugullu et al., 2016). In hematopoietic cells, B and T lymphocytes and monocytes have been shown to produce NTRK2 ligand (Kerschensteiner et al., 1999). NTRK2 and its ligand, brain-derived neurotrophic factors (BDNF), are co-expressed in acute leukemia blasts and negatively correlate with leukemia patients' survival. Studies have shown that mice with bone marrow transduced with both NTRK2 and BDNF developed AML and T-ALL (Uren and Turnley, 2014). NTRK2 overexpression is enriched in a subset of PTEN-deficient T-ALL (Yuzugullu et al., 2016). Additionally, NTRK2 activation cooperates with PTEN deficiency to promote the proliferation of Ba/F3 cells in the absence of IL3 in T-ALL (Yuzugullu et al., 2016).

Our assessment of the clinical profiles showed that patients with ADAM6 HOM:DEL were more likely to have the CNS as the site of relapse. This is interesting as two genes, namely *NOVA2* and SEMA7A, were among common players linking the unique genomic, transcriptomic, and miRNA profiles in ADAM6 HOM:DEL ALL patients play important roles in CNS development and regulation. Neuro-Oncological Ventral Antigen 2 (*NOVA2*) is one of two NOVA proteins involved in neuronal-specific alternative splicing and is mainly expressed in the cerebral cortex and hippocampus (Yang et al., 1998). *NOVA2* seems to be mainly associated with a splicing regulation of genes involved in axonal guidance and projection during the development of the cortex and genes implicated in the cerebellar function of synapse formation (Saito et al., 2016). It regulates a series of alternative splicing events linked to neurite outgrowth and axonal projections in human neural stem cells (Mattioli et al., 2020). Semaphorin 7A (*SEMA7A*) is a membrane-anchored protein that plays a critical role in neuronal pathfinding and axon guidance in selected areas of the developing nervous system. It is also known to be expressed widely with diverse functions, including immune cell modulation, bone remodeling, and drug resistance (Yazdani and Terman, 2006). SEMA7A is the only GPI-linked protein in the semaphorin family that is prominently expressed in the embryo, in the lymphoid organs, and in the nervous system of adult mice (Sato and Takahashi, 1998), it enhances central and peripheral axon growth and is required for proper axon tract formation during embryonic development (Pasterkamp et al., 2003). Though the precise function of Sema7A in the immune system remains unclear, Sema7A has been shown to stimulate human monocytes (Holmes et al., 2002), and its function as a negative regulator of T-cell responses has also been reported (Czopik et al., 2006).

Overall, our findings provide the first insight to indicate that these genes might work together in the context of ADAM6 deletion. We hypothesize that they might play critical roles in determining the disease pathogenesis and progression in patients with deletion of ADAM6. This is in keeping with the poor patient survival trends demonstrated for ADAM6 HOM:DEL. Therefore, the identification ADAM6 deletion in BCP-ALL can be used as a genetic biomarker disease progression and prognosis.

## CONCLUSION

The findings suggest that ADAM6 can be a novel genetic biomarker for risk stratification and prognosis of childhood BCP-ALL. The ADAM6 HOM:DEL is significantly associated with unique microRNA gene expression and is significantly associated with the deletion of essential genes. More research on the underlying signal to explore the molecular pathways and interacting genes is warranted. Comparing ALL patients with and without ADAM6 HOM:DEL in the prospective study can evaluate the predictive value of this promising marker, and making stable lymphoid cancer cells carrying such deletion to compare its biological and signaling derangement might explore such novel molecular changes related to ALL.

## DATA AVAILABILITY STATEMENT

The datasets presented in this study can be found in online repositories. The names of the repository/repositories and accession number(s) can be found in the article/supplementary material.

## AUTHOR CONTRIBUTIONS

All authors listed have made a substantial, direct and intellectual contribution to the work, and approved it for publication.

## REFERENCES

Agarwal, V., Bell, G. W., Nam, J. W., and Bartel, D. P. (2015). Predicting effective microRNA target sites in mammalian mRNAs. *eLife* 4:e05005.

Bagger, F. O., Sasivarevic, D., Sohi, S. H., Laursen, L. G., Pundhir, S., Sønderby, C. K., et al. (2015). BloodSpot: a database of gene expression profiles and transcriptional programs for healthy and malignant haematopoiesis. *Nucleic Acids Res.* 44, D917–D924.

Brocker, C. N., Vasiliou, V., and Nebert, D. W. (2009). Evolutionary divergence and functions of the ADAM and ADAMTSgene families. *Hum. Genomics* 4, 43–55. doi: 10.1186/1479-7364-4-1-43

Brown, F. C., Still, E., Koche, R. P., Yim, C. Y., Takao, S., Cifani, P., et al. (2018). MEF2C phosphorylation is required for chemotherapy resistance in acute myeloid leukemia. *Cancer Discov.* 8, 478–497.

Canté-Barrett, K., Pieters, R., and Meijerink, J. P. (2014). Myocyte enhancer factor 2C in hematopoiesis and leukemia. *Oncogene* 33, 403–410. doi: 10.1038/onc.2013.56

Cerami, E., Gao, J., Dogrusoz, U., Gross, B. E., Sumer, S. O., Aksoy, B. A., et al. (2012). The cBio cancer genomics portal: an open platform for exploring multidimensional cancer genomics data. *Cancer Discov.* 2, 401–404. doi: 10.1158/2159-8290.cd-12-0095

Chen, Y., and Wang, X. (2019). miRDB: an online database for prediction of functional microRNA targets. *Nucleic Acids Res.* 48, D127–D131.

Czopik, A. K., Bynoe, M. S., Palm, N., Raine, C. S., and Medzhitov, R. (2006). Semaphorin 7A is a negative regulator of T Cell responses. *Immunity* 24, 591–600. doi: 10.1016/j.immuni.2006.03.013

Giddings, B. M., Whitehead, T. P., Metayer, C., and Miller, M. D. (2016). Childhood leukemia incidence in California: high and rising in the hispanic population. *Cancer* 122, 2867–2875. doi: 10.1002/cncr.30129

Greaves, M. (2018). A causal mechanism for childhood acute lymphoblastic leukaemia. *Nat. Rev. Cancer* 18, 471–484. doi: 10.1038/s41568-018-0015-6

Holmes, S., Downs, A. M., Fosberry, A., Hayes, P. D., Michalovich, D., Murdoch, P., et al. (2002). Sema7A is a potent monocyte stimulator. *Scand. J. Immunol.* 56, 270–275. doi: 10.1046/j.1365-3083.2002.01129.x

Howlader, N., Noone, Am, Krapcho, M., Miller, D., Brest, A., Yu, M., et al. (eds) (2021). *SEER Cancer Statistics Review, 1975-2018*. Bethesda, MD: National Cancer Institute.

Hung, J. Y., Chiang, S. R., Liu, K. T., Tsai, M. J., Huang, M. S., Shieh, J. M., et al. (2017). Overexpression and proliferation dependence of acyl-CoA thioesterase 11 and 13 in lung adenocarcinoma. *Oncol. Lett,* 14, 3647–3656. doi: 10.3892/ol.2017.6594

Ibrahimova, A., Pommert, L., and Breese, E. H. (2021). Acute leukemia in infants. *Curr. Oncol. Rep.* 23:27.

Kerschensteiner, M., Gallmeier, E., Behrens, L., Leal, V. V., Misgeld, T., Klinkert, W. E., et al. (1999). Activated human T cells, B cells, and monocytes produce brain-derived neurotrophic factor in vitro and in inflammatory brain lesions: a neuroprotective role of inflammation? *J. Exp. Med.* 189, 865–870. doi: 10.1084/jem.189.5.865

Laszlo, G. S., Alonzo, T. A., Gudgeon, C. J., Harrington, K. H., Kentsis, A., Gerbing, R. B., et al. (2015). High expression of myocyte enhancer factor 2C (MEF2C) is associated with adverse-risk features and poor outcome in pediatric acute myeloid leukemia: a report from the Children's Oncology Group. *J. Hematol. Oncol.* 8:115.

Luo, H., Qin, Y., Reu, F., Ye, S., Dai, Y., Huang, J., et al. (2016). Microarray-based analysis and clinical validation identify ubiquitin-conjugating enzyme E2E1 (UBE2E1) as a prognostic factor in acute myeloid leukemia. *J. Hematol. Oncol.* 9:125.

Malard, F., and Mohty, M. (2020). Acute lymphoblastic leukaemia. *Lancet* 395, 1146–1162.

Mattioli, F., Hayot, G., Drouot, N., Isidor, B., Courraud, J., Hinckelmann, M. V., et al. (2020). De Novo frameshift variants in the neuronal splicing factor NOVA2 result in a common C-Terminal extension and cause a severe form of neurodevelopmental disorder. *Am. J. Hum. Genet.* 106, 438–452.

Mochizuki, S., and Okada, Y. (2007). ADAMs in cancer cell proliferation and progression. *Cancer Sci.* 98, 621–628. doi: 10.1111/j.1349-7006.2007.00434.x

Pasterkamp, R. J., Peschon, J. J., Spriggs, M. K., and Kolodkin, A. L. (2003). Semaphorin 7A promotes axon outgrowth through integrins and MAPKs. *Nature* 424, 398–405. doi: 10.1038/nature01790

Pastorczak, A., Domka, K., Fidyt, K., Poprzeczko, M., and Firczuk, M. (2021). Mechanisms of immune evasion in acute lymphoblastic leukemia. *Cancers* 13:1536. doi: 10.3390/cancers13071536

Rank, C. U., Wolthers, B. O., Grell, K., Albertsen, B. K., Frandsen, T. L., Overgaard, U. M., et al. (2019). Asparaginase-associated pancreatitis in acute lymphoblastic leukemia: results from the NOPHO ALL2008 treatment of patients 1-45 Years of Age. *J. Clin. Oncol.* 38, 145–154. doi: 10.1200/jco.19.02208

Saito, Y., Miranda-Rottmann, S., Ruggiu, M., Park, C. Y., Fak, J. J., Zhong, R., et al. (2016). NOVA2-mediated RNA regulation is required for axonal pathfinding during development. *eLife* 5:e14371.

Sato, Y., and Takahashi, H. (1998). Molecular cloning and expression of murine homologue of semaphorin K1 gene. *Biochim. Biophys. Acta* 1443, 419–422. doi: 10.1016/s0167-4781(98)00245-0

Schwab, C. J., Chilton, L., Morrison, H., Jones, L., Al-Shehhi, H., Erhorn, A., et al. (2013). Genes commonly deleted in childhood B-cell precursor acute lymphoblastic leukemia: association with cytogenetics and clinical features. *Haematologica* 98, 1081–1088. doi: 10.3324/haematol.2013.085175

Siegel, R. L., Miller, K. D., and Jemal, A. (2016). Cancer statistics, 2016. *CA A Cancer J. Clin.* 66, 7–30. doi: 10.3322/caac.21332

Starý, J., and Hrušák, O. (2016). Recent advances in the management of pediatric acute lymphoblastic leukemia. *F1000Res.* 5:2635.

Uren, R. T., and Turnley, A. M. (2014). Regulation of neurotrophin receptor (Trk) signaling: suppressor of cytokine signaling 2 (SOCS2) is a new player. *Front. Mol. Neurosci.* 7:39. doi: 10.3389/fnmol.2014.00039

Ward, E., DeSantis, C., Robbins, A., Kohler, B., and Jemal, A. (2014). Childhood and adolescent cancer statistics, 2014. *CA Cancer J. Clin.* 64, 83–103.

Weber, S., and Saftig, P. (2012). Ectodomain shedding and ADAMs in development. *Development* 139, 3693–3709. doi: 10.1242/dev.076398

Wei, J., Xie, Q., Liu, X., Wan, C., Wu, W., Fang, K., et al. (2020). Identification the prognostic value of glutathione peroxidases expression levels in acute myeloid leukemia. *Ann. Transl. Med.* 8:678. doi: 10.21037/atm-20-3296

Wolfsberg, T. G., Straight, P. D., Gerena, R. L., Huovila, A. P., Primakoff, P., Myles, D. G., et al. (1995). ADAM, a widely distributed and developmentally regulated gene family encoding membrane proteins with a disintegrin and metalloprotease domain. *Dev. Biol.* 169, 378–383. doi: 10.1006/dbio.1995.1152

Wolthers, B. O., Frandsen, T. L., Patel, C. J., Abaji, R., Attarbaschi, A., Barzilai, S., et al. (2019). Trypsin-encoding PRSS1-PRSS2 variations influence the risk of asparaginase-associated pancreatitis in children with acute lymphoblastic leukemia: a Ponte di Legno toxicity working group report. *Haematologica* 104, 556–563. doi: 10.3324/haematol.2018.199356

Yang, H., Zhang, J., Li, J., Zhao, F., Shen, Y., and Xing, X. (2018). Overexpression of miR-574-3p suppresses proliferation and induces apoptosis of chronic myeloid leukemia cells via targeting IL6/JAK/STAT3 pathway. *Exp. Ther. Med.* 16, 4296–4302.

Yang, Y. Y., Yin, G. L., and Darnell, R. B. (1998). The neuronal RNA-binding protein Nova-2 is implicated as the autoantigen targeted in POMA patients with dementia. *Proc. Natl. Acad. Sci. U.S.A.* 95, 13254–13259. doi: 10.1073/pnas.95.22.13254

Yazdani, U., and Terman, J. R. (2006). The semaphorins. *Genome Biol.* 7:211.

Yuzugullu, H., Von, T., Thorpe, L. M., Walker, S. R., Roberts, T. M., Frank, D. A., et al. (2016). NTRK2 activation cooperates with PTEN deficiency in T-ALL through activation of both the PI3K–AKT and JAK–STAT3 pathways. *Cell Discov.* 2:16030.

Zapata-Tarrés, M., Balandrán, J. C., Rivera-Luna, R., and Pelayo, R. (2021). Childhood acute leukemias in developing nations: successes and challenges. *Curr. Oncol. Rep.* 23:56.

Zhou, Y., You, M. J., Young, K. H., Lin, P., Lu, G., Medeiros, L. J., et al. (2012). Advances in the molecular pathobiology of B-lymphoblastic leukemia. *Hum. Pathol.* 43, 1347–1362. doi: 10.1016/j.humpath.2012.02.004

**Conflict of Interest:** The authors declare that the research was conducted in the absence of any commercial or financial relationships that could be construed as a potential conflict of interest.

frontiers in Cell and Developmental Biology

ORIGINAL RESEARCH
published: 08 February 2022
doi: 10.3389/fcell.2022.712484

# Effects of *NRAS* Mutations on Leukemogenesis and Targeting of Children With Acute Lymphoblastic Leukemia

*Jiabi Qian*[1,2,3†], *Zifeng Li*[4†], *Kunlin Pei*[2], *Ziping Li*[1], *Chunjie Li*[1], *Muxia Yan*[2], *Maoxiang Qian*[3*], *Yuanbin Song*[5*], *Hui Zhang*[2*] and *Yingyi He*[2*]

[1]Guangzhou Women and Children's Medical Center, Institute of Pediatrics, Guangzhou, China, [2]Department of Hematology/Oncology, Guangzhou Women and Children's Medical Center, Guangzhou, China, [3]Department of Hematology and Oncology, The Shanghai Key Laboratory of Medical Epigenetics, International Co-laboratory of Medical Epigenetics and Metabolism, Institute of Pediatrics, Institutes of Biomedical Sciences, Children's Hospital of Fudan University, Ministry of Science and Technology, Fudan University, Shanghai, China, [4]Department of Hematology and Oncology, National Children's Medical Center, Children's Hospital of Fudan University, Shanghai, China, [5]Department of Hematologic Oncology, State Key Laboratory of Oncology in South China, Collaborative Innovation Center for Cancer Medicine, Sun Yat-sen University Cancer Center, Guangzhou, China

OPEN ACCESS

**Edited by:**
Claudia Scotti,
University of Pavia, Italy

**Reviewed by:**
Sheik Pran Babu Sardar Pasha,
University of California, Davis,
United States
Peng Xu,
Soochow University, China

***Correspondence:**
Maoxiang Qian
mxqian@fudan.edu.cn
Yuanbin Song
jimmysong@foxmail.com
Hui Zhang
zhanghuirjh@gwcmc.org
Yingyi He
hyybbs@163.com

[†]These authors have contributed equally to this work

**Specialty section:**
This article was submitted to Molecular and Cellular Pathology, a section of the journal Frontiers in Cell and Developmental Biology

**Received:** 20 May 2021
**Accepted:** 04 January 2022
**Published:** 08 February 2022

**Citation:**
Qian J, Li Z, Pei K, Li Z, Li C, Yan M, Qian M, Song Y, Zhang H and He Y (2022) Effects of NRAS Mutations on Leukemogenesis and Targeting of Children With Acute Lymphoblastic Leukemia. Front. Cell Dev. Biol. 10:712484. doi: 10.3389/fcell.2022.712484

Through the advancements in recent decades, childhood acute lymphoblastic leukemia (ALL) is gradually becoming a highly curable disease. However, the truth is there remaining relapse in ~15% of ALL cases with dismal outcomes. *RAS* mutations, in particular *NRAS* mutations, were predominant mutations affecting relapse susceptibility. *KRAS* mutations targeting has been successfully exploited, while NRAS mutation targeting remains to be explored due to its complicated and compensatory mechanisms. Using targeted sequencing, we profiled *RAS* mutations in 333 primary and 18 relapsed ALL patients and examined their impact on ALL leukemogenesis, therapeutic potential, and treatment outcome. Cumulative analysis showed that *RAS* mutations were associated with a higher relapse incidence in children with ALL. *In vitro* cellular assays revealed that about one-third of the *NRAS* mutations significantly transformed Ba/F3 cells as measured by IL3-independent growth. Meanwhile, we applied a high-throughput drug screening method to characterize variable mutation-related candidate targeted agents and uncovered that leukemogenic-*NRAS* mutations might respond to MEK, autophagy, Akt, EGFR signaling, Polo–like Kinase, Src signaling, and TGF–$\beta$ receptor inhibition depending on the mutation profile.

**Keywords: NRAS proto-oncogene, acute lymphoblastic leukemia, signaling pathway activation, therapeutic targeting, leukemogenic potential**

## INTRODUCTION

Translational genomic research and risk stratification-directed therapy have gradually made childhood acute lymphoblastic leukemia (ALL) a highly curable cancers (Vora et al., 2013; Pui et al., 2018), with over 90% leukemia-free survival in developed countries. However, about 15–20% children with ALL eventually relapse with dismal outcome (Mullighan et al., 2008; Ding et al., 2012; Bhojwani and Pui, 2013; Meyer et al., 2013; Pierro et al., 2017; Brown and Ferrando, 2018). Among the genetic alterations, *RAS* mutations, in particular *NRAS* mutations, are over presented in children with ALL (Ma et al., 2015). Studies have shown that the prevalence of *NRAS* mutations varies from 15 to 34% in children with ALL (Case et al., 2008; Irving et al., 2014; Ma et al., 2015). Impressively, Ma et al. has reported that *NRAS* mutations conferred susceptibilities on B cell ALL (B-ALL) relapse (Ma et al., 2015). Consequently, the oncogenic mutations in the NRAS represented crucial therapeutic targets (Ward et al., 2012). Therefore, it's highly needed to explore the translational potential of NRAS mutations in pediatric ALL.

RAS GTPase (HRAS, KRAS and NRAS) family members play a critical role in human malignancies via regulating cell growth, differentiation, survival, motility, and adhesion through transmitting signals to activate downstream signaling cascades, including the RAF-MEK-ERK and PI3K-AKT pathways (Karnoub and Weinberg, 2008; Stephen et al., 2014; Burgess et al., 2017). In this regard, NRAS mutations have been found to be able to lead to constitutive activation, which in turn activate its downstream signaling pathways, including mitogen-activated protein kinase (MAPK), phosphatidylinositol 3-kinase (PI3K)-AKT, and others (i.e., RalGDS, and janus kinase (JAK) - signal transducer and activator of transcription (STAT)) (Brunet et al., 1999; Cox and Der, 2003; Downward, 2003; Xu et al., 2007; Wang et al., 2013; Kong et al., 2014; Zhang and Cheong, 2016; Bery et al., 2018). In the therapeutic targeting facet, much attentions have been paid to the breakthrough of $KRAS^{G12C}$ targeting by several small molecules, such as AMG-510, MRTX849, and ARS-1620 (Janes et al., 2018; Canon et al., 2019; Hallin et al., 2020). Moreover, the $KRAS^{G12C}$ targeting has been successfully translated into clinics with very promising results (Lito et al., 2016; Hallin et al., 2020). However, effective NRAS targeting remains to be explored.

It's well established that NRAS stimulates proliferation through activating RAS-RAF-MAPK-ERK signaling pathway. Unfortunately, trials using ERK or MEK inhibitors to treated leukemic patients with NRAS mutations do not generate satisfactory results as expected. For example, Jain et al. has reported that three AML patients with *NRAS* mutations fail to respond to the MAPK inhibitor (selumetinib [AZD6244]) (Jain et al., 2014). Similarly, the reported NRAS-targeting agents have failed to demonstrate the satisfying outcomes. Furthermore, multiple *in vitro* and *in vivo* evidences has shown that *NRAS* mutated myeloma and/or leukemic cells are resistant to $KRAS^{G12C}$-targeted small molecules (Welsch et al., 2017; Janes et al., 2018; Canon et al., 2019; Hallin et al., 2020), indicating the specificity of NRAS targeting. Taken together, all these evidence has pointed out that the complex NRAS downstream signals and their compensatory effect might be the bottle-neck of precise targeting (Posch et al., 2013; Samatar and Poulikakos, 2014).

To this end, we retrospectively evaluated the impact of *RAS* mutations on children with ALL enrolled onto CCCG-ALL-2015 clinical trial and tested the contributions of *NRAS* mutations on ALL leukemogenesis and drug response. Furthermore, we utilized high-throughput drug screening (HDS) method to explore the candidates for *NRAS* targeting.

# METHODS

## Patients

Newly Diagnosed ($N = 333$) and relapsed ($N = 18$) B-ALL patients enrolled onto CCCG-ALL-2015 clinical trial were included for this study. Ethical approval was obtained from the ethics committee at Guangzhou Women and Children's Medical Centre 2015020936, 2017102307, and 2020-04500). Informed consent was provided by the patients' legal guardians, or patients themselves if they were over 8 years old according to the Helsinki Declaration, and their related clinical information was collected for this study. The survival and relapse analyses were performed using Cox proportional hazards regression model.

## Reagents and Cell Lines

All the reagents used in this study were listed in the **Supplementary Table S1**. The HEK-293T cells were purchased from the American Type Culture Collection (ATCC, United States), and Ba/F3 cells were gifted by Jun Yang at St. Jude Children's Research Hospital (Xu et al., 2015). The HEK-293T cells were maintained in Dulbecco's Modified Eagle Medium (DMEM) (Invitrogen, United Kingdom) supplemented with 10% fetal bovine serum, and the Ba/F3 cells were maintained in RPMI1640 supplemented with 10% fetal bovine serum and 10 ng/ml recombinant mouse interleukin 3 (IL3) (PeproTech EC, London, United Kingdom).

## Targeted Next-Generation Sequencing and Validation

DNA was extracted among the diagnostic bone marrow and their matched saliva samples by Trizol (Thermofisher, United States) according to the manufacturer's protocol. Targeted sequencing of hematological malignancies related genes (**Supplementary Table S2**) was completed at Kindstar Global (Beijing) Technology, Inc. As detailed, targeted gene capture and library construction for NGS were performed using NimbleGen Sequence Capture Arrays (Roche, Basel, Switzerland) according to the manufacturer's protocol. Then, the NGS libraries were sent to generate 150-bp paired-end reads for sequencing on the Illumina HiSeq X10 platform (San Diego, CA, United States). Sequencing reads were aligned to the human reference genome (hg19) using Burrows–Wheeler Aligner (BWA-0.7.10). Duplicated reads were then marked and removed using Picard (picard-tools-2.17.0). Variant calls were performed using VarDictJava (1.5.8) (Lai et al., 2016) with pre-curated blacklist variant filters and custom Annovar scripts. Finally, the confident variants were then annotated and manually checked using IGV. Structural variants were called using Delly (Rausch et al., 2012; Hunger and Mullighan, 2015) and filtered using BreakTrans. In the meanwhile, we have retrieved and analyzed the RAS family mutation data from St. Jude PeCan Data Portal (McLeod et al., 2021).

## Cytokine-independent Growth Assay in Ba/F3 Cells

The full-length *NRAS* cDNA was amplified and cloned into the cL20c-IRES-GFP lentiviral vector. *NRAS* mutations were generated using Q5 Site-Directed Mutagenesis Kit (New England Biolabs, United States) with primers listed in **Supplementary Table S3**. Lentiviral supernatants expressing *NRAS* mutants were generated by transient transfection of HEK-293T cells using Lipofectamine 3000 (Invitrogen, United Kingdom) following the manufacturer's protocol. Ba/F3 cells were transduced with lentiviral supernatants expressing different NRAS mutants with MOI = 10, following with NRAS expressing cell sorting 48 h after lentiviral transduction by FACSAria II (BD, United States). Then, sorted Ba/F3 cells were washed three times with pre-cold PBS, seeded in the 96-well plate with $1\times10^6$/ml cell density, and maintained with full RPMI1640 media in the absence of murine IL3 cytokines. Cell viability was evaluated with Trypan blue using a TC10 automated cell counter (BIO-RAD) daily for at least 7 days.

## High-Throughput Drug Screening Assay

High-throughput drug screening (HDS) was used to evaluate the cytotoxic effect of different candidate agents on NRAS$^{G12}$-transformed Ba/F3 cells (**Supplementary Figure S1**). Transformed Ba/F3 cells were grown in RPMI160 supplemented with 10% FBS and seeded in a 384-well plate (Corning, NY, United States) at a density of 1200 cells per well. The initial concentration of targeting drugs (**Supplementary Table S4**) was 10 μM and then serial diluted to generate the drug concentration series (10, 3.3, 1.1, 0.37, 0.12, 0.04, 0.013, 0.0045, 0.0015, and 0.0005 μM). The serial drug concentrations were added to the cells using an automated liquid handling system (PerkinElmer, MA, United States). Cell viability was assessed using CellTiter-Glo™ kits (Promega, WI, United States) after 72 h of drug exposure. The inhibition rate of each drug concentration was calculated after normalization using the formula below. The IC50 was calculated using GraphPad Prism v7.0 (GraphPad Software, Inc.). The HDS experiments were performed in triplicate and independently repeated three times.

$$\text{Inhibition rate (\%)} = 100\% - \frac{RLUDrug - RLUBackground}{RLUDMSO - RLUBackground} \times 100\%$$

## Cell Counting Kit-8 (CCK-8) Assays

NRAS$^{G12}$-transformed Ba/F3 cells were seeded at a density of $2\times10^5$/ml in a 96-well plate, and treated with increasing doses of tested agents listed in **Supplementary Table S1** for 72 h. The cell viability was tested using CCK-8 assay kit (Dojindo Molecular Technologies Inc., Japan) and colorimetric density was measured using a Multiscan MS spectrophotometer (Labsystems, Stockholm, Sweden). The experiments were performed in triplicate and repeated at least three times.

**TABLE 1** | Characteristics of enrolled patients from CCCG-ALL-2015 cohort.

| Characteristics | Primary ALL (*N* = 333) | Relapse ALL (*N* = 18) | *p* Value |
|---|---|---|---|
| Age (yrs, mean ± sd) | 4.8 ± 0.15 | 3.9 ± 0.46 | 0.1 |
| Gender (Male/Female) | 205/128 | 10/8 | 0.48 |
| FAB | | | |
| L1 | 59 | 7 | 0.49 |
| L2 | 214 | 5 | — |
| L3 | 60 | 0 | — |
| Immunophenotype | | | |
| B-ALL | 303 | 12 | 0.47 |
| T-ALL | 30 | 0 | — |
| Risk | | | |
| Low risk | 168 | 4 | 0.46 |
| Intermediate risk | 158 | 12 | — |
| High risk | 7 | 2 | — |
| Liver | | | |
| <2 cm | 160 | 12 | 0.19 |
| ≥ 2 cm, < 5 cm | 145 | 5 | — |
| ≥ 5 cm | 28 | 1 | — |
| Spleen | | | |
| <2 cm | 207 | 12 | 0.43 |
| ≥ 2 cm, < 5 cm | 105 | 6 | — |
| ≥ 5 cm | 21 | 0 | — |
| Mediastinal mass | | | |
| No | 326 | 18 | 0.46 |
| Yes | 7 | 0 | — |
| CNSL | | | |
| No | 324 | 15 | 0.45 |
| Yes | 8 | 3 | — |
| WBC | | | |
| $<50 \times 10^9$/L | 263 | 16 | 0.41 |
| $\geq 50 \times 10^9$/L | 170 | 2 | — |
| *KRAS* mutation | | | |
| No | 282 | 13 | 0.16 |
| Yes | 51 | 5 | — |
| *NRAS* mutation | | | |
| No | 300 | 16 | 0.868 |
| Yes | 33 | 2 | — |
| *HRAS* mutation | | | |
| No | 331 | 18 | 0.742 |
| Yes | 2 | 0 | — |

## Western Blotting Assay

Ba/F3 cells with *NRAS* mutants were lysed in 1× lysis buffer (Cell Signaling Technology, United Kingdom). Proteins (20 mg) were electrophoresis on 10% PAGE gel (BIO-RAD) and then transferred onto PVDF membranes. After blocking membranes with 5% milk for 1 h at room temperature, the membranes were incubated with anti- Phospho- Erk1/2 antibody (Cell Signaling Technology, United Kingdom, 4370S, 1:1,000 dilution), anti- Erk1/2 antibody [Cell Signaling Technology, United Kingdom, 4696S, 1:1,000 dilution], anti-Phospho- Stat5 (Tyr694) antibody [Cell Signaling Technology, United Kingdom, 4322S, 1:1,000 dilution], and anti- Stat5 antibody (Cell Signaling Technology, United Kingdom, 94205S, 1:1,000 dilution). Tubulin was used as internal control. The blots were incubated with HRP-conjugated secondary antibodies for 1 h and visualized using the ECL system. All the antibodies we used were listed in **Supplementary Table S1**.

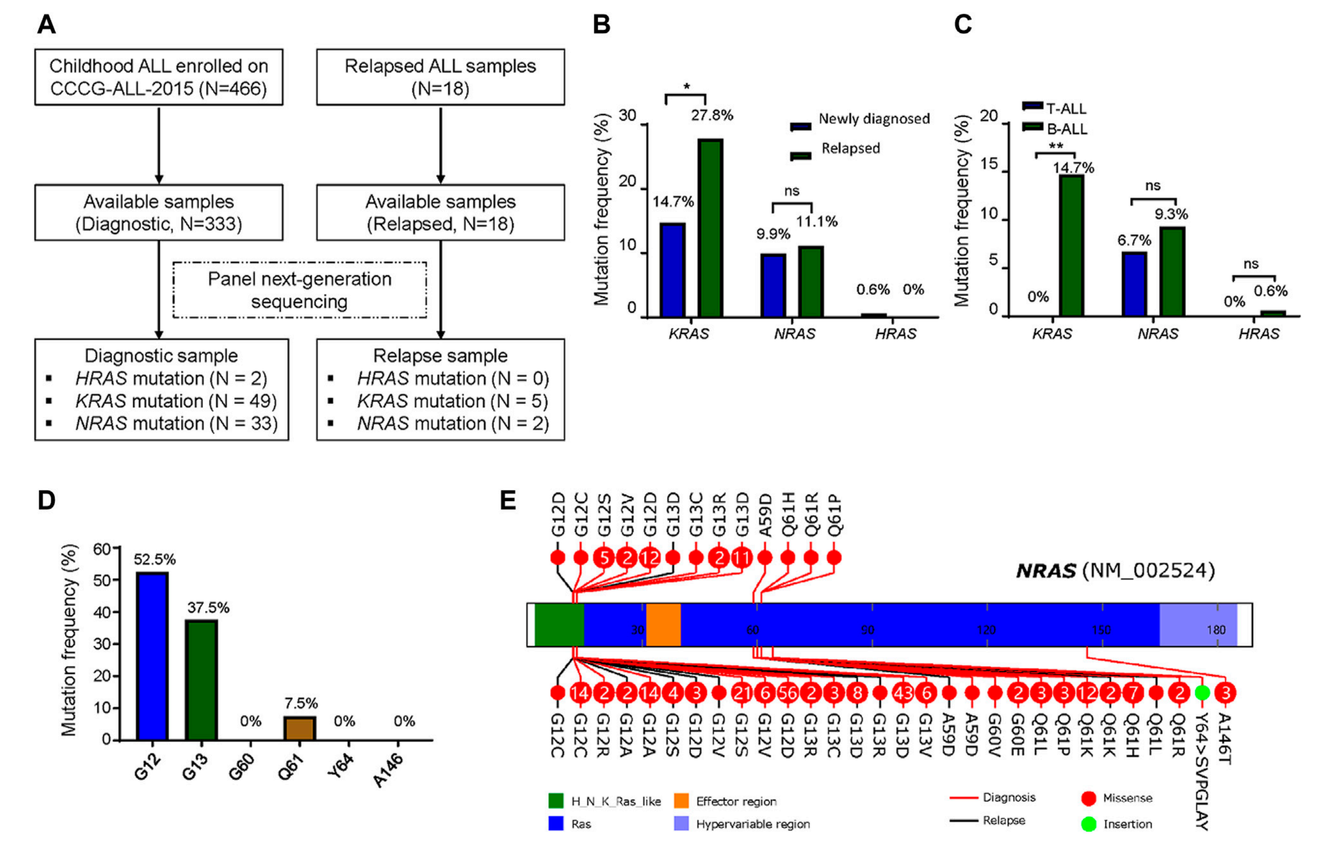


**FIGURE 1 |** *RAS* mutations in patients with newly diagnosed and relapsed ALL. **(A)** Identification of *HRAS*, *KRAS* and *NRAS* mutations in patients with newly diagnosed and relapsed ALL enrolled onto CCCG-ALL-2015 clinical trial at Guangzhou Women and Children's Medical Center. **(B)** *RAS* mutations frequency between newly diagnosed (*N* = 333) and relapsed (*N* = 18) cases. **(C)** *RAS* mutations frequency between diagnostic T-ALL and B-ALL. **(D)** *NRAS* mutations frequency including G12, G13, G60, Q61, Y64 and A146 residues in this study cohort. **(E)** *NRAS* mutation profile from our study cohort (upper panel) and PCGP study cohort. *NRAS* mutations spanned the full length of the gene (upper panel, our study cohort; lower panel, PCGP; red line, newly diagnosed ALL; black line, relapsed ALL; solid red circle, missense mutations; solid green circle, insertion mutations; number in this circle represents case number). McNemar chi-square test was performed to compare the frequency of *KRAS*, *NRAS*, and *HRAS*. $p$ < 0.05 (*, <0.05; **, <0.01) was considered statistically significant.

## Statistical Analysis

All statistical analyses were performed using R (version 3.3.1) and GraphPad Prism v7.0 (GraphPad Software, Inc.). Kaplan–Meier survival analysis was performed and survival differences between groups were assessed with the log-rank test, assuming significance at $p < 0.05$. The other data values were presented as the mean ± SD. Statistical analysis methods were denoted in independent figure legends. $p < 0.05$ was considered statistically significant.

# RESULTS

## RAS Family Alterations in Acute Lymphoblastic Leukemia Patients

Total 333 children with newly diagnosed ALL and 18 children with relapsed ALL from CCCG-ALL-2015 study at the Guangzhou Women and Children's Medical Center were enrolled onto this study (**Table 1**; **Figure 1A**; **Supplementary Figure S2**). Targeted next-generation sequencing was performed to identify the ALL-related genetic alterations. We first analyzed the RAS mutation frequency and profile among newly diagnosed patients. As shown in **Figure 1B**, the frequency of *KRAS*, *NRAS*, and *HRAS* was 14.7, 9.9, and 0.6% respectively, while the frequency of *K*-, *N*-, and *H*- *RAS* mutation among relapsed patients was 27.8, 11.1, and 0% respectively (**Figure 1B**; **Supplementary Tables S5–S7**). Notably, *KRAS* mutation frequency in relapsed ALL was ~1.9 folds higher than that of newly diagnosed ALL (27.8 vs. 14.7%; **Figure 1B**). In the PCGP cohort (McLeod et al., 2021), the mutation frequency of *KRAS*, *NRAS*, and *HRAS* were 13.9, 13.7, and 0% in *HRAS* among diagnostic samples and 25.5, 22.6, and 0% in relapsed samples (**Supplementary Figure S3**). To demonstrate the difference between B-ALL and T-cell ALL (T-ALL) as confirmed by flow cytometric immunophenotyping assay, we identified a higher *RAS* mutation frequency in newly diagnostic B-ALL patients than that in T-ALL patients (14.7 vs 0% in *KRAS*; 9.3 vs 6.7% in *NRAS*; 0.6 vs 0% in *HRAS*, **Figure 1C**). Because NRAS mutations were associated with B-ALL relapse, we then focused on exploring the *NRAS* mutation profiles in our study cohort. As shown in **Figure 1D**, most *NRAS* mutations located at G12, G13, and

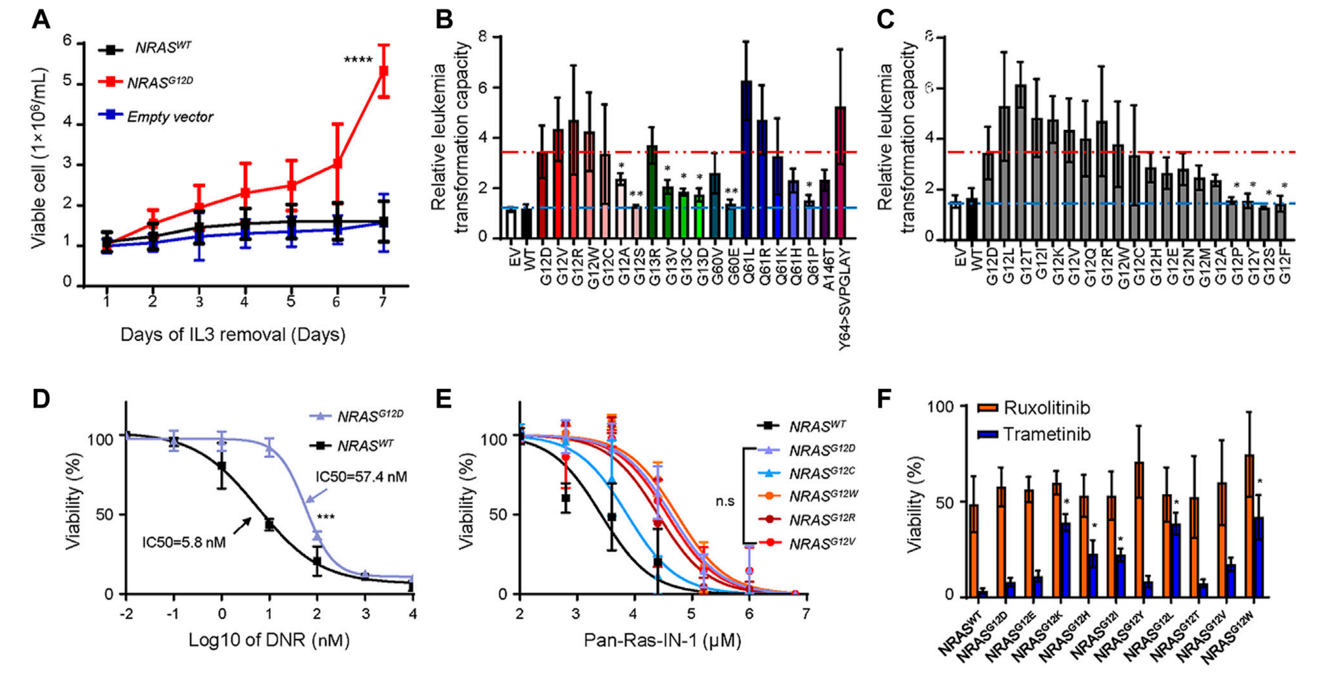


**FIGURE 2 |** Transforming potentials and drug response of NRAS mutation s in Ba/F3 cell line. **(A)** IL-3 independent cell growth of Ba/F3 cells transduced with $NRAS^{G12D}$, $NRAS^{WT}$ and empty vector. **(B–C)** Relative leukemogenic capacity between reported NRAS mutations **(B)** and G12 saturated mutant forms **(C)**. Differences were calculated between $NRAS^{G12D}$ and other *NRAS* mutants by student *t* test. Dark red dash line represents the $NRAS^{G12D}$ transforming capacity as positive control, and light blue dash line represents non-transforming capacity. The relative capacity was calculated by the ratio of viable cells between day7 and day1. Cytotoxicity of DNR **(D)**, Pan-Ras-IN-1 **(E)**, trametinib and ruxolotinib **(F)** were examined in Ba/F3 cells with *NRAS* mutations (black line, $NRAS^{WT}$; purple line, $NRAS^{G12D}$; blue line, $NRAS^{G12C}$; orange line, $NRAS^{G12w}$; brown line, $NRAS^{G12R}$; red line, $NRAS^{G12V}$). The cell viability was measured after 72 h of drug exposure using an CCK-8 assay. All these experiments were performed in triplicate and independently repeated three times. Two-way ANOVA method was used to perform the statistical analysis for **(D,E)**, and student *t* test was applied for **(F)**". $p$ < 0.05 (*, <0.05; **, <0.01; ****, <0.0001) was considered statistically significant.

Q61 residues, with 52.5, 37.5, and 7.5% frequency, respectively. The *NRAS* mutations on other residues (G60, Y64, and A146) were very rare, which was in line with previous reports (**Supplementary Figure S5A**) (Prior et al., 2012). Similar pattern was also observed in *KRAS* mutations but not in HRAS mutations (**Supplementary Figures S5B,C**). To address the *NRAS* mutation profile, we retrieved the NRAS mutation data from pediatric Cancer Genome Project (PCGP) (McLeod et al., 2021) and identified a very similar pattern between our study cohort and PCGP study cohort. (upper panel, GWCMC study cohort; lower panel, PCGP study cohort; **Figure 1E**) (Hunger and Mullighan, 2015). To examine the association of *RAS* family mutations and ALL outcomes, we performed the survival analysis using Cox proportional hazards regression model. As shown in **Supplementary Figure S4**, we did not identify a significant lower overall survival (OS) was identified in ALL patients with *RAS* mutations (Hazard ratio [HR], 2.1, 95% CI, 0.6 to 6.8, $p$ = 0.23, log-rank test). Similarly, the association of *KRAS* or *NRAS* mutations and ALL survival was not statistically significant, suggesting that RAS mutations might not impair the overall survival (**Supplementary Figure S4**). Next, we explored the effect of *RAS* mutations on ALL relapse and observed a higher risk of relapse among patients with *RAS* mutations than those with wild-type RAS (3-year cumulative relapse incidence: 18.7 ± 9.1% vs. 3.8 ± 1.3%, $p$ = 0.0021, Gray test; **Supplementary Figure S4**). This pattern was observed in the *KRAS* mutation subgroup ($p$ = 0.0012) but not in the *NRAS*-mutation subgroup ($p$ = 0.18) (**Supplementary Figure S4**). Meanwhile, we did not identify an association of *NRAS* mutations with the therapeutic response as reflected by the minimal residual diseases (MRD) (**Supplementary Table S5**).

## The Effect of *NRAS* Mutations on Acute Lymphoblastic Leukemia Leukemogenesis

The association of *NRAS* mutations with ALL relapse has been well studied by several groups. Thus, we next experimentally evaluated the role of *NRAS* mutations in ALL leukemogenesis, we cloned all *NRAS* mutants as we identified in **Figure 1**. We utilized a mouse hematopoietic progenitor Ba/F3 cell line with an IL3-dependent cell growth feature as a study model to test the leukemic transformation capacity of different *NRAS* mutations. As shown in **Figure 2A**, ectopic over-expression of $NRAS^{G12D}$ but not wild-type *NRAS* or empty vector significantly induced Ba/F3 cells IL-3 independent growth ($p$ < 0.0001). Using $NRAS^{G12D}$ as a positive control, we next tested the leukemic transformation capacity of all *NRAS* mutations and found that nine of twenty mutations ($NRAS^{G12V}$, $NRAS^{G12R}$, $NRAS^{G12W}$, $NRAS^{G12C}$, $NRAS^{G13R}$, $NRAS^{Q61L}$, $NRAS^{Q61R}$, $NRAS^{Q61K}$, $NRAS^{Y64>SVPGLAY}$) significantly potentiated Ba/F3 cells transformation after removing IL3 from culture media, with the comparable or stronger capacity to $NRAS^{G12D}$ (**Figure 2B**). However, the other eleven *NRAS* mutant forms could not induce IL-3 independent growth. Since G12 residue is the mutation hot spot, we then used the saturated mutagenesis method to establish all nineteen G12 mutant forms and test their leukemic transformation capacity by the same strategy. Interestingly, not all *NRAS* G12 mutant forms could significantly activate or potentiate leukemogenesis (**Figure 2C**). Among of which, seven (36.8%) *NRAS* G12 mutants ($NRAS^{G12L}$, $NRAS^{G12T}$, $NRAS^{G12I}$, $NRAS^{G12K}$, $NRAS^{G12V}$, $NRAS^{G12Q}$, and $NRAS^{G12R}$) demonstrated stronger leukemogenic capacity than $NRAS^{G12D}$, and another seven (36.8%) mutant forms ($NRAS^{G12W}$, $NRAS^{G12C}$, $NRAS^{G12H}$, $NRAS^{G12E}$, $NRAS^{G12N}$, $NRAS^{G12M}$, and $NRAS^{G12A}$) showed comparable to or a little bit weaker capacity. The remaining four (26.4%) *NRAS* G12 mutants ($NRAS^{G12P}$, $NRAS^{G12Y}$, $NRAS^{G12S}$, and $NRAS^{G12F}$) could not transform Ba/F3 cells at all. Taken together, our data suggest that not all *NRAS* mutants have leukemogenic potentials or pathogenic effects (**Supplementary Table S8**).

Building upon the findings above, we further asked how to target ALL cells with NRAS mutations. To address this question, we first tried to answer that whether NRAS mutations conferred resistance to conventional and novel agents, such as daunorubicin (DNR) and tyrosine kinase inhibitors. We treated with $NRAS^{mut}$ transformed Ba/F3 cells with DNR and found that $NRAS^{G12D}$ ALL cells were more resistant to DNR than those with wild-type NRAS (IC50: 57.4 vs. 5.8 nM) (**Figure 2D**), which was in line with previous reports (Irving et al., 2014; Irving et al., 2016). Using a similar approach, we compared the effect of RAS inhibitors on $NRAS^{G12}$-transfected Ba/F3 cells. Ba/F3 cells transfected with distinct *NRAS* mutants ($NRAS^{G12D}$, $NRAS^{G12C}$, $NRAS^{G12W}$, $NRAS^{G12R}$, and $NRAS^{G12V}$) were more resistant to Pan-Ras-IN-1 (a pan-Ras inhibitor) variably than those with *NRAS* wild-type (**Figure 2E**). Similar results were observed for other RAS inhibitors, including Fendiline, ARS1620, and AMG510 (**Supplementary Figure S6**). As reported by Kirchberger et al. that MEK inhibition chemo-sensitized $NRAS^{G12D}$-mutated ALL cells to conventional therapeutic agents (i.e., DNR and dexamethasone) (Irving et al., 2016), we thus tested the MEK inhibition response among those $NRAS^{G12}$ mutants transformed Ba/F3 cells. Interestingly, we identified that Ba/F3 cells with $NRAS^{G12E}$, $NRAS^{G12T}$, and $NRAS^{G12Y}$ mutation were as sensitive as Ba/F3 cells with $NRAS^{G12D}$ mutation to trametinib treatment. Meanwhile, Ba/F3 cells with $NRAS^{G12K}$, $NRAS^{G12H}$, $NRAS^{G12I}$, $NRAS^{G12L}$, $NRAS^{G12V}$, and $NRAS^{G12W}$ mutation just demonstrated a moderate response to trametinib treatment (**Figure 2F**). However, all tested $NRAS^{mut}$ transformed Ba/F3 cells did not respond to ruxolitinib, a JAK2 inhibitor.

## Translational Potential of Differential *NRAS* Mutations on Acute Lymphoblastic Leukemia Therapeutics

The findings above suggested that ALL cells with NRAS mutation might differently respond to signaling inhibition. To address this question, we applied HDS strategy as an attempt to identify candidate agents that could preferentially target NRAS mutations. Among the 843 tested agents (**Figure 3A**; **Supplementary Table S9**), we observed that $NRAS^{G12D}$ mutation well responded to MEK inhibition (GDC-0623, pimasertib, and TAK-733), which was in consistent with current clinical reports (Nakamura et al., 2013; Johnson et al., 2014; Kirchberger et al., 2018). Interestingly, $NRAS^{G12L}$ and $NRAS^{G12N}$ mutations also well responded to MEK inhibition. However, $NRAS^{G12C}$ mutation well responded to autophagy inhibition and mTOR inhibition (WYE–354), and mix-lineage kinase inhibition (E–Necrosulfonamide), while $NRAS^{G12V}$ and $NRAS^{G12T}$ mutations responded to Akt inhibition (deguelin), EGFR inhibitor (mubritinib), Polo–like Kinase (PLK) inhibition (CFI–400945), Src inhibition (MCB–613), and TGF–$\beta$ receptor inhibitor (LDN–212854). The distinctive drug response among *NRAS* mutations drove us mechanistically validate our findings above. We first utilized immunoblot assay to profile the impact of NRAS mutations on Erk, Jak2-Stat5 signaling pathway. As illustrated in **Figures 3B,C**, we found that $NRAS^{G12C}$, $NRAS^{G12K}$ $NRAS^{G12E}$, $NRAS^{G12H}$ and $NRAS^{G12N}$ mutations did not activate Jak2-Stat5, or Erk signaling. $NRAS^{G12D}$ strongly activated Erk signaling, while $NRAS^{G12I}$, $NRAS^{G12F}$, $NRAS^{G12W}$ and $NRAS^{G12R}$, $NRAS^{G12S}$, $NRAS^{G12Y}$, $NRAS^{G12P}$, and $NRAS^{G12Q}$ activated Jak2-Stat5 alone. Intriguingly, $NRAS^{G12T}$, $NRAS^{G12A}$, $NRAS^{G12L}$, $NRAS^{G12V}$, and $NRAS^{G12M}$ co-stimulated Erk and Jak2-Stat5 signaling.

# DISCUSSION

This study identified a group of *RAS* gene mutations with a high frequency in childhood ALL. Our data analysis showed that *NRAS*, *KRAS*, and *HRAS* mutations were almost mutually exclusive within our study cohort, with only eleven patients with *KRAS* and *NRAS* mutations concurrently. In consistent with reports from several other groups (Case et al., 2008; Davidsson et al., 2010; Irving et al., 2014; Oshima et al., 2016), we did not detect any changes in the frequency of *RAS* mutations based on gender or age. Irving et al. have identified that *NRAS* mutations were associated with an increased risk of progression within hyperdiploidy standard-risk patient group by analyzing cytogenetic data from 427 children with relapsed B-ALL (Irving et al., 2016). The impact of *NRAS* mutations on childhood ALL relapse in our study cohort was slightly different from other groups (Ma et al., 2015; Irving et al., 2016), which might be explained by several factors, including but not limited to patient demographics, socioeconomic status, clinical characteristics, and study sample size. Meanwhile, we found that the detectable genomic alteration in this cohort was only 36.55% (**Supplementary Figure S1**), suggesting whole transcriptome sequencing is highly needed to capture all genomic lesions.

Several reports have successfully linked genetic defects (i.e., RAS pathway alterations, drug-metabolism related genes [*FPGS*, *NT5C2*, *NR3C1*, and *PRPS1*], transcription factor [*TP53*, *IKZF1*, *CREBBP*]) with ALL relapse (Mullighan et al., 2011; Tzoneva et al., 2013; Mar et al., 2014; Song et al., 2020). Many study groups have reported that RAS mutations could be detected

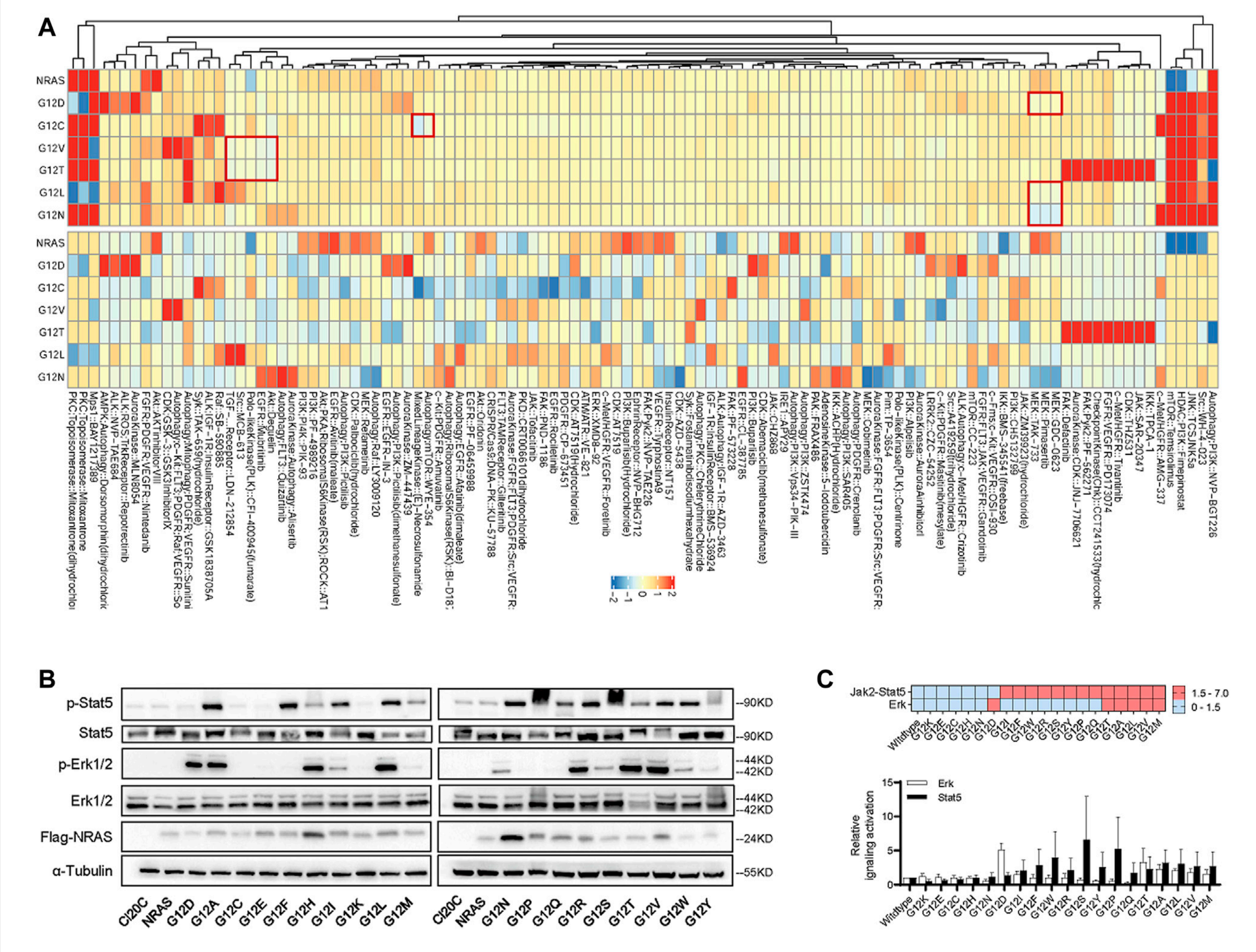


**FIGURE 3 |** The impact of NRAS$^{G12}$ mutation on drug sensitivity. **(A)** Normalized heatmap of HDS results (log10 of IC50 concentration) among Ba/F3 cells with different *NRAS* mutation. All these experiments were performed in triplicate and independently repeated three times. **(B)** Western blotting assay of Ba/F3 cells transduced with *NRAS$^{G12}$* mutants. **(C)** Heatmap (upper panel) and grey intensity plot (lower panel) to Erk and Jak2-Stat5 signaling pathways activation in Ba/F3 transduced with *NRAS$^{G12}$* mutants.

in ~50% relapsed ALL patients (Irving et al., 2014; Malinowska-Ozdowy et al., 2015; Oshima et al., 2016; Tasian and Hunger, 2017; Ding, 2018; Jerchel et al., 2018), indicating the importance of RAS mutations in ALL relapse. Attractively, a recent study by Zhang et al. has shown that more than 50% of relapsed pediatric ALL patients have RAS pathway mutations (*KRAS*, *NRAS*, *NF1*, *EPOR*), further consolidating the role of *RAS* mutations in relapsed ALL. In this study, we included 333 newly-diagnosed and 18 relapsed B-ALL patients, which is the largest single institutional cohort in China to systemically explore the role of *RAS* mutations in childhood ALL. The prevalence of *RAS* mutations was 25.2 and 38.9% in newly-diagnosed and relapsed children with ALL in our study cohort, respectively (**Figure 1**), which was in line with recent reports (Irving et al., 2014; Ma et al., 2015). It has been reported that *RAS* mutations were more likely to be enriched in high-risk ALL group, including patients with early relapse (*H*-, *K*-, and *N*- *RAS* mutations) and with central nervous system (CNS) involvement (*NRAS* and *KRAS* mutations) (Reshmi et al., 2017; Takashima et al., 2018). Our report here demonstrated a correlation between *KRAS* mutations and ALL relapse (**Supplementary Figure S4**). However, we did not observe a significant association between *RAS* mutations and treatment outcome (i.e., early treatment response (defined by MRD), OS, CNS involvement, risk stratification). There may be several possibilities, including relatively small sample size, patient demographics, and treatment protocols. Additional studies or multi-institutional cooperation were warranted to further define their relationship.

It was reported that RAS activation in malignant hematopoietic cells induces multi-drug resistance (i.e., glucocorticoids and anthracyclines) in ALL therapy (McCubrey et al., 2007; Garza et al., 2009; Irving et al., 2014). Thus, it is critical to rescue the therapeutic response so as to improve the treatment outcome. Interestingly, we found that *NRAS* mutants differed in their ability to leukemic transformation, strongly indicating that not all *NRAS* mutations are driver mutations which can be potentially targeted (**Figure 2**). In combination with the *in vitro* cytotoxic and signaling activation results (**Figures 2**, **3**), we believed that those leukemogenic *NRAS* mutants might contribute to leukemogenesis and therapeutic targeting via different mechanisms, which is supported by other groups. For example, Jerchel et al. have identified that NRAS mutation-related BCP-ALL may not activate the MAPK pathway (Jerchel et al., 2018). In contrast, Chan et al. have demonstrated NRAS mutation may promote B-cell leukemogenesis via STAT5 or MAPK (Chan et al., 2020), suggesting complicated mechanisms underlying the *NRAS* mutations in B-ALL. In this study, we confirmed the well response of $NRAS^{G12D}$ to MEK inhibition by HDS assay and western blot (**Figure 3**). Interestingly, we had identified a distinctive signaling activation profile. It's well established that $NRAS^{G12D}$ activated ERK signaling and well responded to MEK inhibition. In the meanwhile, we also found that different $NRAS^{G12}$ mutant activated different down-steam signaling pathways (**Figures 3B,C**), which might partially explain the different drug response among NRAS $^{G12}$ mutations (**Figure 3A**). Though we did not find that $NRAS^{G12N}$ activated the ERK signaling with a similar pattern as $NRAS^{G12D}$ did, $NRAS^{G12N}$ surprisingly well responded to ERK inhibition (**Figure 3A**), suggesting some compensatory mechanisms might be existed. It's noted that $NRAS^{G12C}$ did not activate Jak2-Stat5 or Erk signaling as shown in the western blot, and the HDS assay showed that $NRAS^{G12C}$ was resistant to MEK or JAK inhibition, again pointing to that one targeting strategy did not fit for all $NRAS^{G12}$ mutations. $NRAS^{G12T}$, and $NRAS^{G12V}$ co-stimulated Erk and Jak2-Stat5 signaling, and demonstrated a similar drug responding pattern to Akt inhibition, autophagy inhibition, and TGF-$\beta$ inhibition. Taken together, introducing proper NRAS targeting agents into current chemotherapy regimens might be of help in further improving current ALL treatment.

## DATA AVAILABILITY STATEMENT

The datasets presented in this study can be found in online repositories. The name of the repository and accession number can be found below: National Genomics Data Center (NGDC) Genome Sequence Archive for Human (GSA-Human), https://ngdc.cncb.ac.cn/gsa-human, HRA000708

## ETHICS STATEMENT

The studies involving human participants were reviewed and approved by This study was approved by the Institutional Review Board of Guangzhou Women and Children's Medical Center (2015020936, 2017102307, and 2020-04500). . Written informed consent to participate in this study was provided by the participants' legal guardian/next of kin.

## AUTHOR CONTRIBUTIONS

JQ, MQ, YS, YH, and HZ designed the research; JQ, KP, FQ, ZL, and CL performed experiments; KP, YH, and MY collected the samples and recruited patients; JQ, KP, FQ, YS, MQ, YH, and HZ analyzed the results; and JQ, FQ, YS, MQ, YH, and HZ wrote the manuscript.

## FUNDING

This work was supported by research grants from St. Baldrick's Foundation International Scholar (581580), Natural Science Foundation of Guangdong Province (2015A030313460), and Guangzhou Women and Children's Medical Center Internal Program (IP-2018-001, 5001-1600006, and 5001-1600008). HZ, YS, MQ, and CL were supported by the National Natural Science Foundation of China (82170152), (81800122), (81973997) and (32000392) respectively.

## ACKNOWLEDGMENTS

The authors would like to show their gratitude and thanks to all of the patients for their kind participation. In the meanwhile, we would also like to thank Xujie Zhao at St. Jude Children's Research Hospital for scientific editing.

## SUPPLEMENTARY MATERIAL

The Supplementary Material for this article can be found online at: https://www.frontiersin.org/articles/10.3389/fcell.2022.712484/full#supplementary-material

## REFERENCES

Bery, N., Cruz-Migoni, A., Bataille, C. J., Quevedo, C. E., Tulmin, H., Miller, A., et al. (2018). BRET-based RAS Biosensors that Show a Novel Small Molecule Is an Inhibitor of RAS-Effector Protein-Protein Interactions. *Elife* 7. doi:10.7554/elife.40515

Bhojwani, D., and Pui, C.-H. (2013). Relapsed Childhood Acute Lymphoblastic Leukaemia. *Lancet Oncol.* 14, e205–e217. doi:10.1016/s1470-2045(12)70580-6

Brown, J. A., and Ferrando, A. (2018). Glucocorticoid Resistance in Acute Lymphoblastic Leukemia: BIM Finally. *Cancer Cell* 34, 869–871. doi:10.1016/j.ccell.2018.11.011

Brunet, A., Bonni, A., Zigmond, M. J., Lin, M. Z., Juo, P., Hu, L. S., et al. (1999). Akt Promotes Cell Survival by Phosphorylating and Inhibiting a Forkhead Transcription Factor. *Cell* 96, 857–868. doi:10.1016/s0092-8674(00)80595-4

Burgess, M. R., Hwang, E., Mroue, R., Bielski, C. M., Wandler, A. M., Huang, B. J., et al. (2017). KRAS Allelic Imbalance Enhances Fitness and Modulates MAP Kinase Dependence in Cancer. *Cell* 168, 817–829. doi:10.1016/j.cell.2017.01.020

Canon, J., Rex, K., Saiki, A. Y., Mohr, C., Cooke, K., Bagal, D., et al. (2019). The Clinical KRAS(G12C) Inhibitor AMG 510 Drives Anti-tumour Immunity. *Nature* 575, 217–223. doi:10.1038/s41586-019-1694-1

Case, M., Matheson, E., Minto, L., Hassan, R., Harrison, C. J., Bown, N., et al. (2008). Mutation of Genes Affecting the RAS Pathway Is Common in

Childhood Acute Lymphoblastic Leukemia. *Cancer Res.* 68, 6803–6809. doi:10.1158/0008-5472.can-08-0101

Chan, L. N., Murakami, M. A., Robinson, M. E., Caeser, R., Sadras, T., Lee, J., et al. (2020). Signalling Input from Divergent Pathways Subverts B Cell Transformation. *Nature* 583, 845–851. doi:10.1038/s41586-020-2513-4

Cox, A. D., and Der, C. J. (2003). The Dark Side of Ras: Regulation of Apoptosis. *Oncogene* 22, 8999–9006. doi:10.1038/sj.onc.1207111

Davidsson, J., Paulsson, K., Lindgren, D., Lilljebjörn, H., Chaplin, T., Forestier, E., et al. (2010). Relapsed Childhood High Hyperdiploid Acute Lymphoblastic Leukemia: Presence of Preleukemic Ancestral Clones and the Secondary Nature of Microdeletions and RTK-RAS Mutations. *Leukemia* 24, 924–931. doi:10.1038/leu.2010.39

Ding, L., Ley, T. J., Larson, D. E., Miller, C. A., Koboldt, D. C., Welch, J. S., et al. (2012). Clonal Evolution in Relapsed Acute Myeloid Leukaemia Revealed by Whole-Genome Sequencing. *Nature* 481, 506–510. doi:10.1038/nature10738

Ding, Z.-C. (2018). The Promise and Challenges of Chimeric Antigen Receptor T Cells in Relapsed B-Cell Acute Lymphoblastic Leukemia. *Ann. Transl. Med.* 6, 235. doi:10.21037/atm.2018.05.35

Downward, J. (2003). Targeting RAS Signalling Pathways in Cancer Therapy. *Nat. Rev. Cancer* 3, 11–22. doi:10.1038/nrc969

Garza, A. S., Miller, A. L., Johnson, B. H., and Thompson, E. B. (2009). Converting Cell Lines Representing Hematological Malignancies from Glucocorticoid-Resistant to Glucocorticoid-Sensitive: Signaling Pathway Interactions. *Leuk. Res.* 33, 717–727. doi:10.1016/j.leukres.2008.10.006

Hallin, J., Engstrom, L. D., Hargis, L., Calinisan, A., Aranda, R., Briere, D. M., et al. (2020). The KRASG12C Inhibitor MRTX849 Provides Insight toward Therapeutic Susceptibility of KRAS-Mutant Cancers in Mouse Models and Patients. *Cancer Discov.* 10, 54–71. doi:10.1158/2159-8290.cd-19-1167

Hunger, S. P., and Mullighan, C. G. (2015). Acute Lymphoblastic Leukemia in Children. *N. Engl. J. Med.* 373, 1541–1552. doi:10.1056/nejmra1400972

Irving, J. A. E., Enshaei, A., Parker, C. A., Sutton, R., Kuiper, R. P., Erhorn, A., et al. (2016). Integration of Genetic and Clinical Risk Factors Improves Prognostication in Relapsed Childhood B-Cell Precursor Acute Lymphoblastic Leukemia. *Blood* 128, 911–922. doi:10.1182/blood-2016-03-704973

Irving, J., Matheson, E., Minto, L., Blair, H., Case, M., Halsey, C., et al. (2014). Ras Pathway Mutations Are Prevalent in Relapsed Childhood Acute Lymphoblastic Leukemia and Confer Sensitivity to MEK Inhibition. *Blood* 124, 3420–3430. doi:10.1182/blood-2014-04-531871

Jain, N., Curran, E., Iyengar, N. M., Diaz-Flores, E., Kunnavakkam, R., Popplewell, L., et al. (2014). Phase II Study of the Oral MEK Inhibitor Selumetinib in Advanced Acute Myelogenous Leukemia: a University of Chicago Phase II Consortium Trial. *Clin. Cancer Res.* 20, 490–498. doi:10.1158/1078-0432.ccr-13-1311

Janes, M. R., Zhang, J., Li, L.-S., Hansen, R., Peters, U., Guo, X., et al. (2018). Targeting KRAS Mutant Cancers with a Covalent G12C-specific Inhibitor. *Cell* 172, 578–589. doi:10.1016/j.cell.2018.01.006

Jerchel, I. S., Hoogkamer, A. Q., Ariës, I. M., Steeghs, E. M. P., Boer, J. M., Besselink, N. J. M., et al. (2018). RAS Pathway Mutations as a Predictive Biomarker for Treatment Adaptation in Pediatric B-Cell Precursor Acute Lymphoblastic Leukemia. *Leukemia* 32, 931–940. doi:10.1038/leu.2017.303

Johnson, D. B., Smalley, K. S. M., and Sosman, J. A. (2014). Molecular Pathways: Targeting NRAS in Melanoma and Acute Myelogenous Leukemia. *Clin. Cancer Res.* 20, 4186–4192. doi:10.1158/1078-0432.ccr-13-3270

Karnoub, A. E., and Weinberg, R. A. (2008). Ras Oncogenes: Split Personalities. *Nat. Rev. Mol. Cel Biol* 9, 517–531. doi:10.1038/nrm2438

Kirchberger, M. C., Ugurel, S., Mangana, J., Heppt, M. V., Eigentler, T. K., Berking, C., et al. (2018). MEK Inhibition May Increase Survival of NRAS-Mutated Melanoma Patients Treated with Checkpoint Blockade: Results of a Retrospective Multicentre Analysis of 364 Patients. *Eur. J. Cancer* 98, 10–16. doi:10.1016/j.ejca.2018.04.010

Kong, G., Wunderlich, M., Yang, D., Ranheim, E. A., Young, K. H., Wang, J., et al. (2014). Combined MEK and JAK Inhibition Abrogates Murine Myeloproliferative Neoplasm. *J. Clin. Invest.* 124, 2762–2773. doi:10.1172/jci74182

Lai, Z., Markovets, A., Ahdesmaki, M., Chapman, B., Hofmann, O., McEwen, R., et al. (2016). VarDict: a Novel and Versatile Variant Caller for Next-Generation Sequencing in Cancer Research. *Nucleic Acids Res.* 44, e108. doi:10.1093/nar/gkw227

Lito, P., Solomon, M., Li, L.-S., Hansen, R., and Rosen, N. (2016). Allele-specific Inhibitors Inactivate Mutant KRAS G12C by a Trapping Mechanism. *Science* 351, 604–608. doi:10.1126/science.aad6204

Ma, X., Edmonson, M., Yergeau, D., Muzny, D. M., Hampton, O. A., Rusch, M., et al. (2015). Rise and Fall of Subclones from Diagnosis to Relapse in Pediatric B-Acute Lymphoblastic Leukaemia. *Nat. Commun.* 6, 6604. doi:10.1038/ncomms7604

Malinowska-Ozdowy, K., Frech, C., Schönegger, A., Eckert, C., Cazzaniga, G., Stanulla, M., et al. (2015). KRAS and CREBBP Mutations: a Relapse-Linked Malicious Liaison in Childhood High Hyperdiploid Acute Lymphoblastic Leukemia. *Leukemia* 29, 1656–1667. doi:10.1038/leu.2015.107

Mar, B. G., Bullinger, L. B., McLean, K. M., Grauman, P. V., Harris, M. H., Stevenson, K., et al. (2014). Mutations in Epigenetic Regulators Including SETD2 Are Gained during Relapse in Paediatric Acute Lymphoblastic Leukaemia. *Nat. Commun.* 5, 3469. doi:10.1038/ncomms4469

McCubrey, J. A., Steelman, L. S., Chappell, W. H., Abrams, S. L., Wong, E. W. T., Chang, F., et al. (2007). Roles of the Raf/MEK/ERK Pathway in Cell Growth, Malignant Transformation and Drug Resistance. *Biochim. Biophys. Acta (Bba) - Mol. Cel Res.* 1773, 1263–1284. doi:10.1016/j.bbamcr.2006.10.001

McLeod, C., Gout, A. M., Zhou, X., Thrasher, A., Rahbarinia, D., Brady, S. W., et al. (2021). St. Jude Cloud: A Pediatric Cancer Genomic Data-Sharing Ecosystem. *Cancer Discov.* 11 (5), 1082–1099. doi:10.1158/2159-8290.CD-20-1230

Meyer, J. A., Wang, J., Hogan, L. E., Yang, J. J., Dandekar, S., Patel, J. P., et al. (2013). Relapse-specific Mutations in NT5C2 in Childhood Acute Lymphoblastic Leukemia. *Nat. Genet.* 45, 290–294. doi:10.1038/ng.2558

Mullighan, C. G., Phillips, L. A., Su, X., Ma, J., Miller, C. B., Shurtleff, S. A., et al. (2008). Genomic Analysis of the Clonal Origins of Relapsed Acute Lymphoblastic Leukemia. *Science* 322, 1377–1380. doi:10.1126/science.1164266

Mullighan, C. G., Zhang, J., Kasper, L. H., Lerach, S., Payne-Turner, D., Phillips, L. A., et al. (2011). CREBBP Mutations in Relapsed Acute Lymphoblastic Leukaemia. *Nature* 471, 235–239. doi:10.1038/nature09727

Nakamura, A., Arita, T., Tsuchiya, S., Donelan, J., Chouitar, J., Carideo, E., et al. (2013). Antitumor Activity of the Selective Pan-RAF Inhibitor TAK-632 in BRAF Inhibitor-Resistant Melanoma. *Cancer Res.* 73, 7043–7055. doi:10.1158/0008-5472.can-13-1825

Oshima, K., Khiabanian, H., da Silva-Almeida, A. C., Tzoneva, G., Abate, F., Ambesi-Impiombato, A., et al. (2016). Mutational Landscape, Clonal Evolution Patterns, and Role of RAS Mutations in Relapsed Acute Lymphoblastic Leukemia. *Proc. Natl. Acad. Sci. USA* 113, 11306–11311. doi:10.1073/pnas.1608420113

Pierro, J., Hogan, L. E., Bhatla, T., and Carroll, W. L. (2017). New Targeted Therapies for Relapsed Pediatric Acute Lymphoblastic Leukemia. *Expert Rev. anticancer Ther.* 17, 725–736. doi:10.1080/14737140.2017.1347507

Posch, C., Moslehi, H., Feeney, L., Green, G. A., Ebaee, A., Feichtenschlager, V., et al. (2013). Combined Targeting of MEK and PI3K/mTOR Effector Pathways Is Necessary to Effectively Inhibit NRAS Mutant Melanoma *In Vitro* and *In Vivo*. *Proc. Natl. Acad. Sci.* 110, 4015–4020. doi:10.1073/pnas.1216013110

Prior, I. A., Lewis, P. D., and Mattos, C. (2012). A Comprehensive Survey of Ras Mutations in Cancer. *Cancer Res.* 72, 2457–2467. doi:10.1158/0008-5472.can-11-2612

Pui, C.-H., Yang, J. J., Bhakta, N., and Rodriguez-Galindo, C. (2018). Global Efforts toward the Cure of Childhood Acute Lymphoblastic Leukaemia. *Lancet Child. Adolesc. Health* 2, 440–454. doi:10.1016/s2352-4642(18)30066-x

Rausch, T., Zichner, T., Schlattl, A., Stutz, A. M., Benes, V., and Korbel, J. O. (2012). DELLY: Structural Variant Discovery by Integrated Paired-End and Split-Read Analysis. *Bioinformatics* 28, i333–i339. doi:10.1093/bioinformatics/bts378

Reshmi, S. C., Harvey, R. C., Roberts, K. G., Stonerock, E., Smith, A., Jenkins, H., et al. (2017). Targetable Kinase Gene Fusions in High-Risk B-ALL: a Study from the Children's Oncology Group. *Children's Oncol. Group* 129, 3352–3361. doi:10.1182/blood-2016-12-758979

Samatar, A. A., and Poulikakos, P. I. (2014). Targeting RAS-ERK Signalling in Cancer: Promises and Challenges. *Nat. Rev. Drug Discov.* 13, 928–942. doi:10.1038/nrd4281

Song, M., Pebworth, M.-P., Yang, X., Abnousi, A., Fan, C., Wen, J., et al. (2020). Cell-type-specific 3D Epigenomes in the Developing Human Cortex. *Nature* 587, 644–649. doi:10.1038/s41586-020-2825-4

Stephen, A. G., Esposito, D., Bagni, R. K., and McCormick, F. (2014). Dragging Ras Back in the Ring. *Cancer Cell* 25, 272–281. doi:10.1016/j.ccr.2014.02.017

Takashima, Y., Sasaki, Y., Hayano, A., Homma, J., Fukai, J., Iwadate, Y., et al. (2018). Target Amplicon Exome-Sequencing Identifies Promising Diagnosis and Prognostic Markers Involved in RTK-RAS and PI3K-AKT Signaling as central Oncopathways in Primary central Nervous System Lymphoma. *Oncotarget* 9, 27471–27486. doi:10.18632/oncotarget.25463

Tasian, S. K., and Hunger, S. P. (2017). Genomic Characterization of Paediatric Acute Lymphoblastic Leukaemia: an Opportunity for Precision Medicine Therapeutics. *Br. J. Haematol.* 176, 867–882. doi:10.1111/bjh.14474

Tzoneva, G., Perez-Garcia, A., Carpenter, Z., Khiabanian, H., Tosello, V., Allegretta, M., et al. (2013). Activating Mutations in the NT5C2 Nucleotidase Gene Drive Chemotherapy Resistance in Relapsed ALL. *Nat. Med.* 19, 368–371. doi:10.1038/nm.3078

Vora, A., Goulden, N., Wade, R., Mitchell, C., Hancock, J., Hough, R., et al. (2013). Treatment Reduction for Children and Young Adults with Low-Risk Acute Lymphoblastic Leukaemia Defined by Minimal Residual Disease (UKALL 2003): a Randomised Controlled Trial. *Lancet Oncol.* 14, 199–209. doi:10.1016/s1470-2045(12)70600-9

Wang, J., Kong, G., Liu, Y., Du, J., Chang, Y.-I., Tey, S. R., et al. (2013). NrasG12D/+ Promotes Leukemogenesis by Aberrantly Regulating Hematopoietic Stem Cell Functions. *Blood* 121, 5203–5207. doi:10.1182/blood-2012-12-475863

Ward, A. F., Braun, B. S., and Shannon, K. M. (2012). Targeting Oncogenic Ras Signaling in Hematologic Malignancies. *Blood* 120, 3397–3406. doi:10.1182/blood-2012-05-378596

Welsch, M. E., Kaplan, A., Chambers, J. M., Stokes, M. E., Bos, P. H., Zask, A., et al. (2017). Multivalent Small-Molecule Pan-RAS Inhibitors. *Cell* 168, 878–889. doi:10.1016/j.cell.2017.02.006

Xu, H., Zhang, H., Yang, W., Yadav, R., Morrison, A. C., Qian, M., et al. (2015). Inherited Coding Variants at the CDKN2A Locus Influence Susceptibility to Acute Lymphoblastic Leukaemia in Children. *Nat. Commun.* 6, 7553. doi:10.1038/ncomms8553

Xu, J., Shi, S., Matsumoto, N., Noda, M., and Kitayama, H. (2007). Identification of Rgl3 as a Potential Binding Partner for Rap-Family Small G-Proteins and Profilin II. *Cell Signal.* 19, 1575–1582. doi:10.1016/j.cellsig.2007.02.004

Zhang, F., and Cheong, J. K. (2016). The Renewed Battle against RAS-Mutant Cancers. *Cell. Mol. Life Sci.* 73, 1845–1858. doi:10.1007/s00018-016-2155-8

**Conflict of Interest:** The authors declare that the research was conducted in the absence of any commercial or financial relationships that could be construed as a potential conflict of interest.

**Publisher's Note:** All claims expressed in this article are solely those of the authors and do not necessarily represent those of their affiliated organizations, or those of the publisher, the editors and the reviewers. Any product that may be evaluated in this article, or claim that may be made by its manufacturer, is not guaranteed or endorsed by the publisher.

frontiers in Cell and Developmental Biology

ORIGINAL RESEARCH
published: 14 February 2022
doi: 10.3389/fcell.2022.811479

# The G-Protein–Coupled Estrogen Receptor Agonist G-1 Inhibits Proliferation and Causes Apoptosis in Leukemia Cell Lines of T Lineage

*Liliana Torres-López, Miguel Olivas-Aguirre, Kathya Villatoro-Gómez and Oxana Dobrovinskaya**

*Laboratory of Immunobiology and Ionic Transport Regulation, Centro Universitario de Investigaciones Biomédicas, Universidad de Colima, Colima, Mexico*

OPEN ACCESS

**Edited by:**
*Claudia Scotti,*
*University of Pavia, Italy*

**Reviewed by:**
*Yves Combarnous,*
*Centre National de la Recherche Scientifique (CNRS), France*
*Jessica S. Blackburn,*
*University of Kentucky, United States*

***Correspondence:**
*Oxana Dobrovinskaya*
*oxana@ucol.mx*

**Specialty section:**
*This article was submitted to Molecular and Cellular Pathology, a section of the journal Frontiers in Cell and Developmental Biology*

**Received:** 08 November 2021
**Accepted:** 13 January 2022
**Published:** 14 February 2022

**Citation:**
*Torres-López L, Olivas-Aguirre M, Villatoro-Gómez K and Dobrovinskaya O (2022) The G-Protein–Coupled Estrogen Receptor Agonist G-1 Inhibits Proliferation and Causes Apoptosis in Leukemia Cell Lines of T Lineage. Front. Cell Dev. Biol. 10:811479. doi: 10.3389/fcell.2022.811479*

The G-protein–coupled estrogen receptor (GPER) mediates non-genomic action of estrogen. Due to its differential expression in some tumors as compared to the original healthy tissues, the GPER has been proposed as a therapeutic target. Accordingly, the non-steroidal GPER agonist G-1, which has often demonstrated marked cytotoxicity in experimental models, has been suggested as a novel anticancer agent for several sensitive tumors. We recently revealed that cell lines derived from acute T-cell (query) lymphoblastic leukemia (T-ALL) express the GPER. Here, we address the question whether G-1 is cytotoxic to T-ALL. We have shown that G-1 causes an early rise of intracellular $Ca^{2+}$, arrests the cell cycle in G2/M, reduces viability, and provokes apoptosis in T-ALL cell lines. Importantly, G-1 caused destabilization and depolymerization of microtubules. We assume that it is a disturbance of the cytoskeleton that causes G-1 cytotoxic and cytostatic effects in our model. The observed cytotoxic effects, apparently, were not triggered by the interaction of G-1 with the GPER as pre-incubation with the highly selective GPER antagonist G-36 was ineffective in preventing the cytotoxicity of G-1. However, G-36 prevented the intracellular $Ca^{2+}$ rise provoked by G-1. Finally, G-1 showed only a moderate negative effect on the activation of non-leukemic $CD4^+$ lymphocytes. We suggest G-1 as a potential antileukemic drug.

**Keywords: acute lymphoblastic leukemia, GPER agonist G-1, proliferation, apoptosis, cell cycle, microtubules**

**Abbreviations:** ALL, acute lymphoblastic leukemia; ANOVA, analysis of variance; ATCC, American Type Culture Collection; CFSE, carboxy-fluorescein succinimidyl ester; CTCF, corrected total cell fluorescence; DCF, 2′,7′dichlorofluorescin diacetate; FBS, fetal bovine serum; FCCP, carbonyl cyanide 4 (trifluoromethoxy) phenylhydrazone; FCS, fetal calf serum; GPER, G-protein–coupled estrogen receptor(s); MFI, median fluorescence intensity; PBMC, peripheral blood mononuclear cells; PI, propidium iodide; PMA, phorbol myristate acetate; Rhod-123, rhodamine-123; ROS, reactive oxygen species; SEM, standard error of mean; T-ALL, acute lymphoblastic leukemia of T lineage; TCR, T-cell receptor; ΔΨm, mitochondrial membrane potential.

## INTRODUCTION

Acute lymphoblastic leukemia of T lineage (T-ALL) represents an aggressive hematologic neoplasia with a significant morbidity rate in children and adults. Although ALL of immature B lymphocytes is of the highest incidence among ALL pediatric patients, T-ALL shows a higher rate of refractory and relapse in all age groups (Raetz and Teachey, 2016; Vadillo et al., 2018), being an important clinical problem and a challenge in search for new drug targets.

Estrogens are pleiotropic steroid hormones that contribute to the maturation and differentiation of the immune cells (Yakimchuk et al., 2013). Their immunomodulating effects as suppressors or activators of immune responses seem to depend largely on the cell type and cellular context (Khan et al., 2012; Kovats, 2015). The biological effects of estrogens can occur through nuclear estrogen receptors (ERs) and the G-protein–coupled ER (GPER, initially denominated as GPR30), which mediate rapid non-genomic cell signaling events (Filardo et al., 2000; Revankar et al., 2005). The GPER expression was revealed in most if not all normal tissues, and it has also been shown that the GPER plays an important role in the progression of various types of cancer, especially those dependent on hormones (Prossnitz and Barton., 2011; Jala et al., 2012; Girgert et al., 2019; Hsu et al., 2019; Jung, 2019; Xu et al., 2019). Some authors reported an increased GPER expression in neoplastic cells as compared to the original healthy tissue (Jala et al., 2012). There are several works linking the GPER expression or specific subcellular GPER localization with the outcome in cancer patients (Filardo et al., 2006; Sjöström et al., 2014; Tutzauer et al., 2020). GPER has been proposed as a novel therapeutic target in different cancer types (Ariazi et al., 2010; Wang et al., 2012; Lv and Wang, 2014; Weißenborn et al., 2014; Chimento et al., 2015; Kurt et al., 2015; Mori et al., 2015; Rudelius et al., 2015).

As estrogens were demonstrated to bind and modulate both the nuclear ER and GPER, specific GPER ligands were necessary for research purpose to dissect physiological effects attributed to each specific receptor type. Accordingly, the highly selective non-steroid GPER agonist G-1 (Bologa et al., 2006) and antagonists G-15 (Dennis et al., 2009) and G-36 (Dennis et al., 2011) have been developed. Numerous studies reported antiproliferative and cytotoxic effects of G-1 in different experimental models (**Supplementary Table S1**), and therefore, it was suggested as a possible candidate for anticancer therapies (Wang et al., 2012; Lv and Wang, 2014; Mori et al., 2015; Chimento et al., 2015; Kurt et al., 2015; Zhou et al., 2021). Eventually, it was noted that in different experimental systems G-1 displayed diverse and even opposite effects, sometimes suppressing cell proliferation and causing cell death or, on the contrary, inducing cell growth and proliferation (**Supplementary Table S1**). There are numerous studies that reported a specific GPER-dependent cytotoxic effect of G-1 in different cancer models (Albanito et al., 2007; Dennis et al., 2011; Imesch et al., 2013; Luo et al., 2014; Wei et al., 2014; Weißenborn et al., 2014; Cirillo et al., 2017; Ribeiro et al., 2017; Lee et al., 2019; Liu et al., 2019; Han et al., 2021; Zhou et al., 2021). But several studies have evidenced that G-1 is able to cross the plasma membrane and suppress cell viability through mechanisms independent from the GPER (Holm et al., 2012; Wang et al., 2012; Gui et al., 2015; Mori et al., 2015; Lv et al., 2017). There is also evidence that cytoskeleton microtubules may represent the main intracellular G-1 target and that the microtubule network is disrupted by G-1 treatment (Holm et al., 2012; Wang et al., 2013; Lv et al., 2017).

Hematological malignances are not considered to be estrogen-dependent. However, it is very likely that they are influenced by estrogens because gender differences in their incidence and prognosis were reported (Yakimchuk et al., 2013). There is accumulated evidence for the ER expression in lymphoid progenitors, healthy and malignant lymphocytes, and for the role which they play in immune system physiology and in the pathogenesis of different lymphoproliferative disorders (Catusse et al., 2010; Yakimchuk et al., 2013; Rudelius et al., 2015; Ladikou and Kassi., 2017; Hasni and Yakumchuk., 2019). Modulation of hematopoietic progenitors by estrogens was suggested as a basis for novel antileukemic strategies for acute myeloid leukemia (Sánchez-Aguilera and Méndez-Ferrer, 2016).

We have recently demonstrated that healthy activated T lymphocytes express both the nuclear ER and GPER. In contrast, lymphoblasts of cell lines derived from male and female T-ALL patients preferentially expressed the GPER (Torres-López et al., 2019). The present work was designed to evaluate the biological effects of the selective GPER agonist G-1 in the T-ALL Jurkat cell line.

## MATERIALS AND METHODS

### Cell Lines and Culture Conditions

Human T-ALL cell lines Jurkat (clone E6-1, ATCC®TIB™, male, 14 years); MOLT-3 (ATCC®CRL-1552™, male, 19 years), and CCRF-CEM (ATCC®CCL-119™, female, 4 years) were purchased from ATCC. Cells were cultured in suspension in an Advanced RPMI 1640 medium supplemented with 5% (v/v) heat-inactivated fetal bovine serum (FBS), 2 mM GlutaMAX, 100 U/ml penicillin, 100 μg/ml streptomycin, and 10 mM HEPES (all from Gibco, Thermo Fisher Scientific, Waltham, MA, United States). In some experiments, Jurkat cells were maintained in a phenol red–free RPMI 1640 medium supplemented with 10% (v/v) heat-inactivated dialyzed fetal calf serum (FCS, Gibco). Adherent breast cancer cell lines MDA-MB-231 (ATCC®HTB-26™) and MCF-7 (ATCC® HTB-22™) were cultured in the DMEM supplemented with 10% (v/v) of heat-inactivated FBS, 100 U/ml of penicillin, 100 μg/ml streptomycin, and 1% of GlutaMAX. All cell lines were maintained in a logarithmic growth phase by medium refreshment, in a humidified incubator in atmosphere with 5% $CO_2$ at 37°C.

### Chemicals

G-1, 1-[(3aS,4R,9bR)-4-(6-bromo-1,3-benzodioxol-5-yl)-3a,4,5,9b-tetrahydro-3Hcyclopenta[c]quinolin-8-yl] ethanone (10008933) and G-36, (3aS,4R,9bR)-4-(6bromo-1,3-benzodioxol-5-yl)-8-propan-2-yl-3a,4,5,9b-tetrahydro-3H-cyclopenta[c] quinoline

(14397), both from Cayman Chemical, were dissolved in DMSO. Typically, stock solutions were prepared at a concentration of 20 mM and stored at −20°C. Working solutions were prepared from stock solutions in a growth medium immediately before the experiments. The effect of the vehicle (DMSO at 0.05% v/v), corresponding to the highest used concentrations of G-1 and G-36 (10 μM), was tested in all protocols and showed no effect. 2-aminoethyl diphenylborinate (2-APB, D9754), carbonyl cyanide 4-(trifluoromethoxy) phenylhydrazone (FCCP, C2920), and phorbol 12-myristate 13-acetate (PMA, P8139) were purchased from Sigma-Aldrich. 2-APB and FCCP were dissolved in ethanol, while PMA was dissolved in DMSO.

## Purification and Activation of Primary $CD4^+$ Lymphocytes

Peripheral blood mononuclear cells (PBMCs) were isolated by the Ficoll-Paque method (Ficoll-Paque PLUS, 17-1440-02, GE Healthcare) from heparinized blood of apparently healthy donors. The protocol was approved by the Bioethics and Biosecurity Committee of the Biomedical Research Centre in accordance with federal (Artículo 100, Ley General de Salud), state, and local laws. PBMCs were subjected to negative selection, to avoid untimely activation, using a human $CD4^+$ T-cell isolation kit (130-096-533, Miltenyi Biotec) following manufacturers' specifications. For synchronous polyclonal activation, $1 \times 10^5$ resting $CD4^+$ lymphocytes were seeded in 24-well plates pretreated with anti-CD3 monoclonal antibodies (BD 555336, 5 μg/ml in phosphate-buffered saline solution (PBS), 2 h at 37°C) and incubated with anti-CD28 monoclonal antibodies (BD 555725, 2 μg/ml in RPMI 1640 Medium) for 4 days. Co-stimulation with CD3/CD28 provides a potent antigen-independent activating stimulus by cross-linking T-cell receptors (TCR) of resting T lymphocytes.

## Fluorescent Immunocytochemistry

To evaluate subcellular GPER localization, trypsinized adherent MCF-7 and MDA-MB-231 cells and suspension cells were washed with PBS and fixed on silanized glass slides with ice-cold 100% methanol for 5 min at room temperature, washed three times again, and incubated for 30 min in the permeabilization/blocking buffer (1% of bovine serum albumin: BSA, 22.52 mg/ml glycine and 0.1% Tween 20 dissolved in PBS). After this, cells were incubated with primary anti-human GPER rabbit antibodies (Novus Biologicals NBP1-31239, dilution 1:200) and then with Texas Red–conjugated goat anti-rabbit IgG (Abcam ab7088, dilution 1:100), as secondary antibodies. For $Na^+/K^+$- ATPase detection, primary anti-human $Na^+/K^+$—ATPase α1 mouse antibodies (Santa Cruz Biotechnology sc-21712, dilution 1:100) and secondary Chromeo™ 488-conjugated goat anti-mouse IgG antibodies (Abcam ab60313, dilution 1:1500) were used. For visualization of microtubules, primary mouse anti-human α-tubulin monoclonal antibodies conjugated with Alexa Fluor 488 were used (Invitrogen 32-2588, dilution 1:100). All antibodies were diluted in a PBS-T (PBS-0.1% Tween 20) solution containing 1% BSA, and samples were incubated in a humidified chamber for 1-2 h at room temperature. A ProLong™ Gold Antifade mountant was used for mounting samples (Invitrogen P36934). Slides were observed by confocal microscopy. Two sets of microscopes were used: A Carl Zeiss LSM 700 system coupled to an inverted Observer Z1 microscope equipped with 488 and 555 nm lasers and with 40x objective or, alternatively, a custom-made confocal microscope (Solamere Technology Group, Salt Lake City, United States) based on a Yokogawa spin disk confocal scan head (CSUX1M1, Yokogawa Electronic Co., Tokyo, Japan), equipped with solid state Coherent Obis lasers (405, 488, 561, and 640 nm) and 100x objective was used. Images were analyzed by ZEN lite software 3.0 (ZEISS) and ImageJ software (National Institutes of Health). To assess microtubule integrity, the corrected total cell fluorescence (CTCF) was calculated, as described previously (Shakya et al., 2018) by the following formula:

$$CTCF = Integrated\ Density - (Area\ of\ selected\ cell * mean\ fluorescence\ of\ background\ readings).$$

## Cell Viability Assays

Cell viability was evaluated using a resazurin-based metabolic *in vitro* toxicology assay kit (Sigma TOX-8) and by live cell count (trypan blue dye exclusion test). Cells ($1 \times 10^5$) were seeded in 96-well plates in 180 μl of RPMI per well. When specified, samples were pretreated with G-36 (10 μM, 30 min). The vehicle (DMSO) or G-1 in different concentrations were added, and cells were cultivated for 4–72 h, as indicated. For metabolic assay, 20 μl of the resazurin buffer was added to each well to complete volume to 200 μl, and plates were incubated 4 h at 37°C. To evaluate resazurin (non-fluorescent) to resorufin (fluorescent, Ex/Em max = 560/590 nm) conversion, a GloMax®Discover Multimode Microplate reader (Cat. GM3000, Promega) was used. Samples were run in triplicates, in at least three independent experiments. RPMI medium fluorescence was subtracted for each condition, and data obtained from resorufin fluorescence were averaged, normalized to their controls, and expressed as % of cell viability.

## CFSE-Based Cell Proliferation Assay

Carboxy-fluorescein succinimidyl ester (CFSE)-based cell proliferation assay (ThermoFisher C34554) with some modifications was used (Quah et al., 2007; Torres-López et al., 2019). Cells ($1 \times 10^6$) were washed with PBS and resuspended in 1 ml of CFSE-contained PBS, in a final concentration of 0.5 μM or 1 μM for cell lines and $CD4^+$ lymphocytes, respectively. To ensure uniform staining of cells in the population, the samples were incubated for 30 min at room temperature with agitation by inverting the tube every 5 min. After the completion of staining, the cells were seeded in 24-well plates in a fresh, complete growth medium ($5 \times 10^5$/well) with a drug (vehicle or different concentrations of G-1) and cultivated during different time periods. $CD4^+$ lymphocytes were stained with CFSE and then activated, as described previously. G-1 was added after 24 h, and the further activation continued in its presence. At set intervals, cells were harvested, washed in PBS, and CFSE fluorescence intensity was measured by flow cytometry (FACSCanto II, BD Biosciences). A total of 10,000 events in the live cell gate were collected for every sample. Data analysis was performed by FlowJo 10.2 Software. The median fluorescence intensity (MFI) of treated populations was normalized to control for leukemic cell lines, while the proliferation index was calculated for $CD4^+$ lymphocytes.

## Monitoring of Cell Cycle Progression

Cells were treated with G-1 for 24–48 h. After that, cells were counted, washed with cold PBS, and fixed with ice-cold 70% ethanol overnight. The next day, cells were washed twice with PBS and permeabilized with 0.1% Triton X-100 in PBS (15 min). Finally, 500 µl of the PI working solution was added to each $1 \times 10^6$ cells and incubated at least 24 h at 4°C. The composition of the working solution was as follows: 0.15 µM PI (Invitrogen, PNN1011), 10 µg/ml RNase (Sigma, R4875), and 0.1% BSA (Research Organics, 1336A) in PBS. The DNA content was evaluated by flow cytometry (FACSCanto II, BD Biosciences). For this, the PI fluorescence intensity (Ex/Em max = 538/617 nm) was measured, where 50,000 events in the intact cells gate were collected in each sample. Basing on the DNA content, the peaks corresponding to G1 and G2 cell cycle phases were determined. To exclude debris, appropriate gating of cell population in FSC versus SSC was made, following by gating in the PI-area versus PI-weight plot to exclude doublets. Data analysis was performed with ModFit 5.0 Software in trial version. Sub-G1 events were excluded from the analysis of cell cycle progression.

## Apoptosis/Necrosis Assay

To evaluate the type of cell death after treatments, a dead cell apoptosis kit (Invitrogen V13245) was used, following manufacturer's specifications. Briefly, for each sample, $1 \times 10^6$ cells were washed and stained in 100 µl of 1X annexin binding buffer containing 3 µl Annexin V-Alexa Fluor 488 (Ex/Em max: 488/510 nm) and 0.2 µl PI (Ex/Em max= 535/617 nm) for 15 min protected from light. Cells were analyzed by flow cytometry (FACSCanto II, BD Biosciences). The compensation procedure (Alexa Fluor 488 vs PI) was performed previously for data acquisition. For excitation, a 488 nm laser was used. PI fluorescence was measured using a 556LP mirror and a 585/42 filter; Alexa Fluor 488 fluorescence was measured using a 502LP mirror and a 530/30 filter. Debris and doublets were gated out, and 10,000 events in the gate of single cells per sample were collected. Autofluorescence control was used to settle on the threshold for positive fluorescence. Populations were classified as viable (Annexin V-Alexa Fluor 488 and PI negative, or double negative), apoptotic (Annexin V-Alexa Fluor 488 positive, PI negative), necrotic (Annexin V-Alexa Fluor 488 negative, PI positive), and late apoptotic/necrotic (Annexin V-Alexa Fluor 488 and PI positive, or double positive). Data analysis was performed with FlowJo 10.2.

## Measurements of Intracellular Free $Ca^{2+}$ Concentration

For intracellular free $Ca^{2+}$ concentration ($[Ca^{2+}]_i$) measurements, leukemic cells were loaded with the intensiometric $Ca^{2+}$ indicator Fluo 4-AM (Thermo Fisher Scientific Cat. F14201). Briefly, the cells were counted, collected, washed twice with PBS, and resuspended in Hanks balanced salt solution (HBSS, containing NaCl 143 mM, KCl 6 mM, $MgSO_4$ 5 mM, HEPES 20 mM, BSA 0.1%, glucose 5 mM, $CaCl_2$ 1.5 mM, $pH = 7.4$, ≈300 mOsm) and 2 µM of Fluo 4-AM (Ex/Em max of the $Ca^{2+}$-bound form = 494/506 nm). Cells in HBSS were incubated for 30 min at room temperature in dark. Then, cells were washed to remove excessive (not incorporated) dye and resuspended in HBSS. Measurements were performed using a F7000, HITACHI spectrofluorometer (Hitachi High Technologies). Samples were placed in quartz cuvettes ($1 \times 10^6$ cells /ml), and data acquisition was performed every 2.5 s by exciting the samples at 488 nm and collecting emitted fluorescence at 510 nm. For $Ca^{2+}$- free conditions, $Ca^{2+}$-free HBSS containing 1 mM of EGTA was used. Data were normalized to initial fluorescence.

## Evaluation of Mitochondrial Membrane Potential Changes

To evaluate changes of the mitochondrial membrane potential (ΔΨm), the fluorescent dye rhodamine-123 (Rhod-123, Sigma R8004) was used. Binding of Rhod-123 (Ex/Em max = 507/530) to the mitochondria is directly proportional to ΔΨm. After treatments, cells were counted (trypan blue exclusion test), harvested ($2.5 \times 10^5$ cells), washed with PBS, and stained in 100 µl PBS containing 2 µM Rhod-123 (30 min at room temperature). Uncoupler FCCP (2 µM) was used as a positive control of mitochondrial membrane depolarization. To exclude dead necrotic cells, a double staining of Rhod-123 with PI (Dead Cell Apoptosis Kit, Invitrogen V13245) was performed. Changes in ΔΨm in PI-negative cells were estimated by flow cytometry (FACSCanto II, BD Biosciences). For excitation, a 488 nm laser was used. Rhod-123 fluorescence was measured using a 502LP mirror and 530/30 filter. A total of 10,000 events were collected in the gate of live cells for each sample. Data analysis was performed by FlowJo 10.2 Software.

## Measurement of ROS Production

To measure reactive oxygen species (ROS) production, cell-permeable 2',7'-Dichlorofluorescin diacetate (DCFDA, D6883, Merck) was used following manufacturer's recommendations. The method is based on the fact that the dye DCFH-DA is deacetylated by cellular esterases to a non-fluorescent compound which is later oxidized by ROS into its fluorescent form DCF (Ex/Em max = 495/529 nm). PMA (5 µM) was used as a positive control. After 1–2 h of treatment, Jurkat cells ($5 \times 10^5$) were washed with PBS and incubated with 5 µM DCFH-DA for 30 min at 37°C. DCF fluorescence in individual cells was estimated by flow cytometry (FACSCanto II, BD Biosciences). For excitation, a 488 nm laser was used, and the fluorescent signal was recollected

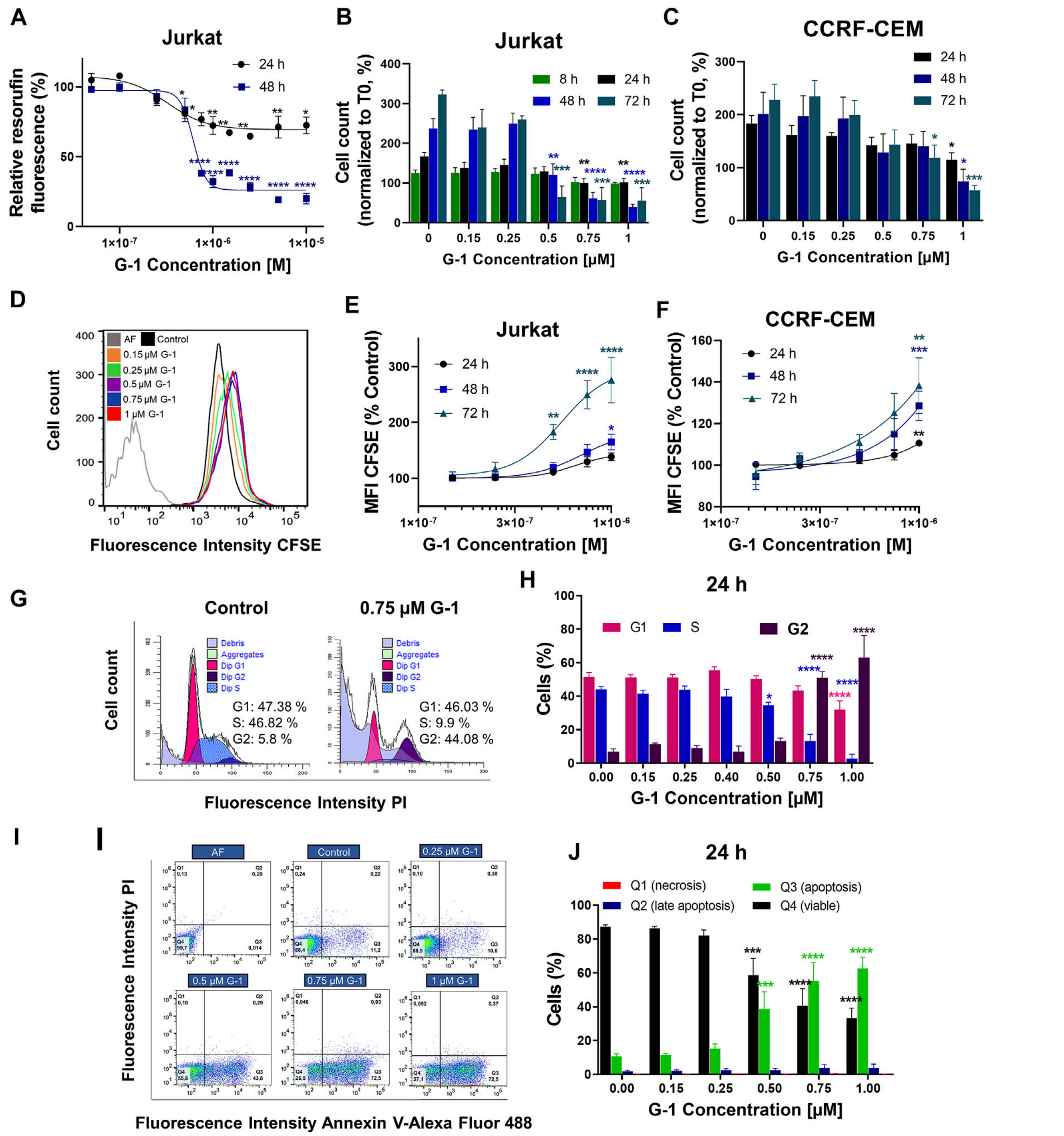

**FIGURE 1 |** G-1 possesses antileukemic properties. Cells were incubated in the presence of growing concentrations of G-1 for the indicated periods of time. **(A)** Cell viability was evaluated by the resazurin-based metabolic assay, as a function of G-1 concentration. Data (resorufin fluorescence intensity, arbitrary units) of treated samples are normalized to the vehicle-treated control. **(B,C)** Cell viability was evaluated by live cell count (trypan blue exclusion test) at indicated time points. Data are normalized to the initial time point (0 h). **(A–C)** Data are mean ± SEM; N ≥ 3; $^{*}p < 0.05$, $^{**}p < 0.01$, $^{***}p < 0.001$, $^{****}p < 0.0001$; one-way ANOVA with Dunnett *post hoc* testing. **(D)** A representative histogram of changes in the CFSE fluorescence intensity of Jurkat cells growing in the presence of increasing concentrations of G-1 after 72 h of treatment; the shift of the mean fluorescence peak (MFI) to the left reflects cell proliferation. The autofluorescent population (AF, without CFSE staining) is shown. **(E,F)** MFI of CFSE of Jurkat **(E)** and CCRF-CEM **(F)** cells treated with G-1 normalized to control (untreated) cells as a function of G-1 concentration. Data are mean ± SEM; N ≥ 3; $^{*}p < 0.05$, $^{**}p < 0.01$, $^{***}p < 0.001$, $^{****}p < 0.0001$; one-way ANOVA with Dunnett *post hoc* testing. **(G)** Representative ModFit histograms of untreated cells and cells incubated with G-1 (0.75 μM, 24 h). The G0/G1 peak is pink, G2/M peak is purple, S phase between G0/G1 and G2/M is blue, and subG1 damaged population is light-purple. **(H)** Bar charts showing the percentage of the Jurkat cells in different subpopulations corresponding to G1, S, and G2 phases at 24 h of G-1 treatment. **(I)** Representative dot plots obtained by flow cytometry of Jurkat cells treated with G-1 during 24 h. Populations are as follows: Q1 necrotic (Annexin V/AlexaFluor488$^{-}$ PI$^{+}$), Q2 late apoptotic/necrotic (Annexin V/AlexaFluor488$^{+}$PI$^{+}$), Q3 apoptotic (Annexin V/AlexaFluor488$^{+}$PI$^{-}$), and Q4 viable (Annexin V/AlexaFluor488$^{-}$PI$^{-}$). **(J)** Bar charts showing the percentage of cells in Q1–Q4 population after 24 h of G-1 treatment. **(H,J)** Data are mean ± SEM; *N* = 3; $^{*}p < 0.05$, $^{***}p < 0.001$, $^{****}p < 0.0001$. Comparison between control (without treatment) and G-1–treated samples was made by two-way ANOVA with Dunnett *post hoc* testing.

using a 502LP mirror and 530/30 filter. In total, 10,000 events were collected for each sample. Data analysis was performed with FlowJo 10.2 software, and MFI was normalized to control.

## Data Analysis and Statistics

All experiments were performed at least three times ($n \geq 3$) in an independent manner. Data were analyzed by GraphPad Prism 8.3 software and were expressed as mean values ± standard error (SEM). We compared the mean values in individual treatments with their control or, for the indicated experiments, the mean values between different treatments. The statistical significance was obtained with one-way analysis of variance (ANOVA) for comparison within the same group or two-way analysis for comparison between groups, with a *post hoc* analysis of Tukey for comparison between mean values of different groups, Dunnett for comparison of means values in respect to the control, or Sidak to compare the mean values of two different independent columns. The statistical significance was defined as $p < 0.05$.

# RESULTS

## G-1 Suppresses Proliferation and Induces Apoptosis in T-ALL Cell Lines

Comparative expression patterns of the ER in healthy and leukemic T lymphocytes were reported by our group recently, both on mRNA and protein levels (Torres-López et al., 2019). While healthy T cells express both the nuclear ER and GPER, leukemic ones preferentially express GPER localized, especially at the cell periphery, including the plasma membrane (Torres-López et al., 2019; **Supplementary Figure S1**). Taking in mind that G-1 can trigger different, sometimes opposite, cellular events depending on cell types (**Supplementary Table S1**), first we decided to prove whether G-1 is cytotoxic for T-ALL cell lines, Jurkat, and CCRF-CEM. Two widely recognized complementary tests were used, namely, resazurin-based metabolic assay (**Figure 1A**) and live/dead cell count (the trypan blue exclusion test, **Figures 1B,C**). For metabolic assay, Jurkat cells were cultured in the presence of G-1 in the range of 0.05–10 μM, as was reported for other cellular types (**Supplementary Table S1**), during 24 or 48 h. We observed that G-1 was toxic to Jurkat cells at concentrations ≥0.5 μM, and the highest effect was achieved at 1 μM (**Figure 1A**). Therefore, for further studies, the concentrations of up to 1 μM were chosen. G-1 caused a concentration-dependent reduction in both Jurkat and CCRF-CEM live cell counts, with the CCRF-CEM cell line being slightly less sensitive (**Figures 1B,C**). Considering the biological effects of 17-β-estradiol on Jurkat cells (Jenkins et al., 2001; Yedjou et al., 2015) and the weak estrogen-like activity of phenol red (Berthois et al., 1986), some additional experiments were undertaken in the phenol red–free RPMI medium supplemented with estrogen-free dialyzed FCS. Under these conditions, G-1 decreased the cell viability with similar $EC_{50}$ for both conditions (**Supplementary Figures S2A–D**, **Supplementary Table S2**). Reduction in metabolism and the cell number may be caused by a decrease in the proliferation rate and/or induction of cell death. Thus, the contribution of both these processes to the observed cytotoxicity of G-1 was further addressed.

Classical proliferation assay based on cell staining with a nontoxic fluorescent cell tracker CFSE, adapted for continuously proliferating cell lines, was performed (Torres-López et al., 2019). In this assay, the cell tracker is equally distributed between two daughter cells during cell division, resulting in halving of the fluorescence intensity of individual cells, which can be evaluated by flow cytometry. In a dividing cell population, the histogram of CFSE fluorescence intensity is shifted to the left when compared to initial values (**Figure 1D**). If the drug has an antiproliferative effect, this shift is reduced. In our experiments, CFSE-stained Jurkat and CCRF-CEM cells were cultured in the presence of growing G-1 concentrations and evaluated by flow cytometry every 24 h for 3 days. In both cell lines, G-1 caused an antiproliferative effect, in some degree more pronounced in Jurkat cells (**Figures 1E,F**). We also analyzed the cell cycle progression in Jurkat cells, to reveal which phase of the cell cycle is being delayed. For this, the DNA content at the single-cell level was estimated by flow cytometry in populations of Jurkat cells, treated with different concentrations of G-1. Representative cell cycle histograms obtained in the control and in the G-1-treated (0.75 μM) populations at 24 h of culture are shown at the **Figure 1G**. We observed an increased event number in the Sub-G1 interval (DNA content less that in G1 phase), indicating cell death. Accordingly, cell cycle analysis was performed in the population of intact cells. Notably, in this population, the G1 peak and events in the S phase were decreased, whereas the G2 peak was increased. The percentage distribution of cell cycle phases in intact cells was determined at different G-1 concentrations (**Figure 1H**). One can appreciate that treatment with G-1, starting with 0.5 μM, caused a significant cell accumulation in the G2 phase. A similar effect was observed in Jurkat cells cultured in a phenol red–free RPMI medium (**Supplementary Figures S2E,F**). Next, Annexin V/PI assay was performed to determine the type of cell death caused by G-1. We have observed that G-1 effectively caused apoptosis in Jurkat cells (**Figures 1I,J**; **Supplementary Figures S2G–I**). Taken together, our data prove that G-1 causes cell cycle arrest in the G2 phase and subsequent apoptotic cell death.

## GPER Antagonist G-36 Did Not Prevent Cytotoxic Effects of G-1

In order to reveal whether the cytotoxic effects of G-1 are triggered through GPER activation, the pharmacological blockage of this receptor by pretreatment with selective antagonists G-15 or G-36 is commonly used (see **Supplementary Table S1** for references). G-36 has a higher selectivity toward the GPER than G-15 (Dennis et al., 2011). Additionally, no significant effect of G-36 on cell viability has been reported (Moreno-Ulloa, et al., 2018; Torres-López et al., 2019; Zhou et al., 2021), in contrast to G-15, which by itself can reduce cell growth (Bai et al., 2013; Imesch et al., 2013; Mori et al., 2015). In our previous study, pre-incubation with G-36 (10 μM, 30 min) efficiently prevented the autophagy induced by

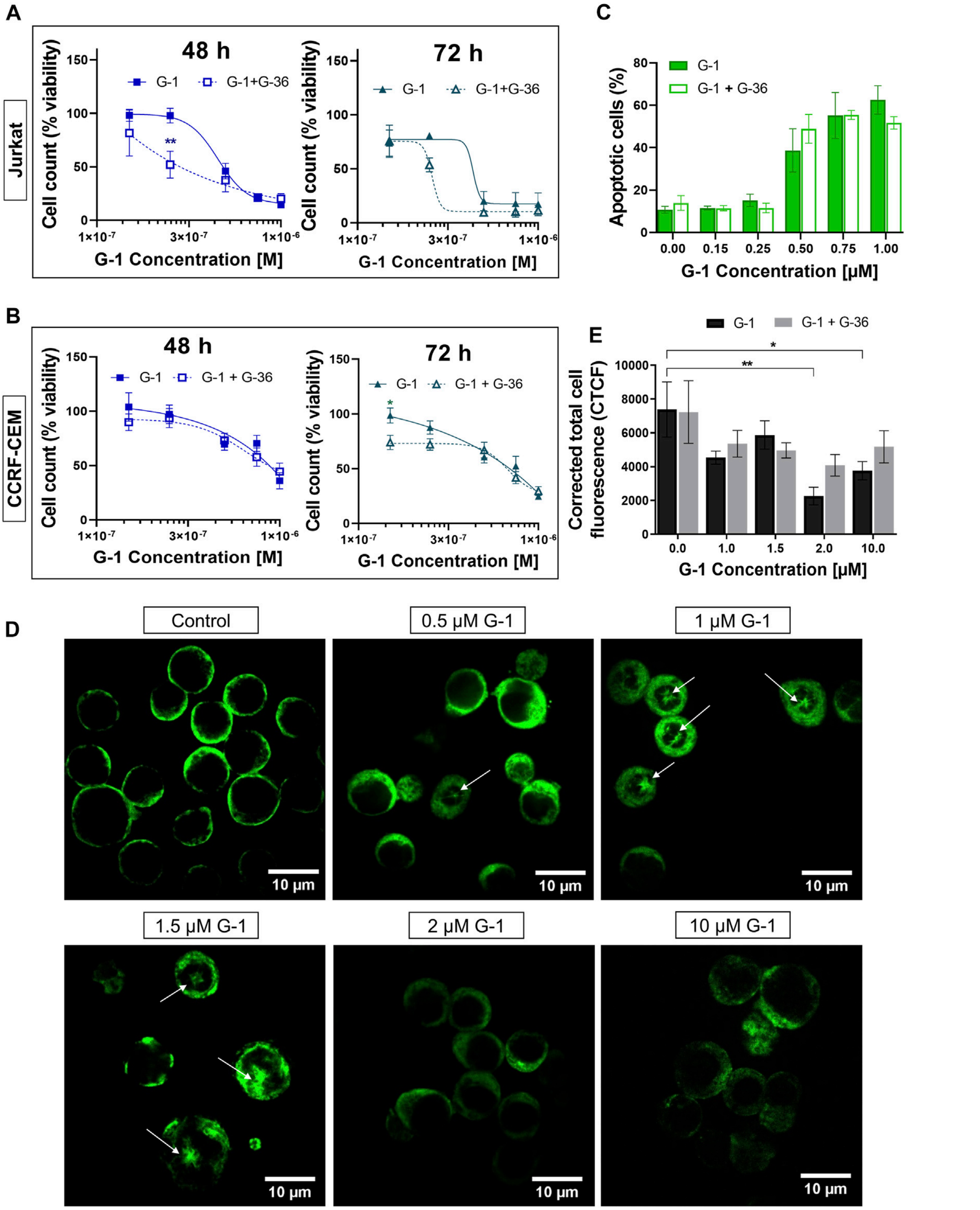


**FIGURE 2** | G-36 does not prevent antileukemic effects of G-1. **(A,B)** Jurkat **(A)** and CCRF-CEM **(B)** cells were pre-incubated with G-36 (10 μM, 30 min), seeded in a growth medium containing different concentrations of G-1 and cultivated during indicated periods of time. Cell viability was evaluated by cell count (trypan blue exclusion test) and graphed as function of G-1 concentration. Data are normalized to control and shown as mean ± SEM; N ≥ 3; *$p < 0.05$, **$p < 0.01$. Comparison between G-1 (solid line) and G1 + G-36 (dashed line) was performed by two-way ANOVA with Sidak *post hoc* testing. **(C)** Percentage of apoptotic cells (flow cytometry, Q3 population of Annexin V/AlexaFluor488$^{+}$PI$^{-}$ cells) at 24 h of treatment. Data are mean ± SEM; N ≥ 3; Comparison between G-1 and G-1 + G-36 groups was performed by two-way ANOVA with Sidak *post hoc* testing. No statistical difference was revealed. **(D)** Immunostaining of α-tubulin (green) in Jurkat cells treated with (*Continued*)

**FIGURE 2 |** different concentrations of G-1 during 24 h. Representative images obtained by laser scanning confocal microscopy and processed by ImageJ software. Mouse antihuman α-tubulin monoclonal antibodies conjugated with Alexa Fluor 488 were used. White arrows indicate microtubule asters. Scale bar: 10 μm. **(E)** Bar charts showing the mean ± SEM of corrected total cell fluorescence. Mean fluorescence of ~5–20 cells per field was evaluated; at least two fields per sample were analyzed in a minimum of three independent experiments. The means of each sample were compared to their control using a two-way ANOVA and a Dunnett *post hoc*, $^{*}p < 0.05$, $^{**}p < 0.01$. Similarly, each G-1 data was compared with the corresponding G-1 + G-36 one using two-way ANOVA and the Sidak *post hoc* test, but no statistically significant difference was obtained.

tamoxifen in Jurkat cells (Torres-López et al., 2019). Cell viability, proliferation, and apoptosis assays were performed in the same manner, as described above, but cells were pre-incubated with G-36 (10 μM, 30 min), then G-1 was added, and cells were cultured as usual in the presence of both drugs. First, G-36 itself did not affect cell proliferation and was not cytotoxic for Jurkat and CCRF-CEM cell lines (**Supplementary Figures S3A–E**). Contrary to expectations, G-36 neither prevented toxicity nor prevented antiproliferative effects of G-1 (**Figures 2A–C**; **Supplementary Figures S3F–K**). Interestingly, G-36-potentiated cytotoxicity of G-1, but only in the growth medium with phenol red supplemented with FBS (**Figures 2A,B**, **Supplementary Figure S3J**), and more evidently in Jurkat cells (see $EC_{50}$ values in **Supplementary Table S3**). Our finding evidenced that the G-1 cytotoxicity against T-ALL cells is most likely triggered by mechanisms independent of the GPER, similar to some previous reports (Holm et al., 2012; Wang et al., 2012; Gui et al., 2015; Mori et al., 2015; Lv et al., 2017).

## G-1 Disrupts the Microtubule Structure in Jurkat Cells

Originally, G-1 was developed as a selective GPER agonist that did not bind to the nuclear ER (Bologa et al., 2006). But being fat-soluble and permeable through the plasma membrane, G-1 can bind to other intracellular molecular structures and cause the so named "off-target" effects. Some research groups reported the ability of G-1 to destroy the microtubules in different cell models, including ovarian adenocarcinoma (Wang et al., 2013), mantle B cell lymphoma (Rudelius et al., 2015), and breast cancer (Lv et al., 2017). Therefore, it was intriguing to evaluate, whether G-1 produces a change in the microtubule structure in leukemic cells. **Figure 2D** shows representative laser scanning confocal microscopy images of Jurkat cells, treated with increasing concentrations of G-1 (24 h), fixed and immunostained for α-tubulin. The normal morphology of untreated Jurkat lymphoblasts is characterized by their round shape, big nucleus with a high nucleus-to-cytoplasm ratio, and fine filaments of microtubules, arrayed in the cytoplasm. After treatment with G-1, the microtubule structure was changed dramatically. Remarkably, the pattern of changes was different in samples, treated with different concentrations of G-1. First of all, multiple microtubule asters were observed in cells treated with lower (0.5–1.5 μM) concentrations. Asters are formed during the prophase of mitosis, and their accumulation evidences the suppression of normal microtubule dynamics, which is necessary for progression through mitosis phases and cellular division. This phenomenon has been previously reported in ovarian cancer (Wang et al., 2013) and triple-negative breast cancer (Lv et al., 2017) cell lines, treated with G-1. Similar to our observations (**Figures 1G,H**), the cells were accumulated in the G2/M phase of the cell cycle due to the impossibility to form the mitotic spindle. G-1 was determined to attach to the colchicine binding site of tubulin (Lv et al., 2017) and can be considered as a colchicine analog. At a high concentration, colchicine analogs induce depolymerization of microtubules (Stanton et al., 2011). Indeed, at higher concentrations of G-1 (2–10 μM), the long microtubule fibers were completely disrupted and what was visualized as diffusely distributed staining was accompanied by a significant decrease in the fluorescence intensity. Then, we decided to measure total fluorescence of individual cells, as an indicator of microtubule integrity, as it was proposed earlier (Kasioulis et al., 2017; Shakya et al., 2018). At high concentrations of G-1, a significant decrease of CTCF was observed (**Figure 2E**). Cell appearance has also changed markedly; both the cells and their nuclei shrunk and the nucleus-to-cytoplasm ratio decreased. To reveal whether the effect was mediated by the GPER, some cultures were pre-treated with the GPER antagonist G-36, as described earlier. Pre-incubation with G-36 did not prevent the attenuation of the fluorescence intensity provoked by G-1 (**Figure 2E**). Accordingly, the observed effect of microtubule depolymerization was more likely caused by direct interaction of G-1 with tubulin and was not mediated by the interaction with the GPER.

## G-1 Induced Rapid Intracellular Calcium Rise in a GPER-Dependent Manner

It was demonstrated in several non-lymphoid cellular models that activation of the GPER by natural estrogen or artificial modulators caused rapid non-genomic responses, including $Ca^{2+}$ mobilization (Ariazi et al., 2010; Ren and Wu., 2012; Yang et al., 2017). In the present study, we evaluated the intracellular $Ca^{2+}$ dynamics in response to G-1 administration (1 μM) in Jurkat cells, loaded with Fluo 4. As expected, G-1 elicited a rapid cytosolic $Ca^{2+}$ ($[Ca^{2+}]_c$) rise, which did not return to the basal level over at least 10 min (**Figures 3A–D**, red). The observed $Ca^{2+}$ response was efficiently inhibited by pre-incubation with G-36 (**Figures 3A–D**, blue). Thus, the response was mediated by the GPER. Increase of $[Ca^{2+}]_c$ may be caused by the influx of $Ca^{2+}$ from the extracellular space or by its release from the intracellular stores. It has been demonstrated previously that G-1 can cause endoplasmic reticulum stress, accompanied by $Ca^{2+}$ release from the endoplasmic reticulum into the cytosol, which, in turn, contributes to the triggering of cell death (Ariazi et al., 2010; Vo et al., 2019). It is also well known that in signaling pathways, triggered by G-protein–coupled receptors, the formation of inositol 1, 4, 5 trisphosphate (IP3) frequently occurs. IP3 binds to the IP3 receptor (IP3R) channel in the endoplasmic reticulum membrane,

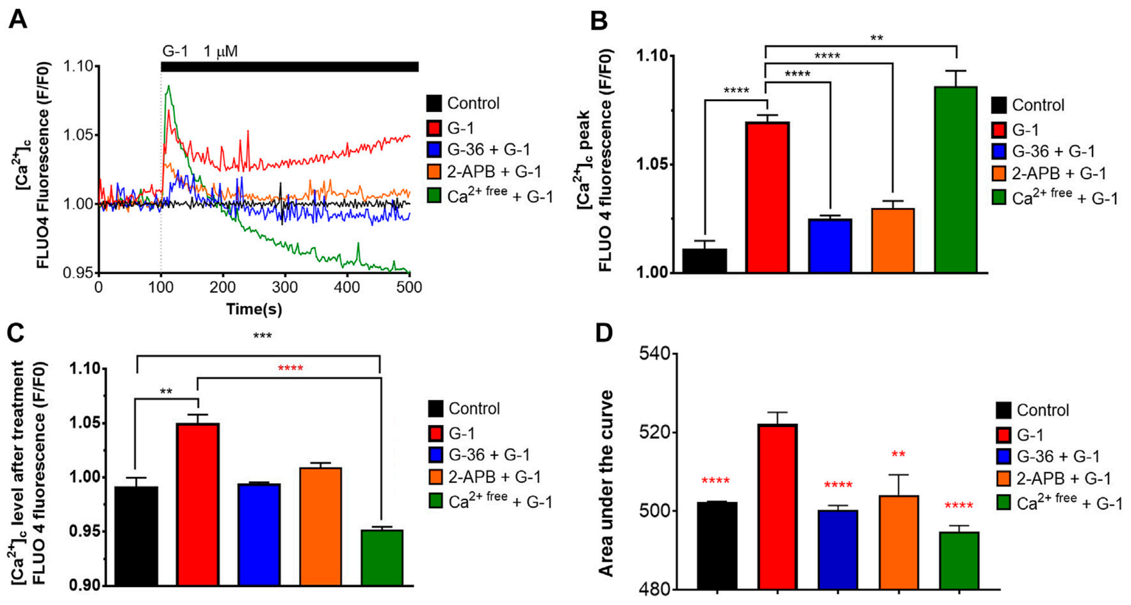


**FIGURE 3 |** Cytosolic $Ca^{2+}$ rise induced by G-1 in Jurkat cells is mediated by the GPER. **(A)** $[Ca^{2+}]_c$ monitoring in Jurkat cells loaded with Fluo 4. The time of G-1 injection is indicated. Traces represent the mean of at least six samples from three independent experiments. **(B–D)** Peak **(B)**, steady state at 500 s of monitoring **(C)** and the area under the curve, AUC **(D)** of $[Ca^{2+}]_c$ transients. Data are mean + SEM for at least six samples from independent experiments. For statistical analysis, one-way ANOVA was used. In **(B–D)**, the means were compared to the G-1–treated mean value. In **(C)**, comparisons with control (black asterisks) and with G-1–treated values (red asterisks) were conducted (**$p$ < 0.01, ***$p$ < 0.001, ****$p$ < 0.0001).

which, upon this activation, mediates the $Ca^{2+}$ release from the endoplasmic reticulum (Marks, 1997). To test this possibility, a permeable IP3R blocker 2-APB was used (Maruyama et al., 1997). We observed that 2-APB efficiently suppressed the $[Ca^{2+}]_c$ rise generated by G-1 (**Figures 3A–D**, orange). Hence, G-1, through the GPER, orchestrates the IP3-dependent $Ca^{2+}$ release from intracellular stores. It is also well known that the $Ca^{2+}$ release from the endoplasmic reticulum causes the activation of store-operated $Ca^{2+}$ channels in the plasma membrane. To estimate the contribution of $Ca^{2+}$ entry from the extracellular space to the observed $[Ca^{2+}]_c$ rise, the experiments were carried out in a $Ca^{2+}$-free medium (see methods). In contrast to the results obtained in the solutions containing $Ca^{2+}$, under $Ca^{2+}$-free conditions, G-1 provoked a rapid transient $[Ca^{2+}]_c$ rise followed by a decrease to levels lower than the basal one (**Figures 3A–D**, green). Summarizing, we demonstrate that G-1, through GPER and IP3R, initially triggered $Ca^{2+}$ release from the endoplasmic reticulum, which consequently activates the store-operated $Ca^{2+}$ entry. Correspondingly, the GPER-mediated $Ca^{2+}$ rise and the functional impact of such $Ca^{2+}$ signals have been recently addressed (DingGao et al., 2019; Vo et al., 2019; Tran 2020).

## G-1 Causes Rapid Generation of ROS

ROS production is an important mechanism, involved in cytotoxicity of many anticancer drugs (Kim et al., 2019). Intracellular ROS accumulation was observed in assays with human breast adenocarcinoma and colorectal cancer cells treated with G-1 (Wei et al., 2014; Liu et al., 2017). We evaluated the effect of G-1 on intracellular ROS production by loading the Jurkat cells with the non-fluorescent compound DCFH-DA and measuring the fluorescence intensity of its oxidized (fluorescent) form DCF by flow cytometry (**Figures 4A,B**). We observed a significant increase in intracellular ROS production within 1 h of G-1 treatment. The same elevated levels of ROS were recorded in cultures pre-incubated with G-36, indicating that the GPER was not involved in the underlying mechanism (**Figure 4B**). G-36 alone did not stimulate the production of ROS (data not shown). ROS are known to have a very short half-life (Novo and Parola, 2008); then, ROS-related fluorescence decreased to its initial value after 2 h of incubation (**Figure 4C**).

## G-1 Damages the Mitochondria

Mitochondria are important players in neoplastic re-programming of T-ALL. They are involved in the crosstalk between cell bioenergetics, biosynthesis, proliferation, and regulated cell death (Olivas-Aguirre et al., 2019). ΔΨm loss is a classical indicator of mitochondrial damage, and it was observed in tumor cells treated with G-1 (Wei et al., 2014; Liu et al., 2017). ΔΨm changes in Jurkat cells were monitored within 4–48 h of treatment with G-1, using a mitochondrial-specific fluorescent probe Rhod-123 and flow cytometry. Since dead necrotic cells lose ΔΨm independently on the underlying cell death mechanism, they were excluded from the analysis. In other words, cells were co-stained with PI and only PI-negative population, which includes live and early apoptotic cells, was analyzed (**Figure 5A**, Q3). This approach allows the determination of the initial moment of mitochondrial damage. The protonophore FCCP (20 μM) was used as a positive control. In our experimental conditions, the statistically significant ΔΨm

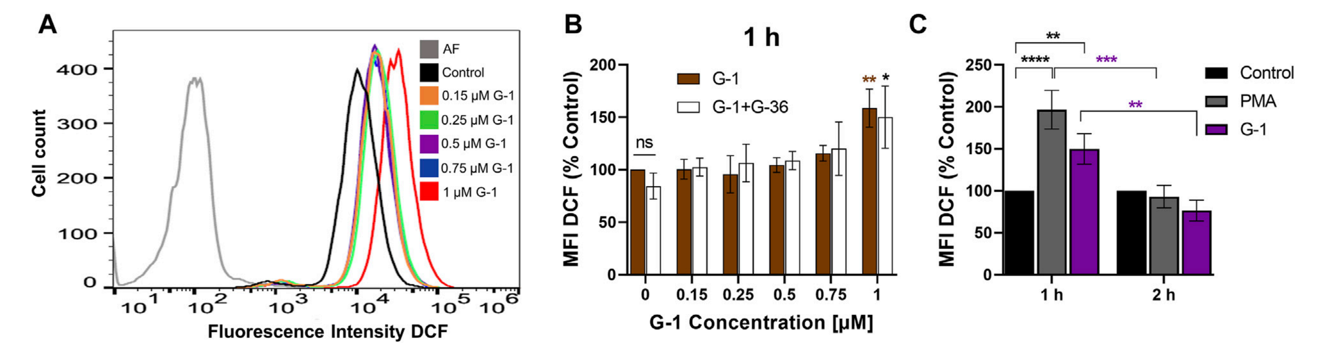


**FIGURE 4 |** G-1 induces ROS production in Jurkat cells. Cells were treated as indicated during 1 or 2 h and stained with the indicator of ROS activity DCF-DA (5 µM, 30 min). DCF fluorescence was collected by flow cytometry, and mean fluorescence intensity (MFI) was determined. **(A)** Representative histogram obtained with G-1–treated cells. The autofluorescent population (AF) is shown in gray. **(B)** Jurkat cells were pre-incubated with G-36 (10 µM, 30 min), or not, and treated with growing concentrations of G-1 for 1 h. MFI values of treated cells were normalized to control (untreated cells) and shown as mean ± SEM. Comparison of the mean of treated samples to untreated control was performed using two-way ANOVA and a Dunnett *post hoc* test, **p* < 0.05, ***p* < 0.01. Comparison of G-36 pre-incubated with the corresponding not pre-incubated samples was also performed for each G-1 concentration, using two-way ANOVA and Sidak *post hoc* testing; no statistical significance was found. **(C)** MFI DCF values were obtained after 1 and 2 h of incubation with G-1 (1 µM) or PMA (5 µM) as a positive control and normalized to untreated control. Data are mean ± SEM, N ≥ 3. Statistical analysis was performed by comparing the mean of treated and control samples using two-way ANOVA and Tukey *post hoc* analysis (black asterisks); the same treatments after 1 and 2 h were also compared using two-way ANOVA and Sidak *post hoc* analysis (purple asterisks); ***p* < 0.01, ****p* < 0.001, *****p* < 0.0001.

decrease (evaluated by normalized Rhod MFI in PI-negative cells) was observed at 48 h of treatment with 0.75–1 µM G-1 (**Figure 5B**). Unexpectedly, nontoxic concentration of the GPER antagonist G-36 produced a notable decrease of ΔΨm in Jurkat cells already after 4 h of incubation (**Figure 5C**). It can be assumed that it was due to this effect on the mitochondria that G-36 potentiated the cytotoxic effect of G-1 in Jurkat cells (**Figure 2A**).

## Activated CD4⁺ T Cells are Less Sensitive to the G-1 Antiproliferative Effect.

Non-leukemic CD4⁺ lymphocytes were activated and subsequently treated with G-1 during 24–72 h, and the number of viable cells was estimated every 24 h (**Figure 6A**). It was demonstrated that non-leukemic lymphocytes presented a lower sensitivity to G-1 than leukemic Jurkat cells (**Figure 6B**, **Supplementary Table S4**). Additionally, the classical CFSE-based assay was undertaken, in which CD4⁺ lymphocytes isolated from non-leukemic patients were activated in the presence of increasing concentrations of G-1 over 72 h (**Figure 6C**). The proliferation rate was evaluated by calculating the proliferation index, which was decreased at high G-1 concentrations (**Figure 6D**). Comparative analysis revealed that G-1 has a stronger antiproliferative effect on Jurkat cells than on healthy T lymphocytes (**Figure 6E**, **Supplementary Table S4**).

## DISCUSSION

The anticancer effect of G-1 was previously demonstrated on tumors of various histogenesis (**Supplementary Table S1**) but not on T-ALL. In the present work, using leukemic Jurkat and CCRF-CEM cell lines, we have demonstrated that G-1 possesses antileukemic properties. In particular, G-1 suppresses cell proliferation by arresting cell cycle progression in the G2/M phase and induces apoptosis (**Figure 1**). G-1 sensitivity was slightly different in the two cell lines used, with Jurkat being more sensitive, which may reflect the variability between patients. G-1 is a highly selective GPER agonist, and many research groups have demonstrated that its cytotoxic and anti-proliferative effects are mediated by this receptor in the lungs (Liu et al., 2019), breast (Wei et al., 2014; Weißenborn et al., 2014), gastric (Lee et al., 2019), ovarian (Albanito et al., 2007; Han et al., 2021), and mantle cell lymphoma (Zhou et al., 2021) cell lines. However, there is also evidence that G-1 directly targets and disrupts microtubules in endothelial (Holm et al., 2012), ovarian (Wang et al., 2013), and breast cancer (Lv et al., 2017) cells. An essential role of microtubules in many cellular processes such as motility, intracellular trafficking, cell growth, and division is widely recognized. Importantly, the functions of microtubules are crucially dependent on their precisely regulated polymerization dynamics (Mukhtar et al., 2014). The direct suppressive effect of G-1 on the assembly of microtubules was demonstrated using the *in vitro* microtubule assembly test (Lv et al., 2017). More precisely, it was shown that G-1 attaches to the colchicine binding site on tubulin, preventing its polymerization and subsequent assembly of the mitotic spindle. As a result, cells are arrested in the G2 phase and early mitosis (Wang et al., 2013; Lv et al., 2017). Here, we present evidence for similar mechanisms of the G-1 action on Jurkat cells, where antiproliferative and damaging effects were reached at the narrow range of G-1 concentrations (0.25–1 µM) (**Figures 1A–C,I,J**). Highly cooperative G-1 effects seem to be associated with a disturbed dynamics and damage of microtubules, manifested from 0.5 µM (**Figure 2D**). Remarkably, cytoskeleton disorders, cell cycle

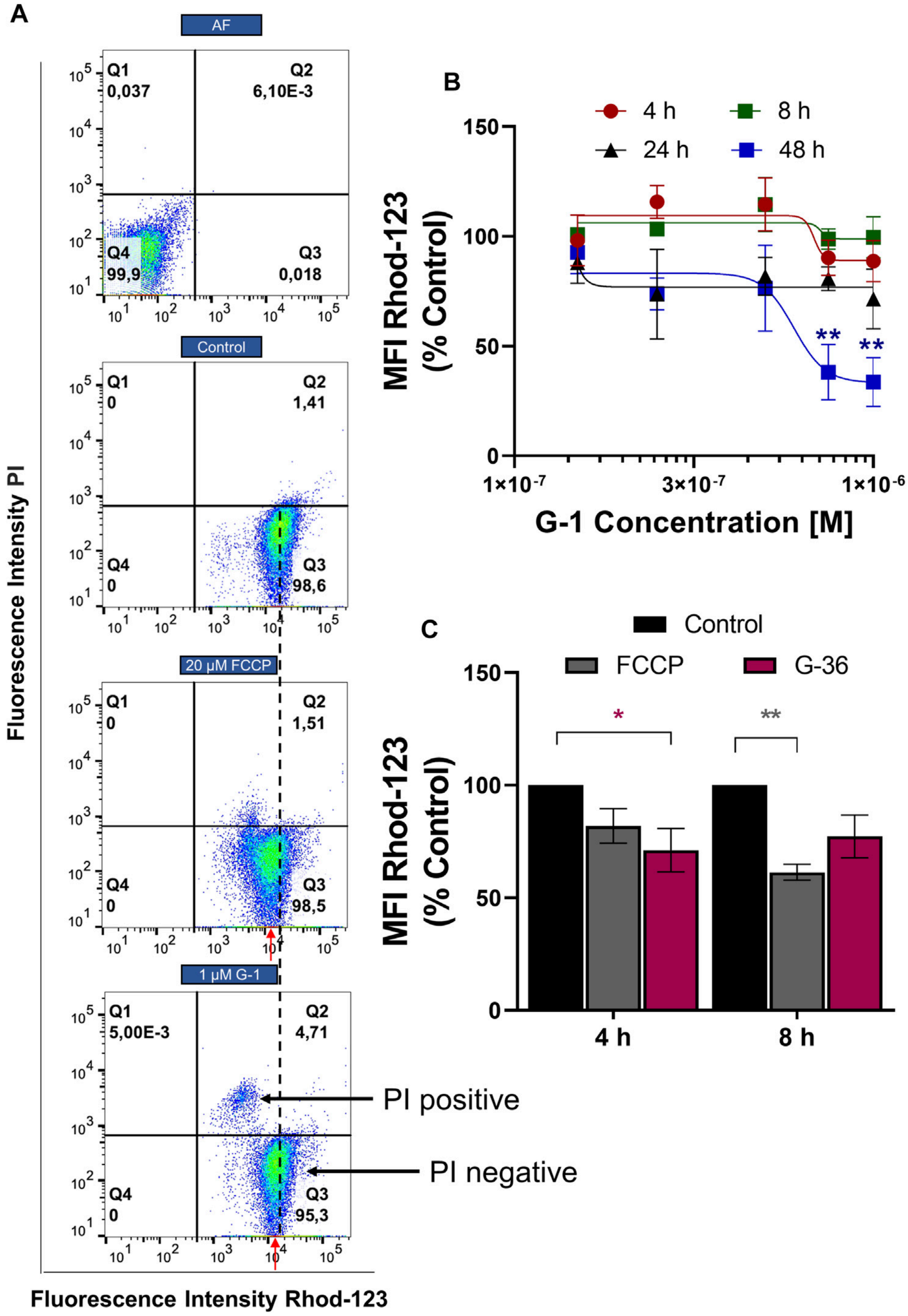


**FIGURE 5 |** ΔΨm monitoring in Jurkat cells treated with G-1 or G-36. Jurkat cells were treated as indicated for different time intervals, stained with Rhod-123 and PI, and analyzed by flow cytometry. **(A)** Representative dot plots obtained by flow cytometry at 12 h of incubation. FCCP was used as a positive control. The MFI value (Rhod-123) for control population is drawn by a black dotted line. MFI values (Rhod123) for treated populations are indicated by red arrows to demonstrate the shift to the left from the control value. **(B)** MFI mean values (Rhod-123) for PI-negative populations (Q3 as indicated in A) are normalized to control and graphed as a function of G-1 concentrations. Data are mean ± SEM; N ≥ 3. For each time, comparison of control vs. treated samples was performed by one-way ANOVA with Dunnett *post hoc* testing, $^{**}p < 0.01$. **(C)** Bar charts showing the change in ΔΨm induced by G-36 (10 µM) and FCCP (20 µM). Data are mean ± SEM; N ≥ 3. Two-way ANOVA and a *post hoc* Sidak analysis were performed to compare MFI values (G-36 or FCCP) with corresponding control. $^{*}p < 0.05$, $^{**}p < 0.01$.

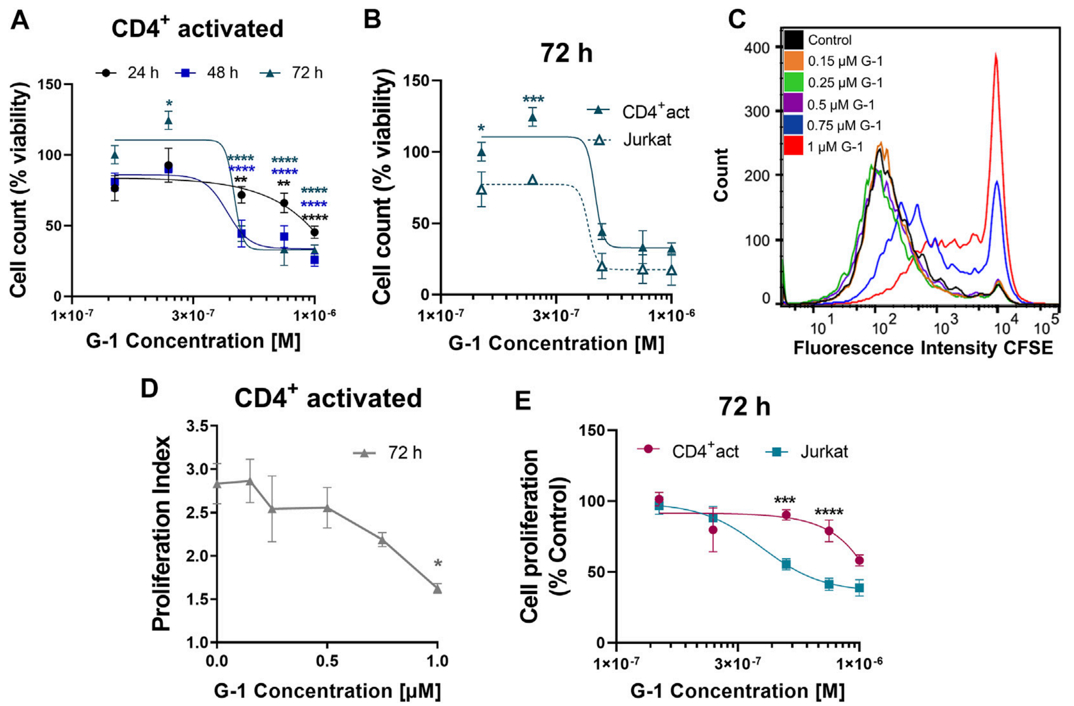


**FIGURE 6 |** Effect of G-1 on cell viability and proliferation of $CD4^+$ lymphocytes. **(A)** Viability of activated non-leukemic $CD4^+$ lymphocytes evaluated by cell count (the trypan blue exclusion test) and expressed as a function of G-1 concentration. Data are mean ± SEM. Comparison between control and treated samples was performed by one-way ANOVA with Dunnett *post hoc* testing. N ≥ 3; $^*p < 0.05$, $^{**}p < 0.01$, $^{****}p < 0.0001$. **(B)** Comparison of viability (cell count) non-leukemic $CD4^+$ lymphocytes and Jurkat cells treated with different concentrations of G-1 was performed by two-way ANOVA with the Sidak *post hoc* test. Data are mean ± SEM; N ≥ 3; $^*p < 0.05$, $^{***}p < 0.001$. **(C)** Representative flow cytometry histogram of CFSE fluorescence intensity measured in activated $CD4^+$ lymphocytes treated with different concentrations of G-1 for 72 h. **(D)** Proliferation index expressed as a function of G-1 concentration (FlowJo Software, proliferation tool). Data are mean ± SEM; $N = 3$; $^*p < 0.05$. Statistical significance was obtained by means of comparing each G-1 concentration to their control with a one-way ANOVA and a Dunnett *post hoc* testing. **(E)** Comparison of the decrease in cell proliferation caused by G-1 in $CD4^+$ lymphocytes and Jurkat cells. Data are mean ± SEM; $^{***}p < 0.001$, $^{****}p < 0.0001$. Comparison between the $CD4^+$-activated lymphocyte group (pink line) and Jurkat cell line (blue line) was made by two-way ANOVA with Sidak *post hoc* testing.

arrest, and apoptosis were not prevented by a specific GPER antagonist G-36 (**Figures 2A–C,E; Supplementary Figures S3F–K**).

GPER belongs to the superfamily of seven transmembrane receptors (7TMR). Activation of 7TMR often leads to a $Ca^{2+}$ response (Gudermann and Bader, 2015). Such an effect has been observed when activating the GPER (Revankar et al., 2005; Ariazi et al., 2010; Dennis et al., 2011; Luo et al., 2014; Ding et al., 2019; Vo et al., 2019; Tran 2020). In our experiments, G-1 caused a rapid increase in $[Ca^{2+}]_c$, which was initially mediated by the $Ca^{2+}$ release from the endoplasmic reticulum through the IP3R channel, followed by a prolonged influx of $Ca^{2+}$ from the extracellular space (**Figure 3**), most likely due to the activation of so named store-operated calcium entry (SOCE), which is the main $Ca^{2+}$ entry channel in lymphocytes (Zweifach and Lewis, 1993). Notably, G-36 effectively prevented this G-1-mediated $Ca^{2+}$ response (**Figure 3**), pointing out that this effect is triggered through the GPER. Hence, it is unlikely that this early $[Ca^{2+}]_c$ rise is related to the cytotoxic effects of G-1, which were independent of the GPER (**Figure 2**). However, considering that mitochondria acts as the main regulator of intracellular $Ca^{2+}$, we cannot rule out that the prolonged $Ca^{2+}$ entry influences the mitochondrial energetic or redox status.

Chemical compounds targeting microtubules are an important strategy in chemotherapeutic protocols. Due to the high toxicity and undesirable side effects of the currently used drugs, the search for new tubulin polymerization inhibitors, both natural and synthetic, continues (Kaur et al., 2014). Microtubule-destabilizing agents such as vinca alkaloids, including vincristine, vinblastine, and vinorelbine, are often used in chemotherapeutic protocols for hematological malignancies (Stanton et al., 2011). G-1 can be suggested as a possible alternative in chemotherapeutic protocols for T-ALL treatment, although additional experiments are still needed to identify the benefits of its use. To date, *in vivo* studies in xenograft mouse models have shown that the concentrations of G-1, which effectively suppress the growth of breast and ovarian cancer, do not affect the body weight, social behavior, and reproductive physiology, indicating a relatively low toxicity of G-1 for healthy tissues (Lv et al., 2017). Notably, T-ALL leukemic cells are quite sensitive to G-1, when compared to other types of cancers (**Supplementary Table S1**), and are also more sensitive than healthy T lymphocytes.

Finally, the phase 1 clinical trial (NCT04130516) is currently in progress to assess the safety, tolerability, pharmacokinetics, and antitumor effects of LNS8801 (SRR G-1, Linnaeus Therapeutics Inc.) in patients with advanced or recurrent treatment-refractory solid malignancies, upon oral administration. Very encouraging data from these studies, which demonstrated good tolerability and antitumor activity of LNS8801 both as monotherapy or in combination with pembrolizumab, have been reported recently (Muller et al., 2021). Since G-1 shows antileukemic activity in pre-clinical studies and LNS8801 (SRR G-1) is well tolerated in patients, T-ALL may, in the near future, be recommended to the list of malignancies for clinical trials with this compound.

## DATA AVAILABILITY STATEMENT

The original contributions presented in the study are included in the article/**Supplementary Material**; further inquiries can be directed to the corresponding author.

## ETHICS STATEMENT

The studies involving human participants were reviewed and approved by the Bioethics and Biosecurity Committee of the Biomedical Research Centre (University of Colima). The patients/participants provided their written informed consent to participate in this study.

## AUTHOR CONTRIBUTIONS

OD conceived and designed the study and received grants. LT-L conceived, designed, and performed most of experiments, analyzed the data, and prepared the figures. MO-A performed $Ca^{2+}$ measurement experiments and took the confocal microscopy images, analyzed the data, and prepared the figures. KV-G performed experiments in the phenol red–free medium. All authors contributed to data analysis and wrote the manuscript.

## FUNDING

This study was funded by CONACyT: Grants FC 2015-1/114 and FORDECyT #303072 to OD, and fellowships to LT-L, MO-A, and KV-G.

## ACKNOWLEDGMENTS

We are thankful for MC Liliana Liñán-Rico for acquisition of flow cytometry data and Dr. Arturo Hernández-Cruz (Institute of Cellular Physiology, UNAM) for sharing the custom-made confocal microscope (Solamere Technology Group, Salt Lake City, United States). We also thank Dr. Igor Pottosin (University of Colima) for critical reading of the MS and his indispensable help in MS editing for English language and style.

## SUPPLEMENTARY MATERIAL

The Supplementary Material for this article can be found online at: https://www.frontiersin.org/articles/10.3389/fcell.2022.811479/full#supplementary-material

**Supplementary Figure S1 |** Subcellular localization of GPER in breast cancer and T leukemic cell lines. Confocal micrographs showing localization of GPER (red), $Na^+$/$K^+$ ATPase (green), and their merged images. MCF-7 and MDA-MB-231 breast cancer cell lines were included in the panel for comparison. $Na^+$/$K^+$ ATPase localization was used for reference. Images taken with 40x objective and edited with ZEN lite software 3.0. Nucleus: DAPI. Scale bar: 20 µm.

**Supplementary Figure S2 |** Cytotoxic effect of G-1 in two different RPMI media. Jurkat cells were cultured in RPMI medium without phenol red and supplemented with 10% FCS dialyzed and treated with growing concentrations of G-1 for the indicated periods of time. **(A)** Cell viability evaluated by live cell count (trypan blue exclusion test) at indicated time points. Data (normalized to 0 h time point) are mean ± SEM; N ≥ 3; $^{*}p < 0.05$, $^{***}p < 0.001$, $^{****}p < 0.0001$; one-way ANOVA with Dunnett post hoc testing. **(B–D)** Cell count of Jurkat cells treated with different concentrations of G-1 for 24 h **(B)**, 48 h **(C)** and 72 h **(D)** cultured in Advanced RPMI medium with phenol red and supplemented with 5% FBS (red lines), and RPMI medium without phenol red and supplemented with 10% FCS dialyzed (black lines). Data are mean ± SEM; N ≥ 3. Comparison was done by two-way ANOVA with Sidak post hoc test; no statistically significant difference was obtained. **(E,F)** Jurkat cells were incubated without treatment (control) and in presence of G-1 (0.15–1 µM) for 24 h. Cells were fixed, stained with PI and processed for flow cytometry. **(E)** Representative ModFit histograms of untreated cells and cells incubated with G-1 (1 µM, 24 h). G0/G1 peak is pink, G2/M peak is purple, S phase and subG1 damaged population is light-purple. **(F)** Bar charts showing the percentage of the Jurkat cells in different subpopulations corresponding to G1, S and G2 phases at 24 h of G-1 treatment. **(G)** Jurkat cells treated with G-1 for 24 h. Bar charts showing percentage of cells in Q1 necrotic (Annexin V/AlexaFluor488$^-$PI$^+$); Q2 late apoptotic/necrotic (Annexin V/AlexaFluor488$^+$PI$^+$); Q3 apoptotic (Annexin V/AlexaFluor488$^+$PI$^-$); Q4 viable (Annexin V/AlexaFluor488$^-$PI$^-$). Data are shown as mean ± SEM; N ≥ 3; $^{****}p < 0.0001$. Comparison between control (without treatment) and G-1 - treated samples was made by two-way ANOVA with Dunnett post hoc testing. **(H,I)** Percentage of viable cells (Annexin V/AlexaFluor488$^-$PI$^-$ cells) **(H)** and apoptotic cells (Annexin V/AlexaFluor488$^+$PI$^-$) **(I)** at 24 h of treatment. Data are mean ± SEM; N ≥ 3; Comparison between Jurkat cells cultured in Advanced RPMI medium with phenol red and RPMI medium without phenol red was performed by two-way ANOVA with Sidak post hoc testing. No statistical difference was revealed.

**Supplementary Figure S3 |** Effect of G-1 + G-36 in Jurkat and CCRF-CEM cell lines. **(A–C)** Bar charts show cell count (trypan blue exclusion test) of Jurkat **(A,B)** and CCRF-CEM **(C)** cells treated with G-36 10 µM for 4–72 h. Data are normalized to control. **(D,E)** Bar charts showing the mean fluorescence peak (MFI) of CFSE in Jurkat **(D)** and CCRF-CEM **(E)** cells treated with G-36 10 µM for 24–72 h. Data are normalized to control. **(A–E)** Comparison between G-36 and the control of its corresponding time was made by two-way ANOVA with Sidak post hoc testing. **(F–I)** Jurkat **(F–G)** and CCRF-CEM **(H,I)** cells were pre-incubated with G-36 (10 µM, 30 min), seeded in Advanced RPMI medium with different concentrations of G-1 and cultivated during indicated periods of time. Cell viability **(F,H)** and cell proliferation **(G,I)** was evaluated and graphed as function of G-1 concentration. **(J)** Jurkat cells cultured in RPMI medium without phenol red and supplemented with 10% FCS dialyzed were treated with G-1 (0.15–10 µM) + G-36 (10 µM, pre-incubated) for 24–72 h. **(F–J)** Data are normalized to control and shown as mean ± SEM; N ≥ 3. Comparison between G-1 and G1+G-36 was performed by two-way ANOVA with Sidak post hoc testing. **(K)** Jurkat cells cultured in Advanced RPMI medium were treated with growing concentrations of G-1 for 24 h. Bar charts showing percentage of different gates obtained by flow cytometric corresponding to necrotic (Q1), late apoptotic/necrotic (Q2), apoptotic (Q3) and viable cells (Q4). Data are shown as mean ± SEM; N ≥ 3; $^{****}p < 0.0001$. Comparison between control (without treatment) and samples treated with G-1 + G-36 was made by two-way ANOVA with Dunnett post hoc testing.

# REFERENCES


Albanito, L., Madeo, A., Lappano, R., Vivacqua, A., Rago, V., Carpino, A., et al. (2007). G Protein-Coupled Receptor 30 (GPR30) Mediates Gene Expression Changes and Growth Response to 17β-Estradiol and Selective GPR30 Ligand G-1 in Ovarian Cancer Cells. *Cancer Res.* 67 (4), 1859–1866. doi:10.1158/0008-5472.CAN-06-2909

Altmann, J. B., Yan, G., Meeks, J. F., Abood, M. E., Brailoiu, E., and Brailoiu, G. C. (2015). G Protein-Coupled Estrogen Receptor-Mediated Effects on Cytosolic Calcium and Nanomechanics in Brain Microvascular Endothelial Cells. *J. Neurochem.* 133 (5), 629–639. doi:10.1111/jnc.13066

Ariazi, E. A., Brailoiu, E., Yerrum, S., Shupp, H. A., Slifker, M. J., Cunliffe, H. E., et al. (2010). The G Protein-Coupled Receptor GPR30 Inhibits Proliferation of Estrogen Receptor-Positive Breast Cancer Cells. *Cancer Res.* 70 (3), 1184–1194. doi:10.1158/0008-5472.CAN-09-3068

Bai, L.-Y., Weng, J.-R., Hu, J.-L., Wang, D., Sargeant, A. M., and Chiu, C.-F. (2013). G15, a GPR30 Antagonist, Induces Apoptosis and Autophagy in Human Oral Squamous Carcinoma Cells. *Chemico-Biological Interactions* 206 (2), 375–384. doi:10.1016/j.cbi.2013.10.014

Berthois, Y., Katzenellenbogen, J. A., and Katzenellenbogen, B. S. (1986). Phenol Red in Tissue Culture media Is a Weak Estrogen: Implications Concerning the Study of Estrogen-Responsive Cells in Culture. *Proc. Natl. Acad. Sci.* 83 (8), 2496–2500. doi:10.1073/pnas.83.8.2496

Bologa, C. G., Revankar, C. M., Young, S. M., Edwards, B. S., Arterburn, J. B., Kiselyov, A. S., et al. (2006). Virtual and Biomolecular Screening Converge on a Selective Agonist for GPR30. *Nat. Chem. Biol.* 2 (4), 207–212. doi:10.1038/nchembio775

Brailoiu, G. C., Arterburn, J. B., Oprea, T. I., Chitravanshi, V. C., and Brailoiu, E. (2013). Bradycardic Effects Mediated by Activation of G Protein-Coupled Estrogen Receptor in Rat Nucleus Ambiguus. *Exp. Physiol.* 98 (2), 679–691. doi:10.1113/expphysiol.2012.069377

Catusse, J., Wollner, S., Leick, M., Schröttner, P., Schraufstätter, I., and Burger, M. (2010). Attenuation of CXCR4 Responses by CCL18 in Acute Lymphocytic Leukemia B Cells. *J. Cel. Physiol.* 225 (3), 792–800. doi:10.1002/jcp.22284

Chimento, A., Sirianni, R., Casaburi, I., Zolea, F., Rizza, P., Avena, P., et al. (2015). GPER Agonist G-1 Decreases Adrenocortical Carcinoma (ACC) Cell Growthin Vitroandin Vivo. *Oncotarget* 6 (22), 19190–19203. doi:10.18632/oncotarget.4241

Cirillo, F., Pellegrino, M., Malivindi, R., Rago, V., Avino, S., Muto, L., et al. GPER Is Involved in the Regulation of the Estrogen-Metabolizing CYP1B1 Enzyme in Breast Cancer. *Oncotarget* (2017) 8(63):106608–106624. doi:10.18632/oncotarget.22541

Dennis, M. K., Burai, R., Ramesh, C., Petrie, W. K., Alcon, S. N., Nayak, T. K., et al. (2009). *In Vivo* effects of a GPR30 Antagonist. *Nat. Chem. Biol.* 5 (6), 421–427. doi:10.1038/nchembio.168

Dennis, M. K., Field, A. S., Burai, R., Ramesh, C., Petrie, W. K., Bologa, C. G., et al. (2011). Identification of a GPER/GPR30 Antagonist with Improved Estrogen Receptor Counterselectivity. *J. Steroid Biochem. Mol. Biol.* 127 (3–5), 358–366. doi:10.1016/j.jsbmb.2011.07.002

Ding, X., Gao, T., Gao, T., Gao, P., Meng, Y., Zheng, Y., et al. (2019). Activation of the G Protein-Coupled Estrogen Receptor Elicits Store Calcium Release and Phosphorylation of the Mu-Opioid Receptors in the Human Neuroblastoma SH-Sy5y Cells. *Front. Neurosci.* 13, 1351. doi:10.3389/fnins.2019.01351

Filardo, E. J., Graeber, C. T., Quinn, J. A., Resnick, M. B., Giri, D., DeLellis, R. A., et al. (2006). Distribution of GPR30, a Seven Membrane-Spanning Estrogen Receptor, in Primary Breast Cancer and its Association with Clinicopathologic Determinants of Tumor Progression. *Clin. Cancer Res.* 12 (21), 6359–6366. doi:10.1158/1078-0432.CCR-06-0860

Filardo, E. J., Quinn, J. A., Bland, K. I., and Frackelton, A. R. (2000). Estrogen-induced Activation of Erk-1 and Erk-2 Requires the G Protein-Coupled Receptor Homolog, GPR30, and Occurs via Trans-activation of the Epidermal Growth Factor Receptor through Release of HB-EGF. *Mol. Endocrinol.* 14 (10), 1649–1660. doi:10.1210/mend.14.10.0532

Girgert, R., Emons, G., and Gründker, C. (2019). Estrogen Signaling in ERα-Negative Breast Cancer: ERβ and GPER. *Front. Endocrinol.* 9 (871), 1–12. doi:10.3389/fendo.2018.00781

Gudermann, T., and Bader, M. (2015). Receptors, G Proteins, and Integration of Calcium Signalling. *J. Mol. Med.* 93, 937–940. doi:10.1007/s00109-015-1330-y

Gui, Y., Shi, Z., Wang, Z., Li, J.-J., Xu, C., Tian, R., et al. (2015). The GPER Agonist G-1 Induces Mitotic Arrest and Apoptosis in Human Vascular Smooth Muscle Cells Independent of GPER. *J. Cel. Physiol.* 230 (4), 885–895. doi:10.1002/jcp.24817

Han, N., Heublein, S., Jeschke, U., Kuhn, C., Hester, A., Czogalla, B., et al. (2021). The G-Protein-Coupled Estrogen Receptor (GPER) Regulates Trimethylation of Histone H3 at Lysine 4 and Represses Migration and Proliferation of Ovarian Cancer Cells *In Vitro*. *Cells* 10 (3), 619–642. doi:10.3390/cells10030619

Hasni, M. S., and Yakimchuk, K. (2019). Expression and Effects of Ligand-Activated Estrogen Receptors in Chronic Lymphocytic Leukemia. *Anticancer Res.* 39 (1), 167–172. doi:10.21873/anticanres.13093

Holm, A., Grände, P.-O., Ludueña, R. F., Olde, B., Prasad, V., Leeb-Lundberg, L. M. F., et al. (2012). The G Protein-Coupled Oestrogen Receptor 1 Agonist G-1 Disrupts Endothelial Cell Microtubule Structure in a Receptor-independent Manner. *Mol. Cel Biochem* 366 (1–2), 239–249. doi:10.1007/s11010-012-1301-3

Hsu, L.-H., Chu, N.-M., Lin, Y.-F., and Kao, S.-H. (2019). G-protein Coupled Estrogen Receptor in Breast Cancer. *Ijms* 20 (2), 306–322. doi:10.3390/ijms20020306

Imesch, P., Samartzis, E. P., Dedes, K. J., Fink, D., and Fedier, A. (2013). Histone Deacetylase Inhibitors Down-Regulate G-Protein-Coupled Estrogen Receptor and the GPER-Antagonist G-15 Inhibits Proliferation in Endometriotic Cells. *Fertil. Sterility* 100 (3), 770–776. doi:10.1016/j.fertnstert.2013.05.008

Jala, V. R., Radde, B. N., Haribabu, B., and Klinge, C. M. (2012). Enhanced Expression of G-Protein Coupled Estrogen Receptor (GPER/GPR30) in Lung Cancer. *BMC Cancer* 12 (1), 264–276. doi:10.1186/1471-2407-12-624

Jenkins, J. K., Suwannaroj, S., Elbourne, K. B., Ndebele, K., and McMurray, R. W. (2001). 17-β-Estradiol Alters Jurkat Lymphocyte Cell Cycling and Induces Apoptosis through Suppression of Bcl-2 and Cyclin A. *Int. Immunopharmacology* 1 (11), 1897–1911. doi:10.1016/S1567-5769(01)00114-X

Jung, J. (2019). Role of G Protein-Coupled Estrogen Receptor in Cancer Progression. *ToxicolRes* 35 (3), 209–214. doi:10.5487/TR.2019.35.3.209

Kasioulis, I., Das, R. M., and Storey, K. G. (2017). Inter-dependent Apical Microtubule and Actin Dynamics Orchestrate Centrosome Retention and Neuronal Delamination. *ELife* 6, e26215. doi:10.7554/eLife.26215

Kaur, R., Kaur, G., Gill, R. K., Soni, R., and Bariwal, J. (2014). Recent Developments in Tubulin Polymerization Inhibitors: An Overview. *Eur. J. Med. Chem.* 87, 89–124. doi:10.1016/j.ejmech.2014.09.051

Khan, D., Cowan, C., and Ahmed, S. A. (2012). Estrogen and Signaling in the Cells of Immune System. *Adv. Neuroimmune Biol.* 3 (1), 73–93. doi:10.3233/NIB-2012-012039

Kim, S. J., Kim, H. S., and Seo, Y. R. (2019). Understanding of ROS-Inducing Strategy in Anticancer Therapy. *Oxidative Med. Cell Longevity* 2019, 1–12. doi:10.1155/2019/5381692

Kovats, S. (2015). Estrogen Receptors Regulate Innate Immune Cells and Signaling Pathways. *Cell Immunol.* 294 (2), 63–69. doi:10.1016/j.cellimm.2015.01.018

Kurt, A. H., Çelik, A., and Kelleci, B. M. (2015). Oxidative/antioxidative Enzyme-Mediated Antiproliferative and Proapoptotic Effects of the GPER1 Agonist G-1 on Lung Cancer Cells. *Oncol. Lett.* 10 (5), 3177–3182. doi:10.3892/ol.2015.3711

Ladikou, E.-E., and Kassi, E. (2017). The Emerging Role of Estrogen in B Cell Malignancies. *Leuk. Lymphoma* 58 (3), 528–539. doi:10.1080/10428194.2016.1213828

Lappano, R., Mallet, C., Rizzuti, B., Grande, F., Galli, G., Byrne, C., et al. (2019). The Peptide ERα17p Is a GPER Inverse Agonist that Exerts Antiproliferative Effects in Breast Cancer Cells. *Cells* 8 (6), 590. doi:10.3390/cells8060590

Lee, S.-J., Kim, T. W., Park, G. L., Hwang, Y. S., Cho, H. J., Kim, J.-T., et al. (2019). G Protein-Coupled Estrogen Receptor-1 Agonist Induces Chemotherapeutic Effect via ER Stress Signaling in Gastric Cancer. *BMB Rep.* 52, 647–652. doi:10.5483/BMBRep.2019.52.11.007

Liu, C., Liao, Y., Fan, S., Fu, X., Xiong, J., Zhou, S., et al. (2019). G-protein-coupled Estrogen Receptor Antagonist G15 Decreases Estrogen-Induced Development of Non-small Cell Lung Cancer. *Oncol. Res.* 27 (3), 283–292. doi:10.3727/096504017X150357959046710.3727/096504017x15035795904677

Liu, Q., Chen, Z., Jiang, G., Zhou, Y., Yang, X., Huang, H., et al. (2017). Epigenetic Down Regulation of G Protein-Coupled Estrogen Receptor (GPER) Functions as a Tumor Suppressor in Colorectal Cancer. *Mol. Cancer* 16 (1), 1–14. doi:10.1186/s12943-017-0654-3

Luo, H., Yang, G., Yu, T., Luo, S., Wu, C., Sun, Y., et al. (2014). GPER-mediated Proliferation and Estradiol Production in Breast Cancer-Associated Fibroblasts. *Endocr. Relat. Cancer* 21 (2), 355–369. doi:10.1530/ERC-13-0237

Lv, X., and Wang, C. (2014). G-1: New Potential Therapeutic Option for Ovarian Cancer. *Cancer Cell Microenviron* 1, e27. doi:10.14800/ccm.27

Lv, X., He, C., Huang, C., Hua, G., Wang, Z., Remmenga, S. W., et al. (2017). G-1 Inhibits Breast Cancer Cell Growth via Targeting Colchicine-Binding Site of Tubulin to Interfere with Microtubule Assembly. *Mol. Cancer Ther.* 16, 1080–1091. doi:10.1158/1535-7163.MCT-16-0626

Marks, A. R. (1997). Intracellular Calcium-Release Channels: Regulators of Cell Life and Death. *Am. J. Physiol.* 272 (2Pt2), H597–H605. doi:10.1152/ajpheart.1997.272.2.H5910.1152/ajpheart.1997.272.2.H597

Maruyama, T., Kanaji, T., Nakade, S., Kanno, T., and Mikoshiba, K. (1997). 2APB, 2-Aminoethoxydiphenyl Borate, a Membrane-Penetrable Modulator of Ins(1,4,5)P3-Induced Ca2+ Release. *J. Biochem.* 122 (3), 498–505. doi:10.1093/oxfordjournals.jbchem.a021780

Moreno-Ulloa, A., Miranda-Cervantes, A., Licea-Navarro, A., Mansour, C., Beltrán-Partida, E., Donis-Maturano, L., et al. (2018). (-)-Epicatechin Stimulates Mitochondrial Biogenesis and Cell Growth in C2C12 Myotubes via the G-Protein Coupled Estrogen Receptor. *Eur. J. Pharmacol.* 822, 95–107. doi:10.1016/j.ejphar.2018.01.014

Mori, T., Ito, F., Matsushima, H., Takaoka, O., Tanaka, Y., Koshiba, A., et al. (2015). G Protein-Coupled Estrogen Receptor 1 Agonist G-1 Induces Cell Cycle Arrest in the Mitotic Phase, Leading to Apoptosis in Endometriosis. *Fertil. Sterility* 103 (5), 1228–1235. doi:10.1016/j.fertnstert.2015.01.026

Mukhtar, E., Adhami, V. M., and Mukhtar, H. (2014). Targeting Microtubules by Natural Agents for Cancer Therapy. *Mol. Cancer Ther.* 13 (2), 275–284. doi:10.1158/1535-7163.MCT-13-0791

Muller, C., Brown-Glaberman, U. A., Chaney, M. F., Garyantes, T., LoRusso, P., McQuade, J. L., et al. (2021). Phase 1 Trial of a Novel, First-In-Class G Protein-Coupled Estrogen Receptor (GPER) Agonist, LNS8801, in Patients with Advanced or Recurrent Treatment-Refractory Solid Malignancies. *Jco* 39 (15Suppl. l), 3084. doi:10.1200/JCO.2021.39.15_suppl.3084

Natale, C. A., Li, J., Pitarresi, J. R., Norgard, R. J., Dentchev, T., Capell, B. C., et al. (2020). Pharmacologic Activation of the G Protein-Coupled Estrogen Receptor Inhibits Pancreatic Ductal Adenocarcinoma. *Cell Mol. Gastroenterol. Hepatol.* 10 (4), 868–880. doi:10.1016/j.jcmgh.2020.04.016

Nayak, T. K., Dennis, M. K., Ramesh, C., Burai, R., Atcher, R. W., Sklar, L. A., et al. (2010). Influence of Charge on Cell Permeability and Tumor Imaging of GPR30-Targeted 111In-Labeled Nonsteroidal Imaging Agents. *ACS Chem. Biol.* 5 (7), 681–690. doi:10.1021/cb1000636

Novo, E., and Parola, M. (2008). Redox Mechanisms in Hepatic Chronic Wound Healing and Fibrogenesis. *Fibrogenesis Tissue Repair* 1 (1), 5. doi:10.1186/1755-1536-1-5

Olivas-Aguirre, M., Pottosin, I., and Dobrovinskaya, O. (2019). Mitochondria as Emerging Targets for Therapies against T Cell Acute Lymphoblastic Leukemia. *J. Leukoc. Biol.* 105 (5), 935–946. doi:10.1002/JLB.5VMR0818-330RR

Prossnitz, E. R., and Barton, M. (2011). The G-Protein-Coupled Estrogen Receptor GPER in Health and Disease. *Nat. Rev. Endocrinol.* 7 (12), 715–726. doi:10.1038/nrendo.2011.122

Quah, B. J. C., Warren, H. S., and Parish, C. R. (2007). Monitoring Lymphocyte Proliferation *In Vitro* and *In Vivo* with the Intracellular Fluorescent Dye Carboxyfluorescein Diacetate Succinimidyl Ester. *Nat. Protoc.* 2 (9), 2049–2056. doi:10.1038/nprot.2007.296

Raetz, E. A., and Teachey, D. T. (2016). T-cell Acute Lymphoblastic Leukemia. *Hematology* 2016 (1), 580–588. doi:10.1182/asheducation-2016.1.580

Ren, J., and Wu, J. H. (2012). 17β-Estradiol Rapidly Activates Calcium Release from Intracellular Stores via the GPR30 Pathway and MAPK Phosphorylation in Osteocyte-like MLO-Y4 Cells. *Calcif Tissue Int.* 90 (5), 411–419. doi:10.1007/s00223-012-9581-x

Revankar, C. M., Cimino, D. F., Sklar, L. A., Arterburn, J. B., and Prossnitz, E. R. (2005). A Transmembrane Intracellular Estrogen Receptor Mediates Rapid Cell Signaling. *Science* 307 (5715), 1625–1630. doi:10.1126/science.1106943

Ribeiro, M. P. C., Santos, A. E., and Custódio, J. B. A. (2017). The Activation of the G Protein-Coupled Estrogen Receptor (GPER) Inhibits the Proliferation of Mouse Melanoma K1735-M2 Cells. *Chemico-Biological Interactions* 277, 176–184. doi:10.1016/j.cbi.2017.09.017

Rudelius, M., Rauert-Wunderlich, H., Hartmann, E., Hoster, E., Dreyling, M., Klapper, W., et al. (2015). The G Protein-Coupled Estrogen Receptor 1 (GPER-1) Contributes to the Proliferation and Survival of Mantle Cell Lymphoma Cells. *Haematologica* 100, e458–e461. doi:10.3324/haematol.2015.127399

Sánchez-Aguilera, A., and Méndez-Ferrer, S. (2016). Regulation of Hematopoietic Progenitors by Estrogens as a Basis for New Antileukemic Strategies. *Mol. Cell Oncol.* 3 (1), e1009728. doi:10.1080/23723556.2015.1009728

Shakya, S., Sharma, P., Bhatt, A. M., Jani, R. A., Delevoye, C., and Gangi Setty, S. R. (2018). Rab22A Recruits BLOC -1 and BLOC -2 to Promote the Biogenesis of Recycling Endosomes. *EMBO Rep.* 19 (12), 1–17. doi:10.15252/embr.201845918

Sjöström, M., Hartman, L., Grabau, D., Fornander, T., Malmström, P., Nordenskjöld, B., et al. (2014). Lack of G Protein-Coupled Estrogen Receptor (GPER) in the Plasma Membrane Is Associated with Excellent Long-Term Prognosis in Breast Cancer. *Breast Cancer Res. Treat.* 145 (1), 61–71. doi:10.1007/s10549-014-2936-4

Stanton, R. A., Gernert, K. M., Nettles, J. H., and Aneja, R. (2011). Drugs that Target Dynamic Microtubules: A New Molecular Perspective. *Med. Res. Rev.* 31, 443–481. doi:10.1002/med.20242

Torres-López, L., Maycotte, P., Liñán-Rico, A., Liñán-Rico, L., Donis-Maturano, L., Delgado-Enciso, I., et al. (2019). Tamoxifen Induces Toxicity, Causes Autophagy, and Partially Reverses Dexamethasone Resistance in Jurkat T Cells. *J. Leukoc. Biol.* 105 (5), 983–998. doi:10.1002/JLB.2VMA0818-328R

Tran, Q.-K. (2020). Reciprocality between Estrogen Biology and Calcium Signaling in the Cardiovascular System. *Front. Endocrinol.* 11, 568203. doi:10.3389/fendo.2020.568203

Tutzauer, J., Sjöström, M., Bendahl, P.-O., Rydén, L., Fernö, M., Leeb-Lundberg, L. M. F., et al. (2020). Plasma Membrane Expression of G Protein-Coupled Estrogen Receptor (GPER)/G Protein-Coupled Receptor 30 (GPR30) Is Associated with Worse Outcome in Metachronous Contralateral Breast Cancer. *PLoS One* 15 (4), e0231786. doi:10.1371/journal.pone.0231786

Vadillo, E., Dorantes-Acosta, E., Pelayo, R., and Schnoor, M. (2018). T Cell Acute Lymphoblastic Leukemia (T-ALL): New Insights into the Cellular Origins and Infiltration Mechanisms Common and Unique Among Hematologic Malignancies. *Blood Rev.* 32 (1), 36–51. doi:10.1016/j.blre.2017.08.006

Vo, D.-K. H., Hartig, R., Weinert, S., Haybaeck, J., and Nass, N. (2019). G-protein-coupled Estrogen Receptor (GPER)-specific Agonist G1 Induces ER Stress Leading to Cell Death in MCF-7 Cells. *Biomolecules* 9 (9), 503–521. doi:10.3390/biom9090503

Wang, C., Lv, X., Jiang, C., and Davis, J. S. (2012). The Putative G-Protein Coupled Estrogen Receptor Agonist G-1 Suppresses Proliferation of Ovarian and Breast Cancer Cells in a GPER-independent Manner. *Am. J. Transl Res.* 4 (4), 390–402.

Wang, C., Lv, X., He, C., Hua, G., Tsai, M.-Y., and Davis, J. S. (2013). The G-Protein-Coupled Estrogen Receptor Agonist G-1 Suppresses Proliferation of Ovarian Cancer Cells by Blocking Tubulin Polymerization. *Cell Death Dis* 4 (10), e869. doi:10.1038/cddis.2013.397

Wei, W., Chen, Z.-J., Zhang, K.-S., Yang, X.-L., Wu, Y.-M., Chen, X.-H., et al. (2014). The Activation of G Protein-Coupled Receptor 30 (GPR30) Inhibits Proliferation of Estrogen Receptor-Negative Breast Cancer Cells *In Vitro* and *In Vivo*. *Cel Death Dis* 5 (10), e1428. doi:10.1038/cddis.2014.398

Weißenborn, C., Ignatov, T., Ochel, H.-J., Costa, S. D., Zenclussen, A. C., Ignatova, Z., et al. (2014). GPER Functions as a Tumor Suppressor in Triple-Negative Breast Cancer Cells. *J. Cancer Res. Clin. Oncol.* 140 (5), 713–723. doi:10.1007/s00432-014-1620-8

Xu, S., Yu, S., Dong, D., and Lee, L. T. O. (2019). G Protein-Coupled Estrogen Receptor: A Potential Therapeutic Target in Cancer. *Front. Endocrinol.* 10, 725. doi:10.3389/fendo.2019.00725

Yakimchuk, K., Jondal, M., and Okret, S. (2013). Estrogen Receptor α and β in the normal Immune System and in Lymphoid Malignancies. *Mol. Cell Endocrinol.* 375 (1–2), 121–129. doi:10.1016/j.mce.2013.05.016

Yang, D.-L., Xu, J.-W., Zhu, J.-G., Zhang, Y.-L., Xu, J.-B., Sun, Q., et al. (2017). Role of GPR30 in Estrogen-Induced Prostate Epithelial Apoptosis and Benign Prostatic Hyperplasia. *Biochem. Biophysical Res. Commun.* 487 (3), 517–524. doi:10.1016/j.bbrc.2017.04.047

Yedjou, C., Cameron, J., Mbemi, A. T., and Tchounwou, P. (2015). β-ESTRADIOL INDUCES CYTOTOXIC EFFECTS TO HUMAN T-LYMPHOMA (JURKAT) CELLS THROUGH OXIDATIVE STRESS. *J. Miss. Acad. Sci.* 60 (Suppl. 1), 279–283.

Zhang, Q., Wu, Y.-Z., Zhang, Y.-M., Ji, X.-H., and Hao, Q. (2015). Activation of G-Protein Coupled Estrogen Receptor Inhibits the Proliferation of Cervical

Cancer Cells via Sustained Activation of ERK1/2. *Cell Biochem Funct* 33 (3), 134–142. doi:10.1002/cbf.3097

Zhou, L., Yu, T., Yang, F., Han, J., Zuo, B., Huang, L., et al. (2021). G Protein-Coupled Estrogen Receptor Agonist G-1 Inhibits Mantle Cell Lymphoma Growth in Preclinical Models. *Front. Oncol.* 11, 668617. doi:10.3389/fonc.2021.668617

Zweifach, A., and Lewis, R. S. (1993). Mitogen-regulated Ca2+ Current of T Lymphocytes Is Activated by Depletion of Intracellular Ca2+ Stores. *Proc. Natl. Acad. Sci.* 90 (13), 6295–6299. doi:10.1073/pnas.90.13.6295

**Conflict of Interest:** The authors declare that the research was conducted in the absence of any commercial or financial relationships that could be construed as a potential conflict of interest.

**Publisher's Note:** All claims expressed in this article are solely those of the authors and do not necessarily represent those of their affiliated organizations, or those of the publisher, the editors, and the reviewers. Any product that may be evaluated in this article, or claim that may be made by its manufacturer, is not guaranteed or endorsed by the publisher.

frontiers | Frontiers in Cell and Developmental Biology

ORIGINAL RESEARCH
published: 13 May 2022
doi: 10.3389/fcell.2022.899752

# *In Silico* Integration of Transcriptome and Interactome Predicts an ETP-ALL-Specific Transcriptional Footprint that Decodes its Developmental Propensity

*Soumyadeep Mukherjee*[1†], *Arpita Kar*[2†], *Paramita Paul*[1], *Souvik Dey*[3], *Avik Biswas*[2]* *and Subhasis Barik*[1]*

[1]*Department of In Vitro Carcinogenesis and Cellular Chemotherapy, Chittaranjan National Cancer Institute, Kolkata, India,* [2]*Department of Signal Transduction and Biogenic Amines, Chittaranjan National Cancer Institute, Kolkata, India,* [3]*Manipal Centre for Biotherapeutics Research, Manipal Academy of Higher Education, Manipal, India*

OPEN ACCESS

**Edited by:**
*Maristella Maggi,*
*University of Pavia, Italy*

**Reviewed by:**
*Deepak Verma,*
*Johns Hopkins Medicine, United States*
*Sumedha Bagga,*
*Boston University, United States*

***Correspondence:**
*Avik Biswas*
*avikbiswas@cnci.ac.in*
*Subhasis Barik*
*subhasisbarik@cnci.ac.in*

†*These authors have contributed equally to this work and share first authorship*

**Specialty section:**
*This article was submitted to Molecular and Cellular Pathology, a section of the journal Frontiers in Cell and Developmental Biology*

**Received:** *19 March 2022*
**Accepted:** *22 April 2022*
**Published:** *13 May 2022*

**Citation:**
*Mukherjee S, Kar A, Paul P, Dey S, Biswas A and Barik S (2022) In Silico Integration of Transcriptome and Interactome Predicts an ETP-ALL-Specific Transcriptional Footprint that Decodes its Developmental Propensity. Front. Cell Dev. Biol. 10:899752. doi: 10.3389/fcell.2022.899752*

Early T precursor acute lymphoblastic leukemia (ETP-ALL) exhibits poor clinical outcomes and high relapse rates following conventional chemotherapeutic protocols. Extensive developmental flexibility of the multipotent ETP-ALL blasts with considerable intra-population heterogeneity in terms of immunophenotype and prognostic parameters might be a target for novel therapeutic interventions. Using a public gene expression dataset (GSE28703) from NCBI GEO DataSets with 12 ETP-ALL and 40 non-ETP-ALL samples, such heterogeneity was found to be reflected in their transcriptome as well. Hub genes were identified from the STRING-derived functional interaction network of genes showing differential expression between ETP-ALL and non-ETP-ALL as well as variable expression across ETP-ALL. Nine genes (*KIT*, *HGF*, *NT5E*, *PROM1*, *CD33*, *ANPEP*, *CDH2*, *IL1B,* and *CXCL2*) among the hubs were further validated as possible diagnostic ETP-ALL markers using another gene expression dataset (GSE78132) with 17 ETP-ALL and 27 non-ETP-ALL samples. Linear dimensionality reduction analysis with the expression levels of the hub genes in ETP-ALL revealed their divergent inclinations towards different hematopoietic lineages, proposing them as novel indicators of lineage specification in the incompletely differentiated ETP-ALL blasts. This further led to the formulation of a personalized lineage score calculation algorithm, which uncovered a considerable B-lineage-bias in a substantial fraction of ETP-ALL subjects from the GSE28703 and GSE78132 cohorts. In addition, STRING-derived physical interactome of the potential biomarkers displayed complete segregation of the B-lineage-skewed markers from other lineage-associated factors, highlighting their distinct functionality and possible druggability in ETP-ALL. A panel of these biomarkers might be useful in pinpointing the dominant lineage specification programmes in the ETP-ALL blasts on a personalized level, urging the development of novel lineage-directed precision therapies as well as repurposing of existing therapies against leukemia of different hematopoietic lineages; which might overcome the drawbacks of conventional chemotherapy.

**Keywords: ETP-ALL, transcriptome analysis, multipotency, lineage specification, biomarker, personalized medicine, interactome**

## INTRODUCTION

T cell acute lymphoblastic leukemia (T-ALL) is an aggressive hematologic neoplasm of the T lymphocytic compartment, accounting for 15 and 25% of total pediatric and adult acute lymphoblastic leukemia (ALL) cases, respectively (Vadillo et al., 2018). The disease mostly involves cancerous transformation of the T-lineage primed progenitors (Kraszewska et al., 2012), reflected in its immunophenotypic resemblance to that of the T cells (Bene et al., 1995). Interestingly, early T precursor acute lymphoblastic leukemia (ETP-ALL), a recently discovered subgroup of T-ALL, shows a considerably divergent immunophenotype, including low levels of T-lineage commitment markers along with high expression of one or more stem cell or myeloid antigens (Coustan-Smith et al., 2009; Chopra et al., 2014). The leukemic blasts of ETP-ALL arise from a bone marrow-derived multipotent hematopoietic progenitor called early thymic progenitor (ETP), designated as the earliest precursor of thymic T-lymphocytes (Treanor et al., 2014; Booth et al., 2018). In spite of persisting debates regarding the deterministic ontogeny of the ETPs, their capability of producing cells of myeloid (Bell and Bhandoola, 2008; Wada et al., 2008; Luc et al., 2012) as well as B-lymphocytic (Luc et al., 2012) lineages have been undisputed. A spectrum of potencies exists within the ETP population, often marked by lineage-specific signatures (Haymaker et al., 2012), which gives rise to considerable intra-population heterogeneity among the ETPs and influences their developmental outcome according to microenvironmental cues (Barik et al., 2017; Barik et al., 2018). This multitude of potencies is reflected in the variability of lineage-restricted marker expression in the ETP-ALL blasts on a patient-to-patient basis.

In spite of a relatively low rate of incidence among children (11%) as well as adults (7.4%), the clinical outcome for ETP-ALL is often remarkably poor; even worse than other T-ALL subtypes (Coustan-Smith et al., 2009; Inukai et al., 2012). However, chemotherapy is the only available tool in defence of this disease due to the paucity of United States Food and Drug Administration (FDA)-approved targeted therapies (Castaneda Puglianini and Papadantonakis, 2020). Conventional chemotherapeutic strategies to combat T-ALL exhibit suboptimal clinical efficiency against ETP-ALL (Wood et al., 2014; Jain et al., 2016; Yang et al., 2019). The presence of minimal residual disease and the resultant chances of relapse after such chemotherapeutic interventions constitute a point of serious concern regarding this disease (Wood et al., 2009; Zhang et al., 2020). Therefore, making a successful diagnosis is crucial for the clinical efficiency in case of ETP-ALL treatment, since being misdiagnosed as a case of generic T-ALL might lead to application of fallacious therapies.

Several studies have explored the genetic traits of ALL samples and have identified various mutational and transcriptional signatures unique to ETP-ALL (Zhang et al., 2012; Neumann et al., 2013; Zuurbier et al., 2014; Kumar et al., 2019; Wang and Zhang, 2020). Although these biomarkers successfully discriminate ETP-ALL from other incidences of T-ALL, one important caveat still remains: the developmental plasticity of the ETP-ALL blasts. Several targeted therapies against ETP-ALL are currently under evaluation, such as Peg-L-Asparaginase (Patrick et al., 2014), Ruxolitinib (Maude et al., 2015; Verbeke et al., 2019), Venetoclax (Numan et al., 2018), Venetoclax-plus-Nelarabine (McEwan et al., 2020) etc., with demonstrated efficacies against the disease. However, because of the miscellany of potencies in possession of the ETP-ALL blasts, any single therapeutic regimen being universally effective against every single case of ETP-ALL is extremely unlikely, if at all possible. As a result, an individual with majority of B-lineage-biased ETP-ALL blasts may not show satisfactory remission upon treatment with myeloid-targeted therapies, owing to the subtle differences in a vast range of physiological responses of cells from different hematopoietic lineages against the same drug. In fact, different cases of ETP-ALL show different responses against similar kind of therapies (Bernt et al., 2016; Genescà et al., 2020; McEwan et al., 2020; Sin and Man, 2021). Again, the lack of clarity regarding the expression of lineage markers in ETP-ALL often leads to misclassification of individual ETP-ALL cases with aberrant non-T marker expression as non-T-lineage neoplasms (Khurana et al., 2020). Therefore, the so far underappreciated multi-lineage potency of the ETP-ALL blasts might be targeted to aid the diagnosis of as well as the therapy designing against this malignant pathology, especially as a stepping stone for precision medicine (Tarantini et al., 2021).

Against such a backdrop, this study explored the ETP-ALL transcriptome available on public databases to pinpoint the hubs from a functional interaction network of genes showing significant difference in expression between ETP-ALL and non-ETP-ALL subjects as well as substantial variance among the ETP-ALL subjects themselves. Transcript levels of the genes, therefore, might not only classify ALL into ETP-ALL and non-ETP-ALL, but might further categorize ETP-ALL into separate subclasses based on their differential lineage inclinations. This may potentiate the invention of novel precision therapies targeting different lineage propensities, which might eliminate the shortcomings of conventional chemotherapy. Besides, the findings might open new avenues for the prospective use of B-cell acute lymphoblastic leukemia (B-ALL) or acute myelogenous leukemia (AML)-directed therapeutic modalities against ETP-ALL in a case-by-case manner.

## MATERIALS AND METHODS

### Data Acquisition and Processing

The flow of work adopted in this study is depicted in **Figure 1**. Two publicly available transcriptome datasets (accession numbers: GSE28703 and GSE78132) containing normalized gene expression data from ETP-ALL and non-ETP-ALL leukemic blasts were selected from NCBI Gene Expression Omnibus (GEO) DataSets (Barrett et al., 2012) after a search against the keyword “ETP-ALL”. The GSE28703 data, comprising of 12 ETP-ALL and 40 non-ETP-ALL samples, was used to discover differential expression signatures between ETP-ALL and non-ETP-ALL; while the GSE78132 data (GPL96 platform), comprising of 17 ETP-ALL and 27 non-ETP-ALL

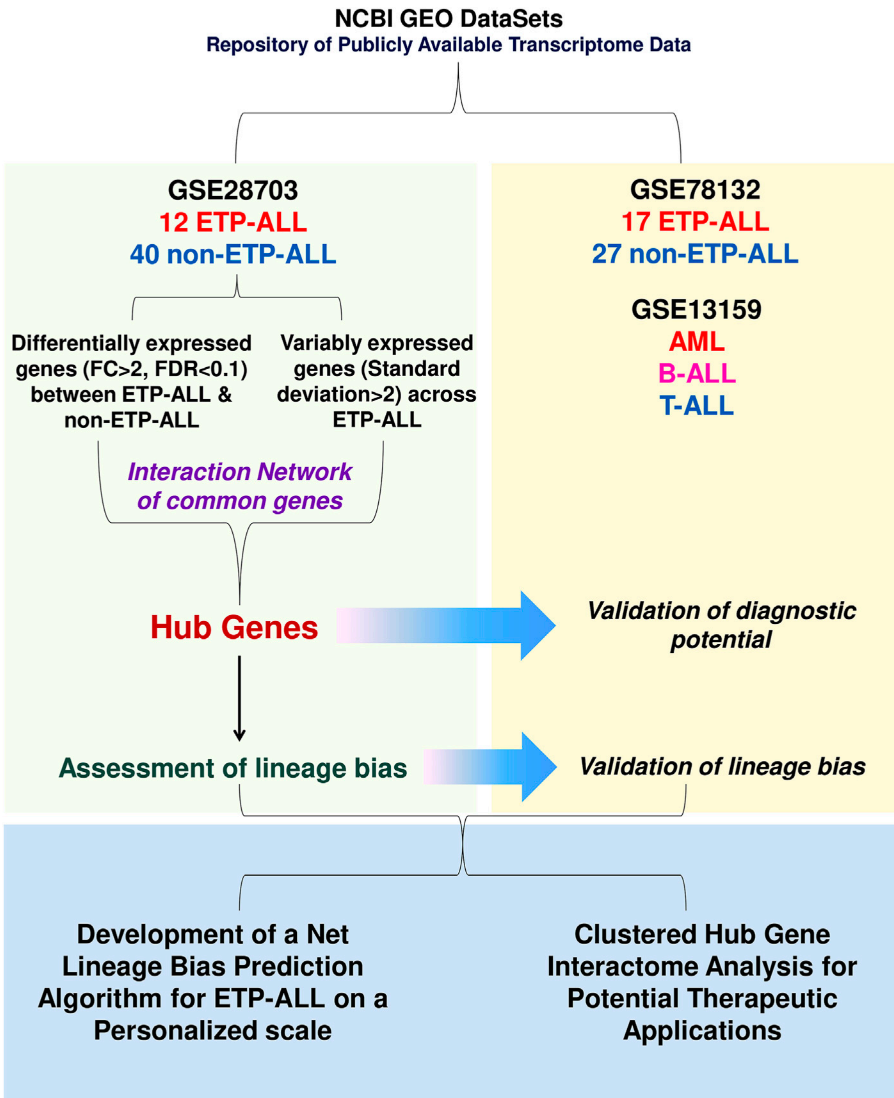


**FIGURE 1 |** Diagrammatic representation of the work-flow. The entire work lies on three segments: discovery of transcriptomic signatures from the GSE28703 dataset, validation of the proposed signatures in the GSE78132 (and GSE13159 in some cases) datasets and amalgamation of the validated findings in order to identify potential lineage-directed diagnostic and therapeutic implementations against ETP-ALL.

samples, was used for validation of the identified signatures. The relatively smaller size of the patient cohorts was accepted due to the relatively rare occurrence rate of ETP-ALL (Coustan-Smith et al., 2009). Another public microarray dataset (accession number: GSE13159) was used to evaluate gene expression levels in acute leukemia of mature leukocytes (T-ALL, B-ALL, AML) as well as progenitor/precursor-B-cell acute lymphoblastic leukemia (pro/pre-B-ALL). Detailed information regarding the datasets is provided in **Supplementary Table S1**. Probe annotations and further processing of the datasets were performed as previously described (Mukherjee et al., 2021).

## Clustering

The unsupervised, agglomerative hierarchical clustering-based dendrogram, constructed on iDEP.92 (Ge et al., 2018) with top 10,000 variable genes, clustered samples on the basis of Euclidean distance and complete linkage. Multidimensional scaling (MDS)-based clustering was conducted on iDEP.92 as a method of non-linear dimensionality reduction.

## Differential Gene Expression Analysis

Identification of differentially expressed genes (DEG) between sample groups was performed on iDEP.92 using the limma function with fold-change >2 and FDR (false discovery rate) <0.1. Genes with standard deviation >2 in expression values within the ETP-ALL group were selected as variably expressed genes within ETP-ALL. Gene expression heatmaps of differentially/variably expressed genes were created on Heatmapper (Babicki et al., 2016). Venn diagram of differentially regulated genes was built using InteractiVenn (Heberle et al., 2015).

## Protein-Protein Interaction Network Construction

Knowledge-based protein-protein interaction maps involving genes of interest were retrieved from STRING (Szklarczyk et al., 2019) and visualized on Cytoscape v3.8.2 (Shannon et al., 2003). Each node represented a protein, while each edge represented an interaction between them. For functional networks, these edges included every possible interaction criterion (gene neighborhood, gene fusion, gene co-occurrence, co-expression etc), whereas for physical networks, the edges signified physical interactions only. For all networks, a confidence cut-off of 0.4 was taken for edge mapping. Only the nodes connected to at least one edge were visualized on the network. Hub genes were identified using the cytoHubba plugin (Chin et al., 2014). Maximal clique centrality (MCC) scores were considered the key metric while ranking the genes in terms of their quality to act as hub genes within the network.

## Enrichment Analysis

Over-representation analysis with the differentially expressed genes between ETP-ALL and non-ETP-ALL was performed on ConsensusPathDB (Kamburov et al., 2009; Kamburov et al., 2011) against the 'REACTOME' database (for significantly enriched pathways) and on Enrichr (Chen et al., 2013; Kuleshov et al., 2016; Xie et al., 2021) against the 'CORUM' database (for significantly enriched protein complexes). Pathways/protein complexes with $p$-value <0.01 and overlap >5 genes were mapped onto the pathway network. Edge thicknesses on the networks described the relative overlap in genes between the two gene set nodes. Gene set enrichment analysis (GSEA) against the 'GO biological process' (for pathways) and 'TF.Target.TRRUST' (for transcription factors) databases for ETP-ALL samples with higher and lower levels of hub gene expression than the corresponding cohort mean was performed on iDEP.92, with FDR <0.2. Pathway enrichment on Cytoscape was carried out using the 'STRING Enrichment' function on the 'StringApp' plugin (Doncheva et al., 2018). The whole genome network was used as the background, while the 'STRING Clusters' database was used as the reference for pathway mappings in the converged network. 'REACTOME pathways' database was used for pathway mappings in the networks of individual hub genes. The 'MSigDB hallmark' and 'CORUM' databases on Enrichr were used as reference for pathway enrichment and protein complex enrichment, respectively, of genes variably expressed among ETP-ALL samples. All enrichment analyses were carried out assuming hyper-geometric probabilistic distributions of the reference gene sets within the respective gene lists in each case.

## Classifier Performance Analysis

The ability of genes as binary classifiers in discriminating between ETP-ALL and non-ETP-ALL was tested using receiver operating characteristic (ROC) analysis on ROCplot (Fekete and Győrffy, 2019). Magnitude of the area under curve (AUC) statistic was considered representative of classifier quality. Corresponding confusion matrices denoted the extent of true and false prediction rates in the classification process for individual classifiers.

## Association Analysis

The pairwise correlation matrix of all ETP-ALL and non-ETP-ALL samples, constructed on iDEP.92, was composed of Pearson's correlation coefficients between each pair of samples, denoting their whole transcriptomic correlation. Linear dimensionality reduction in terms of principal component analysis (PCA) with normalized expression values of selected genes in ETP-ALL was carried out on ClustVis (Metsalu and Vilo, 2015). Normalization of expression values of individual genes was performed with respect to their cognate mean expression levels in the non-ETP-ALL group to yield a measure of co-expression trends across different lineages. For analyzing associations of individual hub gene expression with particular lineages, the ETP-ALL cohort was divided into two groups based on higher and lower expression levels of the individual hub genes compared to their corresponding mean expression, followed by analysis of lineage marker expression in these groups. Correlation between the expression levels of individual genes and the leukemia subtypes based on GSE13159 data was observed on BloodSpot (Bagger et al., 2019).

## Personalized Lineage Score Formulation

For prediction of personalized scores indicating net lineage skew in leukemic blasts from ETP-ALL patients, expression values of each hub gene were normalized with respect to the population mean expression values of the respective genes. Next, the normalized expression values were transformed to a fold-change value with respect to the stem-like condition by the following formula:

$$\begin{aligned} Transformed\,Expression\,Score &= Normalized\,expression\,score\,of\,hub\,gene \\ &\div Normalized\,expression\,score\,of\,PROM1 \end{aligned}$$

Lineage scores were further computed as geometric means of transformed expression scores of all genes displaying skew towards individual lineages (adapted from Ravichandran et al., 2021). Formulae for calculation of the respective lineage scores are as follows (TES: Transformed Expression Score).

$$Myeloid\,lineage\,score = [TES(KIT)\times TES(HGF)\times TES(ANPEP)\times TES(CXCL2)]^{1/4}$$

$$B-lineage\,score = [TES(NT5E)\times TES(CXCL2)]^{1/2}$$

$$T-lineage\,score = TES(CDH2)$$

$$Lineage\,score\,for\,unidentified\,bias = [TES(CD33)\times TES(IL1B)]^{1/2}$$

All lineages with lineage score values within 10% error range of the maximum lineage score for an individual sample were assigned to the respective sample.

## Statistics and Data Visualization

Statistical analyses were carried out on GraphPad Prism v5.0 for Windows, GraphPad Software, La Jolla, California, United States. Column plots were constructed using the mean and standard error of mean (SEM). Box plots represented the mean and interquartile range. Whiskers extended till the 5th and 95th

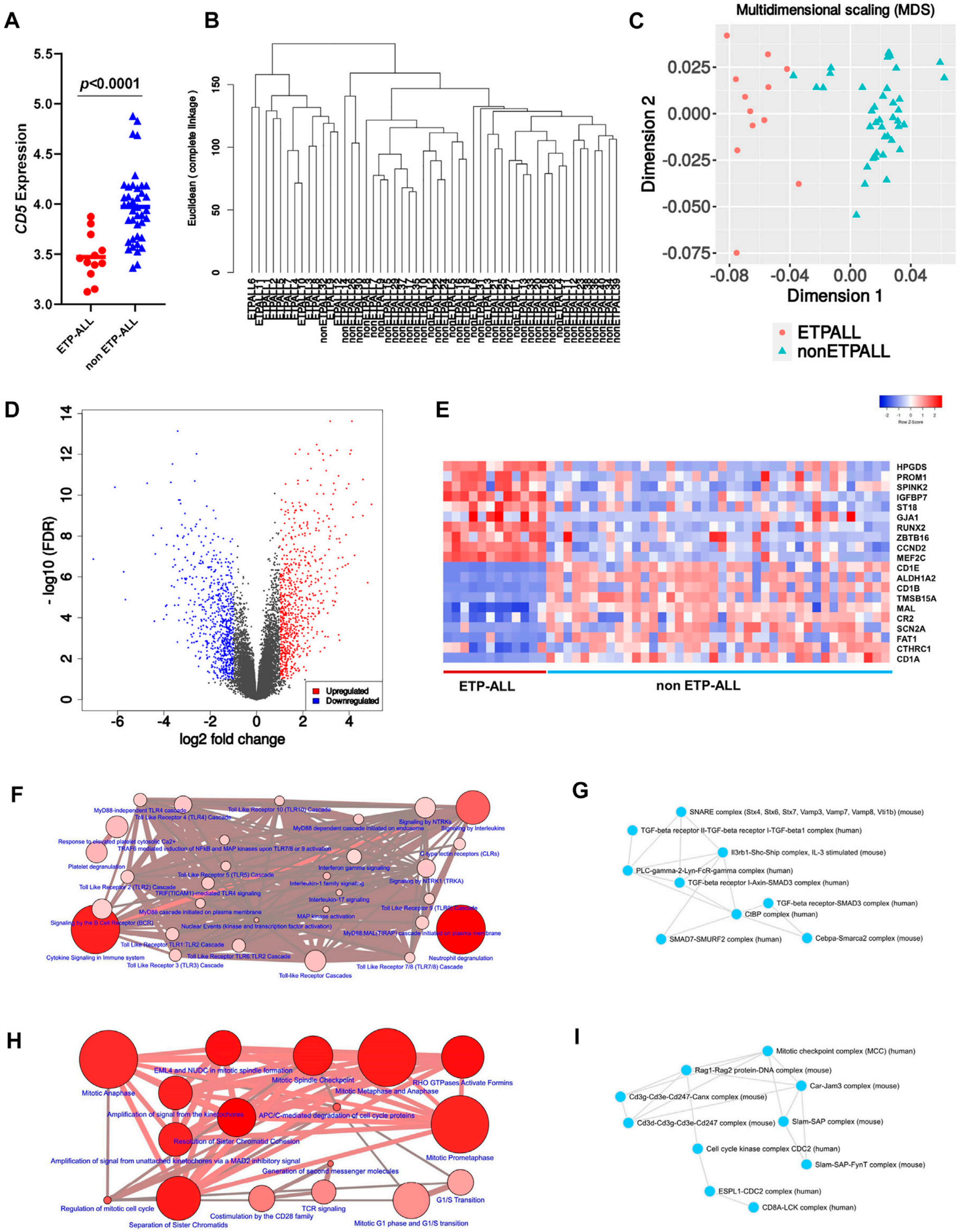

**FIGURE 2 |** Contrasting transcriptomic features between ETP-ALL and non-ETP-ALL. **(A)** Expression level of CD5 in ETP-ALL and non-ETP-ALL groups from GSE28703 dataset. Statistical significance was calculated using two-tailed unpaired Student's t-test. **(B)** Rooted dendrogram of all samples from GSE28703 dataset showing unsupervised hierarchical clustering between ETP-ALL and non-ETP-ALL. **(C)** Multidimensional scaling (MDS) plot of ETP-ALL (red circle) and non-ETP-ALL (cyan triangle) samples from GSE28703. **(D)** Volcano plot representing differentially expressed genes (fold change >2, false discovery rate <0.1) between ETP-ALL and non-ETP-ALL groups from GSE28703. Red dots represent genes upregulated, while blue dots represent genes downregulated in ETP-ALL compared to non-ETP-ALL. **(E)** Row z-score normalized unclustered heatmap of expression levels of top 20 differentially expressed genes between ETP-ALL and non-ETP-ALL groups from GSE28703. **(F)** Network of REACTOME pathways enriched in genes upregulated in ETP-ALL. Diameter and colour intensity of nodes represent gene set size and statistical confidence, respectively. **(G)** Network of protein complexes from CORUM enriched in genes upregulated in ETP-ALL. **(H)** Network of REACTOME pathways enriched in genes downregulated in ETP-ALL (upregulated in non-ETP-ALL). **(I)** Network of protein complexes from CORUM enriched in genes downregulated in ETP-ALL.

percentile, while remaining points were shown as outliers. Violin plots, constructed on BoxPlotR (Spitzer et al., 2014), additionally represented the Kernel density distributions aligned sidewise. For statistical comparisons, two-tailed unpaired Student's t-test with 95% confidence interval was performed. Benjamini–Hochberg procedure was applied to compute false discovery rates for multiple comparisons (Benjamini and Hochberg, 1995). Bubble plots represented the overlap between test and reference gene sets and -$\log_{10}$FDR along the axes, while bubble diameters were proportional to gene set sizes.

# RESULTS

## ETP-ALL Blasts Exhibit Pronounced Transcriptomic Differences in Comparison With Non-ETP-ALL

To design transcriptome-based diagnostic signatures of ETP-ALL, the first step was to test if the immunophenotypic differences between ETP-ALL and non-ETP-ALL (Coustan-Smith et al., 2009) are reflected in their transcriptome. Quality of the processed data from the discovery dataset (GSE28703) was assessed by checking the box plot (**Supplementary Figure S1A**) and density distribution (**Supplementary Figure S1B**) of normalized expression values from individual samples. In addition, significantly different *CD5* expression between the two groups (**Figure 2A**) supported their respective ETP-ALL and non-ETP-ALL status (Chopra et al., 2014). Unsupervised hierarchical clustering on a rooted dendrogram (**Figure 2B**) showed clear divergence between the two groups. Only one non-ETP-ALL sample was present as an outlier in the ETP-ALL branch, while the non-ETP-ALL branch carried no contamination from the ETP-ALL group. Similarly, discernible clustering between the two ALL groups was observed on the multidimensional scaling plot (**Figure 2C**). Such distinguishable transcriptomic patterns between ETP-ALL and non-ETP-ALL not only supported the biological differences between them, but also pointed out the necessity to acknowledge the biological properties of ETP-ALL as a separate entity in order to design prospective therapies against the disease. The extent of upregulated and downregulated transcripts (**Figure 2D**) was comparable between the two groups, indicating no global transcriptional shift in any of them. This idea of balanced transcriptomic alterations was further supported by the MA plot (**Supplementary Figure S1C**) and scatter-plot of average expression values in the two ALL groups (**Supplementary Figure S1D**), showing near-similar counts (**Supplementary Figure S1E**) of DEGs (**Supplementary Table S2**) in both directions. Genes showing higher expression in ETP-ALL were mostly related to non-T lineages as well as hematopoietic stemness, while many of the genes showing elevated expression in non-ETP-ALL were associated with T-lineage commitment (**Figure 2E**). These transcriptomic contrasts underpinned the pathway-level disparity between the two groups. ETP-ALL blasts showed enrichment in Toll like receptor (TLR) cascades and pro-inflammatory cytokine (Interleukin-1, Interleukin-17, Interferon-γ) signalling pathways (**Figure 2F**, **Supplementary Table S3**), likely to be mediated by inflammatory protein complexes containing Transforming Growth Factor (TGF)-β, Phospholipase C-γ etc (**Figure 2G**, **Supplementary Table S4**). Non-ETP-ALL blasts displayed higher propensity towards cell cycle progression, cell division as well as T-cell receptor-mediated and co-stimulatory signalling events (**Figure 2H**, **Supplementary Table S3**), where cell cycle checkpoint complexes and T cell maturation factors such as CD3, RAG (Recombination activating gene) clusters plausibly play a pivotal part (**Figure 2I**, **Supplementary Table S4**).

## ETP-ALL Bears Considerable Intra-Group Transcriptomic Diversity

Interestingly, a high fraction of subjects among the ETP-ALL group showed lower transcriptome-wide correlation (**Figure 3A**), while transcriptome from most of the non-ETP-ALL cases were tightly correlated among themselves; yielding a statistically significant difference between the distributions of their correlation coefficients (**Figure 3B**). Many of the top genes showing very high standard deviations among the ETP-ALL cases were associated with various hematopoietic lineages (**Supplementary Figure S2A**). Top pathways (**Supplementary Figure S2B, Supplementary Table S5**) and protein complexes (**Supplementary Figure S2C, Supplementary Table S6**) associated with these genes, expected to show variable activities across the ETP-ALL cohort, were of diverse functional categories; starting from cell survival and apoptosis to metabolism and hemostasis. Among the 251 genes (**Supplementary Table S7**) contributing most to this intra-group variability of ETP-ALL, 75 and 33 genes, respectively, exhibited higher and lower transcript levels in ETP-ALL compared to non-ETP-ALL (**Figure 3C**, **Supplementary Table S8**). These 108 (75 + 33) genes, supposedly at the root of the transcriptomic heterogeneity within the ETP-ALL group, were also differentially expressed between ETP-ALL and non-ETP-ALL, ensuring this variability to be ETP-ALL-specific. To identify potential key drivers effectuating this transcriptomic diversity of ETP-ALL, the 108 genes were integrated into a functional protein-protein interaction (PPI) network (**Figure 3D**). Based on maximal clique centrality (MCC) scoring (**Supplementary Table S9**), top 10 nodes were selected as hub genes (**Figure 3E**), which displayed the highest degree of centrality across the entire network, therefore could be targeted to achieve maximal success in perturbing the network. An appreciable level of connectivity among the hub genes themselves (**Figure 3F**) supported their operational centrality.

## Most of the Hub Genes Exhibit Contrasting Expression Between ETP-ALL and Non-ETP-ALL

After requisite quality assessments (**Supplementary Figure S3**), a second dataset (GSE78132) was analyzed to affirm the distinctive expression patterns observed in the discovery dataset. Compared to non-ETP-ALL samples, the ETP-ALL group expressed higher

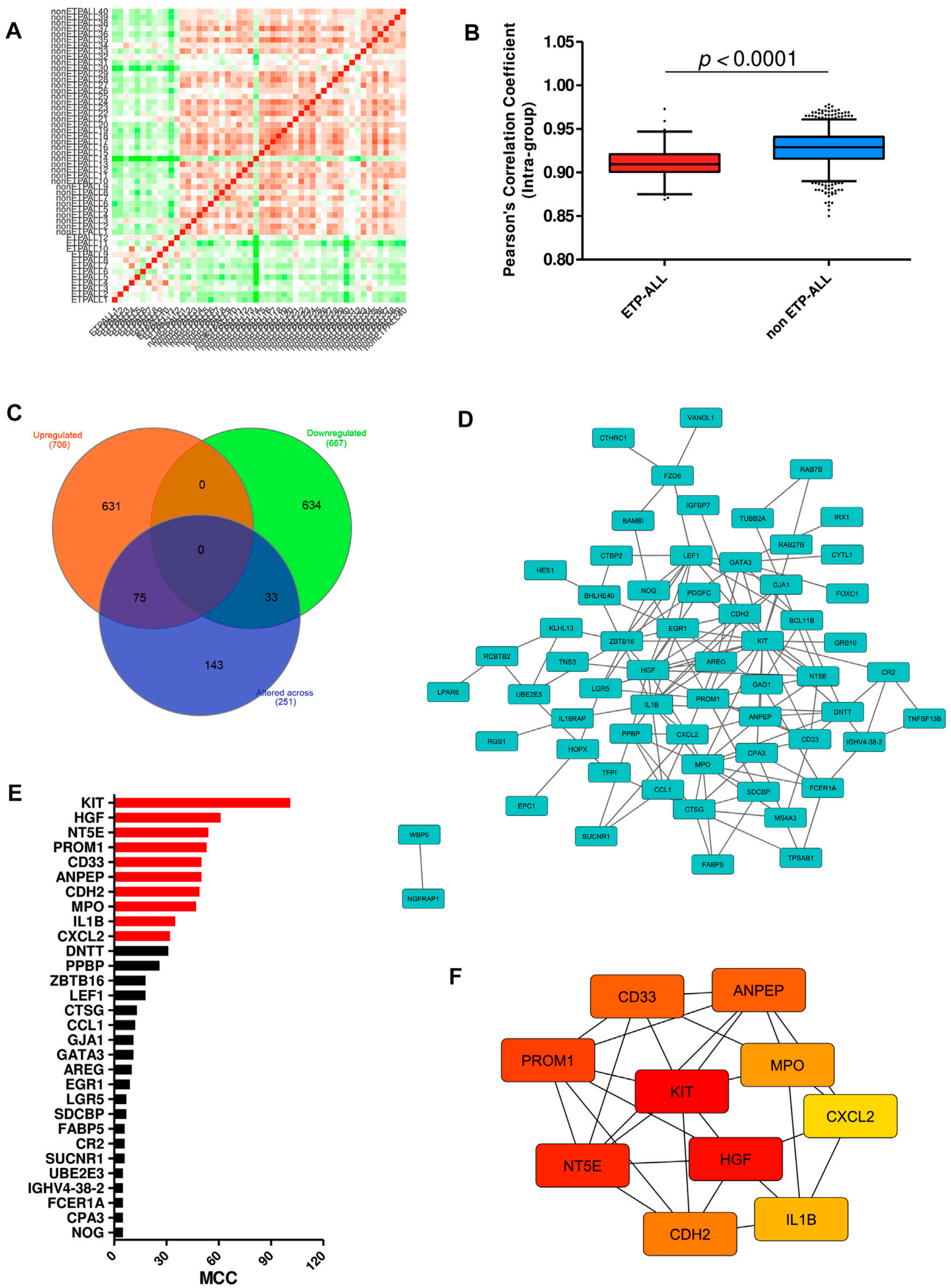


**FIGURE 3 |** Transcriptomic variability within the ETP-ALL group. **(A)** Pair-wise correlation matrix of global gene expression levels between each sample from GSE28703. **(B)** Box-plot of intra-group Pearson's correlation coefficients in ETP-ALL and non-ETP-ALL groups. Statistical significance was calculated using two-tailed unpaired Student's t-test. **(C)** Venn diagram of different sets of differentially expressed genes. Tangerine, green and purple circles represent genes upregulated in, downregulated in and altered (standard deviation >2) across ETP-ALL, respectively. **(D)** Functional protein-protein interaction network of genes up/downregulated in as well as altered across ETP-ALL. Constructed on Cytoscape v3.8.2. **(E)** Maximal Clique Centrality (MCC) score of top 30 hub nodes from the network in **Figure 3D**. Top 10 hub nodes are labelled in red. **(F)** Shortest interaction path of top 10 hub genes within the network. Constructed on Cytoscape v3.8.2.

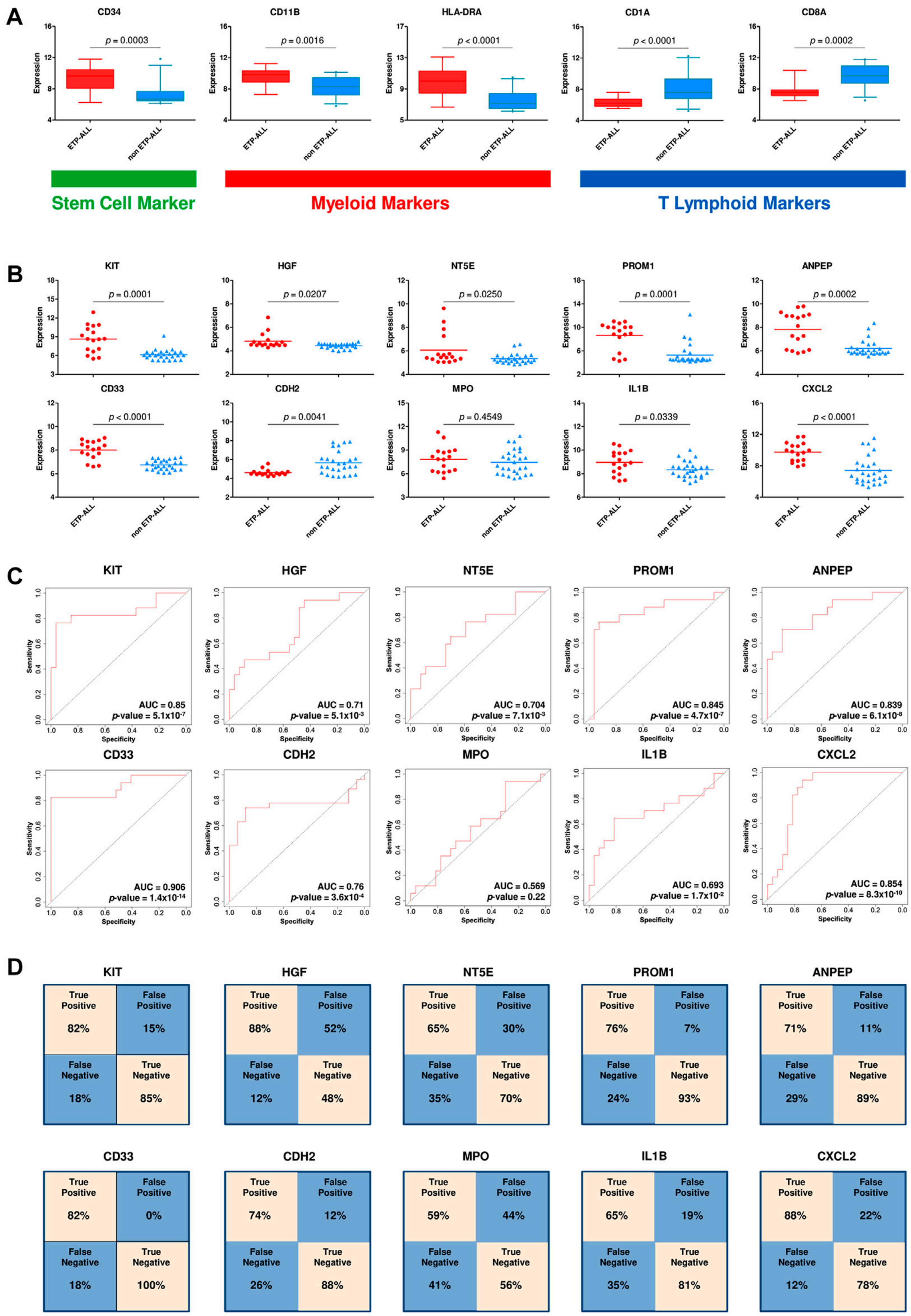


**FIGURE 4 |** Validation of the hub genes as diagnostic biomarkers of ETP-ALL. **(A)** Expression levels of conventional ETP-ALL markers in ETP-ALL and non-ETP-ALL groups from GSE78132 dataset. Statistical significance was calculated using two-tailed unpaired Student's t-test. **(B)** Expression levels of hub genes in ETP-ALL and non-ETP-ALL groups from GSE78132 dataset. Two-tailed unpaired Student's t-test was used to estimate the statistical significance. **(C)** Receiver operating characteristic (ROC) curves of hub genes. AUC (area under curve) values indicate prediction accuracy of the genes as biomarkers. **(D)** Confusion matrices denoting classification qualities of hub genes. For all hub genes apart from CDH2, 'True positive' indicates % of ETP-ALL cases with higher expression than ROC cutoff; 'False negative' indicates % of ETP-ALL cases with lower expression than ROC cutoff; 'False positive' indicates % of non-ETP-ALL cases with higher expression than ROC cutoff; 'True negative' indicates % of non-ETP-ALL cases with lower expression than ROC cutoff. The annotations are opposite for CDH2.

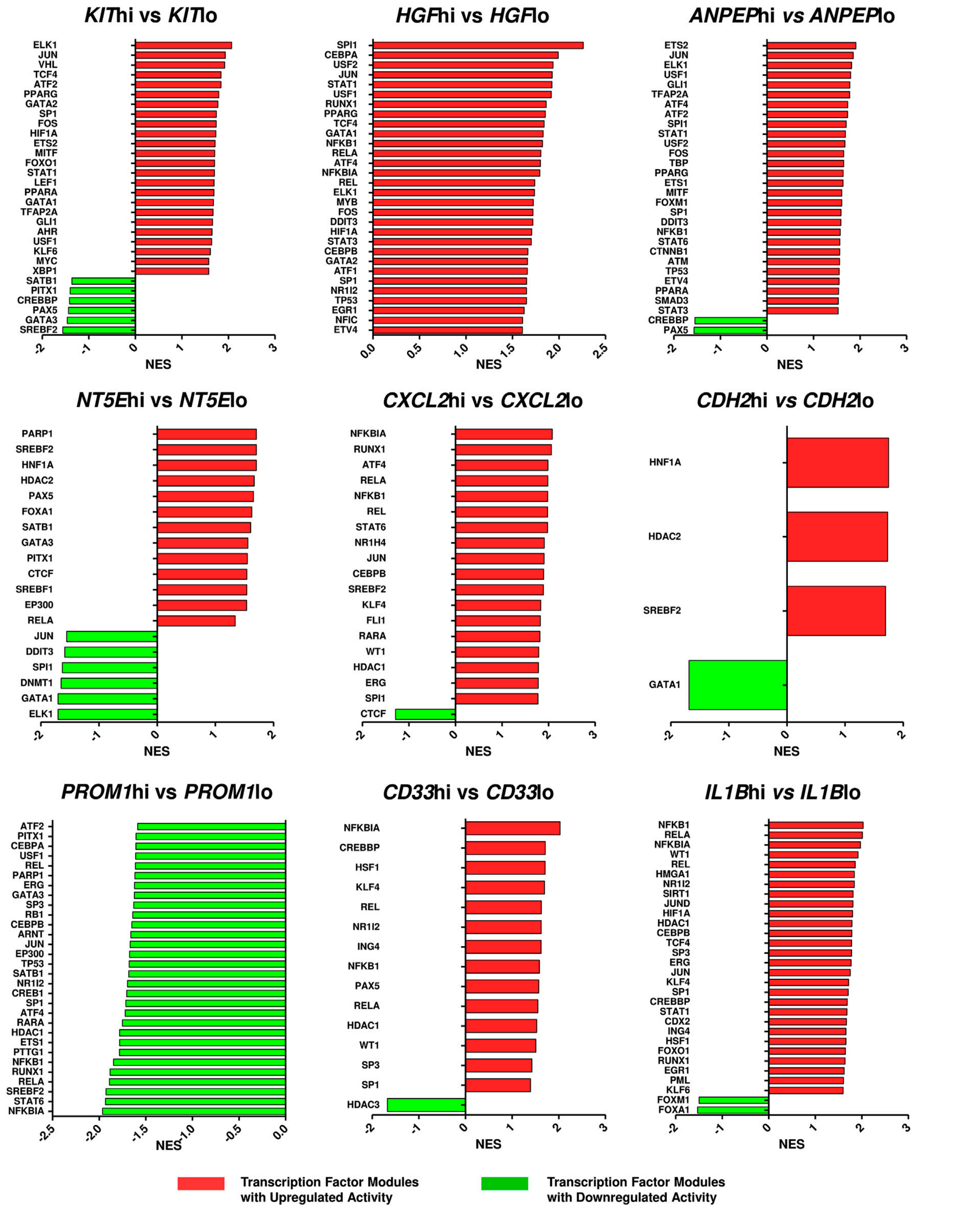


**FIGURE 5 |** Altered activities of transcription factors across ETP-ALL subpopulations expressing different levels of the hub genes. The ETP-ALL cohort from the GSE28703 dataset was divided into subpopulations on the basis of high and low levels of individual hub gene expression (details in 'Enrichment analysis' under 'Materials & Methods'), followed by GSEA against the 'TF.Target.TRRUST' database. Normalized enrichment score (NES) of top 30 transcription factor modules, at most, were represented on the column plots.

levels of stem cell marker *CD34* as well as myeloid markers *CD11B* and *HLA-DRA*, and lower levels of T cell commitment markers *CD1A* and *CD8A*, in this dataset (**Figure 4A**), concordant with the expected trends. Nine of the ten hub genes exhibited statistically significant differences in expression between the two groups, showing good agreement with the findings from the discovery dataset (**Figure 4B**). AUC parameters for six of the nine hub genes (*KIT*, *PROM1*, *ANPEP*, *CD33*, *CDH2* and *CXCL2*) on ROC plots were comprehensively higher (>0.75) than those of the others (**Figure 4C**). Three genes among the latter four, apart from *MPO*, showed satisfactory AUC values (>0.65). Reliability of the classification performances by the genes between ETP-ALL and non-ETP-ALL in terms of true positivity rate and true negativity rate, as observed on the corresponding confusion matrices (**Figure 4D**), was also in the range of reasonable to very good. Therefore, these nine genes (*KIT*, *PROM1*, *ANPEP*, *CD33*, *CDH2*, *CXCL2, HGF, NT5E,* and *IL1B*) were selected as candidate diagnostic biomarkers of ETP-ALL.

## Expression Levels of the Proposed ETP-ALL Biomarkers are Indicative of Their Developmental Bias

Since the hub genes were pivots of the transcriptomic variations across ETP-ALL samples, it was hypothesized that these genes might have crucial involvements in the multi-lineage diversification of the ETP-ALL blasts. Bisection of the GSE28703 ETP-ALL cohort based on individual hub gene expression yielded many genes with differential expression across subpopulations (**Supplementary Figure S4**). Subsequent gene set enrichment analyses between ETP-ALL subpopulations with high and low expression levels of each hub gene revealed marked alterations in several pathways (**Supplementary Figure S5**) and transcription factor activities (**Figure 5**) of hemato-developmental significance. Such observations hinted towards the fact that variable expression of these genes might act as signatures of different hematopoietic lineage induction processes in the multipotent ETP-ALL blasts. To further establish the relationship between hub gene expression and lineage fate decisions, the hub genes as well as certain developmental markers (transcription factors as well as surface proteins) relevant to different hematopoietic branches were overlaid on the two-dimensional PCA plane (**Figure 6A**), where proximity between genes was proportional to the extent of their co-expression within the ETP-ALL cohort from the GSE28703 dataset. The assumed associations between the hub genes and the respective lineages were validated by the expression levels of lineage marker genes in the bisected subpopulations within the ETP-ALL cohort. Expression of T-lineage markers *CD7* and *HES1* varied in concordance with *CDH2* expression (**Figure 6B**), while B-lineage markers *CD19* and *EBF1* significantly varied with *NT5E* levels (**Figure 6C**). Signature of lymphoid commitment at the expense of myeloid potency was ascertained by the expression trends of *IL7R* (common lymphoid marker) and *CEBPA* (myeloid marker) along with *CDH2* and *NT5E* in individual ETP-ALL subjects (**Figure 6D**). Despite their common lymphoid bias, *CDH2* and *NT5E* did not affect B- and T-lineage marker expression, respectively (**Supplementary Figures S6A,B**), while showing a common reciprocal trend with myeloid-associated gene expression (**Supplementary Figure S6C**). *NT5E,* additionally, showed a quasi-significant ($0.05 < p < 0.1$) inverse correlation with stemness marker *CD34* (**Supplementary Figure S6D**), its close neighbour on the PCA plot. *PROM1* expression exhibited positive correlation with its nearest neighbour *CD34*, along with a decline in the levels of *CD38* (**Figure 6E**) as well as the lineage markers (**Supplementary Figure S6E**) in the *PROM1*hi subgroup. The myelo-monocytic marker *CEBPA*, appearing in the vicinity of *HGF*, *KIT* and *ANPEP*, displayed robust association with the expression levels of these genes (**Figure 6F**). Concomitantly, the lymphoid markers exhibited an inverse trend with respect to these three hub genes (**Supplementary Figures S6F,G**). *CXCL2*, juxtaposed to B- as well as myeloid-lineage markers on the PCA plot, showed significant agreement with the levels of B-lineage-specific (**Figure 6G**) as well as myeloid-oriented (**Figure 6H**) markers. However, the myeloid predisposition of *CXCL2* was more pronounced for dendritic cell-specific markers *CD11C* and *IRF8* than granulo-monocytic marker *CEBPA*. Neither *CD33* (**Figure 6I**) nor *IL1B* (**Figure 6J**) exhibited consistency with the expression levels of their nearest neighbour *CD34* as well as *CD19*, which, despite being distant on the PCA plane, was assumed to have a probable association with these genes due to their proximity to *NT5E*. Replication of these observations in the validation cohort (GSE78132) reinforced the proposed biomarkers as indices of lineage bias in ETP-ALL (**Supplementary Figure S7**).

## Developmental Skew of the Proposed ETP-ALL Biomarkers are Corroborated by Their Expression Levels in B-ALL and AML

Understanding the developmental predisposition of the leukemic blasts from ETP-ALL patients might potentiate the use of existing treatment modalities targeting lineage-restricted, mature acute leukemia against ETP-ALL. Considerable consistency was observed in terms of lineage-skewed expression of myeloid-biased *KIT*, *HGF*, *ANPEP*; B-lineage-biased *NT5E*; T-lineage-biased *CDH2* and myeloid plus B-lineage-biased *CXCL2* (**Figure 7A**) in ETP-ALL (from GSE28703; normalized to non-ETP-ALL) and in B-ALL, T-ALL and AML (from GSE13159; normalized to T-ALL). For example, the extent of expression of the myeloid-skewed marker *KIT* in ETP-ALL was comparable to that in AML, and was significantly higher than those in non-myeloid leukemia such as B-ALL and T-ALL, further validating the correlation between its expression and myeloid lineage bias. Despite no correlation with any B-lineage marker, levels of both *CD33* and *IL1B* in ETP-ALL were comparable with those in B-ALL. However, their levels were significantly higher in ETP-ALL than in progenitor/precursor-B-ALLs (**Figure 7B**). Albeit *NT5E*, their close neighbour on the PCA plane, exhibited expressional similitude between ETP-ALL and B-ALL, its levels in pro/pre-B-ALL groups were higher than those

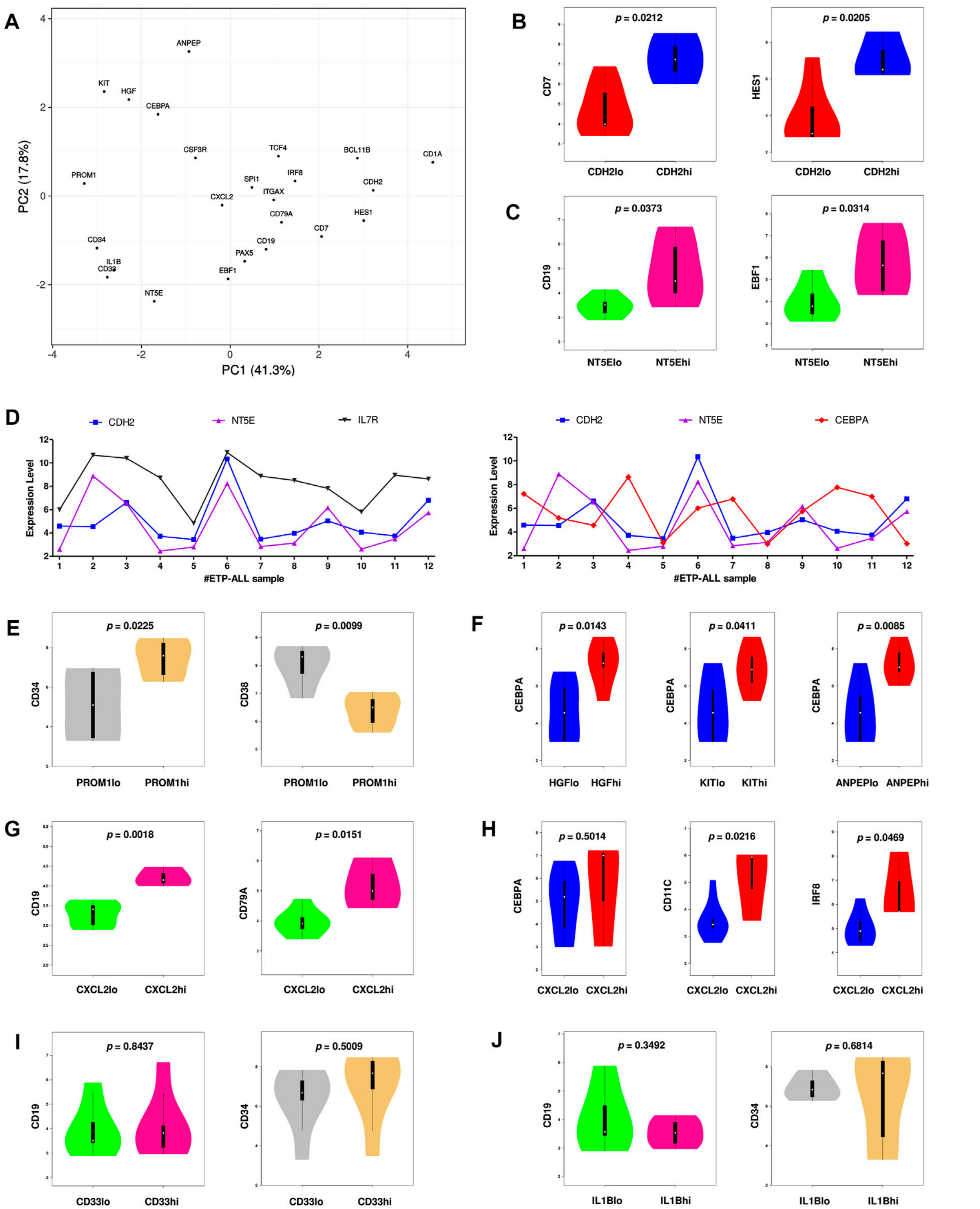


**FIGURE 6 |** Inclination of the proposed biomarkers towards different hematopoietic lineages. **(A)** Principal component analysis (PCA) plot of normalized expression scores (from GSE28703) of the hub genes along with standard markers of hematopoietic lineages. Lineage affiliation of the known markers are as follows; CD34: stemness; CEBPA, CSF3R: myelo-monocytic; EBF1, PAX5, CD19, CD79A: B-lineage; CD7, HES1, BCL11B, CD1A: T-lineage; SPI1, ITGAX, IRF8, TCF4: dendritic cells. **(B)** Expression of CD7 and HES1 along with different levels of CDH2. **(C)** Expression of CD19 and EBF1 along with different levels of NT5E. **(D)** Expression of CDH2, NT5E, IL7R, and CEBPA across different ETP-ALL samples from GSE28703. **(E)** Expression of CD34 and CD38 along with different levels of PROM1. **(F)** Expression of CEBPA along with different levels of HGF, KIT and ANPEP. **(G)** Expression of CD19 and CD79A along with different levels of CXCL2. **(H)** Expression of CEBPA, CD11C, and IRF8 along with different levels of CXCL2. **(I)** Expression of CD19 and CD34 along with different levels of CD33. **(J)** Expression of CD19 and CD34 along with different levels of IL1B. Two-tailed unpaired Student's t-test was used to compute the statistical significance for each comparison.

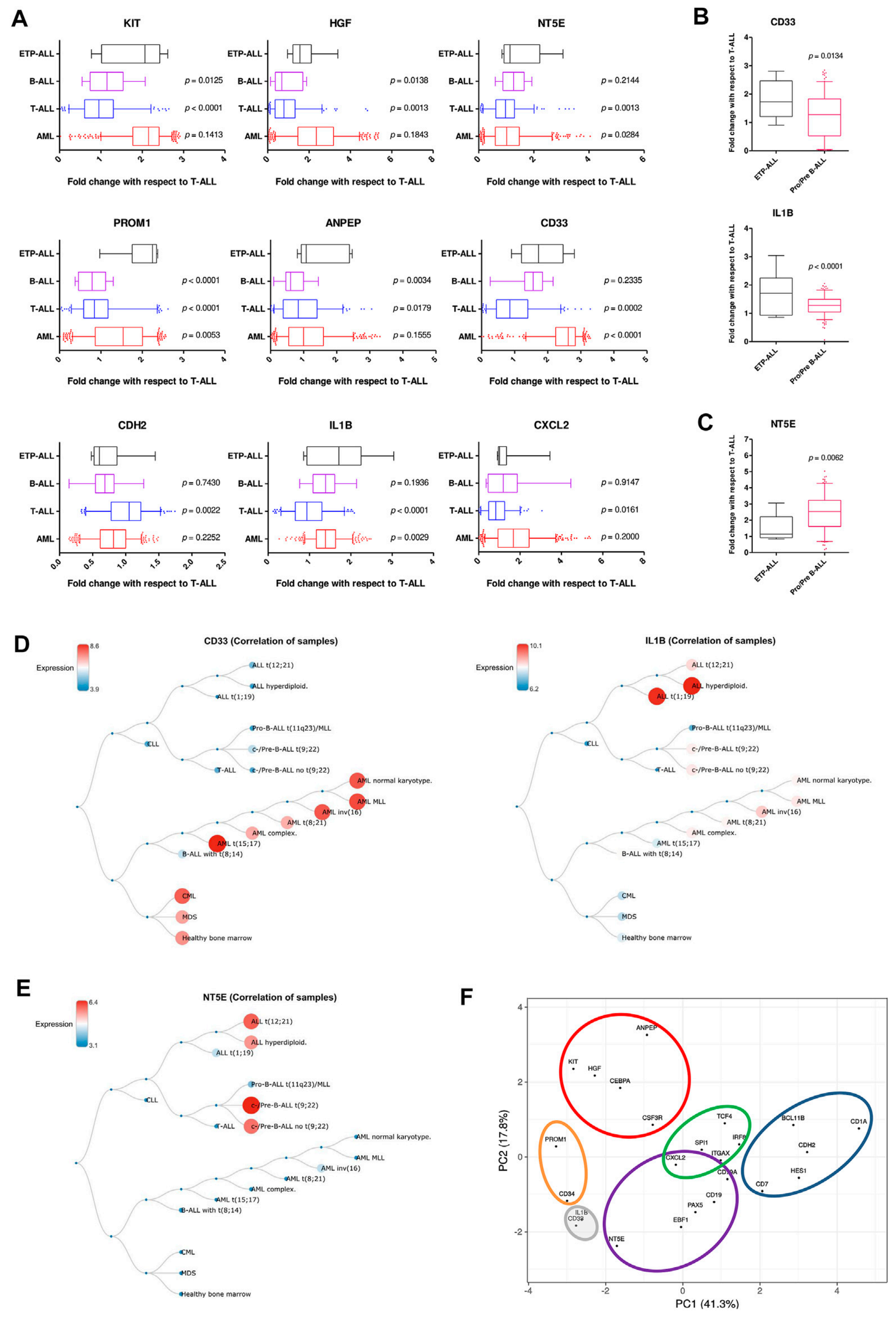

**FIGURE 7 |** Resemblance in expression status of the proposed biomarkers in ETP-ALL and different leukemia subtypes. **(A)** Fold change in expression levels of the proposed biomarkers in ETP-ALL, B-ALL, T-ALL, and AML. **(B)** Fold change in expression levels of CD33 and IL1B in ETP-ALL and pro/pre-B-ALL. **(C)** Fold change in expression levels of NT5E in ETP-ALL and pro/pre-B-ALL. For **(A–C)**, Expression levels of the genes in ETP-ALL were derived from GSE28703 and normalized with respect to their mean expression values in non-ETP-ALL, while expression levels of the genes in pro/pre-B-ALL, B-ALL, T-ALL, and AML were derived from GSE13159 and normalized with respect to their mean expression values in T-ALL. **(D)** Correlation dendrogram of CD33 and IL1B expression levels across different leukemia subtypes from GSE13159. Constructed on BloodSpot. **(E)** Correlation dendrogram of NT5E expression levels across different leukemia subtypes from GSE13159. Constructed on BloodSpot. **(F)** PCA plot of the proposed biomarkers and standard lineage markers (from **Figure 6A**) with lineage demarcation boundaries (orange: stemness, purple: B-lineage, blue: T-lineage, green: dendritic cell, red: myelo-monocytic, grey: unclear lineage skew), drawn on the basis of the consolidated outcomes. Two-tailed unpaired Student's t-test was used to calculate the statistical significance, wherever applicable.

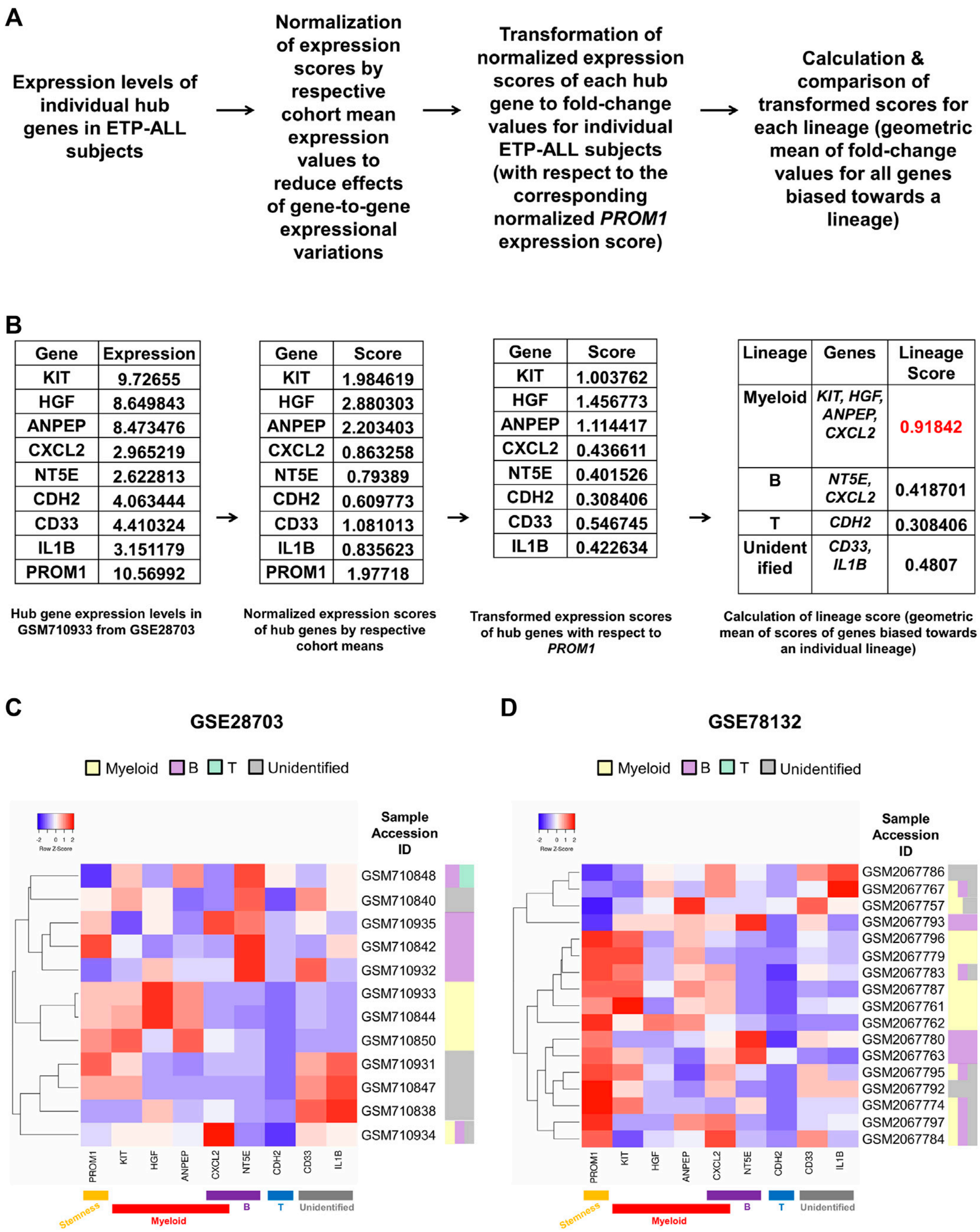


**FIGURE 8 |** Formulation of a personalized score signifying the net lineage bias of the ETP-ALL blasts. **(A)** Mathematical derivation of the lineage score from the expression values of hub genes from individual patient samples. **(B)** Calculation of lineage score for the GSM710933 sample from the GSE28703 dataset. The lineage with the highest lineage score (labeled in red) was assigned to the sample. **(C,D)** Predictive lineage assignments for each sample from GSE28703 **(C)** and GSE78132 **(D)** based on the lineage score calculation.

in ETP-ALL (**Figure 7C**), highlighting possible differences in lineage orientation of these biomarkers. Among all leukemia subtypes, *CD33* exhibited a robust enrichment in AML and CML (chronic myelogenous leukemia), while *IL1B* correlated best with pediatric ALL and considerably with AML (**Figure 7D**). *NT5E*, on the other hand, was not enriched in any malignancy of myeloid origin (**Figure 7E**). Agglomerating all these information, distinct boundaries were drawn on the 2D PCA plane, demarcating the developmental inclinations of the component genes (**Figure 7F**). *CDH2* and *NT5E* belonged to the T-lineage (blue) and B-lineage (purple) clusters, respectively; while *PROM1* existed in the stemness (orange) cluster. Unlike *KIT*, *HGF*, and *ANPEP* belonging exclusively to the myelo-monocytic (red) cluster, *CXCL2* was present in the overlapping zone between

B-lineage and dendritic cell-lineage (green) clusters. *CD33* and *IL1B* were assigned to a separate cluster of uncertainty (grey) owing to their promiscuity in terms of lympho-myeloid specification. Of note, this grey cluster was located right between the B-lineage and stemness clusters, suggestive of their inclination towards a state in between stem cell-like pluripotency and lineage induction.

## Hub Gene Expression Might Predict the Net Lineage Bias of the ETP-ALL Leukemic Blast Populations on a Personalized Level

Owing to the substantial inclination of the hub genes towards different hematopoietic lineages, their collective expression levels might be considered hallmark of the net developmental bias of the entire leukemic blast population in individual ETP-ALL subjects. However, manual predictions in such cases might be erroneous and highly biased. Therefore, the expression scores of all these potential ETP-ALL biomarkers were put into a single quantitative frame (**Figure 8A**), which would enable automated prediction of the net lineage bias of the leukemic blasts on a personalized basis. As ETP-ALL involves leukemic conversion of multipotent stem-like hematopoietic cells, expression level of the stemness marker *PROM1* was selected as reference standard for transformation of the expression levels of individual hub genes into comparable scores. Furthermore, transformed scores for different lineages for individual patients were calculated by considering the geometric means of the personalized transformed score(s) of all the markers inclined towards individual lineages. For example, normalization and transformation of the hub gene expression levels in the GSM710933 sample from the GSE28703 ETP-ALL cohort revealed a strong myeloid bias within the leukemic blasts (**Figure 8B**). Continuing this trend, the proposed framework indicated the net lineage inclination in every single ETP-ALL sample from the GSE28703 (**Figure 8C**) and GSE78132 (**Figure 8D**) datasets. While many samples displayed a robust skew towards the myeloid lineage, a notable proportion of the ETP-ALL cases showed considerable B-lineage bias. Interestingly, many samples exhibited a mixed skew towards myeloid and B-lineages as well as the unidentified process associated with *CD33* and *IL1B*, indicating the existence of individual ETP-ALL patients with a spectrum of multiple lineage inclinations.

## B-Lineage-Oriented Interactome in ETP-ALL Exhibits Exclusive Compartmentalization Within the Hub Gene Physical Interaction Network

Specificity in expression of the proposed markers in ETP-ALL of different lineage inclinations not only supported their presumed lineage bias, but also raised possibilities for these markers and the nexus of their associated proteins to be used directly as druggable targets against cases of ETP-ALL with specific developmental skew(s). Therefore, mining the symbiosis among the total physical interactome of these genes was of utmost importance, as any mode of therapeutic interventions against them is expected to perturb the functioning of all these interactors together. Although enrichment analyses based on the physical interaction networks of the individual genes unveiled the downstream functions performed by their individual interactomes (**Supplementary Figure S8**), this was not enough to recognize the relative overlap among them. Interestingly, the converged physical interactome comprising the proposed biomarkers along with their primary and secondary interactors (**Figure 9A**) exhibited two distinct clusters. The larger cluster consisted of hub genes with different lineage propensities, while the smaller cluster contained only two of the proposed biomarkers: *NT5E* and *CXCL2*, the only genes having strong B-lineage inclination. The larger cluster was enriched in an assorted list of pathways (**Figure 9B**, left panel), where individual pathways were mapped in an overlapping fashion, onto interactors of different hub genes (**Figure 9B**, right panel). The smaller cluster over-represented mostly three events: purine nucleotide signaling, collagen metabolism and CXCR1/2 signaling (**Figure 9C**, left panel). The pathway mappings were well-separated among the interactors of the two hub genes (**Figure 9C**, right panel), indicating their non-redundant actions towards B-lineage priming.

## DISCUSSION

Analysis of the cellular transcriptome is widely used to generate holistic ideas about disease pathogenesis and pinpoint critical markers for their diagnosis, prognosis and therapeutic targeting (Casamassimi et al., 2017). In this study, analyses of the ETP-ALL transcriptome unveiled a pool of genes whose expression levels might act as binary sorters between ETP-ALL and non-ETP-ALL within an ALL cohort and simultaneously predict the specification bias of the leukemic blasts from individual ETP-ALL patients. The study eventually proposes a novel transcriptional phenotype of ETP-ALL as: $KIT^{+}HGF^{+}ANPEP^{+}NT5E^{+}CDH2^{-}PROM1^{+}CXCL2^{+}CD33^{+}IL1B^{+}$, which might be used in conjunction with the conventional biomarkers (Coustan-Smith et al., 2009). The race and ethnicity-dependent variations in global diversity of ETP-ALL (Hunger and Mullighan, 2015) must be taken into account while considering an optimum cut-off for the proposed diagnostic markers in distinguishing ETP-ALL from other ALLs. One strategy to avoid this issue might be to normalize the gene expression scores with respect to the corresponding population mean (as done in the present work) before fixing a diagnostic cut-off, thereby reasonably nullifying the race and ethnicity-associated variations. Of note, ANPEP and CD33 are already enlisted as immunophenotypic ETP-ALL markers (Jain et al., 2016). KIT, NT5E, PROM1, and CDH2 are cell surface proteins, which makes them potentially eligible for being used in immunophenotypic identification of ETP-ALL. Besides, HGF, IL1B, and CXCL2 are potential soluble markers of ETP-ALL due to their secreted nature. Assuming a linear relationship between their observed transcript levels and expected protein levels in these contexts, all these markers might therefore be added to the existing panel of ETP-ALL biomarkers for multiparametric flow cytometry-based immunophenotypic analyses. Use of this updated panel would not only increase the

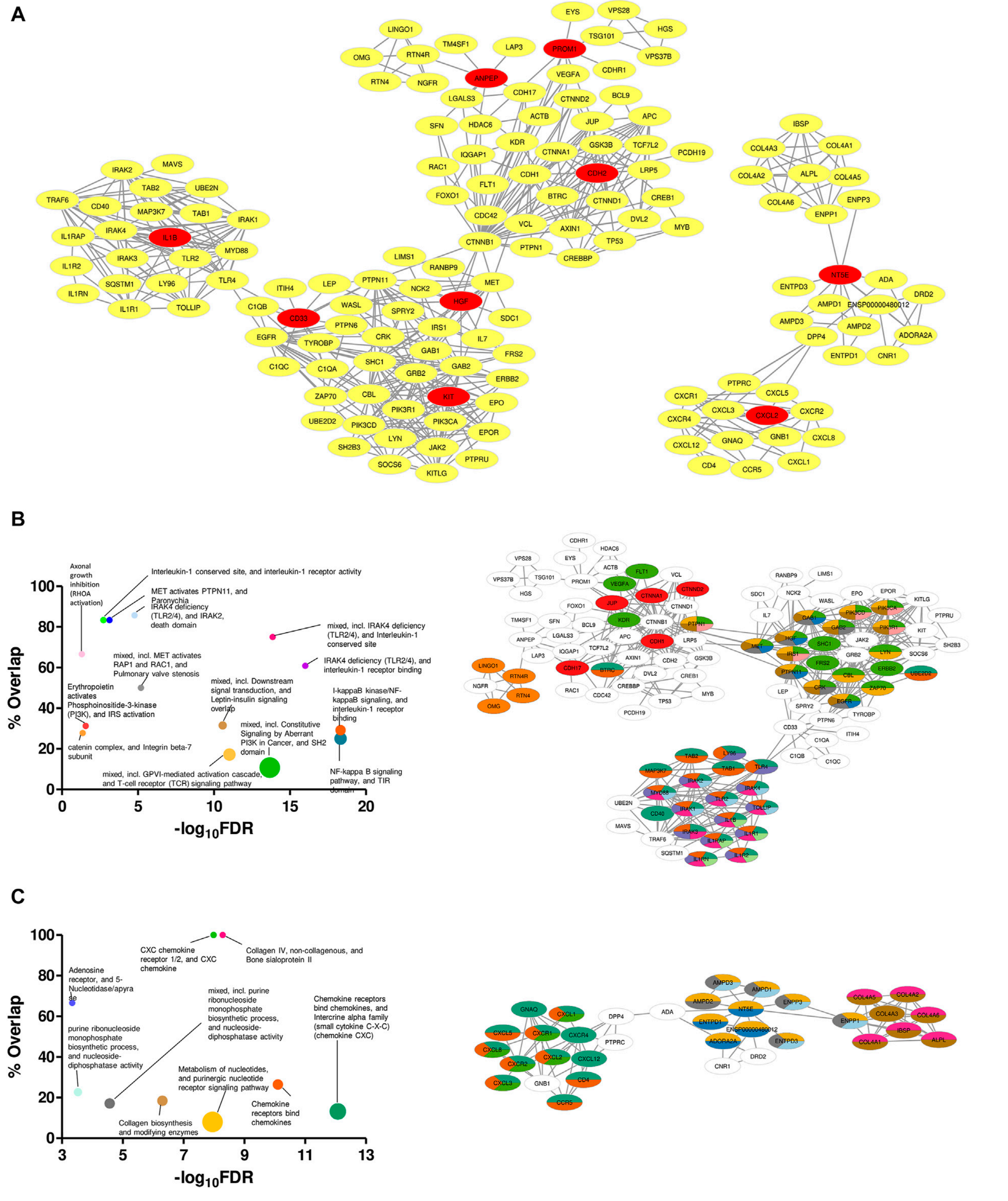

**FIGURE 9 |** Unique clustering pattern within the interactome of the proposed biomarkers. **(A)** Merged physical interactome of the proposed biomarkers. The biomarker genes are denoted by red nodes, while the primary and secondary interactors are denoted by yellow nodes. **(B,C)** Bubble plots (**B**,**C**: left panel) depicting over-represented pathways in the left **(B)** and right **(C)** cluster, respectively. Individual pathways were mapped onto the participant genes (**B**,**C**: right panel). Sizes of the bubbles on the bubble plots are directly proportional to the gene set sizes. Colours on the pathway-mapped networks denote individual pathways, as colour-coded on the corresponding bubble plots.

specificity in diagnosis of ETP-ALL, but would also facilitate early detection of the inherent lineage bias of the ETP-ALL blasts on a personalized basis, effecting prompter and more specific actions by the clinicians.

Despite recent developments in single-cell RNA sequencing explicating the intra-population heterogeneity in ETP-ALL (Anand et al., 2021) as well as ETPs (Zhou et al., 2019; Lavaert et al., 2020), this study did not investigate the ETP-ALL transcriptome on a single-cell resolution. An individual ETP-ALL patient might (and often do) harbour a heterogeneous community of leukemic blasts due to their underlying multipotency (Kumar et al., 2019). Since therapeutic modules targeted against ETP-ALL would act against the entire community of neoplastic lymphoblasts, this study focussed onto the single subject-level transcriptome of ETP-ALL to establish a platform for precision medicine against the dominant leukemic blast subpopulations in individuals. The proposed ETP-ALL markers identified by this study, showing diverse propensities towards different developmental outcomes, might act as hallmarks of lineage priming in ETP-ALL blasts. Consequently, their expression levels in an individual patient might evoke an idea of the net developmental inclination of the entire leukemic blast population in that patient (**Figure 8**). *GATA3*, one of the top 30 hub genes identified by this study (**Figure 3E**), has been reported to split the ETP-ALL patients into subpopulations with different potencies depending upon its expression (Fransecky et al., 2016). This study, in addition to all related studies done so far, provides with a mathematical framework for the detection of potential lineage inclinations on a personalized level. Thus, more such subpopulations within the ETP-ALL patient cohorts might be identified on the basis of such multi-parametric analyses, which might improve the clinical outcome of ETP-ALL to a significant extent by opening new avenues for large-scale drug repurposing.

The incompletely differentiated ETP-ALL blasts are not true mimics of the differentiated leukemic blasts from B-ALL or AML; resonated by their high levels of stem cell-associated gene expression (Coustan-Smith et al., 2009). Therefore it is not easy to devise lineage-targeted therapies against them. Targeting random non-T-lineage markers of mature hematopoietic cells such as CD14 or CD19 in case of ETP-ALL might not be fruitful because of their incompletely differentiated status, where the blasts might not abundantly express those particular lineage markers. Contrarily, expression of the biomarkers proposed in this study varies considerably across ETP-ALL subjects. Distances along the first principal component on the PCA plane (**Figure 7F**) signified greater disparity between the expression patterns of *CD34* and the mature non-T-lineage markers (such as *CSF3R*, *CD19*), compared to those between *CD34* and the corresponding lineage markers proposed in this study (such as *KIT*, *HGF*, *NT5E*). This indicates the ETP-ALL blasts to exist in an intermediate state between absolute stemness and complete lineage fixation, where the expression levels of the proposed markers might act as better indicators of specification than the levels of the mature-stage lineage markers. Close inspection of the physical interactome of the proposed markers, hence, might be profitable in defining the cellular processes associated with the lineage-priming checkpoints within ETP-ALL, which might be ideal therapeutic targets. Since some of the markers are even cell-surface expressed, they might also be exploited for targeted delivery of therapeutics specifically to the ETP-ALL blasts. In fact, CD33-targeted delivery of IMGN779 against ETP-ALL *in vitro* has already yielded promising results (Khogeer et al., 2019), making such superficial biomarkers lucrative targets for the delivery of therapeutics.

The considerable B-lineage inclination in a sizeable fraction of ETP-ALL samples (**Figures 8C,D**) coupled with the isolated presence of the B-lineage-related cluster within the entire interactome associated with the hub genes (**Figure 9A**) highlights the necessity of acknowledging the B-lineage bias of ETP-ALL with utmost importance. Because of the partition between the B- and non-B-lineage networks, therapeutic tweaking inside the non-B interactome would most likely be insufficient against B-lineage-primed ETP-ALL blasts. Incidentally, in a limited sized cohort, relapse after >100 days of remission post-chemotherapy was observed in every single ETP-ALL patient expressing B-lineage markers on the leukemic blasts (Garg et al., 2019). Till date, no chemotherapeutic protocol has exclusively targeted the B-lineage-associated pathways like adenosine receptor signaling in ETP-ALL. This under-appreciation of B-potency in selective ETP-ALL cases might effectuate the prognostic worsening as well as high relapse rates of B-lineage-inclined ETP-ALL over the others. The markers proposed in this study, thus, might facilitate the detection of specific cases of ETP-ALL with significant B-lineage predisposition along with simultaneous targeting of the primary pathways (such as adenosine signaling) encompassing the B-lineage markers.

Multiple studies have uncovered the molecular phenomena behind the lineage plasticity of ETPs, and have designated certain genes as barcodes of particular specification programmes in these multipotent cells (Chiara et al., 2021; Hosokawa and Rothenberg, 2021). However, to the best of our knowledge, this study is the first of its kind to delineate the developmental pliability of the neoplastic forms of these multipotent cells, bringing forth new opportunities to subclassify multipotent ETP-ALL samples based on their lineage bias. This strongly recommends the invention of novel therapeutic approaches as well as opens up possible prospects of repurposing existing B-ALL or AML-directed therapies on a personalized mode. In parallel, the current study suggests the presence of ETP-ALL samples with mixed lineage propensities or unidentified developmental bias, calling for further basic as well as translational research in order to formulate appropriate clinical strategies in these aspects. On top of all, such observations merit many more high-throughput studies with ETP-ALL blast samples from patients of a wide range of socio-biological factors (such as age, ethnicity etc) which affect the hematopoietic quality-control checkpoints, to gain further insights into the deeper mechanisms of leukemogenesis.

## DATA AVAILABILITY STATEMENT

The public microarray gene expression datasets used in this study are available on NCBI GEO DataSets (URL: https://www.ncbi.

nlm.nih.gov/gds) against the respective accession numbers: GSE28703, GSE78132, and GSE13159. Processed data in any form, not reported in the figures/Supplementary Material, will be available from the corresponding authors upon reasonable request.

## AUTHOR CONTRIBUTIONS

SM and AK collected data, conceived and performed the experiments, analyzed the outputs and wrote the manuscript; PP performed some experiments; SD provided with critical inputs during data analysis; AB and SB directed the project and edited the manuscript. All authors discussed and reviewed the results and have read and agreed to the final version of the manuscript.

## FUNDING

This work was supported by the DBT-Ramalingaswami Grant to SB (D.O. No.BT/HRD/35/02/2006 Dated: 19 November 2018). SM was supported by Senior Research Fellowship from Council of Scientific & Industrial Research (CSIR), India. AK was supported by Senior Research Fellowship from University Grants Commission (UGC), India. PP was supported by Junior Research Fellowship from Council of Scientific and Industrial Research (CSIR), India.

## ACKNOWLEDGMENTS

We acknowledge Charles G. Mullighan, St Jude Children's Research Hospital, United States for sharing primary microarray data, and Jayanta Chakrabarti, Director, CNCI, India for providing necessary facilities.

## SUPPLEMENTARY MATERIAL

The Supplementary Material for this article can be found online at: https://www.frontiersin.org/articles/10.3389/fcell.2022.899752/full#supplementary-material

## REFERENCES

Anand, P., Guillaumet-Adkins, A., Dimitrova, V., Yun, H., Drier, Y., Sotudeh, N., et al. (2021). Single-Cell RNA-Seq Reveals Developmental Plasticity with Coexisting Oncogenic States and Immune Evasion Programs in ETP-ALL. *Blood J. Am. Soc. Hematol.* 137 (18), 2463–2480. doi:10.1182/blood.2019004547

Babicki, S., Arndt, D., Marcu, A., Liang, Y., Grant, J. R., Maciejewski, A., et al. (2016). Heatmapper: Web-Enabled Heat Mapping for All. *Nucleic Acids Res.* 44 (W1), W147–W153. doi:10.1093/nar/gkw419

Bagger, F. O., Kinalis, S., and Rapin, N. (2019). BloodSpot: A Database of Healthy and Malignant Haematopoiesis Updated with Purified and Single Cell mRNA Sequencing Profiles. *Nucleic Acids Res.* 47 (D1), D881–D885. doi:10.1093/nar/gky1076

Barik, S., Cattin-Roy, A. N., Miller, M. M., Ukah, T. K., and Zaghouani, H. (2018). IL-4 and IL-13 Guide Early Thymic Progenitors to Mature toward Dendritic Cells. *J. Immunol.* 201 (10), 2947–2958. doi:10.4049/jimmunol.1701186

Barik, S., Miller, M. M., Cattin-Roy, A. N., Ukah, T. K., Chen, W., and Zaghouani, H. (2017). IL-4/IL-13 Signaling Inhibits the Potential of Early Thymic Progenitors to Commit to the T Cell Lineage. *J. Immunol.* 199 (8), 2767–2776. doi:10.4049/jimmunol.1700498

Barrett, T., Wilhite, S. E., Ledoux, P., Evangelista, C., Kim, I. F., Tomashevsky, M., et al. (2012). NCBI GEO: Archive for Functional Genomics Data Sets-Update. *Nucleic Acids Res.* 41 (D1), D991–D995. doi:10.1093/nar/gks1193

Bell, J. J., and Bhandoola, A. (2008). The Earliest Thymic Progenitors for T Cells Possess Myeloid Lineage Potential. *Nature* 452 (7188), 764–767. doi:10.1038/nature06840

Bene, M. C., Castoldi, G., Knapp, W., Ludwig, W. D., Matutes, E., Orfao, A., et al. (1995). Proposals for the Immunological Classification of Acute Leukemias. European Group for the Immunological Characterization of Leukemias (EGIL). *Leukemia* 9 (10), 1783–1786.

Benjamini, Y., and Hochberg, Y. (1995). Controlling the False Discovery Rate: A Practical and Powerful Approach to Multiple Testing. *J. R. Stat. Soc. Ser. B Methodol.* 57 (1), 289–300. doi:10.1111/j.2517-6161.1995.tb02031.x

Bernt, K. M., Hunger, S. P., and Neff, T. (2016). The Functional Role of PRC2 in Early T-Cell Precursor Acute Lymphoblastic Leukemia (ETP-ALL)–Mechanisms and Opportunities. *Front. Pediatr.* 4, 49. doi:10.3389/fped.2016.00049

Booth, C. A. G., Barkas, N., Neo, W. H., Boukarabila, H., Soilleux, E. J., Giotopoulos, G., et al. (2018). Ezh2 and Runx1 Mutations Collaborate to Initiate Lympho-Myeloid Leukemia in Early Thymic Progenitors. *Cancer Cell* 33 (2), 274–291. doi:10.1016/j.ccell.2018.01.006

Casamassimi, A., Federico, A., Rienzo, M., Esposito, S., and Ciccodicola, A. (2017). Transcriptome Profiling in Human Diseases: New Advances and Perspectives. *Int. J. Mol. Sci.* 18 (8), 1652. doi:10.3390/ijms18081652

Castaneda Puglianini, O., and Papadantonakis, N. (2020). Early Precursor T-Cell Acute Lymphoblastic Leukemia: Current Paradigms and Evolving Concepts. *Ther. Adv. Hematol.* 11, 2040620720929475. doi:10.1177/2040620720929475

Chen, E. Y., Tan, C. M., Kou, Y., Duan, Q., Wang, Z., Meirelles, G. V., et al. (2013). Enrichr: Interactive and Collaborative HTML5 Gene List Enrichment Analysis Tool. *BMC Bioinforma.* 14 (1), 128. doi:10.1186/1471-2105-14-128

Chiara, V. D., Daxinger, L., and Staal, F. J. T. (2021). The Route of Early T Cell Development: Crosstalk between Epigenetic and Transcription Factors. *Cells* 10 (5), 1074. doi:10.3390/cells10051074

Chin, C. H., Chen, S. H., Wu, H. H., Ho, C. W., Ko, M. T., and Lin, C. Y. (2014). cytoHubba: Identifying Hub Objects and Sub-networks from Complex Interactome. *BMC Syst. Biol.* 8 (4), S11–S17. doi:10.1186/1752-0509-8-S4-S11

Chopra, A., Bakhshi, S., Pramanik, S. K., Pandey, R. M., Singh, S., Gajendra, S., et al. (2014). Immunophenotypic Analysis of T-Acute Lymphoblastic Leukemia. A CD5-Based ETP-ALL Perspective of Non-ETP T-ALL. *Eur. J. Haematol.* 92 (3), 211–218. doi:10.1111/ejh.12238

Coustan-Smith, E., Mullighan, C. G., Onciu, M., Behm, F. G., Raimondi, S. C., Pei, D., et al. (2009). Early T-Cell Precursor Leukaemia: A Subtype of Very High-Risk Acute Lymphoblastic Leukaemia. *Lancet Oncol.* 10 (2), 147–156. doi:10.1016/s1470-2045(08)70314-0

Doncheva, N. T., Morris, J. H., Gorodkin, J., and Jensen, L. J. (2018). Cytoscape StringApp: Network Analysis and Visualization of Proteomics Data. *J. Proteome Res.* 18 (2), 623–632. doi:10.1021/acs.jproteome.8b00702

Fekete, J. T., and Győrffy, B. (2019). ROCplot.org: Validating Predictive Biomarkers of Chemotherapy/Hormonal Therapy/Anti-HER2 Therapy Using Transcriptomic Data of 3,104 Breast Cancer Patients. *Int. J. Cancer* 145 (11), 3140–3151. doi:10.1002/ijc.32369

Fransecky, L., Neumann, M., Heesch, S., Schlee, C., Ortiz-Tanchez, J., Heller, S., et al. (2016). Silencing of GATA3 Defines a Novel Stem Cell-Like Subgroup of ETP-ALL. *J. Hematol. Oncol.* 9 (1), 95–12. doi:10.1186/s13045-016-0324-8

Garg, S., Gupta, S. K., Bakhshi, S., Mallick, S., and Kumar, L. (2019). ETP-ALL with Aberrant B Marker Expression: Case Series and a Brief Review of Literature. *Int. J. Lab. Hematol.* 41 (2), e32–e37. doi:10.1111/ijlh.12942

Ge, S. X., Son, E. W., and Yao, R. (2018). iDEP: An Integrated Web Application for Differential Expression and Pathway Analysis of RNA-Seq Data. *BMC Bioinforma.* 19 (1), 534. doi:10.1186/s12859-018-2486-6

Genescà, E., Morgades, M., Montesinos, P., Barba, P., Gil, C., Guàrdia, R., et al. (2020). Unique Clinico-Biological, Genetic and Prognostic Features of Adult Early T-Cell Precursor Acute Lymphoblastic Leukemia. *Haematologica* 105 (6), e294–e297. doi:10.3324/haematol.2019.225078

Haymaker, C. L., Guloglu, F. B., Cascio, J. A., Hardaway, J. C., Dhakal, M., Wan, X., et al. (2012). Bone Marrow-Derived IL-13Rα1-Positive Thymic Progenitors are Restricted to the Myeloid Lineage. *J. Immunol.* 188 (7), 3208–3216. doi:10.4049/jimmunol.1103316

Heberle, H., Meirelles, G. V., da Silva, F. R., Telles, G. P., and Minghim, R. (2015). InteractiVenn: A Web-Based Tool for the Analysis of Sets through Venn Diagrams. *BMC Bioinforma.* 16 (1), 169. doi:10.1186/s12859-015-0611-3

Hosokawa, H., and Rothenberg, E. V. (2021). How Transcription Factors Drive Choice of the T Cell Fate. *Nat. Rev. Immunol.* 21 (3), 162–176. doi:10.1038/s41577-020-00426-6

Hunger, S. P., and Mullighan, C. G. (2015). Redefining ALL Classification: toward Detecting High-Risk ALL and Implementing Precision Medicine. *Blood J. Am. Soc. Hematol.* 125 (26), 3977–3987. doi:10.1182/blood-2015-02-580043

Inukai, T., Kiyokawa, N., Campana, D., Coustan-Smith, E., Kikuchi, A., Kobayashi, M., et al. (2012). Clinical Significance of Early T-Cell Precursor Acute Lymphoblastic Leukaemia: Results of the Tokyo Children's Cancer Study Group Study L99-15. *Br. J. Hematol.* 156 (3), 358–365. doi:10.1111/j.1365-2141.2011.08955.x

Jain, N., Lamb, A. V., O'Brien, S., Ravandi, F., Konopleva, M., Jabbour, E., et al. (2016). Early T-Cell Precursor Acute Lymphoblastic Leukemia/Lymphoma (ETP-ALL/LBL) in Adolescents and Adults: A High-Risk Subtype. *Blood, J. Am. Soc. Hematol.* 127 (15), 1863–1869. doi:10.1182/blood-2015-08-661702

Kamburov, A., Pentchev, K., Galicka, H., Wierling, C., Lehrach, H., and Herwig, R. (2011). ConsensusPathDB: Toward a More Complete Picture of Cell Biology. *Nucleic Acids Res.* 39 (Suppl. l_1), D712–D717. doi:10.1093/nar/gkq1156

Kamburov, A., Wierling, C., Lehrach, H., and Herwig, R. (2009). ConsensusPathDB-a Database for Integrating Human Functional Interaction Networks. *Nucleic acids Res.* 37 (Suppl. l_1), D623–D628. doi:10.1093/nar/gkn698

Khogeer, H., Rahman, H., Jain, N., Angelova, E. A., Yang, H., Quesada, A., et al. (2019). Early T Precursor Acute Lymphoblastic Leukemia/Lymphoma Shows Differential Immunophenotypic Characteristics Including Frequent CD 33 Expression and *In Vitro* Response to Targeted CD 33 Therapy. *Br. J. Haematol.* 186 (4), 538–548. doi:10.1111/bjh.15960

Khurana, S., Melody, M. E., Ketterling, R. P., Peterson, J. F., Luoma, I. M., Vazmatzis, G., et al. (2020). Molecular and Phenotypic Characterization of an Early T-Cell Precursor Acute Lymphoblastic Lymphoma Harboring PICALM-MLLT10 Fusion with Aberrant Expression of B-Cell Antigens. *Cancer Genet.* 240, 40–44. doi:10.1016/j.cancergen.2019.11.002

Kraszewska, M. D., Dawidowska, M., Szczepański, T., and Witt, M. (2012). T-Cell Acute Lymphoblastic Leukaemia: Recent Molecular Biology Findings. *Br. J. Hematol.* 156 (3), 303–315. doi:10.1111/j.1365-2141.2011.08957.x

Kuleshov, M. V., Jones, M. R., Rouillard, A. D., Fernandez, N. F., Duan, Q., Wang, Z., et al. (2016). Enrichr: A Comprehensive Gene Set Enrichment Analysis Web Server 2016 Update. *Nucleic Acids Res.* 44 (W1), W90–W97. doi:10.1093/nar/gkw377

Kumar, A., Drusbosky, L. M., Meacham, A., Turcotte, M., Bhargav, P., Vasista, S., et al. (2019). Computational Modeling of Early T-Cell Precursor Acute Lymphoblastic Leukemia (ETP-ALL) to Identify Personalized Therapy Using Genomics. *Leukemia Res.* 78, 3–11. doi:10.1016/j.leukres.2019.01.003

Lavaert, M., Liang, K. L., Vandamme, N., Park, J.-E., Roels, J., Kowalczyk, M. S., et al. (2020). Integrated scRNA-Seq Identifies Human Postnatal Thymus Seeding Progenitors and Regulatory Dynamics of Differentiating Immature Thymocytes. *Immunity* 52 (6), 1088–1104. doi:10.1016/j.immuni.2020.03.019

Luc, S., Luis, T. C., Boukarabila, H., Macaulay, I. C., Buza-Vidas, N., Bouriez-Jones, T., et al. (2012). The Earliest Thymic T Cell Progenitors Sustain B Cell and Myeloid Lineage Potential. *Nat. Immunol.* 13 (4), 412–419. doi:10.1038/ni.2255

Maude, S. L., Dolai, S., Delgado-Martin, C., Vincent, T., Robbins, A., Selvanathan, A., et al. (2015). Efficacy of JAK/STAT Pathway Inhibition in Murine Xenograft Models of Early T-Cell Precursor (ETP) Acute Lymphoblastic Leukemia. *Blood* 125 (11), 1759–1767. doi:10.1182/blood-2014-06-580480

McEwan, A., Pitiyarachchi, O., and Viiala, N. (2020). Relapsed/Refractory ETP-ALL Successfully Treated with Venetoclax and Nelarabine as a Bridge to Allogeneic Stem Cell Transplant. *HemaSphere* 4 (3), e379. doi:10.1097/HS9.0000000000000379

Metsalu, T., and Vilo, J. (2015). ClustVis: A Web Tool for Visualizing Clustering of Multivariate Data Using Principal Component Analysis and Heatmap. *Nucleic Acids Res.* 43 (W1), W566–W570. doi:10.1093/nar/gkv468

Mukherjee, S., Kar, A., Khatun, N., Datta, P., Biswas, A., and Barik, S. (2021). Familiarity Breeds Strategy: In Silico Untangling of the Molecular Complexity on Course of Autoimmune Liver Disease-To-Hepatocellular Carcinoma Transition Predicts Novel Transcriptional Signatures. *Cells* 10 (8), 1917. doi:10.3390/cells10081917

Neumann, M., Heesch, S., Schlee, C., Schwartz, S., Gökbuget, N., Hoelzer, D., et al. (2013). Whole-Exome Sequencing in Adult ETP-ALL Reveals a High Rate of DNMT3A Mutations. *Blood, J. Am. Soc. Hematol.* 121 (23), 4749–4752. doi:10.1182/blood-2012-11-465138

Numan, Y., Alfayez, M., Maiti, A., Alvarado, Y., Jabbour, E. J., Ferrajoli, A., et al. (2018). First Report of Clinical Response to Venetoclax in Early T-Cell Precursor Acute Lymphoblastic Leukemia. *JCO Precis. Oncol.* 2, PO.18.00127. doi:10.1200/PO.18.00127

Patrick, K., Wade, R., Goulden, N., Mitchell, C., Moorman, A. V., Rowntree, C., et al. (2014). Outcome for Children and Young People with Early T-Cell Precursor Acute Lymphoblastic Leukaemia Treated on a Contemporary Protocol, UKALL 2003. *Br. J. Haematol.* 166 (3), 421–424. doi:10.1111/bjh.12882

Ravichandran, S., Banerjee, U., Dr, G. D., Kandukuru, R., Thakur, C., Chakravortty, D., et al. (2021). VB10, a New Blood Biomarker for Differential Diagnosis and Recovery Monitoring of Acute Viral and Bacterial Infections. *EBioMedicine* 67, 103352. doi:10.1016/j.ebiom.2021.103352

Shannon, P., Markiel, A., Ozier, O., Baliga, N. S., Wang, J. T., Ramage, D., et al. (2003). Cytoscape: A Software Environment for Integrated Models of Biomolecular Interaction Networks. *Genome Res.* 13 (11), 2498–2504. doi:10.1101/gr.1239303

Sin, C. F., and Man, M. P. (2021). Early T-Cell Precursor Acute Lymphoblastic Leukaemia (ETP-ALL): Diagnosis, Updates in Molecular Pathogenesis, Management and Novel Therapies. *Front. Oncol.* 11, 750789. doi:10.3389/fonc.2021.750789

Spitzer, M., Wildenhain, J., Rappsilber, J., and Tyers, M. (2014). BoxPlotR: A Web Tool for Generation of Box Plots. *Nat. Methods* 11 (2), 121–122. doi:10.1038/nmeth.2811

Szklarczyk, D., Gable, A. L., Lyon, D., Junge, A., Wyder, S., Huerta-Cepas, J., et al. (2019). STRING V11: Protein-Protein Association Networks with Increased Coverage, Supporting Functional Discovery in Genome-Wide Experimental Datasets. *Nucleic acids Res.* 47 (D1), D607–D613. doi:10.1093/nar/gky1131

Tarantini, F., Cumbo, C., Anelli, L., Zagaria, A., Specchia, G., Musto, P., et al. (2021). Inside the Biology of Early T-Cell Precursor Acute Lymphoblastic Leukemia: The Perfect Trick. *Biomark. Res.* 9 (1), 89. doi:10.1186/s40364-021-00347-z

Treanor, L. M., Zhou, S., Janke, L., Churchman, M. L., Ma, Z., Lu, T., et al. (2014). Interleukin-7 Receptor Mutants Initiate Early T Cell Precursor Leukemia in Murine Thymocyte Progenitors with Multipotent Potential. *J. Exp. Med.* 211 (4), 701–713. doi:10.1084/jem.20122727

Vadillo, E., Dorantes-Acosta, E., Pelayo, R., and Schnoor, M. (2018). T Cell Acute Lymphoblastic Leukemia (T-ALL): New Insights into the Cellular Origins and Infiltration Mechanisms Common and Unique Among Hematologic Malignancies. *Blood Rev.* 32 (1), 36–51. doi:10.1016/j.blre.2017.08.006

Verbeke, D., Gielen, O., Jacobs, K., Boeckx, N., De Keersmaecker, K., Maertens, J., et al. (2019). Ruxolitinib Synergizes with Dexamethasone for the Treatment of T-Cell Acute Lymphoblastic Leukemia. *HemaSphere* 3 (6), e310. doi:10.1097/hs9.0000000000000310

Wada, H., Masuda, K., Satoh, R., Kakugawa, K., Ikawa, T., Katsura, Y., et al. (2008). Adult T-Cell Progenitors Retain Myeloid Potential. *Nature* 452 (7188), 768–772. doi:10.1038/nature06839

Wang, M., and Zhang, C. (2020). Low LEF1 Expression is a Biomarker of Early T-Cell Precursor, an Aggressive Subtype of T-Cell Lymphoblastic Leukemia. *PloS One* 15 (5), e0232520. doi:10.1371/journal.pone.0232520

Wood, B. L., Winter, S. S., Dunsmore, K. P., Devidas, M., Chen, S., Asselin, B., et al. (2014). T-Lymphoblastic Leukemia (T-ALL) Shows Excellent Outcome, Lack of Significance of the Early Thymic Precursor (ETP) Immunophenotype, and Validation of the Prognostic Value of End-Induction Minimal Residual Disease (MRD) in Children's Oncology Group (COG) Study AALL0434. *Blood* 124 (21), 1. doi:10.1182/blood.v124.21.1.1

Wood, B., Winter, S., Dunsmore, K., Raetz, E., Borowitz, M. J., Devidas, M., et al. (2009). Patients with Early T-Cell Precursor (ETP) Acute Lymphoblastic Leukemia (ALL) Have High Levels of Minimal Residual Disease (MRD) at the End of Induction-A Children's Oncology Group (COG) Study. *Blood* 114 (22), 9. doi:10.1182/blood.v114.22.9.9

Xie, Z., Bailey, A., Kuleshov, M. V., Clarke, D. J. B., Evangelista, J. E., Jenkins, S. L., et al. (2021). Gene Set Knowledge Discovery with Enrichr. *Curr. Protoc.* 1 (3), e90. doi:10.1002/cpz1.90

Yang, Y., Yao, S., Zhang, J., Yan, Z., Chu, J., Wang, H., et al. (2019). Decitabine-containing G-CSF Priming Regimen Overcomes Resistance of Primary Mediastinal Neoplasm from Early T-Cell Precursors to Conventional Chemotherapy: A Case Report. *OncoTargets Ther.* 12, 7039. doi:10.2147/ott.s214905

Zhang, J., Ding, L., Holmfeldt, L., Wu, G., Heatley, S. L., Payne-Turner, D., et al. (2012). The Genetic Basis of Early T-Cell Precursor Acute Lymphoblastic Leukaemia. *Nature* 481 (7380), 157–163. doi:10.1038/nature10725

Zhang, Y., Qian, J.-J., Zhou, Y.-L., Huang, X., Li, J.-H., Li, X.-Y., et al. (2020). Comparison of Early T-Cell Precursor and Non-ETP Subtypes Among 122 Chinese Adults with Acute Lymphoblastic Leukemia. *Front. Oncol.* 10, 1423. doi:10.3389/fonc.2020.01423

Zhou, W., Yui, M. A., Williams, B. A., Yun, J., Wold, B. J., Cai, L., et al. (2019). Single-cell Analysis Reveals Regulatory Gene Expression Dynamics Leading to Lineage Commitment in Early T Cell Development. *Cell Syst.* 9 (4), 321–337. doi:10.1016/j.cels.2019.09.008

Zuurbier, L., Gutierrez, A., Mullighan, C. G., Canté-Barrett, K., Gevaert, A. O., de Rooi, J., et al. (2014). Immature MEF2C-Dysregulated T-Cell Leukemia Patients Have an Early T-Cell Precursor Acute Lymphoblastic Leukemia Gene Signature and Typically Have Non-Rearranged T-Cell Receptors. *Haematologica* 99 (1), 94–102. doi:10.3324/haematol.2013.090233

**Conflict of Interest:** The authors declare that the research was conducted in the absence of any commercial or financial relationships that could be construed as a potential conflict of interest.

frontiers | Frontiers in Cell and Developmental Biology

TYPE Original Research
PUBLISHED 23 September 2022
DOI 10.3389/fcell.2022.990034



OPEN ACCESS

EDITED BY
Maristella Maggi,
University of Pavia, Italy

REVIEWED BY
Feng Jiang,
Fudan University, China
Jinhui Liu,
Nanjing Medical University, China

*CORRESPONDENCE
Xiaocan Jia,
jxc@zzu.edu.cn

SPECIALTY SECTION
This article was submitted to Cancer Cell Biology,
a section of the journal
Frontiers in Cell and Developmental Biology

RECEIVED 09 July 2022
ACCEPTED 05 September 2022
PUBLISHED 23 September 2022

CITATION
Lu J, Zheng G, Dong A, Chang X, Cao X, Liu M, Shi X, Wang C, Yang Y and Jia X (2022), Prognostic characteristics of immune subtypes associated with acute myeloid leukemia and their identification in cell subsets based on single-cell sequencing analysis.
*Front. Cell Dev. Biol.* 10:990034.
doi: 10.3389/fcell.2022.990034



# Prognostic characteristics of immune subtypes associated with acute myeloid leukemia and their identification in cell subsets based on single-cell sequencing analysis

Jie Lu[1], Guowei Zheng[1], Ani Dong[1], Xinyu Chang[1], Xiting Cao[1], Mengying Liu[1], Xuezhong Shi[1], Chunmei Wang[2], Yongli Yang[1] and Xiaocan Jia[1]*

[1]Department of Epidemiology and Biostatistics, College of Public Health, Zhengzhou University, Zhengzhou, Henan, China, [2]Children's Hospital, The First Affiliated Hospital of Zhengzhou University, Zhengzhou, China

Immune genes play an important role in the development and progression of acute myeloid leukemia (AML). However, the role of immune genes in the prognosis and microenvironment of AML remains unclear. In this study, we analyzed 151 AML patients in the TCGA database for relevant immune cell infiltration. AML patients were divided into high and low immune cell infiltration clusters based on ssGSEA results. Immune-related pathways, AML pathways and glucose metabolism pathways were enriched in the high immune cell infiltration cluster. Then we screened the differential immune genes between the two immune cell infiltration clusters. Nine prognostic immune genes were finally identified in the train set by LASSO-Cox regression. We constructed a model in the train set based on the nine prognostic immune genes and validated the predictive capability in the test set. The areas under the ROC curve of the train set and the test set for ROC at 1, 3, 5 years were 0.807, 0.813, 0.815, and 0.731, 0.745, 0.830, respectively. The areas under ROC curve of external validation set in 1, 3, and 5 years were 0.564, 0.619, and 0.614, respectively. People with high risk

**Abbreviations:** AML, acute myelogenous leukemia; AUC, area under curve; PD-L1, programmed cell death 1 ligand 1; CIBERSORT, Cell type Identification by Estimating Relative Subpopulations of RNA Transcription; CTLA-4, cytotoxic T-lymphocyte antigen-4; ESTIMATE, Estimation of Stromal and Immune cells in Malignant Tumor tissues using Expression data; FPKM, Fragments per kilobase million; GSEA, Genome Set Enrichment Analysis; KEGG, Kyoto Encyclopedia of Genes and Genomes; LAG3, lymphocyte-activation gene 3; LASSO, least absolute shrinkage and selection operator; OS, overall survival; PD-1, programmed cell death 1; ROC, The time-dependent receiver operating characteristic; TCGA, The Cancer Genome Atlas; TIM-3, mucin domain-containing molecule-3; TMB, Tumor mutation burden. TIDE, Tumor Immune Dysfunction and Exclusion; TME, tumor microenvironment The median age as well as the interquartile spacing is 57.50 (44.75, 67.00). The minimum value of age is 18, The maximum value of age is 88.Five variables were taken as covariates, including Gender, Age at Diagnosis in Days, Race, FAB Category, Ethnicity. "Gender" taken as categorical variable; "Race" taken as categorical variable; "Age at Diagnosis in Days", expression of genes were taken as numerical variables; "FAB category" taken as categorical variable; "Ethnicity" were taken as categorical variable.

scores accompanied by high TMB had been detected with the worst prognosis. Single-cell sequencing analysis revealed the expression of prognostic genes in AML cell subsets and pseudo-time analysis described the differentiation trajectory of cell subsets. In conclusion, our results reveal the characteristics of immune microenvironment and cell subsets of AML, while it still needs to be confirmed in larger samples studies. The prognosis model constructed with nine key immune genes can provide a new method to assess the prognosis of AML patients.

KEYWORDS

acute myelogenous leukemia, single-cell RNA-seq, prognostic model, SsGSEA, tumor immune microenvironment

## Introduction

Acute myeloid leukemia (AML) is a highly heterogeneous hematological malignancy characterized by uncontrolled proliferation and differentiation of hematopoietic progenitor cells/stem cells in bone marrow, blood, and other hematopoietic organs (Medinger and Passweg, 2017; Short et al., 2018). Cancer statistics 2019 showed that the 5-years relative survival rate for AML was 66.4% in children and 64.2% in adolescents from 2008 to 2014 (Siegel et al., 2019). The median overall survival (OS) after 5 years in adults (18–60 years) with AML was approximately 40% (Schlenk and Döhner, 2013). Current studies have shown that prognosis of AML is closely related to white blood cell count and cytogenetic abnormalities (Kalaiyarasi et al., 2019; Tallman et al., 2019). The main treatment strategies for AML are intensive induction chemotherapy and post-remission therapy. Although most AML patients initially achieve significant remission with chemotherapy. Complete elimination of AML cells remains rare, with no substantial improvement in patient survival (Döhner et al., 2010; Hosono, 2019). As the process of translating the relevant genomic landscape knowledge of AML into clinical treatment has only just begun, the identification of new potential biomarkers will contribute to the diagnosis and prognosis of AML patients.

AML has long been considered an immunoreactive malignancy and multiple mechanisms are implicated in AML's immune evasion (Passweg et al., 2019). AML immune escape is caused by both intrinsic and extrinsic immunosuppressive mechanisms (Teague and Kline, 2013; Mittal et al., 2014). Intrinsic immunosuppressive effects include upregulation of anti-apoptotic mechanisms, regulation of immunomodulatory checkpoints and loss of tumor antigen expression. Extrinsic mechanisms include the accumulation of regulatory cells such as regulatory T-cells (Tregs) and secretion of immunosuppressive cytokines (Austin et al., 2016). The production of immune escape depends on the tumor microenvironment (TME). TME is a dynamic system composed of extracellular matrix, stromal cells and immune cells (Ayala et al., 2009; Roma-Rodrigues et al., 2019). Similar to most tumors, functional interactions between leukemic cells and the bone marrow immune microenvironment constitute a unique hallmark of AML (Isidori et al., 2021). Although the prognosis of AML patients currently mainly depends on cellular and molecular genetic characteristics, the TME also plays an extremely important role in the progression and treatment of AML (Yehudai-Resheff et al., 2019). It was reported that the leukemia TME inhibits the growth of normal hematopoietic cells while promoting and maintaining the proliferation and long-term viability of leukemia cells (Basak et al., 2010). Immune response in the tumor microenvironment is a significant factor in the invasion and progression of various tumors, among which immune cell types, cytokines and immune genes have been widely studied as prognostic markers in many tumors such as lung cancer, ovarian cancer and colorectal cancer (Frey et al., 2017; Lee et al., 2017). In addition, the discovery of numerous immune checkpoints also offers a broader therapeutic prospect for AML and other malignancies (Zhang et al., 2009). Therefore, identifying the characteristics of TME in AML is crucial for designing personalized immune therapy for AML patients.

Single-cell sequencing (scRNA-seq) is a common technique to explore the heterogeneity and diversity of tumor cells. It can describe the functional state of a cell by detecting the transcription level of a single cell (Petti et al., 2019). In AML, enhanced T-cell-mediated clearance of AML is an attractive therapeutic strategy, but immunotherapy trials have been less successful than in other cancers (Lichtenegger et al., 2017). ScRNA-seq provides a powerful means to characterize malignant and stromal cell populations in tumors, which may address questions related to dryness, developmental hierarchies, and interactions between malignant and immune cells (Giustacchini et al., 2017). Therefore, scRNA-seq can further explore the composition and functional status of various immune cell subsets in the AML bone marrow microenvironment (Miles et al., 2020). It could lead to exciting breakthroughs in cancer genomics in the future.

In this study, two immune cell infiltration clusters were identified based on The Cancer Genome Atlas (TCGA) database. We compared the characteristics of TME and pathway enrichment differences between the two clusters. The prognostic model was constructed using differential immune genes to accurately predict the prognosis of AML patients. ScRNA-seq was used to study the expression characteristics and differentiation trajectory of prognostic immune genes in

AML cell subsets. Our comprehensive analysis of AML populations with different immune statuses may provide a new reference for the characteristics, treatment and prognosis of AML.

# Materials and methods

## Acquisition and pre-processing of gene and clinical data

RNA sequencing data of 151 AML patients' samples and the clinical data of 200 AML patients' samples were downloaded from TCGA database (https://www.cancer.gov/about-nci/organization/ccg/research/structural-genomics/tcga), 142 samples with both clinical information and sequencing data. In addition, transcriptome and clinical information from 422 HGU-133A AML patients in the cohort GSE37642 (https://www.ncbi.nlm.nih.gov/geo/query/acc.cgi) were downloaded from the Gene Expression Omnibus (GEO) database for external validation. Then, we downloaded the Genome Reference Consortium Human Build 38 (GRCh38) (https://www.gencodegenes.org/human/) gene annotation file and performed gene annotation for all gene probes. Single-cell sequencing data was downloaded from chip GSE126068 (https://www.ncbi.nlm.nih.gov/geo/query/acc.cgi?acc=GSE126068) which included 5 patients. The original file included 26,454 genes and 813 cells, with 400 cells detected at diagnosis and 413 cells detected at relapse. Normal blood samples were collected from the Genotype-Tissue Expression (GTEx) database (https://xenabrowser.net/datapages/?cohort=GTEX&removeHub=https%3A%2F%2Fxena.treehouse.gi.ucsc.edu%3A443). The RNA sequencing data were transcribed fragments per kilobase per million mapped reads (FPKM) normalized. We used the combat function in the "sva" package of R language to remove the batch effect of high-throughput data to eliminate the data differences caused by different platforms.

## Single sample gene set enrichment analysis algorithm and clustering of acute myeloid leukemia patients

Single sample gene set enrichment analysis (ssGSEA), an extension of Gene Set Enrichment Analysis (GSEA), calculates separate enrichment scores for each sample and gene set (Subramanian et al., 2005). In our study, ssGSEA algorithm calculated a scoring of immune cell types and immune pathways against innate and adaptive immune for each sample. Next, we used "hclust" clustering method to cluster all AML patients according to ssGSEA scores and divide them into clusters with high immune cell infiltration and low immune cell infiltration. The t-distributed stochastic neighbor embedding (t-SNE) algorithm was used to verify and visualize the clustering results.

## Comparison of clinical features and immune-related characteristics between the two cluster patients

The ESTIMATE (Estimation of Stromal and Immune cells in Malignant Tumor tissues using Expression data) (version 2.15.3) algorithm from the website (https://sourceforge.net/projects/estimateproject/) was used to calculate the estimated score, immune score and stromal score (Yoshihara et al., 2013). We used the Wilcoxon test to assess the difference between the two groups for the stromal score, immune score, and ESTIMATE score. The R packages "ggpubr" and "pheatmap" were applied to visualize our results. Next, the CIBERSORT (Cell type Identification by Estimating Relative Subpopulations of RNA Transcription) method was applied to assess the proportion of 22 immune cell subtypes in AML patient samples. Wilcoxon test was also used to evaluate the differences in the degree of infiltration of 22 immune cells between the two clusters.

## Human leukocyte antigen, genome set enrichment analysis, and clinical factors differentials analysis between the two cluster patients

A total of 24 HLAs (human leukocyte antigen), including HLA-E, HLA-DPB2, HLA-C, HLA-J, HLA-DQB1, HLA-DQB2, HLA-DQA2, HLA-DQA1, HLA-A, HLA-DMA, HLA-DOB, HLA-DRB1, HLA-H, HLA-B, HLA-DRB5, HLA-DOA, HLA-DPB1, HLA-DRA, HLA-DRB6, HLA-L, HLA-F, HLA-G, HLA-DMB, and HLA-DPA1 were acquired from a previous study (Gonzalez-Galarza et al., 2013; Mack et al., 2013). Meanwhile, we downloaded the mutation data and tumor mutation burden (TMB) data from TCGA database and further extracted them using "perl" (http://www.perl.org/) language. Similarly, we used the Wilcoxon test to assess whether HLAs and clinically relevant factors differed between the two clusters. GSEA was also performed between two clusters to find enriched biological pathways. Kyoto encyclopedia of genes and genomes (KEGG) gene sets (c2.cp.kegg.v7.4.symbols.gmt) and phenotype tag expression files were loaded into the GSEA software and run 1,000 times to demonstrate the function consistently. The screening criteria were nominal (NOM) $p$-value < 0.05 and |normalized enrichment score (NES)| > 1.

## Construction and validation of prognostic modeling by immune-related genes

The "limma" package was used to identify the different genes between two different immune clusters in the R language. FDR <0.05 and | logFC (fold change) | > 2 were used as thresholds. 1793 immune-associated genes were downloaded from the ImmPort database (https://www.immport.org/home)

TABLE 1 Baseline characteristics for 200 patients with AML in the TCGA database.

| Characteristics | Cases (%) |
|---|---|
| Gender | |
| Female | 91 (45.5) |
| Male | 109 (54.5) |
| Age (year) | |
| 10~ | 1 (0.5) |
| 20~ | 16 (8.0) |
| 30~ | 21 (10.5) |
| 40~ | 26 (13.0) |
| 50~ | 44 (22.0) |
| 60~ | 54 (27.0) |
| 70~ | 32 (16.0) |
| 80~ | 6 (3.0) |
| Race | |
| Asian | 2 (1.0) |
| Black or African American | 15 (7.5) |
| Not reported | 2 (1.0) |
| White | 181 (90.5) |
| FAB Category | |
| M0 Undifferentiated | 19 (9.5) |
| M1 | 44 (12.5) |
| M2 | 44 (12.5) |
| M3 | 21 (10.5) |
| M4 | 42 (21.0) |
| M5 | 22 (11.0) |
| M6 | 3 (1.5) |
| M7 | 3 (1.5) |
| Not classified | 2 (1.0) |
| Ethnicity | |
| Hispanic or Latino | 3 (1.5) |
| Not Hispanic or Latino | 194 (97.0) |
| Not reported | 3 (1.5) |

and further intersected with the differential genes to obtain immune-associated differential genes. We divided the AML patients into the train set and test set according to the ratio of 7:3. Next, Cox regression analysis and Least absolute shrinkage and selection operator (LASSO) regression were used to screen for immune genes associated with AML prognosis in the train set. Patients in the train, test and validation sets were assigned to the high-risk and low-risk groups based on their median risk score. The calculating formula is:

$$\textbf{risk score} = \sum_{i=1}^{n} \textbf{coef}_i * x_i$$

where $coef_i$ means the coefficients, $x_i$ is the FPKM value of each gene associated with the prognosis of AML patients. We constructed a prognostic model by immune-related genes and tested the survival scores, risk status and predictive power of this model for survival in AML patients by the Receiver Operating Characteristic (ROC) curve among the train set, the test set and external set. Finally, we integrated the GTEx database and TCGA data of leukemia patients, and then compared the expression levels of all the prognostic immune genes related to leukemia in normal people and leukemia patients.

## Constructing a predictive nomogram

Nomogram is widely used to predict the prognosis of cancer (Iasonos et al., 2008). All independent prognostic factors, including age, race, bone marrow blast cell percent value, hemoglobin value, monocyte percent value, leukocyte value, FAB stage and risk score were identified by univariate Cox regression and multivariate Cox regression analysis to build a nomogram to investigate the probability of 1 year, 3 years, and 5 years overall survival (OS) of AML. Finally, calibration curves were performed to determine the predictive power of the nomogram for patient survival.

## Discovery of co-expressed transcription factors and construction of PPI networks

318 transcription factors were downloaded from the Cistrome database (http://www.cistrome.org/). Pearson correlation analysis was used to find transcription factors associated with prognosis-related immune genes. We next mapped the PPI (protein-protein interaction) network by string website (https://www.string-db.org/) on the immune prognostic genes and transcription factors with co-expression relationships. The screening criteria were $R \geq 0.4$ and $p < 0.001$.

## Differences in immune checkpoint, tumor mutation characteristics, tumor mutation burden and immunotherapy response between different prognostic risk groups

Differences in the 5 common immune checkpoints and mutation frequency between high and low risk groups were further compared by the Wilcoxon test. The five common immune checkpoints are programmed death 1 (PD-1) (Sharpe and Pauken, 2018) and its ligand 1 (PD-L1) (Daassi et al., 2020), cytotoxic T lymphocyte antigen 4 (CTLA-4) (Agdashian et al., 2019), mucin domain-containing molecule-3 (TIM-3) (Wolf et al., 2020) and lymphocyte-activation gene 3 (LAG3). Spearman correlation method was further applied to explore the correlation between risk scores and immune checkpoints. Since TMB has been identified as a biomarker for several cancer

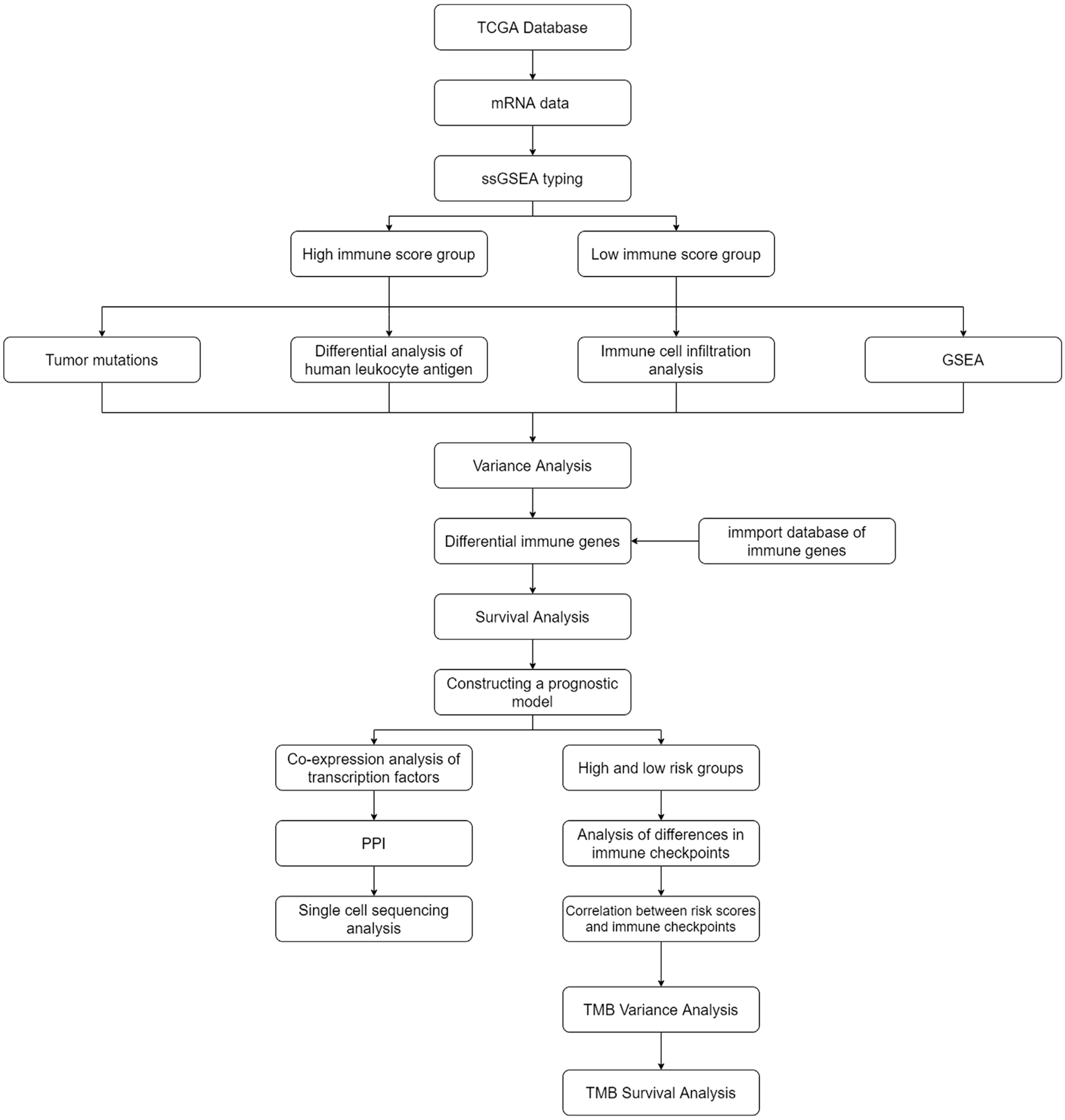


**FIGURE 1**
Flow chart.

types in response to immune checkpoints (Merino et al., 2020), we further analyzed differences in TMB between high and low risk groups. Besides, to further explore the relationship between TMB and survival of AML, AML patients in the TCGA database were divided into high TMB group and low TMB group according to the median value of TMB. Kaplan-Meier survival curve was used to determine whether there was the difference in survival between high and low TMB groups. AML patients in the TCGA database were divided into four groups: high risk with high TMB group, high risk with low TMB group, low-risk with high-TMB group, and low-risk with low-TMB group based on the median risk score and median TMB. Similarly, Kaplan-Meier survival curve was used to determine whether there was difference in survival among four groups. Tumor Immune

TABLE 2 Baseline characteristics for 422 patients with AML in the GEO database ($n$ = 422).

| Characteristics | Cases (%) |
|---|---|
| Age (year) | |
| 10~ | 2 (0.5%) |
| 20~ | 27 (6.4%) |
| 30~ | 48 (11.4%) |
| 40~ | 69 (16.4%) |
| 50~ | 82 (19.4%) |
| 60~ | 128 (30.3%) |
| 70~ | 61 (14.5%) |
| 80~ | 5 (1.2%) |
| FAB Category | |
| M0 | 14 (3.3%) |
| M1 | 84 (19.9%) |
| M2 | 117 (27.7%) |
| M3 | 19 (4.5%) |
| M4 | 104 (24.6%) |
| M5 | 47 (11.1%) |
| M6 | 15 (3.6%) |
| M7 | 2 (0.5%) |
| NA | 20 (4.7%) |
| Survival state | |
| alive | 109 (25.8%) |
| dead | 308 (73.0%) |
| NA | 5 (1.2%) |

Dysfunction and Exclusion (TIDE) algorithms were widely used to predict response to ICI therapy (anti-PD-1 and CTLA-4 therapy). ICI responses and measurements were assessed in the high-risk and low-risk groups using the TIDE algorithm (Jiang et al., 2018).

## Single-cell sequencing analysis

We first integrated the expression levels of the genes in the diagnosis and relapse parts into two matrixes, respectively. Then two matrixes were transformed into "Seurat" objects and carried out quality control and standardization. The "PercentageFeatureSet" function was used to calculate the percentage of mitochondrial genes. Due to the loss of cytoplasmic RNA and leakage of mitochondria from the damaged membrane when the cell is destroyed. So, we removed more than 5% of the cells with mitochondrial genes and fewer than 50 genes. The "FindVariableFeatures" function was used to find the first 1,500 or 5,000 highly variable genes. To preserve the information of the original variables as much as possible, we used principal component analysis (PCA) to reduce the dimensionality of the data by the information of 1,500 or 5,000 highly variable genes. We included statistically significant principal components for the next subsets of cell annotation. Next, the function "FindAllMarkers" was used to identify overexpressed genomes and the "SingleR" package was used to annotate cell subsets.

## Pseudotime analysis

To study the developmental trajectory of various cells in AML during tumor development and progression, monocle (version 2.14.0, used for pseudo-time analysis) was used to analyze the gene expression matrix with Seurat annotation (Trapnell et al., 2014). In the course of a cell's life, many cell states are not completely synchronized. Some cells are at the beginning of a particular process, while others are already in the state of completion of that process, which is called "asynchronous". By ordering cells according to this process to form a trajectory, the process changes associated with the trajectory can be tracked as "pseudotime". We arranged the cells in the pseudo-time analysis along the track and made heatmaps based on the prognostic immune genes. Finally, the expression of prognostic genes in different cells was described to explore their possible roles.

## Statistical analysis

All statistical analyses were conducted using the R software version 4.1.0 (http://www.R-project.org). Unless otherwise mentioned, $p < 0.05$ was regarded as statistically significant.

# Results

## Characteristics of participants in this study

Table 1 presents the baseline characteristics of AML patients in the TCGA database. Figure 1 illustrates the flow chart of this study. Baseline characteristics of the train set and test set populations are shown in Supplementary Tables S1, S2. Table 2 presents the baseline characteristics of AML patients in the GEO database.

## Single sample gene set enrichment analysis algorithm and clustering of acute myeloid leukemia patients

39740 RNAs from 151 AML patients were extracted and integrated into a matrix through the perl language. The ssGSEA method was applied to assess the richness levels of immune cells and immune pathways in 151 AML patients. AML patients were

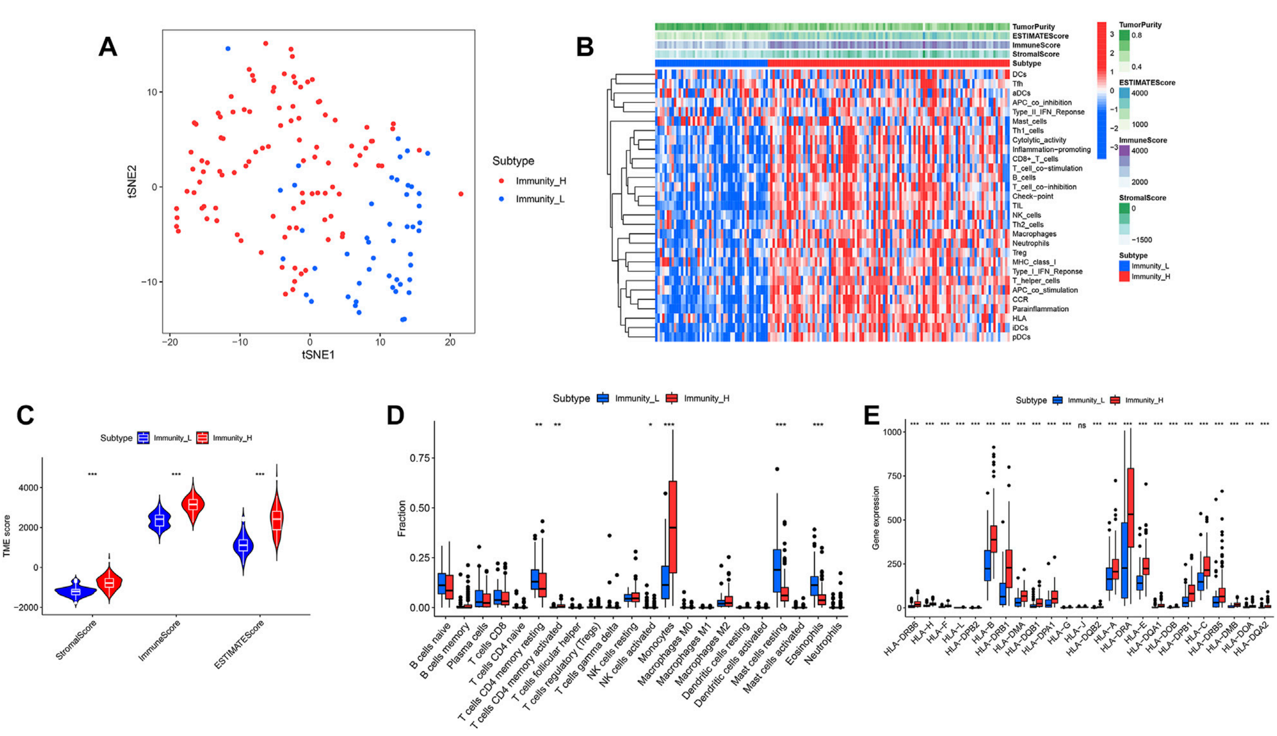


FIGURE 2
"hclust" cluster method and immune-related functions. **(A)** t-SNE was used to test the clustering results of the high and low immune groups. **(B)** Heatmaps of immune-related pathways in the high and low immune groups. **(C)** Stromal score, immune score and total score in the high and low immune groups. **(D)** Comparison of 22 kinds of immune cells in the high and low immune groups. **(E)** Comparison of human leukocyte antigen differences between high and low immune groups.

classified into two categories based on the results of immune infiltration, which include the high immune cell infiltration cluster ($n$ = 103) and low immune cell infiltration cluster ($n$ = 48) by the "hclust" clustering method. The t-SNE method was further used to visualize and validate the clustering results (Figure 2A).

## Immune cell infiltration differential analysis between the two clusters

We calculated and compared the stromal score, immune score, estimate score and tumor purity of the two clusters according to the ESTIMATE algorithm. It showed that the stromal score, immune score and estimate score of high immune cell infiltration cluster were higher than those of low immune cell infiltration cluster, while tumor purity was the opposite (Figure 2B). The violin plot showed that the stromal score, immune score and estimate score were all higher in the high immune cell infiltration cluster than in the low (Figure 2C) ($p < 0.05$). Among the contents of 22 immune cell, we found only 6 of them, including CD4 resting memory T-cells, activated CD4 memory T-cells, NK cells activated, Monocytes, Mast cells resting and Eosinophils, appearing differentially between the high and low immune cell infiltration clusters. The CD4 resting memory T-cells, NK cells activated, Mast cells resting and Eosinophils contents were higher in the low immune cell infiltration cluster than in the high immune cell infiltration cluster, while the activated CD4 memory T-cells and Monocytes contents were opposite (Figure 2D) ($p < 0.05$).

## Human leukocyte antigen, genome set enrichment analysis and clinical factors differentials analysis between the two clusters

We first compared the differences in clinical factors between high and low immune cell infiltration clusters, including monocyte percent value, age, hemoglobin value, bone marrow blast cell percent value and leukocyte value. We found that the age and monocyte percent value of the high immune cell infiltration cluster were higher than that of the low immune cell infiltration cluster, while bone marrow blast cell percent value and leukocyte value were opposite (Supplementary Figures S1A–E) ($p < 0.05$). Next, the results of the boxplot showed that

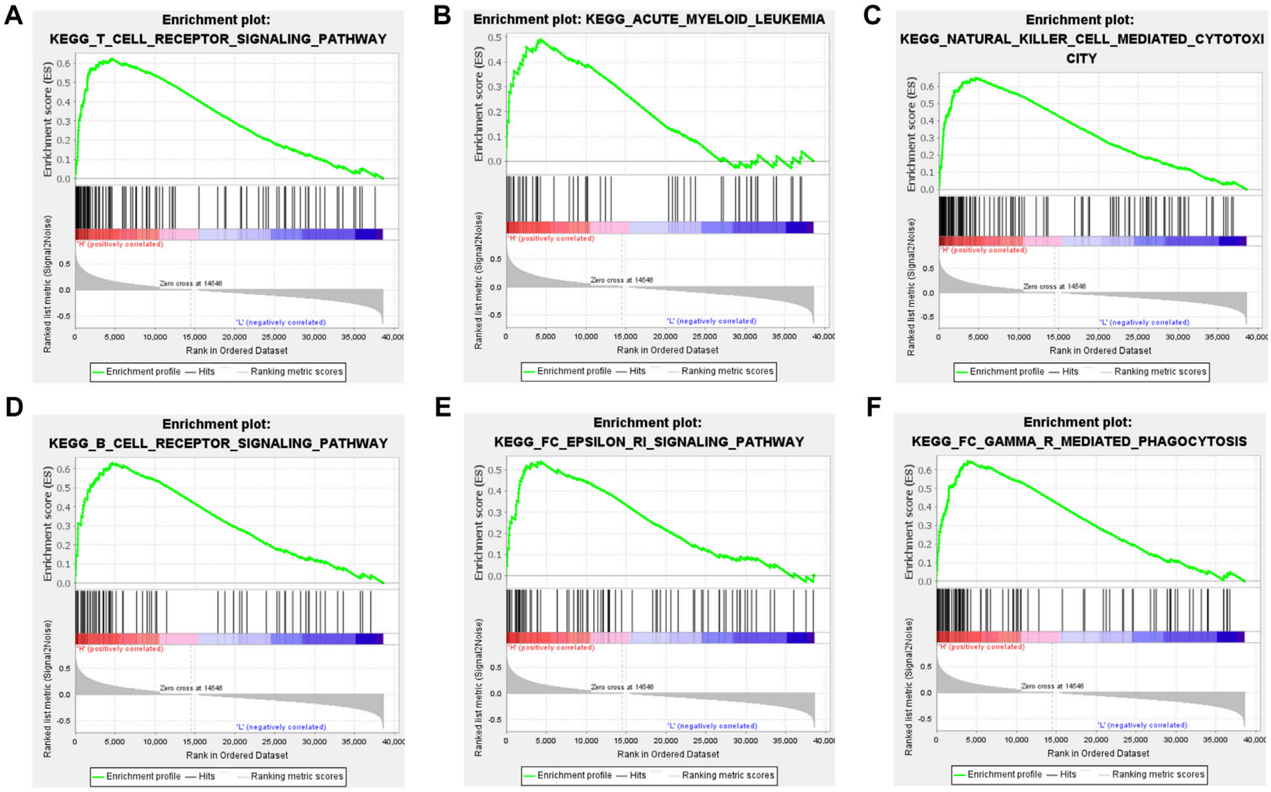


FIGURE 3
GSEA between the high and low immune groups. **(A)** T cell receptor signaling pathway. **(B)** Acute myeloid leukemia pathway. **(C)** Natural killer cell mediated cytotoxicity pathway. **(D)** B cell receptor signaling pathway. **(E)** FC epsilon ri signaling pathway. **(F)** FC gamma r mediated phagocytosis pathway.

the expression level of all 23 HLAs excluding HLA-J was higher in the high immune cell infiltration cluster than in the low immune cell infiltration cluster (Figure 2E) ($p$ < 0.05). GSEA has shown that many immune-related pathways, such as Natural killer cell-mediated cytotoxicity, T-cell receptor signaling pathway, B cell receptor signaling pathway and Fc epsilon RI signaling pathway were enriched in the high immune cell infiltration cluster. Besides, the Insulin signaling pathway, Acute myeloid Leukemia Pathway, Regulation of actin cytoskeleton pathway and other biological pathways were also enriched in the high immune cell infiltration cluster (Figures 3A–F) (Nom $p$-value < 0.05).

## Construction and validation of prognostic modeling by immune-related genes

689 genes upregulated in the high immune group and 65 genes downregulated in the high immune cell infiltration cluster were screened by differential analysis (Figure 5). We next took intersections of the 754 differential genes with 1793 immune-related genes. 183 intersecting genes were obtained using Venn analysis (Supplementary Figure S2C). We integrated 183 gene expression matrixes from 151 AML patients with clinical information from 200 AML patients. 142 AML patients with complete clinical data were eventually obtained. 39 genes were significantly associated with overall survival in AML patients using univariate Cox regression (Supplementary Figure S2I) ($p$ < 0.05). Nine genes including CD74, PLXNB1, THBS1, PTK2, UNC93B1, PPBP, CXCL12, GZMB, and IFI30 were finally identified by LASSO regression analysis to construct the prognostic model. Risk score = (0.00239 * CD74) + (−0.13147 * PLXNB1) + (0.0166 * THBS1) + (−0.11492 * PTK2) + (0.01322 * UNC93B1) + (0.00479 * PPBP) + (−0.01512 * CXCL12) + (0.03528 * GZMB) + (−0.048 * IFI30). The coefficients result was also shown in Table 3. Then, we divided all AML patients into the train set and the test set according to the ratio of 7:3. AML patients in the train set were divided into high-risk and low-risk groups based on the median risk score. Kaplan-Meier (KM) curve showed that the survival rate of patients in the low-risk group was significantly higher than that in the high-risk group

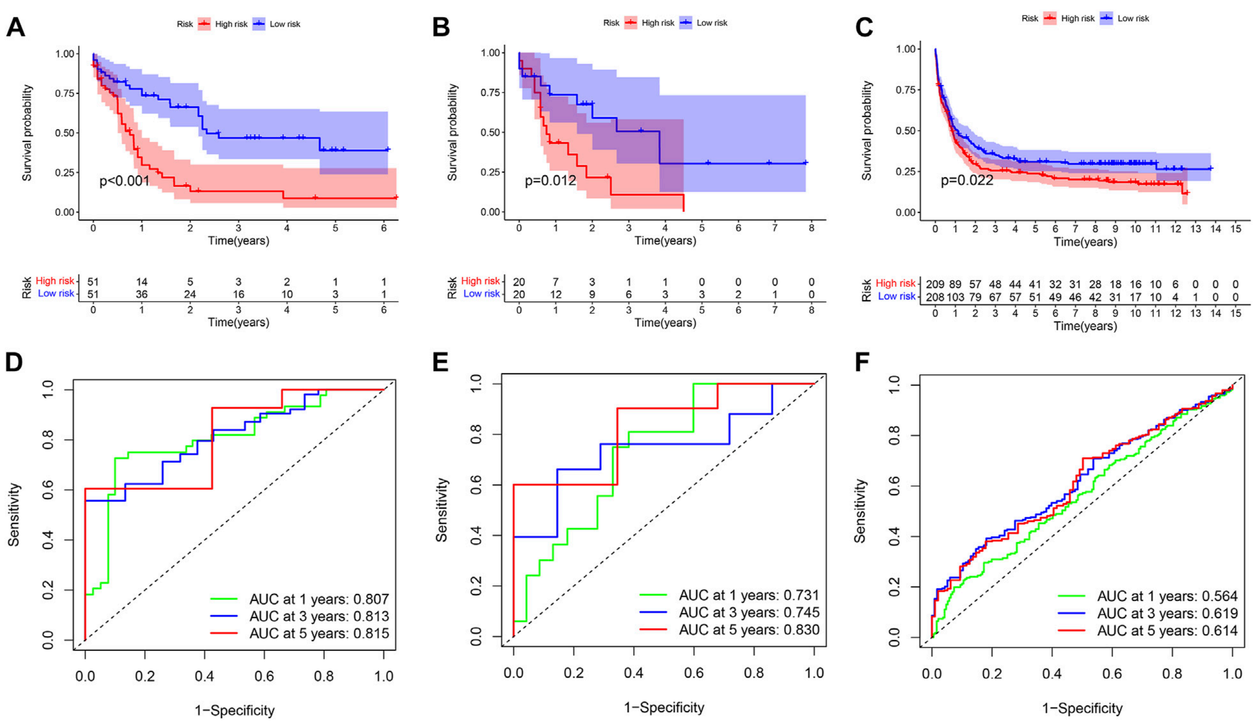

FIGURE 4
Univariate Cox regression analysis and prognosis curve. **(A)** KM curve of train set. **(B)** KM curve of test set. **(C)** KM curve of GEO external validation set. **(D)** ROC curves of model for predicting the 1/3/5-years survival in the train set. **(E)** ROC curves of model for predicting the 1/3/5-years survival in the test set. **(F)** ROC curves of model for predicting the 1/3/5-years survival in the GEO external validation set.

(Figure 4A) ($p < 0.01$). Scatter plot results of risk score and survival status of AML patients showed that the mortality and risk coefficient was lower in the low-risk group than in the high-risk group (Supplementary Figures S1H,I). The AUC of the risk score predicted OS at 1-, 3- and 5- year were 0.807, 0.813, and 0.815, respectively, which means our signature has a good capacity in predicting OS (Figure 4D). The predictive power of our model was also verified in the test set. The KM curve showed that patients in the low-risk group had higher survival rates than those in the high-risk group (Figure 4B) ($p = 0.012$), while lower mortality and risk factors than those in the high-risk group (Supplementary Figures S1J,K). The AUC of the risk score predicted OS at 1-, 3- and 5- year were 0.731, 0.745, and 0.830, respectively (Figure 4E). The calibration curves of the train set and test set were shown in Supplementary Figures S1F,G, respectively. Then, we verify the predictive ability of our model in the GEO external validation set. KM curve results showed that there was a statistical difference in OS between high-risk and low-risk groups ($p = 0.022$) (Figure 4C). The areas under ROC curve in 1, 3 and 5 years were 0.564, 0.619, and 0.614, respectively (Figure 4F). Finally, we compared the expression of 9 immune genes related to the prognosis of leukemia in normal blood samples and leukemia patients. The expression levels of CXCL12, THBS1, PPBP, GZMB, CD74, and UNC93B1 were higher in the cancer group than in the normal group. The expression levels of PLXNB1, PTK2, and IFI30 in the cancer group were lower than those in the normal group (Supplementary Figures S5A,B).

## Constructing a predictive nomogram

Nomogram was designed based on all AML patients to predict the survival probability of patients at 1 year, 3 years, and 5 years. Multivariate Cox regression results showed that age and risk score were prognostic factors for AML patients. Risk score and age were included as variables. Age and risk scores were found to be significantly associated with AML prognosis (Figure 6) (Supplementary Figures S5C,D) ($p < 0.01$).

## Discovery of co-expressed transcription factors and construction of PPI networks

318 transcription factors and 754 genes were used for co-expression analysis. 27 mRNAs and 10 transcription factors were found to be co-expressed ($R = 0.4$, $p < 0.001$). Figure 6A showed the relationship between transcription factors and genes. We

TABLE 3 Coefficient of 9 immune-related prognostic genes.

| Gene | Coefficient | p-value |
|---|---|---|
| CD74 | 0.00239 | <0.05 |
| PLXNB1 | −0.13147 | <0.05 |
| THBS1 | 0.0166 | <0.05 |
| PTK2 | −0.11492 | <0.05 |
| UNC93B1 | 0.01322 | <0.05 |
| PPBP | 0.00479 | <0.05 |
| CXCL12 | −0.01512 | <0.05 |
| GZMB | 0.03528 | <0.05 |
| IFI30 | −0.048 | <0.05 |

used the STRING online database to map the PPI network using the 35 hub nodes, including 27 mRNAs and 10 transcription factors (Figure 6B) ($R$ = 0.4).

## Differences in immune checkpoint, tumor mutation characteristics, tumor mutation burden and immunotherapy response between different prognostic risk groups

We further compared differences in immune checkpoints, tumor mutation characteristics, and TMB between the high-risk and low-risk groups. The results of the boxplot showed that the expression levels of CD274, CTLA4, HAVCR2, LAG3, and PDCD1 in the high immune cell infiltration cluster were higher than those in the low immune cell infiltration cluster (Figures 5A–C) (Supplementary Figures S2A,B) ($p$ < 0.05). The results of the scatter plot showed a positive correlation between the expression of CD274, CTLA4, HAVCR2, LAG3, and PDCD1 and the risk score (Figures 5D–F) (Supplementary Figures S2D,E) ($p$ < 0.05). There was no difference in tumor mutation load between the high-risk and low-risk groups (Supplementary Figure S2H) ($p$ = 0.37). Survival analysis showed that there was no difference in prognosis between the high and low tumor mutation load group (Supplementary Figure S2G) ($p$ = 0.375). More importantly, TMB survival curves combined with risk scores showed that patients in the high-mutation and high-risk groups had the worst survival outcomes (Figure 6C) ($p$ < 0.01). The frequency of gene mutations was higher in the high-risk group (78.85%) than in the low-risk group (66.67%). We found the highest mutation frequency in NPM1 in the high-risk group and the highest mutation frequency in WT1 in the low-risk group (Figures 5G,H). The results of immunotherapy showed that MSI and Exclusion were higher in the low-risk group, while Dysfunction and TIDE were higher in the high-risk group (Supplementary Figures S6A–D).

## Single-cell sequencing analysis

Figures 7A,B and Figures 8A,B showed the Chip quality control in diagnosed and relapsed populations, respectively. We separately performed the "ScaleData" function to scale all the genes extracted from the scRNA-seq dataset GSE126068. Expression of immune-related prognostic genes in cell subsets of the diagnosed and relapsed population was shown in Figures 7D,E and Figures 8D,E. PCA selected the first 15 principal components to screen out possibly rarer cell subsets (Figures 7C, 8C). The 400 cells at diagnosis were divided into seven cell subsets. Seven cell subgroups were annotated and divided into five cell types, including common myeloid progenitor (CMP), Granulocyte-Monocyte progenitor (GMP), B cell, Pro-B_CELL_CD34 + and Monocyte (Figure 7F). The 413 cells at relapse were divided into seven cell subsets. The seven cell subsets were annotated into four cell types, including CMP, GMP, B cell and Pro-B_CELL_CD34 + (Figure 8F). In the diagnostic population, seven of the nine prognostic immune genes were found to be expressed in cell subsets. CD74 was found to be highly expressed in CMP, GMP, B cell, and Monocyte. IFI30 was highly expressed in GMP and Monocyte. However, almost none of the other five genes are expressed in cells. At the same time, seven of the nine prognostic immune genes were also found to be expressed in cell subsets in the relapse population. CD74 was found to be highly expressed in CMP, GMP, B cell and Monocyte. IFI30 was highly expressed in pro-B_cell_CD34 + and B cells. PTK2 was highly expressed in pro-B_cell_CD34 +. Almost none of the other four genes are expressed in cells.

## Pseudo-time analysis of cell subsets

To further explore the differentiation of different cell statuses, we simulated the movement trajectory of different cells in the diagnosed and relapsed AML population and observed the differentiation of cells. The cell track differentiation of the diagnosed patients is shown in Figure 7G–I; Supplementary Figure S3A. CMP cells here show two pathways of differentiation. One was CMP cells differentiated into GMP cells that subsequently gave rise to monocytes, and the other was Pro–B_cell_CD34+ and B cells. Cell track differentiation in patients with relapses is shown in Figures 8G–I; Supplementary Figure S4A. There were still two differentiation pathways shown here in CMP cells. One type of CMP was differentiated into GMP cells, and the other was differentiated into Pro–B_cell_CD34+ and B cells. The expression levels of the seven genes in different cell lines during differentiation in patients with diagnosed and relapsed AML patients were shown in Supplementary Figures S3B,C and Supplementary Figures S4B,C. We found that the expression levels of CD74 were high in all cell subsets. The expression level of PLXNB1 in the diagnosis group increased first and then gradually stabilized with the time of cell differentiation, but it was almost not

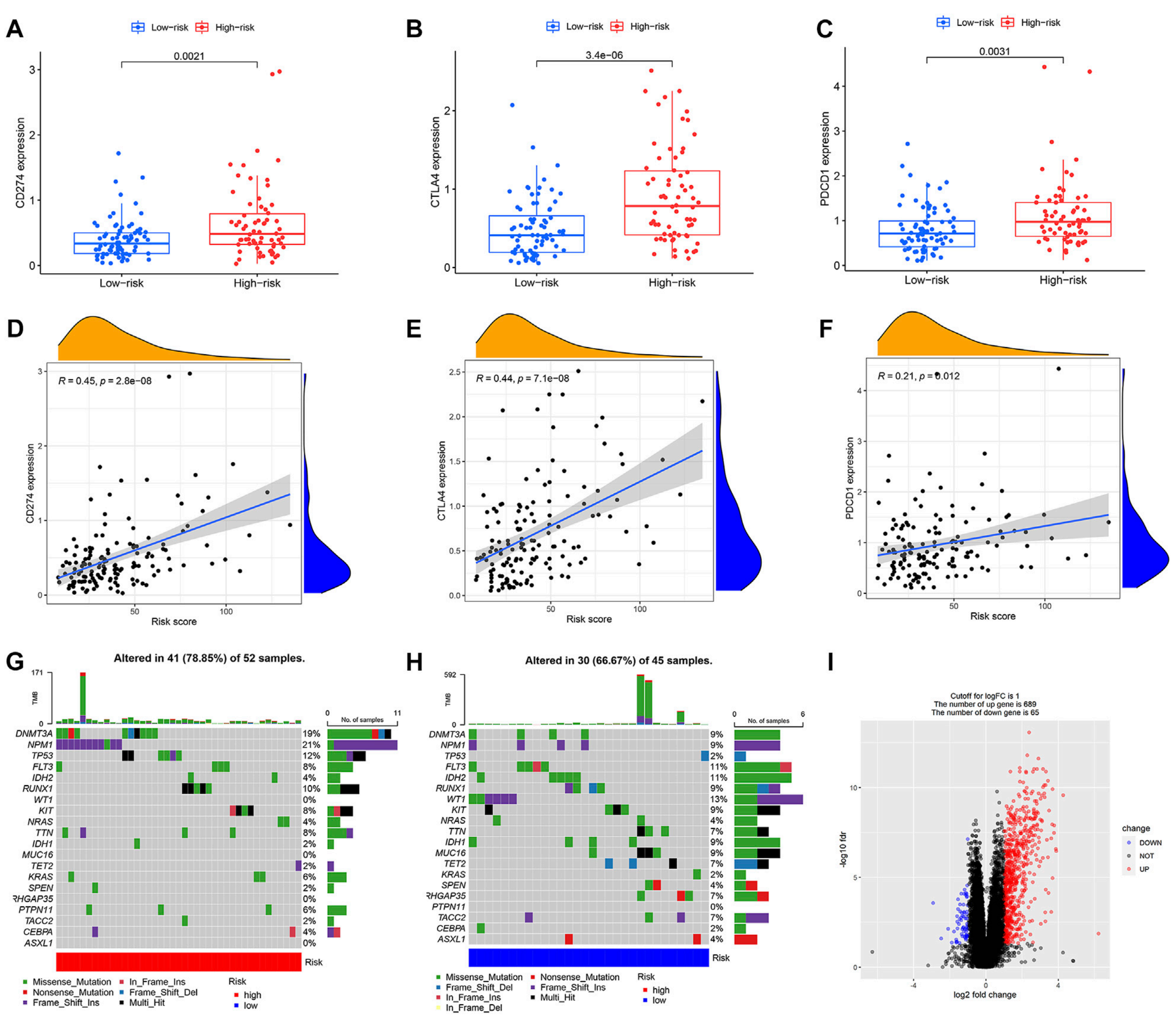

FIGURE 5
Characteristics of mutations and immune checkpoints between high and low risk groups. **(A)** Expression of CD274 between high and low risk groups. **(B)** Expression of CTLA4 between high and low risk groups. **(C)** Expression of PDCD1 between high and low risk groups. **(D)** Correlation between CD274 and risk score. **(E)** Correlation between CTLA4 and risk score. **(F)** Correlation between PDCD1 and risk score. **(G)** Tumor mutations in the high-risk group. **(H)** Tumor mutations in the low-risk group. **(I)** Volcano map of differential gene screening.

expressed in the relapse group. The other five genes were almost unexpressed in all cell differentiation processes. Supplementary Figures S3D, 4D showed the plot of cell density versus pseudotime in patients with AML at diagnosis and relapse.

## 5 Discussion

Previous studies have shown that AML is a tumor with abnormal immune cell differentiation and is morphologically classified into eight subtypes from M0 to M7 (Bennett et al., 1976). The abnormal differentiation of hematopoietic stem cells exhibited by AML is inextricably linked to the expression of immune genes. The expression of tumor immune-related genes is the result of the interaction of immune cells, tumor stem cells, stromal cells and cytokines, which co-evolve and ultimately form the tumor microenvironment that supports the tumor, thus contributing to the development and progression of leukemia (Swartz et al., 2012). Although previous studies have obtained some biomarkers for the prognosis of AML (Jiang et al., 2022; Lu et al., 2022), no studies have explored the overall characteristics of AML-related TME and mutation. Therefore, our study not only explored the TME and mutation-related characteristics of AML but also analyzed the cell trajectory of immune-related prognostic genes

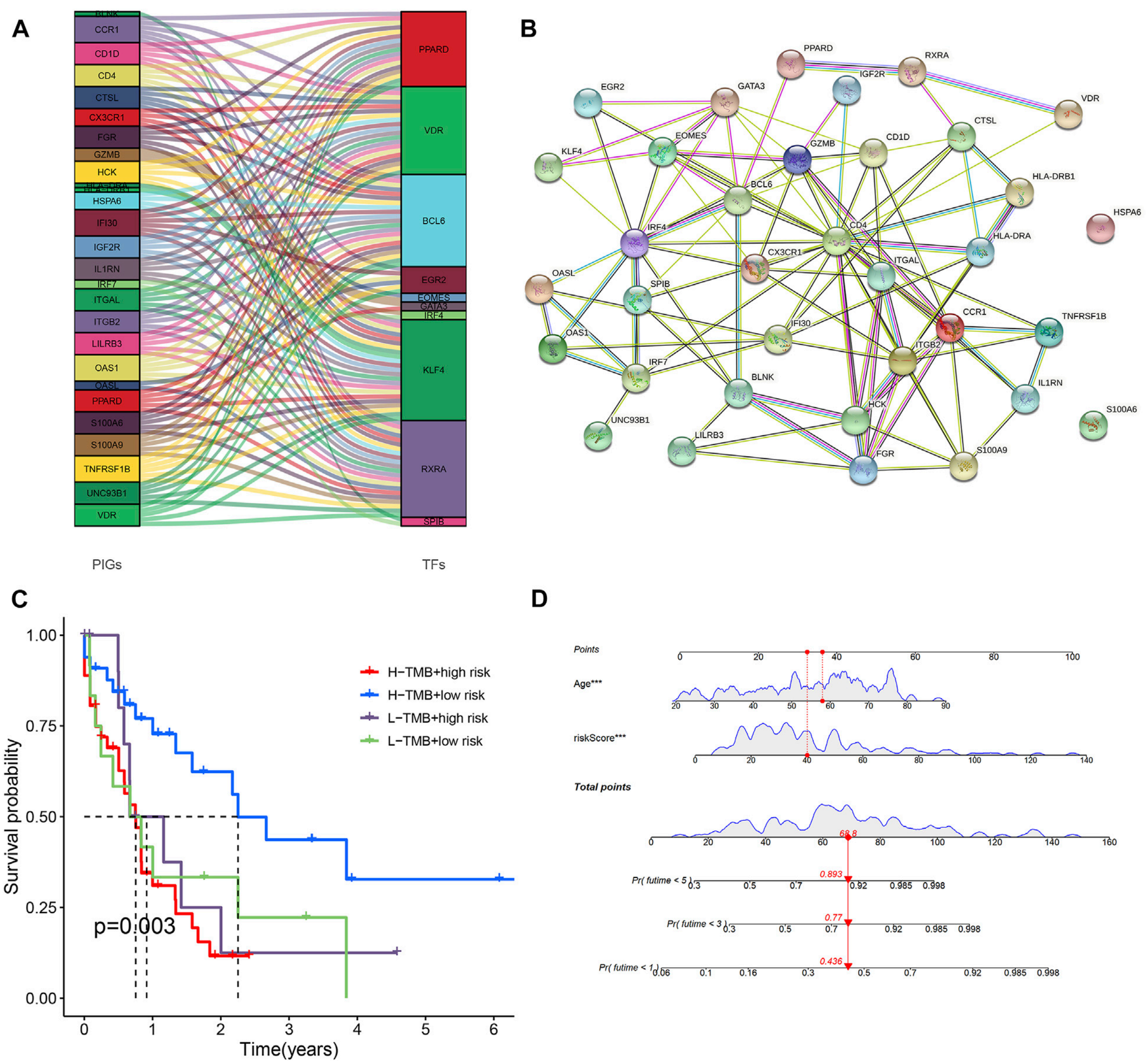

FIGURE 6
Predictive nomogram and PPI network. **(A)** Analysis of co-expressed of transcription factors and immune genes. **(B)** PPI networks of transcription factors and immune genes. **(C)** Comparison of survival rates for different TMB and different risk levels. **(D)** All clinical indicators were included in the nomogram.

obtained in single-cell sequencing chips to observe the expression of immune-related genes in different differentiated cells.

In our study, we divided the population into two groups based on the ssGSEA results using "hclust" method. Compared with the low immune cell infiltration cluster, higher stromal score, higher immune score and higher estimate score were shown in the high immune cell infiltration cluster. In addition to a large number of immune pathways, leukocyte transendothelial migration pathways and leukemia pathways were also enriched in patients with high immune cell infiltration clusters (Puig-Kröger et al., 2000). Since the migration of white blood cells from the blood into tissues is essential for immune surveillance and inflammation. This may mean that the high immune cell infiltration cluster may have more inflammatory responses and metastasis of AML cells.

High immune cell infiltration cluster associated with higher expression of HLA in all HLAs except HLA-J. It was reported that altered expression and function of HLA class I and class II molecules have long been characterized in solid tumors

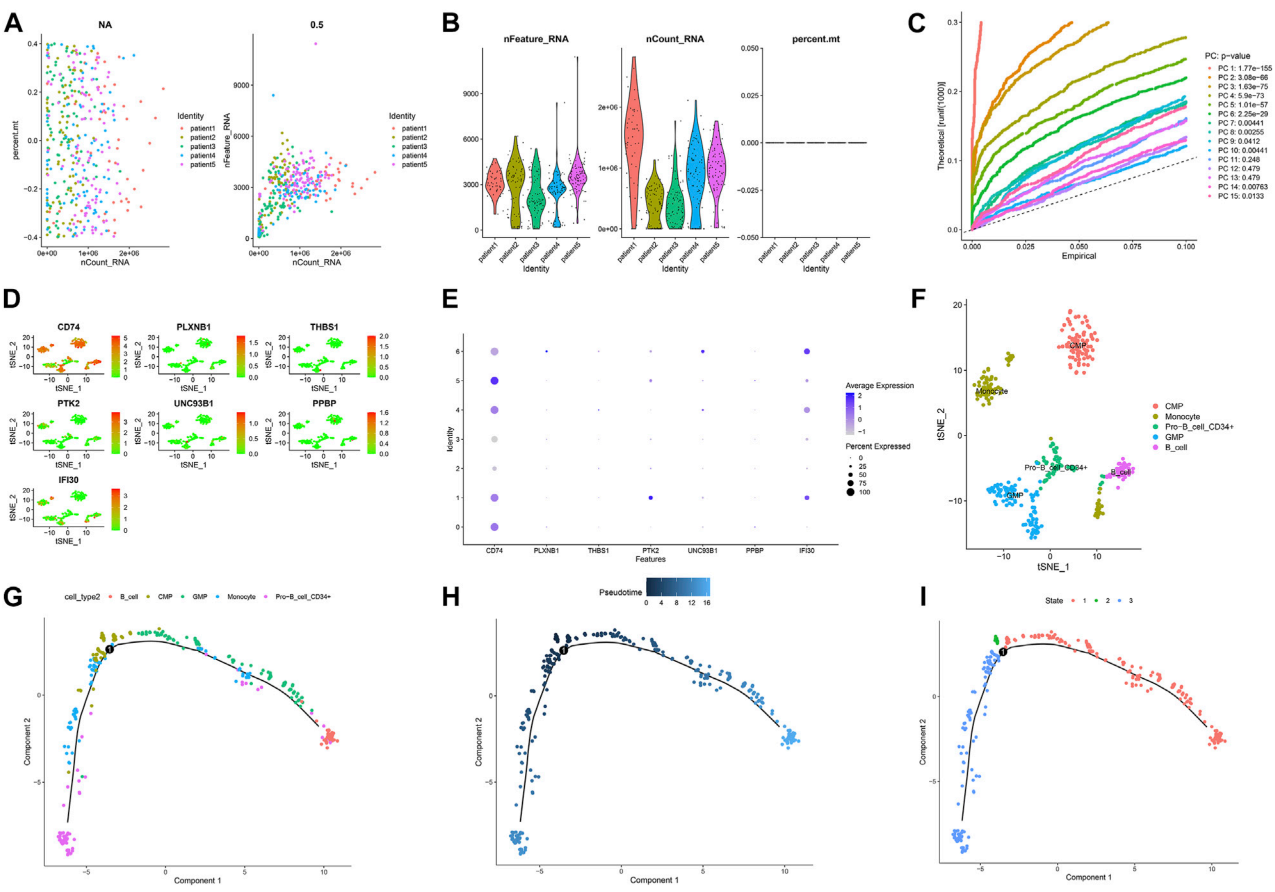

FIGURE 7
Single-cell sequencing results and pseudotime differentiation in AML patients at diagnosis. **(A)** RNA count charts of 5 patients. **(B)** Sequencing depth, gene count, and mitochondrial content of 5 patients. **(C)** PCA dimension reduction was performed on characteristic genes. **(D–E)** Expression of 7 prognostic genes in cell subsets. **(F)** Annotation results of cell subsets. **(G)** Sequence of different cell clusters along pseudo-time. Infer cell sequence from expression of the most dispersed genes in the cell cluster. Each point corresponds to a cell, and each color represents a state. **(H)** The darker the blue, the earlier the differentiation, and the lighter the blue, the later the differentiation. **(I)** Each color represents a different state.

(Rovatti et al., 2020), while both HLA class I and class II antigens on the graft cell surface are strong transplant antigens (Salman et al., 2018). Besides, some studies have found a recurrence of transplantation in AML following genomic HLA loss. When we inject donor-derived T-cells into animals carrying a diagnosis of HLA II expression or relapse of HLA II deficiency, HLA II expression is restored and effective anti-leukemic response is re-established (Toffalori et al., 2019). Based on our results, the higher HLA expression in the high immune cell infiltration cluster than in the low immune cell infiltration cluster implies that the anti-leukemic response was superior in the high immune cell infiltration cluster.

Nine hub immune genes associated with AML prognosis were obtained by Cox analysis. All 9 genes were risk factors for AML prognosis in the forest plot (HR > 1). CD74 is found to be linked to LGALS3 in a protein network and associated with poor survival in AML (Ruvolo et al., 2019). Alterations in PLXNB1 exons are identified as a method of homozygous alteration in AML-associated isoforms (Risueño et al., 2014). There are no reports of its correlation with the prognosis of AML. THBS1 is found to be lowly expressed in AML patients. Patients with low THBS1 have a shorter survival time. So, THBS1 is considered as a possible prognostic target for the treatment of AML patients (Zhu et al., 2019). PTK2 is an adherent spot gene. Its overexpression contributes to poorer prognosis in leukemia in a cohort of AML patients. It can also distinguish subgroups of patients with poor prognosis among those with IR-AML cytogenetics and unfavorable FLT3/NPM1 combinations (Pallarès et al., 2018). UNC93B1 is a key regulator of Toll-like receptors (TLRs), pattern recognition receptors that sense invading pathogens and manage the innate immune response and deliver them from the endoplasmic reticulum to their respective endosomal signaling regions. Several types of TLRs are known to contribute to the

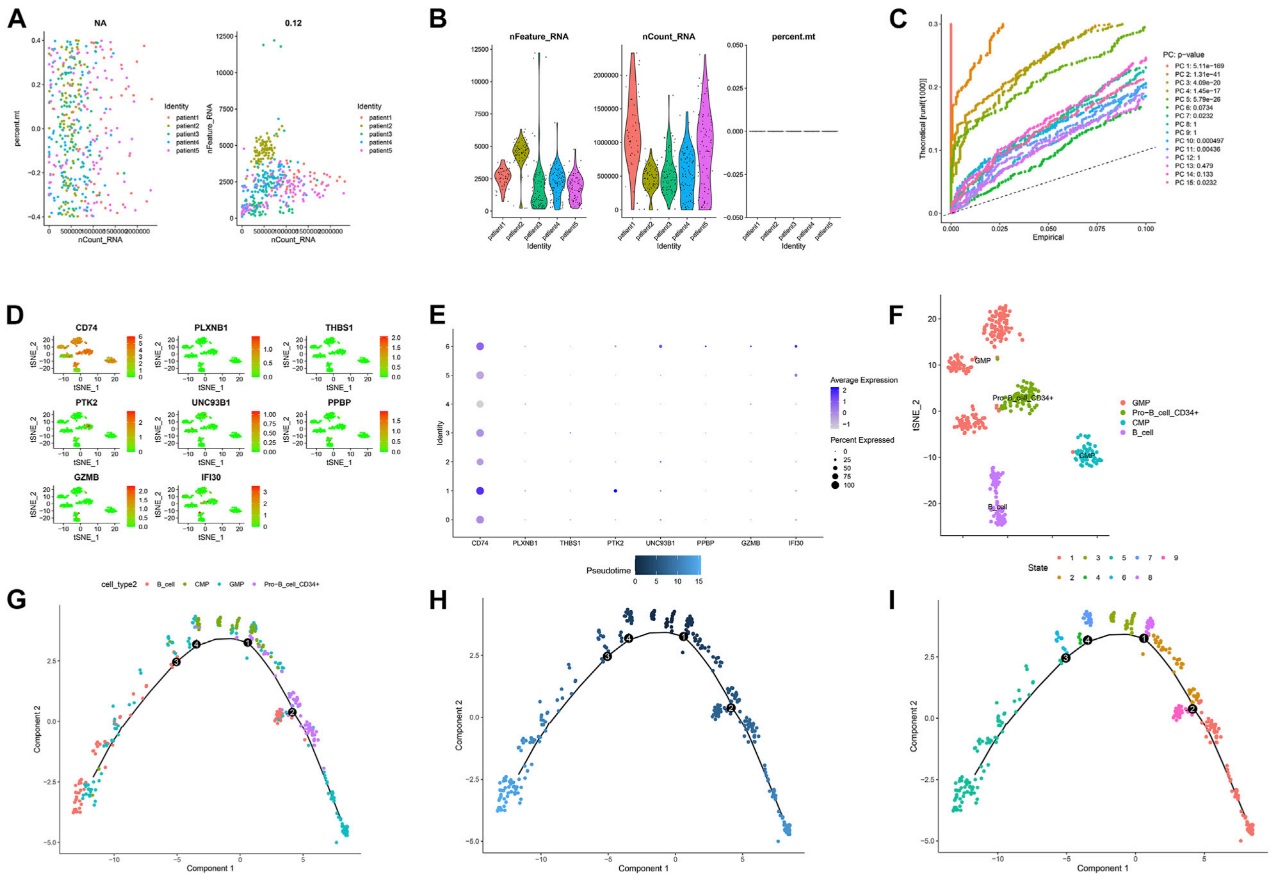

FIGURE 8
Single-cell sequencing results and pseudotime differentiation in AML patients at relapse. **(A)** RNA count charts of 5 patients. **(B)** Sequencing depth, gene count, and mitochondrial content of 5 patients. **(C)** PCA dimension reduction was performed on characteristic genes. **(D–E)** Expression of 7 prognostic genes in cell subsets. **(F)** Annotation results of cell subsets. **(G)** Sequence of different cell clusters along pseudo-time. Infer cell sequence from expression of the most dispersed genes in the cell cluster. Each point corresponds to a cell, and each color represents a state. **(H)** The darker the blue, the earlier the differentiation, and the lighter the blue, the later the differentiation. **(I)** Each color represents a different state.

inflammatory process after allogeneic hematopoietic stem cell transplantation (SCT). Thus, UNC93B1 may play an integral role in this process and influence the prognosis of leukemia (Uchino et al., 2021). PPBP is a proplatelet basic protein that belongs to the CXC chemokine family, High expression of PPBP predicts poor prognosis in adult AML patients (Tang et al., 2020). CXCL12 is produced by the BM microenvironment, binds to and activates the cognate receptor CXCR4 on leukemic cells, promotes transport and homing of leukemic cells in the BM microenvironment, and brings leukemic cells into close contact with stromal cells and the extracellular matrix, thereby constitutively producing growth-promoting and anti-apoptotic signals that ultimately lead to a poor prognosis (Roma-Rodrigues et al., 2019). GZMB is also considered to be a predictor of shorter OS in AML patients (Vadakekolathu et al., 2020). IFI30, a gene involved in antigen processing and HLA presentation, is observed to be transcriptionally downregulated in patients at the time of AML relapse (Sweeney and Vyas, 2019).

The areas under the ROC curve of the train set and the test set for ROC at 1, 3, 5 years were 0.807, 0.813, 0.815, and 0.731, 0.745, 0.830, respectively. The results showed that the model has strong predictive power for the prognosis of AML patients. We investigated the effect of risk score, gender, age, white blood cell count, FAB stage, hemoglobin, monocyte, race, and percentage of bone marrow blast on patient prognosis in AML patients by multivariate Cox regression analysis. Risk score and prognostic status were independent factors that influence the prognosis of leukemia ($p < 0.001$). Then a nomogram was designed that included risk scores and all clinical factors. It allowed us to predict the survival rate of any AML patient at 1, 3, and 5 years by using risk scores and all clinical factors from them. Interestingly, in some studies on biomarkers of leukemia prognosis, we found similar results to our article. Risk score was found to be an independent prognostic factor in these studies (Jiang et al., 2021b).

We constructed the TF hub gene regulatory network to explore the molecular mechanism of AML. A total of 10 transcription factors were found to play a role in the prognosis of AML immune gene expression. PPARD maintains leukemic stem cells through molecules involved in or regulating Wnt signaling, and is a valuable prognostic molecule (Gruszka et al., 2019). VDR functions as a regulator of stem cell homeostasis and leukemic transmission. The combination of VDR agonists and hypomethylating agents can promote leukemic stem cell depletion and reduce tumor burden (Paubelle et al., 2020). B cell lymphoma 6 (BCL6) is a transcriptional repressor and proto-oncogene that can maintain the survival and self-renewal of primary human acute myeloid leukemia cells (Kawabata et al., 2021). High-frequency eomes + T-bet low CD8 + T-cells predict poor clinical outcomes in AML, and targeting eomes may provide therapeutic benefits for AML (Jia et al., 2019). IRF4 expression is associated with the clinical phenotype and clinical hematological response of hydroxyurea in primary thrombocytosis, which may lead to the progression of AML (Huang et al., 2022). HDAC1 and KLF4 interact with each other to regulate the proliferation of human myeloid leukemia cells (Huang et al., 2014). IDH2/R140Q reduced 5 hmc modification and expression of some differentiation-inducing genes (ebf1 and SPIB). This is critical for the development and maintenance of AML stem cell-like cells (Ogawara et al., 2015). The complex interactions between TFs and hub genes have made great contributions to the development of AML.

AML patients were classified into high-risk and low-risk groups based on the median value of the risk score. Besides, we found that several other studies have also identified prognostic immune genes (Lu et al., 2022), but these studies have not systematically analyzed other characteristics of AML patients. In contrast to these studies, we not only constructed prognostic models of immune-related genes. We also comprehensively analyzed the characteristics of mutations, TME, HLA, and PPI in AML patients and identified the expression of these prognostic genes in single-cell sequencing analysis. Since we used immune-related genes to construct the prediction model, the GSEA results showed that we enriched a large number of immune-related pathways in the high-risk group. The expression of immune checkpoints was all higher in high-risk groups than in low-risk groups. Since high expression of immune checkpoints induces T-cell apoptosis or suppresses tumor T-cell responses, this leads to immune escape promoting the progression of AML (Christopher et al., 2018; Rovatti et al., 2020). Compared to the low-risk group, the high-risk group will have a worse prognosis. We found the worst prognosis for the high TMB and high-risk population and the best prognosis for the high TMB and low-risk population in the survival curves integrating TMB with risk profile. Based on the potential hypothesis that tumor mutations produce antigenic peptides, high TMB had been proposed as a prime candidate biomarker for the immunotherapeutic response, thereby enhancing immunogenicity (Chan et al., 2019). Therefore, high-risk with high TMB groups people should have the worst prognosis. Since there was no statistical difference in survival between the high TMB group people and the low TMB group people, the high TMB with the low risk group people might have the best prognosis. In Jiang's study, we found similar results. The expression of ICI was higher in AML patients in the high-risk group (Jiang et al., 2021a). The results of immunotherapy response showed that the TIDE score and Dysfunction scores in the high-risk group were higher than those in the low-risk group, suggesting that patients in the low-risk group may be more sensitive to anti-PD-1 and anti-CTLA4 therapy. The immune microenvironment in high-risk patients is not conducive to ICI treatment because these patients do not benefit from these inhibitors.

Single-cell transcriptome analysis showed that patients with diagnosed AML and patients with relapsed AML had different cell types. Monocytes were the precursors of macrophages and dendritic cells and can influence the tumor microenvironment by inducing immune tolerance, angiogenesis and tumor cell proliferation. It can also induce an immune response that produces antitumor effectors and activates antigen presenting cells (Shen et al., 2021; Ugel et al., 2021). Monocyte subsets were present at the time of AML diagnosis but not at the time of relapse. It suggested that there may be impaired function of monocytes phagocytosis of tumor cells in the development of AML, resulting in immunosuppression and ultimately contributing to the relapse of AML. In addition, we found that CD74 was highly expressed during the development of all cells in both diagnosed and relapsed AML patients. CD74 is a type II transmembrane protein expressed on antigen-presenting cells and has been considered a viable therapeutic target for AML in children and adults (Le et al., 2021). Our results will provide further evidence for CD74 as a target for immunotherapy in AML.

Compared with previous studies, our study has some innovations. For example, compared to Lu's study and Jiang's study (Jiang et al., 2021a; Lu et al., 2022). We not only comprehensively analyzed the TME characteristics, human leukocyte antigen expression and mutation information of AML patients in this study but also used the external adult AML validation dataset to verify the robustness of our prediction model. More importantly, due to single-cell sequencing analysis, we analyzed the expression of prognostic immune genes in cell subpopulations and plotted the change curve of prognostic gene expression with cell trajectory differentiation. In addition, we have successfully correlated the expression of prognostic genes with cell differentiation trajectories and can provide some new insights for targeted therapy of AML patients.

We should acknowledge that our study still has some limitations. In further studies, larger-sample clinical cohorts are needed to validate the accuracy of the prognostic model and the nomogram. Due to the small number of cells detected by the chip selected in this study, some cell subsets could not be detected. Therefore, subsequent studies need to further expand the number of cell tests to present a more complete bone marrow immune microenvironment.

In conclusion, we identified different immune subtypes in AML patients and established a prognostic model with nine prognostic biomarkers to predict the prognosis of patients with different immune cell infiltration clusters. Meanwhile, we revealed the differentiation trajectory of bone marrow microenvironment cells and the expression of prognostic immune genes in AML patients. Our study provided a means to predict prognosis and survival in AML patients and may provide promising targets for immunotherapy.

## Data availability statement

The original contributions presented in the study are publicly available. This data can be found https://github.com/zhengguowei-afk/code-and-input-data.git

## Author contributions

JL and XCJ designed the study. GWZ, MYL, XYC, XTC, and AND participated in data collection and analysis. GWZ drafted this manuscript. GWZ and JL interpreted the data. XCJ, YLY, XZS, CMW and JL reviewed and revised this manuscript.

## Funding

This article was supported by the Natural Science Foundation of He'nan Province, China (Grant No.212300410402).

## Conflict of interest

The authors declare that the research was conducted in the absence of any commercial or financial relationships that could be construed as a potential conflict of interest.

## Publisher's note

All claims expressed in this article are solely those of the authors and do not necessarily represent those of their affiliated organizations, or those of the publisher, the editors and the reviewers. Any product that may be evaluated in this article, or claim that may be made by its manufacturer, is not guaranteed or endorsed by the publisher.

## Supplementary material

The Supplementary Material for this article can be found online at: https://www.frontiersin.org/articles/10.3389/fcell.2022.990034/full#supplementary-material

**SUPPLEMENTARY FIGURE S1**
Comparison of clinical factors between high and low immune groups. (A) Age. (B) BM. (C) Hemoglobin. (D) Monocyte. (E) WB. (F) Calibration curve of train set. (G) Calibration curve of test set. (H) Distributions of risk scores of AML patients in the train set. (I) Distributions of survival status of AML patients in the train set. (J) Distributions of risk scores of AML patients in the test set. (K) Distributions of survival status of AML patients in the test set.

**SUPPLEMENTARY FIGURE S2**
Immune checkpoint inhibitor expression and TMB in high and low risk groups (A) Expression of HAVCR2 between high and low risk groups. (B) Expression of LAG3 between high and low risk groups. (C) Venn diagram of intersection of differential genes and immune genes. (D) Correlation between HAVCR2 and risk score. (E) Correlation between LAG3 and risk score. (F) Screening of genes by LASSO regression. (G) Differences in survival rates between high and low TMB populations. (H) Comparison of TMB between high-risk and low-risk groups. (I) The prognostic genes were screened by univariate Cox regression analysis.

**SUPPLEMENTARY FIGURE S3**
Partial pseudotime distribution of AML patients at diagnosis (A) Cell types on different differentiation trajectories. (B) Pseudotime distribution of seven genes between different cells. The horizontal axis is pseudo time, and the vertical axis is gene expression. (C) Pseudotime heatmap of 7 genes between different cells. The horizontal axis is pseudo time, and the vertical axis is gene expression. (D) Pseudotime distribution of different cell types. Pseudo time on the horizontal axis, cell density on the vertical axis.

**SUPPLEMENTARY FIGURE S4**
Partial pseudotime distribution of AML patients at relapse (A) Cell types on different differentiation trajectories. (B) Pseudotime distribution of seven genes between different cells. The horizontal axis is pseudo time, and the vertical axis is gene expression. (C) Pseudotime heatmap of 7 genes between different cells. The horizontal axis is pseudo time, and the vertical axis is gene expression. (D) Pseudotime distribution of different cell types. Pseudo time on the horizontal axis, cell density on the vertical axis.

**SUPPLEMENTARY FIGURE S5**
Univariate and multivariate Cox regression analysis of risk score and clinical factors (A) The expression levels of 9 AML prognostic genes were different between GTEx database and TCGA database. (B) Differential clustering heat map of the expression levels of 9 AML prognostic genes in GTEx database and TCGA database. (C) Univariate Cox regression analysis was performed for all clinical factors and risk scores. (D) Multivariate Cox regression analysis was performed for all clinical factors and risk scores.

**SUPPLEMENTARY FIGURE S6**
TIDE scores between high and low risk groups (A) Dysfunction scoring in high risk group and low risk group. (B) Exclusion scoring in high risk group and low risk group. (C) MSI scoring in high risk group and low risk group. (D) TIDE scoring in high risk group and low risk group.

## References

Agdashian, D., ElGindi, M., Xie, C., Sandhu, M., Pratt, D., Kleiner, D. E., et al. (2019). The effect of anti-CTLA4 treatment on peripheral and intra-tumoral T cells in patients with hepatocellular carcinoma. *Cancer Immunol. Immunother.* 68 (4), 599–608. doi:10.1007/s00262-019-02299-8

Austin, R., Smyth, M. J., and Lane, S. W. (2016). Harnessing the immune system in acute myeloid leukaemia. *Crit. Rev. Oncol. Hematol.* 103, 62–77. doi:10.1016/j.critrevonc.2016.04.020

Ayala, F., Dewar, R., Kieran, M., and Kalluri, R. (2009). Contribution of bone microenvironment to leukemogenesis and leukemia progression. *Leukemia* 23 (12), 2233–2241. doi:10.1038/leu.2009.175

Basak, P., Chatterjee, S., Das, P., Das, M., Pereira, J. A., Dutta, R. K., et al. (2010). Leukemic stromal hematopoietic microenvironment negatively regulates the normal hematopoiesis in mouse model of leukemia. *Chin. J. Cancer* 29 (12), 969–979. doi:10.5732/cjc.010.10431

Bennett, J. M., Catovsky, D., Daniel, M. T., Flandrin, G., Galton, D. A., Gralnick, H. R., et al. (1976). Proposals for the classification of the acute leukaemias. French-American-British (FAB) co-operative group. *Br. J. Haematol.* 33 (4), 451–458. doi:10.1111/j.1365-2141.1976.tb03563.x

Chan, T. A., Yarchoan, M., Jaffee, E., Swanton, C., Quezada, S. A., Stenzinger, A., et al. (2019). Development of tumor mutation burden as an immunotherapy biomarker: Utility for the oncology clinic. *Ann. Oncol.* 30 (1), 44–56. doi:10.1093/annonc/mdy495

Christopher, M. J., Petti, A. A., Rettig, M. P., Miller, C. A., Chendamarai, E., Duncavage, E. J., et al. (2018). Immune escape of relapsed AML cells after allogeneic transplantation. *N. Engl. J. Med.* 379 (24), 2330–2341. doi:10.1056/NEJMoa1808777

Daassi, D., Mahoney, K. M., and Freeman, G. J. (2020). The importance of exosomal PDL1 in tumour immune evasion. *Nat. Rev. Immunol.* 20 (4), 209–215. doi:10.1038/s41577-019-0264-y

Döhner, H., Estey, E. H., Amadori, S., Appelbaum, F. R., Büchner, T., Burnett, A. K., et al. (2010). Diagnosis and management of acute myeloid leukemia in adults: Recommendations from an international expert panel, on behalf of the European LeukemiaNet. *Blood* 115 (3), 453–474. doi:10.1182/blood-2009-07-235358

Frey, B., Rückert, M., Weber, J., Mayr, X., Derer, A., Lotter, M., et al. (2017). Hypofractionated irradiation has immune stimulatory potential and induces a timely restricted infiltration of immune cells in colon cancer tumors. *Front. Immunol.* 8, 231. doi:10.3389/fimmu.2017.00231

Giustacchini, A., Thongjuea, S., Barkas, N., Woll, P. S., Povinelli, B. J., Booth, C. A. G., et al. (2017). Single-cell transcriptomics uncovers distinct molecular signatures of stem cells in chronic myeloid leukemia. *Nat. Med.* 23 (6), 692–702. doi:10.1038/nm.4336

Gonzalez-Galarza, F. F., Mack, S. J., Hollenbach, J., Fernandez-Vina, M., Setterholm, M., Kempenich, J., et al. (2013). 16(th IHIW: Extending the number of resources and bioinformatics analysis for the investigation of HLA rare alleles. *Int. J. Immunogenet.* 40 (1), 60–65. doi:10.1111/iji.12030

Gruszka, A. M., Valli, D., and Alcalay, M. (2019). Wnt signalling in acute myeloid leukaemia. *Cells* 8 (11), E1403. doi:10.3390/cells8111403

Hosono, N. (2019). New therapeutic agents for acute myeloid leukemia. *Rinsho. Ketsueki.* 60 (9), 1108–1119. doi:10.11406/rinketsu.60.1108

Huang, X., Ma, T., Zhu, Y., Jiao, B., Yu, S., Wang, K., et al. (2022). IRF4 and IRF8 expression are associated with clinical phenotype and clinico-hematological response to hydroxyurea in essential thrombocythemia. *Front. Med.* 16 (3), 403–415. doi:10.1007/s11684-021-0858-1

Huang, Y., Chen, J., Lu, C., Han, J., Wang, G., Song, C., et al. (2014). HDAC1 and Klf4 interplay critically regulates human myeloid leukemia cell proliferation. *Cell Death Dis.* 5 (10), e1491. doi:10.1038/cddis.2014.433

Iasonos, A., Schrag, D., Raj, G. V., and Panageas, K. S. (2008). How to build and interpret a nomogram for cancer prognosis. *J. Clin. Oncol.* 26 (8), 1364–1370. doi:10.1200/jco.2007.12.9791

Isidori, A., Daver, N., and Curti, A. (2021). Editorial: The biological landscape of immunotherapy in AML. *Front. Oncol.* 11, 671252. doi:10.3389/fonc.2021.671252

Jia, B., Zhao, C., Rakszawski, K. L., Claxton, D. F., Ehmann, W. C., Rybka, W. B., et al. (2019). Eomes(+)T-bet(low) CD8(+) T cells are functionally impaired and are associated with poor clinical outcome in patients with acute myeloid leukemia. *Cancer Res.* 79 (7), 1635–1645. doi:10.1158/0008-5472.Can-18-3107

Jiang, F., Mao, Y., Lu, B., Zhou, G., and Wang, J. (2021a). A hypoxia risk signature for the tumor immune microenvironment evaluation and prognosis prediction in acute myeloid leukemia. *Sci. Rep.* 11 (1), 14657. doi:10.1038/s41598-021-94128-1

Jiang, F., Wang, X. Y., Wang, M. Y., Mao, Y., Miao, X. L., Wu, C. Y., et al. (2021b). An immune checkpoint-related gene signature for predicting survival of pediatric acute myeloid leukemia. *J. Oncol.* 2021, 5550116. doi:10.1155/2021/5550116

Jiang, P., Gu, S., Pan, D., Fu, J., Sahu, A., Hu, X., et al. (2018). Signatures of T cell dysfunction and exclusion predict cancer immunotherapy response. *Nat. Med.* 24 (10), 1550–1558. doi:10.1038/s41591-018-0136-1

Jiang, Z., Long, J., Deng, K., Zheng, Y., and Chen, M. (2022). eRNAs identify immune microenvironment patterns and provide a novel prognostic tool in acute myeloid leukemia. *Front. Mol. Biosci.* 9, 877117. doi:10.3389/fmolb.2022.877117

Kalaiyarasi, J. P., Ganesan, P., Kannan, K., Ganesan, T. S., Radhakrishnan, V., Dhanushkodi, M., et al. (2019). Outcomes of intensive treatment of adult acute myeloid leukemia patients: A retrospective study from a single centre. *Indian J. Hematol. Blood Transfus.* 35 (2), 248–254. doi:10.1007/s12288-018-1023-0

Kawabata, K. C., Zong, H., Meydan, C., Wyman, S., Wouters, B. J., Sugita, M., et al. (2021). BCL6 maintains survival and self-renewal of primary human acute myeloid leukemia cells. *Blood* 137 (6), 812–825. doi:10.1182/blood.2019001745

Le, Q., Leonti, A. R., Tang, T. T., Castro, S., Nourigat-Mckay, C., Perkins, L., et al. (2021). Therapeutic targeting of CD74 with STRO-001 antibody-drug conjugate in AML and ALL. *Blood* 138 (1), 509. doi:10.1182/blood-2021-151160

Lee, J. M., Lee, M. H., Garon, E., Goldman, J. W., Salehi-Rad, R., Baratelli, F. E., et al. (2017). Phase I trial of intratumoral injection of CCL21 gene-modified dendritic cells in lung cancer elicits tumor-specific immune responses and CD8(+) T-cell infiltration. *Clin. Cancer Res.* 23 (16), 4556–4568. doi:10.1158/1078-0432.Ccr-16-2821

Lichtenegger, F. S., Krupka, C., Haubner, S., Köhnke, T., and Subklewe, M. (2017). Recent developments in immunotherapy of acute myeloid leukemia. *J. Hematol. Oncol.* 10 (1), 142. doi:10.1186/s13045-017-0505-0

Lu, C., Hu, D., Zheng, J., Cao, S., Zhu, J., Chen, X., et al. (2022). A six-gene risk model based on the immune score reveals prognosis in intermediate-risk acute myeloid leukemia. *Biomed. Res. Int.* 2022, 4010786. doi:10.1155/2022/4010786

Mack, S. J., Cano, P., Hollenbach, J. A., He, J., Hurley, C. K., Middleton, D., et al. (2013). Common and well-documented HLA alleles: 2012 update to the CWD catalogue. *Tissue Antigens* 81 (4), 194–203. doi:10.1111/tan.12093

Medinger, M., and Passweg, J. R. (2017). Acute myeloid leukaemia genomics. *Br. J. Haematol.* 179 (4), 530–542. doi:10.1111/bjh.14823

Merino, D. M., McShane, L. M., Fabrizio, D., Funari, V., Chen, S. J., White, J. R., et al. (2020). Establishing guidelines to harmonize tumor mutational burden (TMB): In silico assessment of variation in TMB quantification across diagnostic platforms: phase I of the friends of cancer research TMB harmonization project. *J. Immunother. Cancer* 8 (1), e000147. doi:10.1136/jitc-2019-000147

Miles, L. A., Bowman, R. L., Merlinsky, T. R., Csete, I. S., Ooi, A. T., Durruthy-Durruthy, R., et al. (2020). Single-cell mutation analysis of clonal evolution in myeloid malignancies. *Nature* 587 (7834), 477–482. doi:10.1038/s41586-020-2864-x

Mittal, D., Gubin, M. M., Schreiber, R. D., and Smyth, M. J. (2014). New insights into cancer immunoediting and its three component phases--elimination, equilibrium and escape. *Curr. Opin. Immunol.* 27, 16–25. doi:10.1016/j.coi.2014.01.004

Ogawara, Y., Katsumoto, T., Aikawa, Y., Shima, Y., Kagiyama, Y., Soga, T., et al. (2015). IDH2 and NPM1 mutations cooperate to activate hoxa9/meis1 and hypoxia pathways in acute myeloid leukemia. *Cancer Res.* 75 (10), 2005–2016. doi:10.1158/0008-5472.Can-14-2200

Pallarès, V., Hoyos, M., Chillón, M. C., Barragán, E., Prieto Conde, M. I., Llop, M., et al. (2018). Focal adhesion genes refine the intermediate-risk cytogenetic classification of acute myeloid leukemia. *Cancers (Basel)* 10 (11), E436. doi:10.3390/cancers10110436

Passweg, J. R., Baldomero, H., Basak, G. W., Chabannon, C., Corbacioglu, S., Duarte, R., et al. (2019). The EBMT activity survey report 2017: A focus on allogeneic HCT for nonmalignant indications and on the use of non-HCT cell therapies. *Bone Marrow Transpl.* 54 (10), 1575–1585. doi:10.1038/s41409-019-0465-9

Paubelle, E., Zylbersztejn, F., Maciel, T. T., Carvalho, C., Mupo, A., Cheok, M., et al. (2020). Vitamin D receptor controls cell stemness in acute myeloid leukemia and in normal bone marrow. *Cell Rep.* 30 (3), 739–754. e734. doi:10.1016/j.celrep.2019.12.055

Petti, A. A., Williams, S. R., Miller, C. A., Fiddes, I. T., Srivatsan, S. N., Chen, D. Y., et al. (2019). A general approach for detecting expressed mutations in AML cells using single cell RNA-sequencing. *Nat. Commun.* 10 (1), 3660. doi:10.1038/s41467-019-11591-1

Puig-Kröger, A., López-Rodriguez, C., Relloso, M., Sánchez-Elsner, T., Nueda, A., Muñoz, E., et al. (2000). Polyomavirus enhancer-binding protein 2/core binding factor/acute myeloid leukemia factors contribute to the cell type-specific activity of the CD11a integrin gene promoter. *J. Biol. Chem.* 275 (37), 28507–28512. doi:10.1074/jbc.M004323200

Risueño, A., Roson-Burgo, B., Dolnik, A., Hernandez-Rivas, J. M., Bullinger, L., and De Las Rivas, J. (2014). A robust estimation of exon expression to identify alternative spliced genes applied to human tissues and cancer samples. *BMC Genomics* 15 (1), 879. doi:10.1186/1471-2164-15-879

Roma-Rodrigues, C., Mendes, R., Baptista, P. V., and Fernandes, A. R. (2019). Targeting tumor microenvironment for cancer therapy. *Int. J. Mol. Sci.* 20 (4), E840. doi:10.3390/ijms20040840

Rovatti, P. E., Gambacorta, V., Lorentino, F., Ciceri, F., and Vago, L. (2020). Mechanisms of leukemia immune evasion and their role in relapse after haploidentical hematopoietic cell transplantation. *Front. Immunol.* 11, 147. doi:10.3389/fimmu.2020.00147

Ruvolo, P. P., Hu, C. W., Qiu, Y., Ruvolo, V. R., Go, R. L., Hubner, S. E., et al. (2019). LGALS3 is connected to CD74 in a previously unknown protein network that is associated with poor survival in patients with AML. *EBioMedicine* 44, 126–137. doi:10.1016/j.ebiom.2019.05.025

Salman, A., Koparde, V., Hall, C. E., Jameson-Lee, M., Roberts, C., Serrano, M., et al. (2018). Determining the quantitative principles of T cell response to antigenic disparity in stem cell transplantation. *Front. Immunol.* 9, 2284. doi:10.3389/fimmu.2018.02284

Schlenk, R. F., and Döhner, H. (2013). Genomic applications in the clinic: Use in treatment paradigm of acute myeloid leukemia. *Hematol. Am. Soc. Hematol. Educ. Program* 2013, 324–330. doi:10.1182/asheducation-2013.1.324

Sharpe, A. H., and Pauken, K. E. (2018). The diverse functions of the PD1 inhibitory pathway. *Nat. Rev. Immunol.* 18 (3), 153–167. doi:10.1038/nri.2017.108

Shen, C. K., Huang, B. R., Yeh, W. L., Chen, C. W., Liu, Y. S., Lai, S. W., et al. (2021). Regulatory effects of IL-1β in the interaction of GBM and tumor-associated monocyte through VCAM-1 and ICAM-1. *Eur. J. Pharmacol.* 905, 174216. doi:10.1016/j.ejphar.2021.174216

Short, N. J., Rytting, M. E., and Cortes, J. E. (2018). Acute myeloid leukaemia. *Lancet* 392 (10147), 593–606. doi:10.1016/s0140-6736(18)31041-9

Siegel, R. L., Miller, K. D., and Jemal, A. (2019). Cancer statistics, 2019. *Ca. Cancer J. Clin.* 69 (1), 7–34. doi:10.3322/caac.21551

Subramanian, A., Tamayo, P., Mootha, V. K., Mukherjee, S., Ebert, B. L., Gillette, M. A., et al. (2005). Gene set enrichment analysis: A knowledge-based approach for interpreting genome-wide expression profiles. *Proc. Natl. Acad. Sci. U. S. A.* 102 (43), 15545–15550. doi:10.1073/pnas.0506580102

Swartz, M. A., Iida, N., Roberts, E. W., Sangaletti, S., Wong, M. H., Yull, F. E., et al. (2012). Tumor microenvironment complexity: Emerging roles in cancer therapy. *Cancer Res.* 72 (10), 2473–2480. doi:10.1158/0008-5472.Can-12-0122

Sweeney, C., and Vyas, P. (2019). The graft-versus-leukemia effect in AML. *Front. Oncol.* 9, 1217. doi:10.3389/fonc.2019.01217

Tallman, M. S., Wang, E. S., Altman, J. K., Appelbaum, F. R., Bhatt, V. R., Bixby, D., et al. (2019). Acute myeloid leukemia, version 3.2019, NCCN clinical practice guidelines in oncology. *J. Natl. Compr. Canc. Netw.* 17 (6), 721–749. doi:10.6004/jnccn.2019.0028

Tang, W., Li, Z., Li, X., and Huo, Z. (2020). High CXCR2 expression predicts poor prognosis in adult patients with acute myeloid leukemia. *Ther. Adv. Hematol.* 11, 2040620720958586. doi:10.1177/2040620720958586

Teague, R. M., and Kline, J. (2013). Immune evasion in acute myeloid leukemia: Current concepts and future directions. *J. Immunother. Cancer* 1 (13), 13. doi:10.1186/2051-1426-1-13

Toffalori, C., Zito, L., Gambacorta, V., Riba, M., Oliveira, G., Bucci, G., et al. (2019). Immune signature drives leukemia escape and relapse after hematopoietic cell transplantation. *Nat. Med.* 25 (4), 603–611. doi:10.1038/s41591-019-0400-z

Trapnell, C., Cacchiarelli, D., Grimsby, J., Pokharel, P., Li, S., Morse, M., et al. (2014). The dynamics and regulators of cell fate decisions are revealed by pseudotemporal ordering of single cells. *Nat. Biotechnol.* 32 (4), 381–386. doi:10.1038/nbt.2859

Uchino, K., Vu Quang, L., Mizuno, S., Horio, T., Yamamoto, H., Hanamura, I., et al. (2021). Donor UNC-93 Homolog B1 genetic polymorphism predicts survival outcomes after unrelated bone marrow transplantation. *Genes Immun.* 22 (1), 35–43. doi:10.1038/s41435-021-00122-y

Ugel, S., Canè, S., De Sanctis, F., and Bronte, V. (2021). Monocytes in the tumor microenvironment. *Annu. Rev. Pathol.* 16, 93–122. doi:10.1146/annurev-pathmechdis-012418-013058

Vadakekolathu, J., Minden, M. D., Hood, T., Church, S. E., Reeder, S., Altmann, H., et al. (2020). Immune landscapes predict chemotherapy resistance and immunotherapy response in acute myeloid leukemia. *Sci. Transl. Med.* 12 (546), eaaz0463. doi:10.1126/scitranslmed.aaz0463

Wolf, Y., Anderson, A. C., and Kuchroo, V. K. (2020). TIM3 comes of age as an inhibitory receptor. *Nat. Rev. Immunol.* 20 (3), 173–185. doi:10.1038/s41577-019-0224-6

Yehudai-Resheff, S., Attias-Turgeman, S., Sabbah, R., Gabay, T., Musallam, R., Fridman-Dror, A., et al. (2019). Abnormal morphological and functional nature of bone marrow stromal cells provides preferential support for survival of acute myeloid leukemia cells. *Int. J. Cancer* 144 (9), 2279–2289. doi:10.1002/ijc.32063

Yoshihara, K., Shahmoradgoli, M., Martínez, E., Vegesna, R., Kim, H., Torres-Garcia, W., et al. (2013). Inferring tumour purity and stromal and immune cell admixture from expression data. *Nat. Commun.* 4, 2612. doi:10.1038/ncomms3612

Zhang, L., Gajewski, T. F., and Kline, J. (2009). PD-1/PD-L1 interactions inhibit antitumor immune responses in a murine acute myeloid leukemia model. *Blood* 114 (8), 1545–1552. doi:10.1182/blood-2009-03-206672

Zhu, L., Li, Q., Wang, X., Liao, J., Zhang, W., Gao, L., et al. (2019). THBS1 is a novel serum prognostic factors of acute myeloid leukemia. *Front. Oncol.* 9, 1567. doi:10.3389/fonc.2019.01567

TYPE Original Research
PUBLISHED 06 October 2022
DOI 10.3389/fimmu.2022.962000



OPEN ACCESS

EDITED BY
Ki-Young Lee,
University of Calgary, Canada

REVIEWED BY
Liang Huang,
Huazhong University of Science and Technology, China
Claudia Scotti,
University of Pavia, Italy

*CORRESPONDENCE
Jiazhu Wu
wujiazhu09@sina.com
Wei Xu
xuwei10000@hotmail.com

†These authors have contributed equally to this work

SPECIALTY SECTION
This article was submitted to Cancer Immunity and Immunotherapy, a section of the journal Frontiers in Immunology

RECEIVED 05 June 2022
ACCEPTED 22 August 2022
PUBLISHED 06 October 2022

CITATION
Pan B, Li Y, Xu Z, Miao Y, Yin H, Kong Y, Zhang X, Liang J, Xia Y, Wang L, Li J, Wu J and Xu W (2022) Identifying a novel ferroptosis-related prognostic score for predicting prognosis in chronic lymphocytic leukemia. *Front. Immunol.* 13:962000. doi: 10.3389/fimmu.2022.962000



# Identifying a novel ferroptosis-related prognostic score for predicting prognosis in chronic lymphocytic leukemia

Bihui Pan[1,2†], Yue Li[1,2†], Zhangdi Xu[1,2], Yi Miao[1,2], Hua Yin[1,2], Yilin Kong[1,2], Xinyu Zhang[1,2], Jinhua Liang[1,2], Yi Xia[1,2], Li Wang[1,2], Jianyong Li[1,2], Jiazhu Wu[1,2*] and Wei Xu[1,2*]

[1]Department of Hematology, The First Affiliated Hospital of Nanjing Medical University, Jiangsu Province Hospital, Nanjing, China, [2]Key Laboratory of Hematology of Nanjing Medical University, Nanjing, China

**Background:** Chronic lymphocytic leukemia (CLL) is the most common leukemia in the western world. Although the treatment landscape for CLL is rapidly evolving, there are still some patients who develop drug resistance or disease refractory. Ferroptosis is a type of lipid peroxidation–induced cell death and has been suggested to have prognostic value in several cancers. Our research aims to build a prognostic model to improve risk stratification in CLL patients and facilitate more accurate assessment for clinical management.

**Methods:** The differentially expressed ferroptosis-related genes (FRGs) in CLL were filtered through univariate Cox regression analysis based on public databases. Least absolute shrinkage and selection operator (LASSO) Cox algorithms were performed to construct a prognostic risk model. CIBERSORT and single-sample gene set enrichment analysis (ssGSEA) were performed to estimate the immune infiltration score and immune-related pathways. A total of 36 CLL patients in our center were enrolled in this study as a validation cohort. Moreover, a nomogram model was established to predict the prognosis.

**Results:** A total of 15 differentially expressed FRGs with prognostic significance were screened out. After minimizing the potential risk of overfitting, we constructed a novel ferroptosis-related prognostic score (FPS) model with nine FRGs (AKR1C3, BECN1, CAV1, CDKN2A, CXCL2, JDP2, SIRT1, SLC1A5, and SP1) and stratified patients into low- and high-risk groups. Kaplan–Meier analysis showed that patients with high FPS had worse overall survival (OS) ($P$<0.0001) and treatment-free survival (TFS) ($P$<0.0001). ROC curves evaluated the prognostic prediction ability of the FPS model. Additionally, the immune cell types and immune-related pathways were correlated with the risk scores in CLL patients. In the validation cohort, the results confirmed that the high-risk group was related to worse OS ($P$<0.0001), progress-free survival (PFS) ($P$=0.0140), and TFS ($P$=0.0072). In the multivariate analysis, only FPS ($P$=0.011) and CLL-IPI ($P$=0.010) were independent risk indicators for OS.

Furthermore, we established a nomogram including FPS and CLL-IPI that could strongly and reliably predict individual prognosis.

**Conclusion:** A novel FPS model can be used in CLL for prognostic prediction. The model index may also facilitate the development of new clinical ferroptosis-targeted therapies in patients with CLL.

KEYWORDS

chronic lymphocytic leukemia, ferroptosis, prognosis, immune infiltrates, nomogram

# Introduction

Chronic lymphocytic leukemia (CLL) is characterized by the accumulation of monoclonal B cells in the bone marrow and lymphoid organs (1). It is the most common leukemia in the western world, with an incidence of approximately 4.2 cases per 100,000 people per year (2). Currently, the biological hallmarks of CLL are well recognized as B-cell receptor and Bruton tyrosine kinase signaling (3), as well as resistance to apoptosis mediated by Bcl-2, which has revolutionized CLL clinical management. In the new era of novel therapies, the choice of CLL treatment varies from conventional chemotherapy to highly effective regimens such as anti-CD20 monoclonal antibodies, BTK inhibitors, Bcl-2 inhibitors, and PI3K inhibitors (4–6). The emergence of novel therapies has benefitted many patients, especially in high-risk cases, including those with p53 deletion/mutations who have a poor outcome with conventional chemoimmunotherapy (7). Allogeneic hematopoietic stem-cell transplantation is another choice for selected fit patients, but severe rejection and bone marrow failure make many patients and hematologists hesitant to use this method. Although all these kinds of techniques are available in fighting CLL, some patients still develop disease refractoriness and relapse, which show CLL's heterogeneity. Therefore, it is important to distinguish high-risk patients from the CLL population during the early stage of disease and apply a more suitable treatment strategy.

Ferroptosis is a distinct form of programmed cell death dependent on iron metabolism. It is quite different from other well-recognized cell death types, such as apoptosis, autophagy, pyroptosis, and necroptosis, in terms of biochemistry, morphology, and genetics. Lipid peroxidation, substantial oxidative stress, and intracellular accumulation of reactive oxygen species (ROSs) are typical characteristics of ferroptosis (8). Dr. Stockwell first introduced the definition of "ferroptosis" in 2012 (9). The action of divalent iron and ester oxygenase catalyzes unsaturated fatty acids that are highly expressed on the cell membrane, leading to lipid peroxidation and inducing ferroptosis (10). Rapidly developing ferroptosis studies suggest the possibility of its prognostic significance in several cancers (11–14). Tumor cells are iron addicted, which means they are more dependent on iron than normal cells. Disorders of iron metabolism can increase the risk of cancer and improve cancer growth (15). Activation of ferroptosis pathways can solve the drug resistance problems of existing chemical agents, providing new therapeutic targets for cancer treatment (16, 17).

To explore the relationship between CLL and ferroptosis, in this study, we filtered differentially expressed ferroptosis-related genes in CLL based on public databases. We built a novel prognostic risk model based on nine ferroptosis-related genes (AKR1C3, BECN1, CAV1, CDKN2A, CXCL2, JDP2, SIRT1, SLC1A5, and SP1). Functional analysis was conducted to elucidate the underlying related biological molecular functions and signaling pathways as well as immune correlations. In addition, we used a CLL patient cohort from our center for validation. Our research aims to build a preliminary prognostic model to improve risk stratification in CLL patients and facilitate more accurate assessment for clinical management.

# Materials and methods

## Database resources

The mRNA sequencing profiles and related clinical information for 151 CLL patients in the GSE22762 dataset were extracted from the Gene Expression Omnibus (GEO) database (https://www.ncbi.nlm.nih.gov/geo/) as the training set. Additionally, the sequencing data of another 188 CLL patients and 32 normal samples from the GSE50006 dataset were used to identify the differentially expressed ferroptosis-related genes. The RNA microarray data were normalized using the "sva" R package. The data from GEO are publicly available.

## Patient and clinical data acquisition

A total of 36 CLL patients diagnosed between 2012 and 2017 at the First Affiliated Hospital of Nanjing Medical University were enrolled in this study as the validation cohort. The diagnosis was established in accordance with the International Workshop on CLL—National Cancer Institute (IWCLL-NCI) criteria. This study was approved by the institutional review board of the First Affiliated Hospital of Nanjing Medical University. Clinical characteristics such as age, sex, Binet stage, B symptoms, lymphocytes, hemoglobin, platelet count, lactate dehydrogenase (LDH), β2-microglobulin (β2-MG), complex karyotype, TP53 disruption, and immunoglobulin heavy-chain gene (IGHV) mutation status were gathered from medical records.

## Sample preparation and RNA-Seq

All the total RNA samples in our center were obtained from the purified $CD19^+$ B cells of CLL patients using a $CD19^+$ B-Cell Selection Kit (Miltenyi Biotech, Gladbach, Germany). The quality of the extracted RNA was assessed using an RNeasy Micro Kit (QIAGEN, Hilden, Germany). The prepared sequencing libraries were sequenced by a HiSeq X Ten high-throughput sequencing system. The sequences were mapped to hg38 (human genome 38) and aligned using Bowtie and BLAT (the BLAST-like alignment tool). The related fragments per kilobase million (FPKM) values in the validation cohort are listed in Table S1.

## Acquisition and functional enrichment analysis of ferroptosis-related gene signatures

A total of 259 FRGs (namely 111 markers, 92 drivers, and 56 suppressors) were obtained from the ferroptosis database FerrDb (http://www.zhounan.org/ferrdb/) (18), as provided in Table S2. We then performed univariate Cox regression analysis on FRGs and survival data to identify differential FRGs with prognostic value based on the GSE22762 set. Further screening of the differentially expressed FRGs between CLL and normal samples in the GSE50006 cohort was performed by t-test or Kruskal–Wallis test. A protein–protein interaction (PPI) network was constructed from the STRING database. Moreover, Kyoto Encyclopedia of Genes and Genomes (KEGG) and Gene Ontology (GO) analyses were performed to explore the functional enrichment of the CLL-related FRGs *via* the "clusterprofiler" R package.

## Construction of the risk score prognostic model

Fifteen FRGs considered statistically significant were subsequently incorporated into least absolute contraction and selection operator (LASSO) regression analysis to minimize the potential risk of overfitting with the "glmnet" R package (19). In LASSO analysis, the optimal λ was used to construct the risk score model by 10-fold cross-validation. The risk score of each patient was calculated as follows: risk score = $\sum_{i=1}^{n}\beta_i * x_i$. The value of $\beta_i$ represents the coefficients, and $\chi_i$ represents the gene expression. We divided the patients into low- and high-risk groups based on the optimal risk cutoff. Heatmap plotting of the FRG expression level was performed by the "pheatmap" R package. Dimensionality reduction using principal component analysis (PCA) and t-distributed stochastic neighbor embedding (tSNE) was performed to visualize the distribution of the groups with the "ggbiplot" R package. Receiver operating characteristic (ROC) curves and the corresponding areas under the curve (AUCs) calculated using the "timeROC" R package were used to assess the prognostic ability of the risk score model.

## Evaluation of the relationship between immune cell infiltration and risk stratification

The relative proportions of 22 infiltrating immune cell subtypes were estimated by the CIBERSORT (https://cibersort.stanford.edu/) algorithm. We compared the relative fraction of the immune cell subtypes between the low- and high-risk groups with the Wilcoxon test. Single-sample gene set enrichment analysis (ssGSEA) was performed to estimate the immune infiltration score of 28 immune cell subtypes and 13 immune pathways. The gene sets included in ssGSEA are listed in Table S3.

## Establishment of the nomogram models

A nomogram model was established to estimate the probability of 2-, 3-, and 5-year OS by the "rms" R package. The capacity for prognostic prediction was evaluated by the concordance index (C-index).

## Statistical analysis

Data were analyzed by R software (version 4.11) and IBM SPSS statistical software (version 21.0). Continuous variables are presented as the mean ± standard deviation (SD) and were compared by the t-test or Kruskal–Wallis test. Survival curves for the overall survival (OS) time, treatment-free survival (TFS) time, and progression-free survival (PFS) time of the low- and high-risk groups were calculated by the Kaplan–Meier method and compared by the log-rank test with the "survminer" R package. Univariate and multivariate regression analyses were performed to determine the independent risk factors. $P<0.05$ was considered statistically significant.

# Results

## Identification of FRGs in CLL

Based on FerrDb, 22 FRGs were found to be related to prognosis in the training cohort (Figure 1A). Among them, 13 genes (AKR1C3, CXCL2, EPAS1, FTH1, IREB2, JDP2, PTGS2, SETD1B, SIRT1, SLC1A5, SP1, TLR4, and VEGFA) were correlated with favorable OS, and 9 genes (AIFM2, BECN1, CAV1, CDKN2A, GABARAPL2, HRAS, PEBP1, SLC1A5, and VDAC2) were associated with poor outcomes. We then compared the expression of FRGs that correlated with CLL prognosis between CLL and normal samples, and 15 genes with statistical significance were screened out (Figure 1B). Moreover, we explored the FRG correlation with STRING, and the ferroptosis-related gene network indicated potential protein–protein interactions. Interestingly, p53 seemed to be associated with these FRGs (Figure 1C). KEGG analysis found that FRGs were enriched in the NOD-like receptor signaling pathway, p53 signaling pathway, NF-κB pathway, and FoxO signaling pathway (Figure 1D). GO enrichment analysis revealed that these genes were highly enriched in the biological processes of cellular responses to oxidative stress and chemical stress and DNA-binding transcription factor binding as well as oxidoreductase activity, acting on NAD(P)H in terms of molecular function (Figure 1E).

## Establishment and assessment of the novel ferroptosis-related risk score prognostic model

We performed correlation analysis of the 15 FRGs, which elucidated the interactions among these genes (Figure 2A). Considering the influence of multicollinearity on prediction accuracy, LASSO Cox regression analysis was applied to establish a novel ferroptosis-related prognostic score (FPS) model. Nine prognostic FRGs (AKR1C3, BECN1, CAV1, CDKN2A, CXCL2, JDP2, SIRT1, SLC1A5, and SP1) were identified by LASSO analysis based on optimal weight coefficients (λ) (Figures 2B, C). Kaplan–Meier analyses based on the expression of nine genes are shown in Figure S1. The risk score model was calculated by the formula FPS =

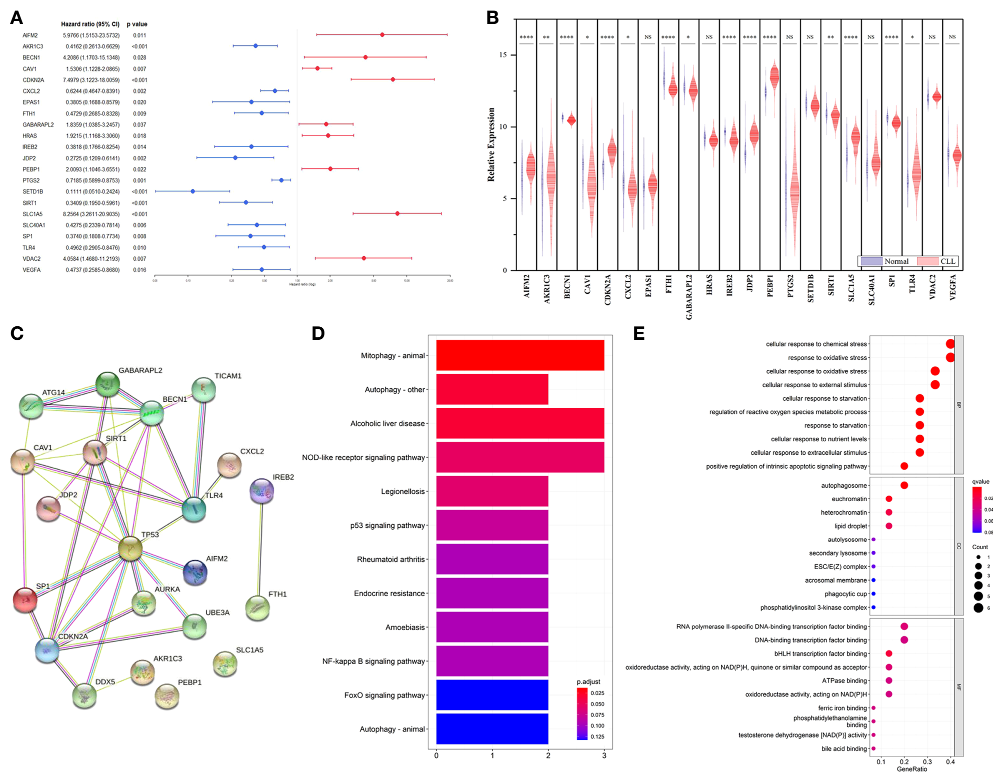


FIGURE 1
Identification of prognostic FRGs in CLL cohort. **(A)** Forest plot with hazard ratios of the univariate Cox regression analysis showing the FRGs with prognostic value in the GSE22762 dataset. **(B)** The differential expression of FRGs between CLL and normal samples in the GSE50006 dataset. **(C)** PPI network showing the interactions among the 15 FRGs. **(D)** KEGG analyses of the pathways enrichment of the CLL related FRGs. **(E)** GO analyses of the functional enrichment of the CLL related FRGs.

(−0.1930)*AKR1C3 + (0.1751)*BECN1 + (0.0897)*CAV1 + (0.5965)*CDKN2A + (−0.0544)*CXCL2 + (−0.1560)*JDP2 + (−0.3307)*SIRT1 + (1.0947)*SLC1A5 + (−0.1027)*SP1. Based on the optimal cutoff values (cutoff = 6.5965), the CLL patients were divided into two groups: 113 (74.83%) patients in the low-risk group and 38 (25.17%) patients in the high-risk group. As shown in Figure 3A, the patients could be stratified into the low- or high-risk group based on the optimal cutoff value. Consistently, the patients with increased risk scores had unfavorable outcomes (Figure 3B). The heatmap displays the expression values of the nine genes across the CLL patients with low- or high-risk scores (Figure 3C). As shown in Figures 3D, E, PCA and tSNE were used to visualize the distributions of different groups according to FPS. The Kaplan–Meier analysis showed that patients with high FPS had a significantly worse OS ($P$<0.0001) and TFS ($P$<0.0001) (Figures 3F, G). Moreover, the AUC values of the ROC curves for predicting the 1-, 3-, and 5-year OS were 0.908, 0.874, and 0.848, respectively, and the 1-, 3-, and 5-year TFS were 0.759, 0.709, and 0.544, respectively (Figures 3H, I).

## Functional analysis of the two groups and immune relationship with the risk score model

The heatmap depicted a total of 226 differentially expressed genes (DEGs) between the low- and high-risk groups in line with FPS (Figure 4A). All of the DEGs were used to perform KEGG and GO functional enrichment analyses to identify potential biological and molecular functions (Figures 4B, C). KEGG analysis showed that several pathways, including Th1- and Th2-cell differentiation, Th17-cell differentiation, the NF-κB signaling pathway, and cytokine–cytokine receptor interactions, were enriched. Notably, DEGs were significantly enriched in T-cell activation, T-cell differentiation, and lymphocyte differentiation by GO functional analysis. We further explored the relationship between the risk scores and immune infiltrates. Considering the uniqueness of the immune microenvironment of hematologic malignancies, we used two algorithms, CIBERSORT and ssGSEA, to estimate the infiltrating immune cell types and related immune pathways. CIBERSORT analysis revealed that the low-risk patients had higher relative fractions of naive $CD4^+$ T cells ($P$=0.047), resting natural killer (NK) cells ($P$<0.001), monocytes ($P$=0.051), and activated mast cells ($P$=0.027), while the high-risk patients had higher relative fractions of follicular helper T cells ($P$=0.007), regulatory T cells ($P$<0.001), and activated NK cells ($P$<0.001) (Figure 4D). Furthermore, the scores of activated $CD4^+$ T cells ($P$<0.001), activated $CD8^+$ T cells ($P$=0.006), CD56 dim natural killer cells ($P$<0.001), central memory $CD8^+$ T cells ($P$=0.013), effector memory $CD8^+$ T cells ($P$=0.033), gamma delta T cells ($P$=0.047), immature dendritic cells ($P$=0.039), mast cells ($P$=0.003), natural killer cells ($P$=0.043), natural killer T cells ($P$=0.007), neutrophils ($P$=0.017), plasmacytoid dendritic cells ($P$=0.010), regulatory T cells ($P$=0.042), follicular helper T cells ($P$=0.003), type 1 T helper cells ($P$=0.008), and type 2 T helper cells ($P$=0.006) were significantly different between the low- and high-risk groups (Figure 4E). Additionally, the scores of immune-related pathways, including APC co-inhibition, C–C chemokine receptor (CCR), cytokine activity, inflammation promotion, T-cell costimulation, and type II IFN response, were lower in the high-risk group, while the score of the HLA pathway was higher (Figure 4F).

## Validation of the nine-FRG signature prognostic model

Thirty-six CLL patients in our center were enrolled in this study as a validation cohort. The clinical characteristics are listed in Table S4. We applied the same formula mentioned above to calculate the FPS level based on the RNA sequencing

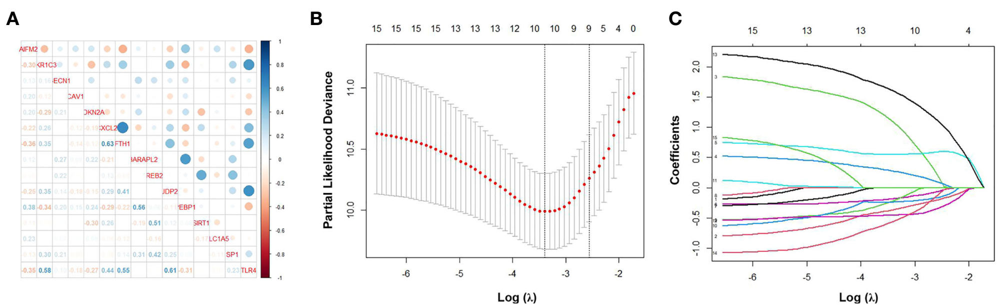


FIGURE 2
Identification of ferroptosis-related genes signature by LASSO regression algorithm in CLL. **(A)** Correlation analysis of the 15 FRGs. **(B)** Nine prognostic FRGs were identified by LASSO analysis based on optimal weight coefficients (λ). **(C)** The LASSO coefficient profiles of the nine-FRG signature.

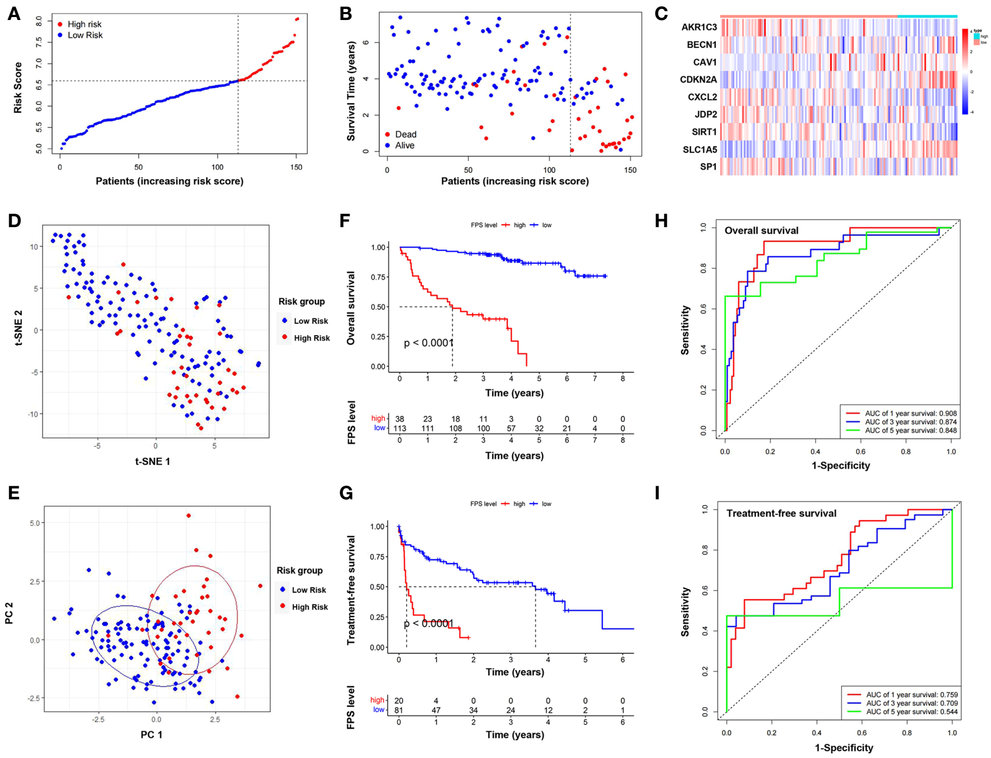

FIGURE 3
Establishment and assessment of the novel ferroptosis-related gene risk score model. **(A)** The distribution and optimal cutoff value of risk scores in training cohort. **(B)** The distributions of OS status, OS, and risk score. **(C)** Heatmap of the expression levels of the nine selected FRGs. **(D)** t-SNE plot of the CLL cohort. **(E)** PCA plot of the CLL cohort visualizing the distribution of the low- and high-risk groups. Kaplan–Meier survival curves for OS **(F)** and TFS **(G)** of CLL patients stratified by FPS risk score. Time-dependent ROC curves of the risk model for predicting the 1-, 3-, and 5-year OS **(H)** and TFS **(I)**.

data. Similar to the GEO cohort, the FPS index divided patients into two different risk groups (Figures 5A, B). The Kaplan–Meier curves revealed that patients with higher FPS levels had a worse OS (*P*<0.0001), and the AUCs of 3- and 5-year OS were 0.703 and 0.723, respectively (Figures 5C, F). The 1-year ROC curve in Figure 5F could not be calculated because the OS was 100%. We performed further Kaplan–Meier analyses of PFS and TFS, and the results confirmed that the high-risk group was related to poorer PFS (*P*=0.0140) and TFS (*P*=0.0072) (Figures 5D, E). The AUCs of PFS and TFS are specifically depicted in Figures 5G, H. In univariate analysis, FPS high risk (*P*=0.001), Binet stage B or C (*P*=0.038), B symptoms (*P*=0.045), age>65 years (*P*=0.047), hemoglobin<100 g/L (*P*=0.002), β2-MG>3.5 mg/L (*P*=0.011), TP53 disruption (*P*=0.032), IGHV unmutated (*P*=0.001), and CLL International Prognosis Index (CLL-IPI) (*P*<0.001) were significantly correlated with inferior OS (Figure 6A). Furthermore, we put these factors into a Cox proportional hazards multivariate model. Because Binet stage, age, β2-MG, TP53 disruption, and unmutated IGHV were included in CLL-IPI, CLL-IPI, B symptoms, hemoglobin, and FPS were subsequently integrated to identify independent prognostic factors in the multivariate analysis. The results showed that only FPS (*P*=0.011) and CLL-IPI (*P*=0.010) were independent prognostic indicators for OS (Figure 6B).

## Construction and evaluation of nomogram models

Since FPS was an independent predictor in patients with CLL, we constructed a novel prognostic model that incorporated the FPS and CLL-IPI score. The nomogram model was used to predict 2-, 3-, and 5-year OS (Figure 6C). The C-index of the nomogram model was 0.903. As shown in Figures 6D–F, the calibration plots of the nomogram demonstrated acceptable consistency between the predicted survival rate and the actual survival rate at 2, 3, and 5 years, indicating that the nomogram model could reliably predict the prognosis of CLL patients to some degree.

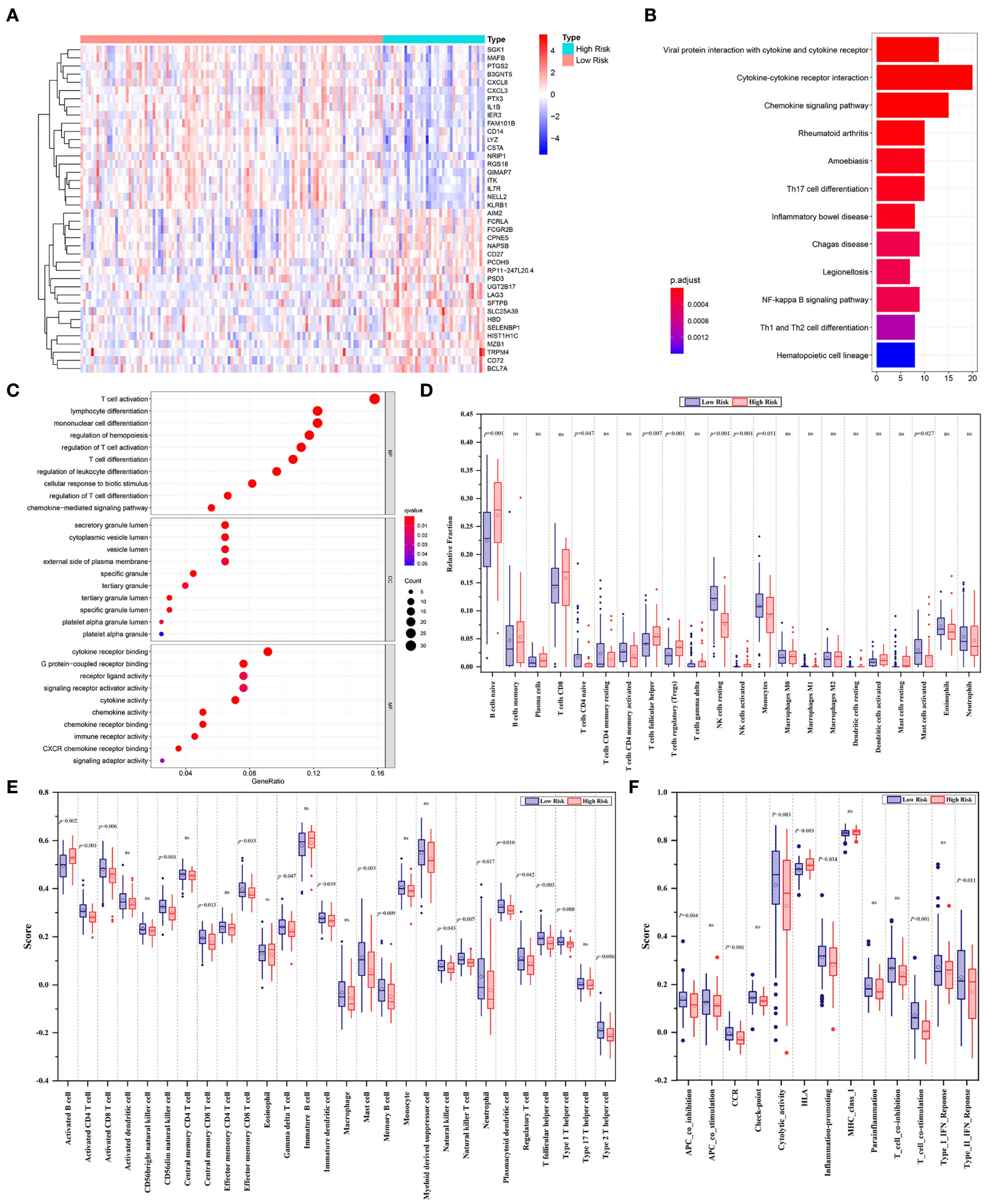

FIGURE 4
**(A)** The heatmap displaying the differentially expressed genes between the low- and high-risk groups. The representative results of KEGG pathways **(B)** and GO analysis **(C)** of DEGs between two groups. **(D)** Boxplots of the relative fraction of 22 immune cell types between two groups. **(E, F)** The score of immune cell types and immune-related functions using ssGSEA analysis, respectively. ns, no significance.

## Discussion

CLL is a highly heterogenous disease. Forty years ago, Rai and Binet risk stratifications were developed as risk score systems, and they have been used for decades. However, with the rapid progress of treatment, these staging systems became insufficient for clinical practice (20). Then, CLL-IPI was introduced (International CLL-IPI working group, 2016). It included TP53 gene mutation/deletion, IGHV mutation status, serum β2-MG, clinical stage, and age. However, the prognosis of some patients cannot be predicted precisely with CLL-IPI. The progression of disease is related to numerous biological parameters, and disease risk stratification remains a great challenge for hematologists.

Ferroptosis is a nonapoptotic form of cell death depending on iron metabolism that can inhibit tumor growth and increase chemotherapy sensitivity. It is widely reported to be associated

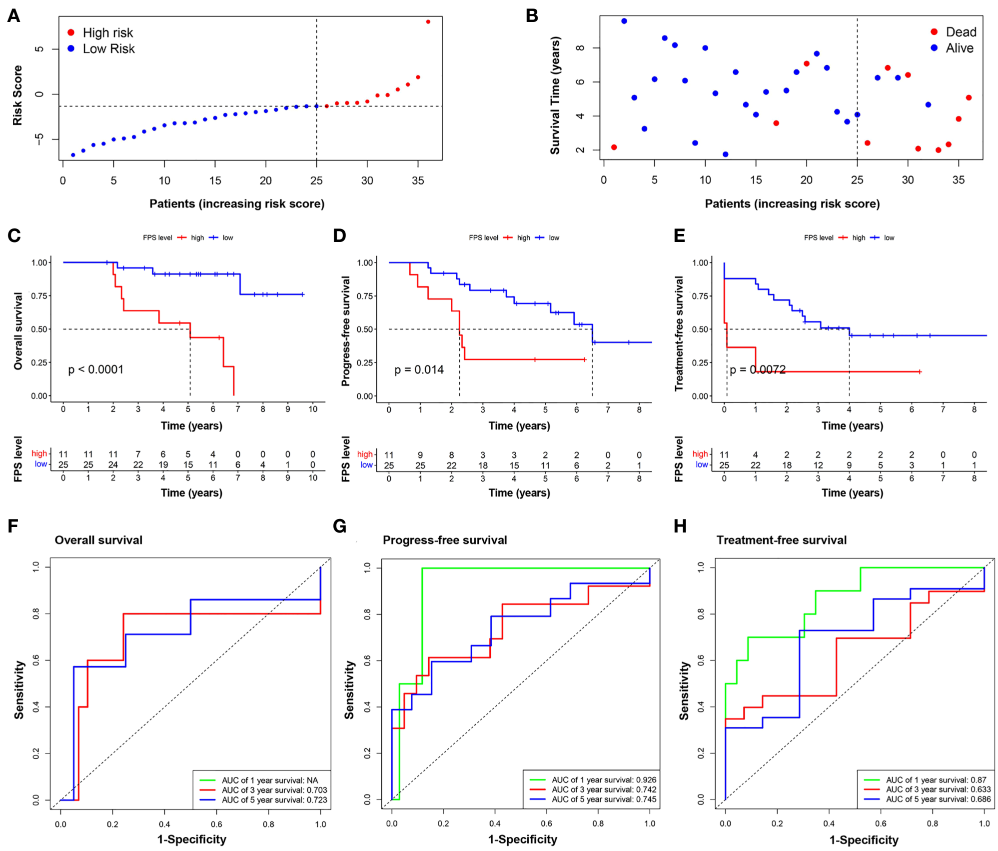

FIGURE 5
Validation of the nine-FRG signature prognostic model. **(A)** The distribution and the value of risk scores in the validation cohort. **(B)** The distributions of OS status, OS, and risk score. Kaplan–Meier survival curves for OS **(C)**, PFS **(D)**, and TFS **(E)** of CLL patients stratified by FPS risk score. Time-dependent ROC curves of the risk model for predicting the 1-, 3-, and 5-year OS **(F)**, PFS **(G)**, and TFS **(H)**.

with carcinogenesis and cancer prognosis (11, 13, 15). Many small molecular compounds have been proven to target iron metabolism and lipid peroxidation by inducing ferroptosis (21), but the prognostic significance and role of the mRNA expression of ferroptosis-related genes in CLL are currently unclear. In our study, a total of 10 differentially expressed FRGs with statistical prognostic significance were screened out. Interestingly, potential protein–protein interaction analysis indicated that p53 appeared to be the hub gene among the net of these FRGs. p53 is a well-known critical regulator in controlling cell proliferation and survival. Accumulating evidence has revealed that p53 plays an important role in regulating ferroptosis (22). Studies have shown that p53 may play a dual role in the control of ferroptosis, in which it could enhance and suppress it (22). In CLL, the aberration of p53 is frequently associated with disease progression and therapeutic resistance (23). Thus, a further understanding of the impact of p53 on ferroptosis in the context of CLL may provide new therapeutic avenues.

After minimizing the potential risk of overfitting, we established nine ferroptosis-related genes associated with CLL prognosis: AKR1C3, BECN1, CAV1, CDKN2A, CXCL2, JDP2, SIRT1, SLC1A5, and SP1. AKR1C3 is overexpressed in acute myeloid leukemia and T-cell acute lymphoblastic leukemia and confers chemotherapeutic resistance to anthracycline, which is the first-line agent for leukemia treatment (24). AKR1C3 and CXCL2 are ferroptosis-related genes associated with the immune microenvironment and prognosis in breast cancer (25). CXCL2 is a chemokine secreted by monocytes and macrophages and is chemotactic for polymorpho-nuclear leukocytes and hematopoietic stem cells. It is reported to be significantly upregulated in primary CLL patient plasma (26). The addition of CXCL2 enhances CLL cell survival. Chen reported that CXCL2 is a significant ferroptosis-related gene signature that can effectively classify DLBCL into different risk groups in terms of survival rate (14). Ferroptosis is a type of autophagy-dependent cell death. BECN1 influences the onset and progression of autophagy, and its recurrent allelic deletion and expression variation are reported in tumors (27). CAV1 is downregulated after treatment in APL patients and can be used as a potential marker (28). It can inhibit ferroptosis in

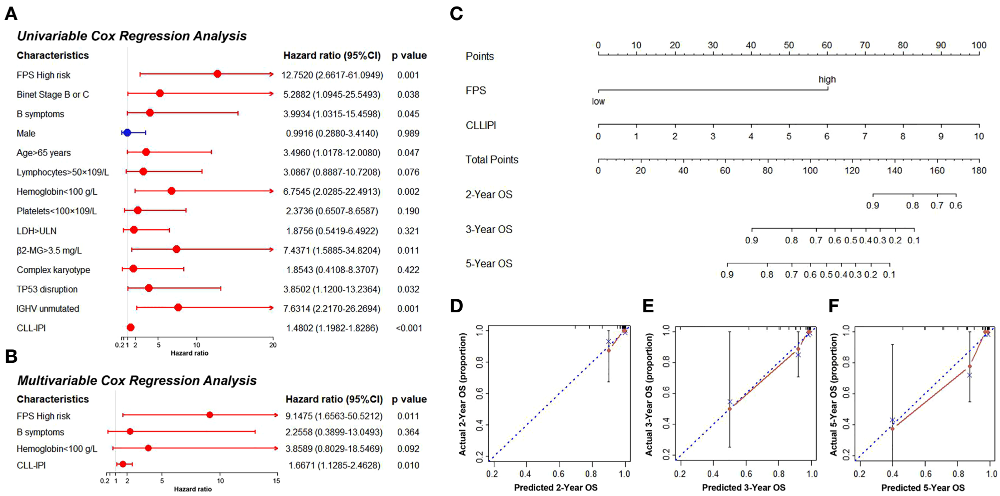


FIGURE 6
**(A, B)** The univariate and multivariate Cox regression model analyses for assessment of the prognostic value of clinical characteristics and PFS. **(C)** The nomogram model for predicting 2-, 3-, and 5-year OS rate of CLL patients. **(D–F)** The calibration plot analysis to assess the nomogram accuracy for OS prediction at 2, 3, and 5 years.

cancer cells and promote proliferation, migration, and invasion. CDKN2A genetic variation is associated with leukemia incidence and prognosis. CDKN2A and AKR1C1 were established as novel ferroptosis-related signatures that could effectively predict colorectal cancer prognosis (29). JDP2 was identified and validated to be a ferroptosis-related gene signature for predicting survival in cutaneous melanoma (30). SIRT1 and NK-κB are antagonistic in controlling inflammatory processes and energy metabolism (31). The SIRT1–autophagy axis inhibits excess iron-induced ferroptosis of foam cells and subsequently increases IL-1B and IL-18 (32). SLC1A5 is a novel prognostic biomarker that correlates with immune infiltrates in stomach adenocarcinoma *via* ferroptosis. The STAT3–MYC axis promotes the survival of leukemia stem cells by regulating SLC1A5 and oxidative phosphorylation (33). SP1 is reported to be a ferroptosis-related marker in gastric cancer (34). Li Lin showed that inhibiting SP1 could repress ferroptosis of endothelial cells and retard the occurrence of atherosclerosis (35). PKCβII overexpression is related to CLL and the pathogenesis of other B-cell malignancies. Ola-Al-Sanabra et al. first reported that SP1 is linked to this mechanism (36). In summary, AKR1C3, BECN1, CAV1, CDKN2A, CXCL2, JDP2, SIRT1, SLC1A5, and SP1 are related to both ferroptosis and cancer pathogenesis or progression in some way. However, more functional studies are needed to explore the detailed mechanism.

The nine-FRG signature prognostic model can divide the CLL population into high- and low-risk groups. Subsequently, gene function enrichment analysis was performed to reveal the potential mechanism between the two groups. We discovered that DEGs were involved in several pathways, including the IL17 signaling pathway, NK-κB signaling pathway, and regulation of immune system processes. IL 17 is a universal proinflammatory cytokine secreted by a variety of cells, including Th17 cells, innate lymphoid cells (ILCs), NK cells, and γδT cells (37). In CLL, the IL17 level was reported to be increased compared with normal controls and was associated with poor outcome (37). Recent studies have reported that the IL-17 signaling pathway may participate in iron metabolism (38). The NK-κB pathway plays an important role in signal transduction and cell metabolism, promoting proliferation and survival in B-cell malignancies. The NK-κB pathway is constitutively activated in CLL patients and contributes to the pathophysiology of the disease (39). Interestingly, the immunoregulation process, which consists of many cell types, such as B cells, T cells, NK cells, monocytes, and macrophages, is involved in iron metabolism and homeostasis (40). Bioinformatic studies in several cancers have shown that ferroptosis may be implicated in immune infiltrates and pathways (41–43). It has been confirmed that immunotherapy-activated CD8$^{+}$ T cells promote tumor ferroptosis (44). In our study, the high-risk group correlated with an impaired immune response, including low scores of activated CD4$^{+}$ T cells, activated CD8$^{+}$ T cells, and CD56 dim natural killer cells, as well as the decreased activity of APC costimulation, CCR, cytokine activity, T-cell costimulation, inflammation promotion, and type II IFN response. It is speculated that the poor prognostic survival outcomes of the high-risk group may be partially due to immunosuppression.

Our research has some limitations. Due to the less abundant data content of samples in the GEO databases, there was some bias. In addition, our validation cohort had only 36 cases. A prospective and well-designed clinical trial is needed to confirm our findings. Moreover, we also need more functional studies to explore the molecular mechanisms of the role of ferroptosis-related genes in CLL progression.

## Data availability statement

The data of our CLL samples presented in the study are deposited in the DRYAD repository at: https://doi.org/10.5061/dryad.z612jm6fp.

## Ethics statement

This study was reviewed and approved by the institutional review board of the First Affiliated Hospital of Nanjing Medical University. The patients/participants provided their written informed consent to participate in this study. Written informed consent was obtained from the individual(s) for the publication of any potentially identifiable images or data included in this article.

## Author contributions

BP performed data analysis and interpretation. BP and YL drafted the manuscript. YM, JW, ZX, and YX were responsible for RNAseq. HY, YK, XZ, JhL, and LW collected and assembled the clinical data. JyL provided the study design. JW and WX revised the manuscript. All authors contributed to the article and approved the submitted version.

## Funding

This work was supported by the National Natural Science Foundation of China (81770166, 81720108002, 81800192, 82100207); Jiangsu Province's Medical Elite Programme (ZDRCA2016022); Project of National Key Clinical Specialty, Jiangsu Provincial Special Program of Medical Science (BE2017751), and National Science and Technology Major Project (2018ZX09734007); Nature Science Foundation for Youths of Jiangsu Province (BK20171079, BK20210962); and Young Scholars Fostering Fund of the First Affiliated Hospital of Nanjing Medical University (PY2021026).

## Conflict of interest

The authors declare that the research was conducted in the absence of any commercial or financial relationships that could be construed as a potential conflict of interest.

## Publisher's note

All claims expressed in this article are solely those of the authors and do not necessarily represent those of their affiliated organizations, or those of the publisher, the editors and the reviewers. Any product that may be evaluated in this article, or claim that may be made by its manufacturer, is not guaranteed or endorsed by the publisher.

## Supplementary material

The Supplementary Material for this article can be found online at: https://www.frontiersin.org/articles/10.3389/fimmu.2022.962000/full#supplementary-material

## References

1. Rozman C, Montserrat E. Chronic lymphocytic leukemia. *N Engl J Med* (1995) 333(16):1052–7. doi: 10.1056/NEJM199510193331606

2. Hallek M. Chronic lymphocytic leukemia: 2020 update on diagnosis, risk stratification and treatment. *Am J Hematol* (2019) 94(11):1266–87. doi: 10.1002/ajh.25595

3. Nguyen PH, Niesen E, Hallek M. New roles for b cell receptor associated kinases: when the b cell is not the target. *Leukemia* (2019) 33(3):576–87. doi: 10.1038/s41375-018-0366-8

4. Hallek M. Signaling the end of chronic lymphocytic leukemia: new frontline treatment strategies. *Hematol Am Soc Hematol Educ Program* (2013) 2013:138–50. doi: 10.1182/asheducation-2013.1.138

5. Efremov DG, Gobessi S, Longo PG. Signaling pathways activated by antigen-receptor engagement in chronic lymphocytic leukemia b-cells. *Autoimmun Rev* (2007) 7(2):102–8. doi: 10.1016/j.autrev.2007.02.021

6. Stevenson FK, Krysov S, Davies AJ, Steele AJ. Packham G. *B-cell receptor Signaling chronic lymphocytic Leuk Blood* (2011) 118(16):4313–20. doi: 10.1182/blood-2011-06-338855

7. Wiestner A. Emerging role of kinase-targeted strategies in chronic lymphocytic leukemia. *Hematol Am Soc Hematol Educ Program* (2012) 2012:88–96. doi: 10.1182/asheducation.V2012.1.88.3801172

8. Hassannia B, Vandenabeele P, Vanden Berghe T. Targeting ferroptosis to iron out cancer. *Cancer Cell* (2019) 35(6):830–49. doi: 10.1016/j.ccell.2019.04.002

9. Dixon SJ, Lemberg KM, Lamprecht MR, Skouta R, Zaitsev EM, Gleason CE, et al. Ferroptosis: an iron-dependent form of nonapoptotic cell death. *Cell* (2012) 149(5):1060–72. doi: 10.1016/j.cell.2012.03.042

10. Xie Y, Hou W, Song X, Yu Y, Huang J, Sun X, et al. Ferroptosis: process and function. *Cell Death Differ* (2016) 23(3):369–79. doi: 10.1038/cdd.2015.158

11. Yu S, Jia J, Zheng J, Zhou Y, Jia D, Wang J. Recent progress of ferroptosis in lung diseases. *Front Cell Dev Biol* (2021) 9:789517. doi: 10.3389/fcell.2021.789517

12. Liu Y, Duan C, Dai R, Zeng Y. Ferroptosis-mediated crosstalk in the tumor microenvironment implicated in cancer progression and therapy. *Front Cell Dev Biol* (2021) 9:739392. doi: 10.3389/fcell.2021.739392

13. Zeng H, You C, Zhao L, Wang J, Ye X, Yang T, et al. Ferroptosis-associated classifier and indicator for prognostic prediction in cutaneous melanoma. *J Oncol* (2021) 2021:3658196. doi: 10.1155/2021/3658196

14. Chen H, He Y, Pan T, Zeng R, Li Y, Chen S, et al. Ferroptosis-related gene signature: A new method for personalized risk assessment in patients with diffuse Large b-cell lymphoma. *Pharmacogenomics Person Med* (2021) 14:609–19. doi: 10.2147/PGPM.S309846

15. Guo Q, Li L, Hou S, Yuan Z, Li C, Zhang W, et al. The role of iron in cancer progression. *Front Oncol* (2021) 11:778492. doi: 10.3389/fonc.2021.778492

16. Yang Y, Zhang ZJ, Wen Y, Xiong L, Huang YP, Wang YX, et al. Novel perspective in pancreatic cancer therapy: Targeting ferroptosis pathway. *World J Gastrointest Oncol* (2021) 13(11):1668–79. doi: 10.4251/wjgo.v13.i11.1668

17. Zaffaroni N, Beretta GL. Nanoparticles for ferroptosis therapy in cancer. *Pharmaceutics* (2021) 13(11):1785. doi: 10.3390/pharmaceutics13111785

18. Zhou N, Bao J. FerrDb: a manually curated resource for regulators and markers of ferroptosis and ferroptosis-disease associations. *Database J Biol Database Curation* (2020) 2020:2020:baaa021. doi: 10.1093/database/baaa021

19. Tibshirani R. The lasso method for variable selection in the cox model. *Stat Med* (1997) 16(4):385–95. doi: 10.1002/(SICI)1097-0258(19970228)16:4<385::AID-SIM380>3.0.CO;2-3

20. Pflug N, Bahlo J, Shanafelt TD, Eichhorst BF, Bergmann MA, Elter T, et al. Development of a comprehensive prognostic index for patients with chronic lymphocytic leukemia. *Blood* (2014) 124(1):49–62. doi: 10.1182/blood-2014-02-556399

21. Vangapandu HV, Alston B, Morse J, Ayres ML, Wierda WG, Keating MJ, et al. Biological and metabolic effects of IACS-010759, an OxPhos inhibitor, on chronic lymphocytic leukemia cells. *Oncotarget* (2018) 9(38):24980–91. doi: 10.18632/oncotarget.25166

22. Ji H, Wang W, Li X, Han X, Zhang X, Wang J, et al. p53: A double-edged sword in tumor ferroptosis. *Pharmacol Res* (2021) 117:106013. doi: 10.1016/j.phrs.2021.106013.

23. Kwok M, Agathanggelou A, Davies N, Stankovic T. Targeting the p53 pathway in CLL: State of the art and future perspectives. *Cancers* (2021) 13 (18):4681. doi: 10.3390/cancers13184681

24. Verma K, Zang T, Penning TM, Trippier PC. Potent and highly selective aldo-keto reductase 1C3 (AKR1C3) inhibitors act as chemotherapeutic potentiators in acute myeloid leukemia and T-cell acute lymphoblastic leukemia. *J Med Chem* (2019) 62(7):3590–616. doi: 10.1021/acs.jmedchem.9b00090

25. Zhang Z, Qiu X, Yan Y, Liang Q, Cai Y, Peng B, et al. Evaluation of ferroptosis-related gene AKR1C1 as a novel biomarker associated with the immune microenvironment and prognosis in breast cancer. *Int J Gen Med* (2021) 14:6189–200. doi: 10.2147/IJGM.S329031

26. Burgess M, Cheung C, Chambers L, Ravindranath K, Minhas G, Knop L, et al. CCL2 and CXCL2 enhance survival of primary chronic lymphocytic leukemia cells M *in vitro*. *Leuk Lymphoma* (2012) 53(10):1988–98. doi: 10.3109/10428194.2012.672735

27. Zhou B, Liu J, Kang R, Klionsky DJ, Kroemer G, Tang D. Ferroptosis is a type of autophagy-dependent cell death. *Semin Cancer Biol* (2020) 66:89–100. doi: 10.1016/j.semcancer.2019.03.002

28. Borutinskaitė V, Žučenka A, Vitkevičienė A, Stoškus M, Kaupinis A, Valius M, et al. Genetic and epigenetic signatures in acute promyelocytic leukemia treatment and molecular remission. *Front Genet* (2022) 13:821676. doi: 10.3389/fgene.2022.821676

29. Shao Y, Jia H, Huang L, Li S, Wang C, Aikemu B, et al. An original ferroptosis-related gene signature effectively predicts the prognosis and clinical status for colorectal cancer patients. *Front Oncol* (2021) 11:711776. doi: 10.3389/fonc.2021.711776

30. Ping S, Wang S, Zhao Y, He J, Li G, Li D, et al. Identification and validation of a ferroptosis-29 related gene signature for predicting survival in skin cutaneous melanoma. *Cancer Med* (2022). doi: 10.1002/cam4.4706

31. Kauppinen A, Suuronen T, Ojala J, Kaarniranta K, Salminen A. Antagonistic crosstalk between NF-κB and SIRT1 in the regulation of inflammation and metabolic disorders. *Cell Signal* (2013) 25(10):1939–48. doi: 10.1016/j.cellsig.2013.06.007

32. Su G, Yang W, Wang S, Geng C, Guan X. SIRT1-autophagy axis inhibits excess iron-induced ferroptosis of foam cells and subsequently increases IL-1β and IL-18. *Biochem Biophys Res Commun* (2021) 561:33–9. doi: 10.1016/j.bbrc.2021.05.011

33. Amaya ML, Inguva A, Pei S, Jones C, Krug A, Ye H, et al. The STAT3-MYC axis promotes survival of leukemia stem cells by regulating SLC1A5 and oxidative phosphorylation. *Blood* (2022) 139(4):584–96. doi: 10.1182/blood.2021013201

34. Shao Y, Jia H, Li S, Huang L, Aikemu B, Yang G, et al. Comprehensive analysis of ferroptosis-related markers for the clinical and biological value in gastric cancer. *Oxid Med Cell Longev* (2021) 2021:7007933. doi: 10.1155/2021/7007933

35. Li L, Wang H, Zhang J, Chen X, Zhang Z, Li Q. Effect of endothelial progenitor cell-derived extracellular vesicles on endothelial cell ferroptosis and atherosclerotic vascular endothelial injury. *Cell Death Discov* (2021) 7(1):235. doi: 10.1038/s41420-021-00610-0

36. Al-Sanabra O, Duckworth AD, Glenn MA, Brown BR, Angelillo P, Lee K, et al. Transcriptional mechanism of vascular endothelial growth factor-induced expression of protein kinase CβII in chronic lymphocytic leukaemia cells. *Sci Rep* (2017) 7:43228. doi: 10.1038/srep43228

37. Zhu F, McCaw L, Spaner DE, Gorczynski RM. Targeting the IL-17/IL-6 axis can alter growth of chronic lymphocytic leukemia *in vivo*/*in vitro*. *Leuk Res* (2018) 66:28–38. doi: 10.1016/j.leukres.2018.01.006

38. Tang B, Zhu J, Li J, Fan K, Gao Y, Cheng S, et al. The ferroptosis and iron-metabolism signature robustly predicts clinical diagnosis, prognosis and immune microenvironment for hepatocellular carcinoma. *Cell Commun Signaling CCS* (2020) 18(1):174. doi: 10.1186/s12964-020-00663-1

39. Mansouri L, Papakonstantinou N, Ntoufa S, Stamatopoulos K, Rosenquist R. NF-κB activation in chronic lymphocytic leukemia: A point of convergence of external triggers and intrinsic lesions. *Semin Cancer Biol* (2016) 39:40–8. doi: 10.1016/j.semcancer.2016.07.005

40. Xiong Y, Zhang Y, Xiong S, Williams-Villalobo AE. A glance of p53 functions in brain development, neural stem cells, and brain cancer. *Biology* (2020) 9(9):285. doi: 10.3390/biology9090285

41. Huang X, Zhou D, Ye X, Jin J. A novel ferroptosis-related gene signature can predict prognosis and influence immune microenvironment in acute myeloid leukemia. *Bosnian J Basic Med Sci* (2021) 22(4):608–28. doi: 10.17305/bjbms.2021.6274

42. He D, Liao S, Xiao L, Cai L, You M, He L, et al. Prognostic value of a ferroptosis-related gene signature in patients with head and neck squamous cell carcinoma. *Front Cell Dev Biol* (2021) 9:739011. doi: 10.3389/fcell.2021.739011

43. Liang JY, Wang DS, Lin HC, Chen XX, Yang H, Zheng Y, et al. A novel ferroptosis-related gene signature for overall survival prediction in patients with hepatocellular carcinoma. *Int J Biol Sci* (2020) 16(13):2430–41. doi: 10.7150/ijbs.45050

44. Wang W, Green M, Choi JE, Gijón M, Kennedy PD, Johnson JK, et al. CD8 (+) T cells regulate tumour ferroptosis during cancer immunotherapy. *Nature* (2019) 569(7755):270–4. doi: 10.1038/s41586-019-1170-y

frontiers | Frontiers in Immunology

TYPE Case Report
PUBLISHED 05 January 2023
DOI 10.3389/fimmu.2022.1052336



OPEN ACCESS

EDITED BY
Claudia Scotti,
University of Pavia, Italy

REVIEWED BY
Pouya Safarzadeh Kozani,
Guilan University of Medical Sciences, Iran
Pooria Safarzadeh Kozani,
Tarbiat Modares University, Iran
Xi Zhang,
Xinqiao Hospital, China

*CORRESPONDENCE
Erlie Jiang
jiangerlie@ihcams.ac.cn
Xin Chen
chenxin@ihcams.ac.cn

†These authors have contributed equally to this work

SPECIALTY SECTION
This article was submitted to Cancer Immunity and Immunotherapy, a section of the journal Frontiers in Immunology

RECEIVED 23 September 2022
ACCEPTED 28 November 2022
PUBLISHED 05 January 2023

CITATION
Cao Y, Liu Y, Zhang R, Zhai W, Ma Q, Wei J, Yang D, Pang A, He Y, Chen X, Jiang E, Feng S and Han M (2023) Cardiac involvement in a patient with B-cell lymphoblastic lymphoma/acute lymphoblastic leukemia and a history of allogeneic hematopoietic stem cell transplantation and CAR T-cell therapy: A case report. *Front. Immunol.* 13:1052336. doi: 10.3389/fimmu.2022.1052336



# Cardiac involvement in a patient with B-cell lymphoblastic lymphoma/acute lymphoblastic leukemia and a history of allogeneic hematopoietic stem cell transplantation and CAR T-cell therapy: A case report

Yigeng Cao[1†], Yadan Liu[2†], Rongli Zhang[1], Weihua Zhai[1], Qiaoling Ma[1], Jialin Wei[1], Donglin Yang[1], Aiming Pang[1], Yi He[1], Xin Chen[1*], Erlie Jiang[1*], Sizhou Feng[1] and Mingzhe Han[1]

[1]State Key Laboratory of Experimental Hematology, National Clinical Research Center for Blood Diseases, Haihe Laboratory of Cell Ecosystem, Institute of Hematology & Blood Diseases Hospital, Chinese Academy of Medical Sciences & Peking Union Medical College, Tianjin, China,
[2]Hematology Department of Ningbo First Hospital, Ningbo Clinical Research Center for Hematologic Malignancies, Ningbo, China

Cardiac involvement in hematological malignancies is uncommon, with only a few cases reported to date, and it often leads to a poor prognosis. Here, we report a case of a 42-year-old woman with a history of allogeneic hematopoietic stem cell transplantation (allo-HSCT) and anti-CD19 chimeric antigen receptor (CAR) T-cell therapy for B-cell lymphoblastic lymphoma/acute lymphoblastic leukemia in whom cardiac mass and myocardial infiltration were detected. Prior to this presentation, massive pericardial effusion had occurred 6 months after CAR T-cell therapy, which was improved *via* ultrasound-guided pericardiocentesis. We observed elevated cytokine levels and increased copy number of CAR DNA in both pericardial effusion and serum. Upon detecting cardiac mass and myocardial infiltration, the patient was administered tocilizumab (a humanized monoclonal antibody against IL-6 receptor), which controlled the serum cytokine levels, and reduced intensity chemotherapy, including vindesine, cyclophosphamide, and prednisolone. However, the patient finally died of multiple organ failure. To the best of our knowledge, this is the first report on the development of a cardiac mass and occurrence of myocardial infiltration after allo-HSCT and CAR T-cell therapy. This report may provide supporting data for the early diagnosis and immediate treatment of patients with cardiac involvement.

KEYWORDS

**B cell acute lymphoblastic leukemia, B cell lymphoblastic lymphoma, allogeneic hematopoietic stem cell transplantation, chimeric antigen receptor T cells, cardiac involvement**

## Introduction

B-cell acute lymphoblastic leukemia (B-ALL) and B-cell lymphoblastic lymphoma (B-LBL) are precursor lymphoid neoplasms of the B lineage, which are considered to be the same disease with different developmental stages and clinical manifestations (1). According to version 1.2016 of the NCCN, less than 20% bone marrow involvement can be used as a diagnostic criterion to distinguish LBL from ALL. B-LBL is a highly malignant non-Hodgkin's lymphoma that commonly occurs in children and adolescents. The most common occurrence sites of B-LBL are the skin, soft tissue, bone, and lymph nodes, while mediastinal or pleural involvement is rare and cardiac involvement is even rarer (2). Some studies have shown that cardiac involvement is common in secondary and malignant tumors through hematogenous metastasis, lymphatic metastasis, transvenous extension, and direct infiltration of tissues surrounding the neoplasms and that lymphoma and leukemia are the most common hematological malignancies involving the heart (3–5). The heart is hidden in the mediastinum, and there are no specific clinical manifestations of cardiac involvement, which can easily lead to misdiagnosis or missed diagnosis relatively easy in patients with cardiac metastasis.

Allogeneic hematopoietic stem cell transplantation (allo-HSCT) is currently the only available methodology to treat B-LBL, and it has been shown to greatly improve the long-term survival of patients (6). However, it is difficult to obtain a complete response (CR) or partial response (PR) in patients with B-ALL who show relapse after transplantation, and these patients exhibit an extremely poor prognosis (7). Chimeric antigen receptor (CAR) T-cell therapy is an emerging cellular immunotherapy and has revolutionized treatment modalities for relapsed or refractory B-ALL (R/R B-ALL) with a CR rate of 70%–90% (8, 9). It has thus significantly prolonged the disease-free survival of such patients (10, 11). Here, we present a case of a 42-year-old woman with an initial diagnosis of B-LBL who developed cardiac involvement after allo-HSCT and anti-CD19 CAR T-cell therapy. To the best of our knowledge, no systematic studies on the efficacy and safety of various treatments for cardiac involvement exist. This report provides relevant data for identifying cardiac involvement and selecting an appropriate treatment.

## Case presentation

A 42-year-old woman with a history of B-LBL was admitted to the Institute of Hematology and Blood Diseases Hospital, Tianjin, China, because of persistent dyspnea. In May 2019, the patient was evaluated at another hospital for recurrent pain in her right hip, which had begun 6 months earlier and gradually worsened with no obvious predisposing causes. PET-CT scans revealed multiple high-density nodules in both the kidneys, left acetabulum, left ilium, bilateral tibia, and right fibula as well as intense FDG uptake by these nodules. Immunohistochemical (IHC) analysis of a left kidney biopsy specimen indicated positivity for CD10, TdT, CD79a, Pax-5, CD43, c-myc (20%), and Ki-67 (90%) and negativity for CD3, CD20, CD5, CD23, Bcl-2, Bcl-6, MUM1, and CyclinD1. Neither bone marrow smear nor flow cytometry revealed any abnormal lymphocytes, and bone marrow biopsy revealed active proliferation of the hematopoietic tissue. Cytogenetic analysis revealed an abnormal karyotype: 46,XX,t(1,19)(q23;p13),-4,+mar[18]/46, XX(2). Gene fusion analysis showed positivity for E2A/PBX1. These findings led to the diagnosis of B-LBL with E2A/PBX1.

The patient had received two cycles of induction chemotherapy with a combination of cyclophosphamide, vincristine, doxorubicin, dexamethasone (hyper-CVAD A), methotrexate, and cytarabine (hyper-CVAD B). Bone marrow examination revealed 10% blasts, while PET-CT revealed no intense FDG uptake. Subsequently, the patient received vindesine, daunorubicin, cyclophosphamide, pegaspargase, prednisone (VDCLP), cyclophosphamide, cytarabine, 6-mercaptopurine (CAM), vindesine, cyclophosphamide, idarubicin, dexamethasone (VICD). Every bone marrow smear after each chemotherapy showed CR, while E2A/PBX1 was undetectable, 3.68% and 0.22% as determined *via* polymerase chain reaction, respectively.

The patient remained well for 3 months. In May 2020, bone marrow smear revealed 47% lymphoblasts, while the rate of E2A/PBX1 rearrangement was 45.55%. Lymphoblasts accounted for 4.96% of the marrow cellularity, as determined using flow cytometry. These results suggested a diagnosis of B-ALL with E2A/PBX1 expression. Treatment with orally administered 6-mercaptopurine and prednisone was initiated to relieve the tumor burden.

In June 2020, the patient underwent allo-HSCT from a matched, sibling donor after a conditioning regimen with cyclophosphamide, fludarabine, idarubicin, and antithymocyte globulin and total body irradiation. Early post-transplantation complications included mild diarrhea and mucositis. The bone marrow smear indicated CR, no E2A/PBX1 amplification, and full donor chimerism. PET-CT revealed that the treatment was effective and that the CR of the disease was achieved, with a Deauville score of 1 point.

In September 2020, the patient complained of left breast pain that had begun 1 week earlier. Breast ultrasound showed multiple nodules in the left breast, while IHC of a left breast biopsy specimen indicated extramedullary recurrence of B-ALL after transplantation. Neither bone marrow aspirate nor flow cytometry showed any abnormal blasts, while E2A/PBX1 was undetectable. PET-CT revealed progressive disease, with a maximum standard uptake value ($SUV_{max}$) of 23.0 and a Deauville score of 5 points (Figure 1A). Then, the administration of decitabine, fludarabine, cytarabine, and granulocyte colony-stimulating factor was initiated. Acute graft-versus-host-disease of the skin occurred after donor lymphocyte infusion. Eventually, the breast nodules decreased in size, and PET-CT revealed PR of the disease, with a Deauville score of 4 points.

In November 2020, the patient underwent donor-derived anti-CD19 CAR T-cell infusion after a conditioning regimen with fludarabine and cyclophosphamide. The sequence of CD19 CAR consists of an anti-CD19 single-chain antibody fragment (FMC63), CD28 transmembrane domain, 4-1BB, CD3zeta, T2A autocleavage sequences, and endodomain-deleted EGFR (tEGFR) (12). Four days later, the patient had a recurrent high fever with a temperature of 40°C, along with lethargy and vomiting. Based on a previous study, a grade-2 cytokine release syndrome (CRS) was identified (13). These clinical issues improved after providing supportive care with antibiotics (meropenem and caspofungin) and dexamethasone. Meanwhile, no clear etiological evidence with next-generation sequencing (NGS) or blood culture was obtained. The patient achieved CR and was negative for minimal residual disease on the 14th day after CAR T-cell therapy and remained well for 5 months.

In May 2021, the patient complained of chest pain that worsened when the patient breathed in or lay flat. Electrocardiogram (ECG) and myocardial enzyme levels were normal. Echocardiography (Echo) revealed massive pericardial effusion with rapid progression to cardiac tamponade. Ultrasound-guided pericardiocentesis, which was performed to alleviate the clinical symptoms and drain the excess fluid around the heart, revealed the presence of a hemorrhagic and exudative liquid. Multiple diagnostic tests for pericardial effusion, including bacterial gram staining, bacterial culture, fungal culture, acid fast bacteria staining, tuberculosis (TB) antibody examination, biopsy, and NGS, were performed. The results of all the above mentioned tests were negative. Flow cytometry of pericardial effusion and bone marrow aspirate did not reveal any tumor cells or CAR T cells. However, quantitative real-time polymerase chain reaction (qPCR) revealed that the copy number of CAR DNA per microgram of genome was $1.92 \times 10^1$. The results of additional laboratory tests, including those of cytokines, are shown in Table 1. Given that some cytokines of the pericardial fluid were notably increased, CRS was considered as the possible cause of pericardial effusion. The pericardial effusion was gradually reduced and removed after immunosuppressive therapy with methylprednisolone and rucotinib. Bone marrow aspirate and PET-CT showed CR, with a Deauville score of 1 point.

On presentation to our hospital (November 2021), the patient complained of dyspnea and fatigue that had begun 2 weeks earlier. The patient's medical history included hypertension. However, the patient did not need to take medications on a regular basis to control it under the guidance of a cardiologist. Immunosuppressive therapy with rucotinib and dexamethasone and preventive fungal treatment with orally administered posaconazole were continued. There were no known drug allergies. The patient lived with her husband and one child in rural China. The patient had previously worked as a farmer and did not smoke or drink.

On examination, the patient's temperature was 36.6°C, her heart rate was 104 beats per minute, blood pressure was 94/68 mmHg, respiratory rate was 25 breaths per minute, and oxygen saturation was 93% while the patient breathed ambient air. Severe edema of the limbs was identified, while the results of the remaining examinations were normal. The copy number of cytomegalovirus (CMV) was 8,953 per milliliter (reference range: <1,000). Other laboratory test results are shown in Table 2. ECG revealed changes in the ST segment, and Echo revealed that the left ventricular ejection fraction (LVEF) had decreased to 49%. The level of serum cytokines was significantly increased (Figure 2A). Chest CT revealed interstitial inflammation of both lungs.

The patient received diuretic, albumin infusion, antiviral with ganciclovir, and supportive treatments. As part of CAR T-cell therapy, tocilizumab was administered to control elevated serum cytokine levels. Clinical symptoms were slightly improved within 1 week of admission. Notably, the level of cardiac troponin I (cTNI) was elevated prior to the administration of tocilizumab.

On the 12th day after presentation, PET-CT of the body and head was performed, which showed cardiac involvement and abnormal uptake in the liver (Figures 1B, C). Bone marrow aspirate and cytogenetic analysis were normal, while flow cytometry revealed lymphoblasts that accounted for 0.15% of the marrow cellularity. E2A/PBX1 rearrangement was also positive. The results of CAR T cells are shown in Figure 2B. A cardiac mass biopsy was needed to achieve the pathological diagnosis but was not performed due to the patient's poor physical condition.

Owing to her poor physical condition, the patient was finally administered a reduced intensity chemotherapy with cyclophosphamide, vindesine, and prednisolone (VCP). Nevertheless, on the third day of chemotherapy, her blood pressure and oxygen saturation suddenly dropped to 61/29 mmHg and 76%, respectively. Along with a heart rate of 170 beats per minute, moist rales could be heard at the base of the left lung. ECG revealed tachycardia, ST-segment depression, and inverted T waves in the V2–6 leads. Although timely first-aid measures were provided, the patient could not be rescued and was eventually discharged from the hospital. The clinical course of the patient is shown in Figure 3.

## Discussion

Cardiac involvement is rare in patients with B-LBL/B-ALL, with only a few cases having been reported in the literature. It thus remains unclear how to identify cardiac involvement quickly and provide effective therapies. Some summative studies have demonstrated that cardiac metastases are detected

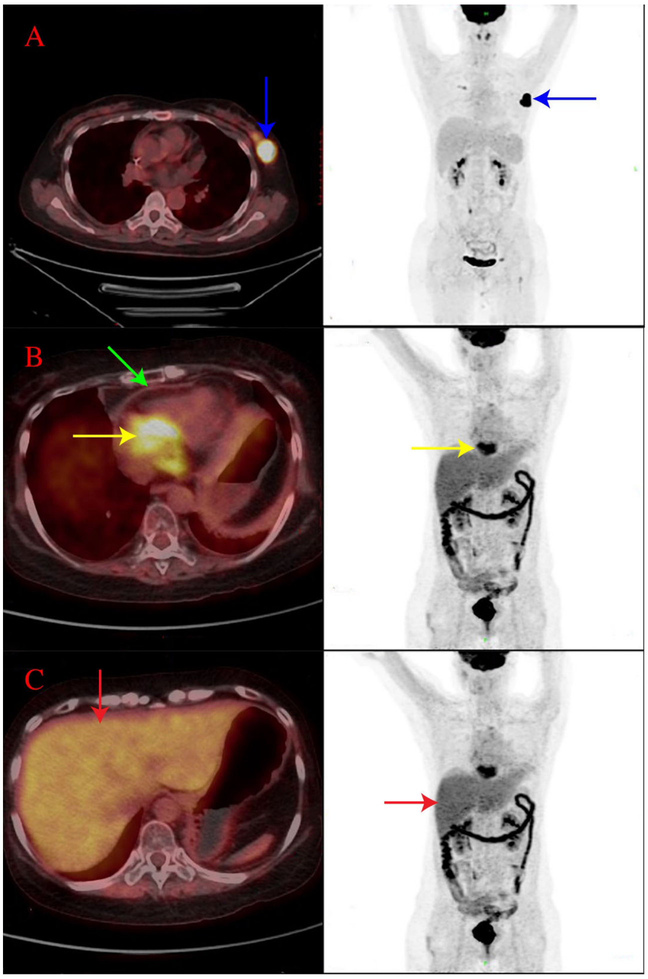


FIGURE 1
PET-CT findings of the patient. **(A)** In September 2020, there was an irregular soft tissue mass in the upper outer quadrant of the breast (4.1 × 2.0 cm), with an $SUV_{max}$ of 23.0, as shown by the blue arrow. **(B)** In November 2021, there were a cardiac mass (6.0 × 4.4 cm), with an $SUV_{max}$ of 10.5, as shown by the yellow arrow and a diffusely thickened pericardium, with an $SUV_{max}$ of 2.0, as shown by the green arrow. **(C)** In November 2021, there was an abnormal uptake in the liver, with an $SUV_{max}$ of 5.0 and a Deauville score of 5 points, as shown by the red arrow.

in many cases at the time of postmortem (4, 5). Given the rarity of performing postmortems, only a few cases of cardiac involvement have been reported. We reviewed recent clinical cases with cardiac involvement and identified some common clinical manifestations (14–16). First, patients with cardiac involvement mostly presented non-specific symptoms, such as chest pain, dyspnea, and edema. Second, non-invasive imaging techniques, such as ECG, Echo, enhanced CT, cardiac magnetic resonance (CMR), and PET-CT, generally produced abnormal images, and PET-CT appears to have a diagnostic value in differentiating benign and malignant cardiac tumors and predicting prognosis, especially for cardiac metastases and lymphoma (17–19). Infiltration of leukemia cells into the myocardium may lead to cardiac conduction system

TABLE 1 Cytokines in pericardial effusion and peripheral blood.

| Cytokines (pg/ml) | IL-6 | IL-8 | IL-10 | IL-17 | IL-12P70 | TNF-α | IFN-γ |
|---|---|---|---|---|---|---|---|
| Pericardial effusion | 35,742.86 | 1,514.66 | 122.41 | 0.36 | 3.71 | 7.76 | 8.74 |
| Peripheral blood | 8.22 | 12.9 | 5.03 | 37.35 | 8.62 | 12.68 | 7.55 |

IL, interleukin; TNF-α, tumor necrosis factor-α; IFN-γ, interferon-γ.

TABLE 2 Patient characteristics on admission.

**Laboratory data[a]**

| Variable | On presentation | Reference rangeThis hospital[b] |
|---|---|---|
| White cell count (per µl) | 1,640 | 4,000–10,000 |
| Differential count (per µl) | | |
| Neutrophils | 1,430 | 2,000–7,000 |
| Lymphocytes | 170 | 800–4,000 |
| Monocytes | 40 | 120–1,000 |
| Eosinophils | 0 | 20–500 |
| Basophils | 0 | 0–100 |
| Hemoglobin (g/L) | 77 | 110–150 |
| Platelet count (per µl) | 22,000 | 100,000–300,000 |
| Hematocrit (%) | 23.7 | 37–48 |
| Total protein (g/dl) | 5.23 | 6.6–8.3 |
| Albumin (g/dl) | 3.14 | 3.5–5.2 |
| Globulin (g/dl) | 2.09 | 2.0–3.5 |
| Aspartate aminotransferase (U/L) | 48.70 | 0–35 |
| Alanine aminotransferase (U/L) | 60.30 | 0–35 |
| Alkaline phosphatase (U/L) | 176.30 | 30–120 |
| Glutamyl transpeptidase (U/L) | 291.80 | 8–57 |
| Lactate dehydrogenase (U/L) | 1,150.20 | 0–248 |
| Total bilirubin (mg/dl) | 0.9 | 0–1 |
| Creatinine (mg/dl) | 0.75 | 0.55–1.0 |
| Cardiac troponin I (ng/ml) | 0.059 | <0.04 |
| Creatine kinase isoenzyme-MB (ng/ml) | 7.5 | 0.5–5.0 |
| B-type natriuretic peptide (pg/ml) | 352 | 0–100 |

[a]To convert the values for bilirubin to micromoles per liter, multiply by 17.1. To convert the values for creatinine to micromoles per liter, multiply by 88.4.
[b]Reference values are affected by many variables, including the patient population and the laboratory methods used. They may therefore not be appropriate for all patients.

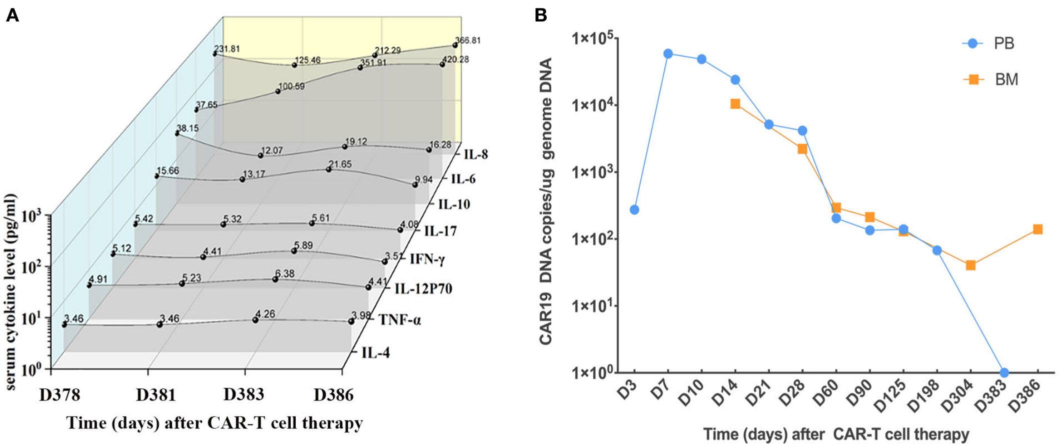


FIGURE 2
Serum cytokines and CAR19 DNA. **(A)** Serum cytokines of the patient during CAR T-cell therapy since admission. **(B)** CAR19 DNA in PB and BM since CAR T-cell therapy.

abnormalities and rhythmic disturbances (20, 21), which mainly included non-specific ST–T wave changes and atrial arrhythmias. Although CMR and PET-CT are not always available, detection of cardiac involvement has benefited from the development of imaging technology in recent years. Unfortunately, the Echo and CT of this patient did not provide adequate imaging evidence of relapse.

For most metastatic cardiac tumors, surgery is not suitable, whereas surgery is a treatment option in case of primary cardiac tumors. Radiation therapy and chemotherapy have been routinely used to treat patients with cardiac metastases (3, 22). In a report by Kakefuda et al., a 61-year-old woman with B-ALL who received hyper-CVAD chemotherapy due to a cardiac mass finally achieved clinical remission (16). In addition, Manabe et al. reported that a 17-year-old patient with B-LBL with an intracardiac mass and myocardial infiltration underwent autologous peripheral blood stem cell transplantation after intensive chemotherapy and finally achieved long-term remission for over 5 years (15). Kahwash et al. reported that a 51-year-old patient with B-ALL with an infiltrative cardiac mass treated with palliative chest radiation ultimately died (14). The case presented in the current study had clinical symptoms similar to those of the above cases but a completely different course of disease progression. Thus, the treatment strategy for this patient differed slightly from those reported previously; this patient was administered tocilizumab and chemotherapy.

In the present study, we report a case of massive pericardial effusion close to tamponade, which occurred 6 months after CAR T treatment, and did not find common infectious causes of pericardial effusion, such as viruses, bacteria, fungi, and parasites, and non-infectious causes, including systemic inflammatory diseases, metabolic diseases, and drug-related factors, were also not considered (23). Although we found CAR DNA copies and abnormal increases in cytokines in pericardial effusion, no tumor cells or masses were found using flow cytometry or CT. The reason behind the occurrence of pericardial effusion remained unknown at the time. However, on reviewing the disease course of the patient, we speculated that the patient may have already had cardiac involvement during pericardial effusion. The main reasons why malignant cells were not detected in the pericardial effusion sample were the small number of leukemia cells and the powerful ability of CAR T cells to target and kill leukemia cells. In addition, the bloody pericardial effusion also supported our speculation of tumor invasion because inflammatory effusions are mostly green or yellow-green. CAR DNA data showed the persistence of CD19 CAR T cells in the patient, and CAR T cell consistently played a role of immunologic surveillance. Nevertheless, when leukemia cells invade the heart again, CAR T cells cannot exert a strong antileukemia effect as before, and the process of infiltration is accelerated to eventually form a cardiac mass owing to the decreased ability of CAR T-cell expansion.

CRS and immune effector cell-associated neurotoxicity syndrome (ICANS) are frequently reported due to the unique and life-threatening toxicity associated with CAR T-cell therapy. The mechanisms of CRS and ICANS have been explored in detail (24, 25). However, cardiovascular (CV) events caused by CAR T-cell therapy have not been explored much, but CV should also be taken seriously with limited data (26, 27). Patients treated with CAR T-cell therapy experienced arrhythmias, decompensated heart failure, and CV-related death. Seventeen patients had a CV event about 21 days after

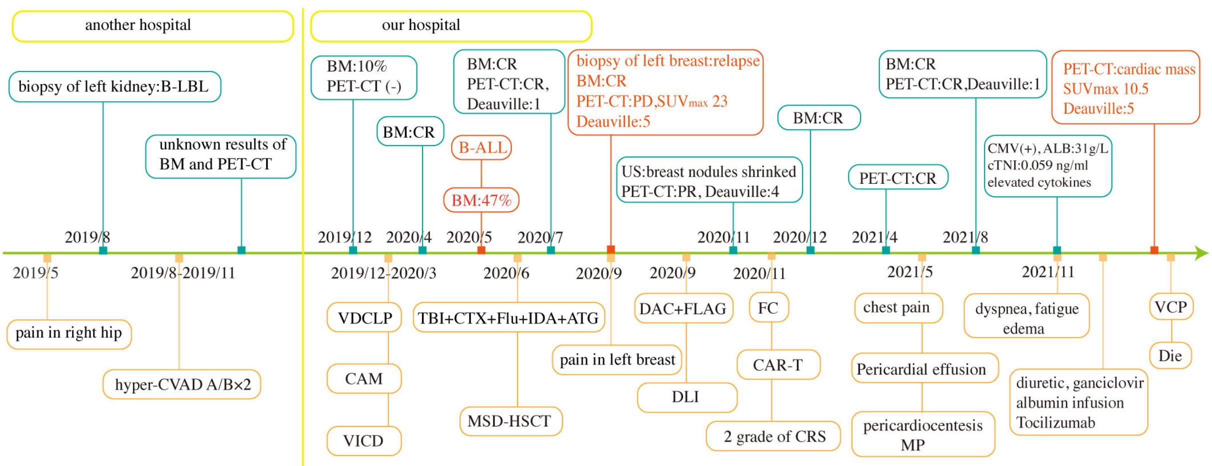


FIGURE 3
Clinical course of the patient. TBI+CTX+Flu+IDA+ATG, total body irradiation, cyclophosphamide, fludarabine, idarubicin, and antithymocyte globulin. BM, bone marrow aspirate; US, ultrasound; MP, methylprednisolone.

CAR T-cell therapy, six patients died from CV-related causes, six had decompensated heart failure, five had a new arrhythmia, and some patients showed decreased LVEF after CAR T treatment. A high grade of CRS (grade ≥2) can increase the incidence of CV events, and an elevated troponin level has been reported as a common clinical event associated with CRS in patients receiving CAR T-cell therapy, which has an evident relationship with CV events (26). Our patient showed abnormal elevations in cTNI and myocardial enzyme levels on the first day of hospitalization, which needed to be differentiated from myocarditis and acute coronary syndrome. However, we surprisingly found that cTNI began to decrease with the administration of tocilizumab, so we believed that the initial elevation of cTNI in this patient was mostly due to CRS associated with CV events rather than leukemia infiltration-induced myocardial injury. Further studies on the mechanism of TNI and CRS are needed.

## Conclusions

To the best of our knowledge, this is the first report of cardiac involvement as an extramedullary manifestation of relapse in a patient with B-LBL/B-ALL treated with allo-HSCT and CAR T-cell therapy. Notably, pericardial effusion may be the first presentation of the underlying relapse of malignancy; hence, diagnostic testing should not be stopped after determining the cytology of pericardial effusion in patients exhibiting CRS after CAR T-cell therapy. The possibility of cardiac involvement needs to be considered in time. Furthermore, simultaneous elevations in serum cytokines and TNI should be considered to distinguish CV associated with CRS from cardiac involvement. There is a need to accumulate more number of clinical cases of cardiac involvement to rapidly identify authentic causes of atypical clinical symptoms. We hope that our experience deepens the understanding of clinicians regarding cardiac involvement in patients with B-BLB/B-ALL who have undergone allo-HSCT and CAR T-cell therapy.

## Data availability statement

The original contributions presented in the study are included in the article/supplementary material. Further inquiries can be directed to the corresponding authors.

## Ethics statement

Written informed consent was obtained from the individual (s) for the publication of any potentially identifiable images or data included in this article.

## Author contributions

YL, YC, and XC were involved in the care of the patient. YL obtained the clinical data and wrote the manuscript. YC, RZ, WZ, QM, AP, DY, YH, and JW reviewed the data. EJ, MH, and SF supervised the entire study. All authors contributed to the article and approved the submitted version.

## Conflict of interest

The authors declare that the research was conducted in the absence of any commercial or financial relationships that could be construed as a potential conflict of interest.

## Publisher's note

All claims expressed in this article are solely those of the authors and do not necessarily represent those of their affiliated organizations, or those of the publisher, the editors and the reviewers. Any product that may be evaluated in this article, or claim that may be made by its manufacturer, is not guaranteed or endorsed by the publisher.

## References


1. Arber DA, Orazi A, Hasserjian R, Thiele J, Borowitz MJ, Le Beau MM, et al. The 2016 revision to the world health organization classification of myeloid neoplasms and acute leukemia. *Blood* (2016) 127(20):2391–405. doi: 10.1182/blood-2016-03-643544

2. Burkhardt B, Hermiston ML. Lymphoblastic lymphoma in children and adolescents: Review of current challenges and future opportunities. *Br J Haematol* (2019) 185(6):1158–70. doi: 10.1111/bjh.15793

3. Goldberg AD, Blankstein R, Padera RF. Tumors metastatic to the heart. *Circulation* (2013) 128(16):1790–4. doi: 10.1161/circulationaha.112.000790

4. Bussani R, De-Giorgio F, Abbate A, Silvestri F. Cardiac metastases. *J Clin Pathol* (2007) 60(1):27–34. doi: 10.1136/jcp.2005.035105

5. Butany J, Leong SW, Carmichael K, Komeda M. A 30-year analysis of cardiac neoplasms at autopsy. *Can J Cardiol* (2005) 21(8):675–80.

6. D'Souza A, Fretham C, Lee SJ, Arora M, Brunner J, Chhabra S, et al. Current use of and trends in hematopoietic cell transplantation in the united states. *Biol Blood Marrow Transplant* (2020) 26(8):e177–e82. doi: 10.1016/j.bbmt.2020.04.013

7. Zhang M, Huang H. How to combine the two landmark treatment methods-allogeneic hematopoietic stem cell transplantation and chimeric antigen receptor T cell therapy together to cure high-risk b cell acute lymphoblastic leukemia? *Front Immunol* (2020) 11:611710. doi: 10.3389/fimmu.2020.611710

8. Maude SL, Frey N, Shaw PA, Aplenc R, Barrett DM, Bunin NJ, et al. Chimeric antigen receptor T cells for sustained remissions in leukemia. *N Engl J Med* (2014) 371(16):1507–17. doi: 10.1056/NEJMoa1407222

9. DasGupta RK, Marini BL, Rudoni J, Perissinotti AJ. A review of Cd19-targeted immunotherapies for relapsed or refractory acute lymphoblastic leukemia. *J Oncol Pharm Pract* (2018) 24(6):453–67. doi: 10.1177/1078155217713363

10. Cordeiro A, Bezerra ED, Hirayama AV, Hill JA, Wu QV, Voutsinas J, et al. Late events after treatment with Cd19-targeted chimeric antigen receptor modified T cells. *Biol Blood Marrow Transplant* (2020) 26(1):26–33. doi: 10.1016/j.bbmt.2019.08.003

11. Gardner RA, Finney O, Annesley C, Brakke H, Summers C, Leger K, et al. Intent-to-Treat leukemia remission by Cd19 car T cells of defined formulation and

dose in children and young adults. *Blood* (2017) 129(25):3322–31. doi: 10.1182/blood-2017-02-769208

12. Ma F, Ho JY, Du H, Xuan F, Wu X, Wang Q, et al. Evidence of long-lasting anti-Cd19 activity of engrafted Cd19 chimeric antigen receptor-modified T cells in a phase I study targeting pediatrics with acute lymphoblastic leukemia. *Hematol Oncol* (2019) 37(5):601–8. doi: 10.1002/hon.2672

13. Lee DW, Santomasso BD, Locke FL, Ghobadi A, Turtle CJ, Brudno JN, et al. Astct consensus grading for cytokine release syndrome and neurologic toxicity associated with immune effector cells. *Biol Blood Marrow Transplant* (2019) 25 (4):625–38. doi: 10.1016/j.bbmt.2018.12.758

14. Kahwash R, Rugg SS, Smith MD. Relapsing b-cell lymphoblastic leukemia in an adult presenting as an infiltrative cardiac mass with tamponade. *J Am Soc Echocardiogr* (2007) 20(11):1319 e1–2. doi: 10.1016/j.echo.2007.04.011

15. Manabe M, Yoshii Y, Mukai S, Sakamoto E, Kanashima H, Nakao T, et al. Precursor b-lymphoblastic lymphoma involving an intracardiac mass and myocardial infiltration: A case report. *Intern Med* (2012) 51(3):315–9. doi: 10.2169/internalmedicine.51.6075

16. Kakefuda Y, Sato A, Hoshi T, Ishizu T, Tada H, Satomi K, et al. Isolated cardiac involvement of b-cell acute lymphoblastic leukemia mimicking acute myocardial infarction with persistent broad St-segment elevation. *Circulation* (2012) 125(22):e979–82. doi: 10.1161/CIRCULATIONAHA.111.050930

17. Meng J, Zhao H, Liu Y, Chen D, Hacker M, Wei Y, et al. Assessment of cardiac tumors by (18)F-fdg Pet/Ct imaging: Histological correlation and clinical outcomes. *J Nucl Cardiol* (2021) 28(5):2233–43. doi: 10.1007/s12350-019-02022-1

18. Shao D, Wang SX, Liang CH, Gao Q. Differentiation of malignant from benign heart and pericardial lesions using positron emission tomography and computed tomography. *J Nucl Cardiol* (2011) 18(4):668–77. doi: 10.1007/s12350-011-9398-4

19. Rahbar K, Seifarth H, Schäfers M, Stegger L, Hoffmeier A, Spieker T, et al. Differentiation of malignant and benign cardiac tumors using 18f-fdg Pet/Ct. *J Nucl Med* (2012) 53(6):856–63. doi: 10.2967/jnumed.111.095364

20. Roberts WC, Bodey GP, Wertlake PT. The heart in acute leukemia. a study of 420 autopsy cases. *Am J Cardiol* (1968) 21(3):388–412. doi: 10.1016/0002-9149(68)90143-4

21. Cates CU, Virmani R, Vaughn WK, Robertson RM. Electrocardiographic markers of cardiac metastasis. *Am Heart J* (1986) 112(6):1297–303. doi: 10.1016/0002-8703(86)90363-7

22. Bruce CJ. Cardiac tumours: Diagnosis and management. *Heart* (2011) 97 (2):151–60. doi: 10.1136/hrt.2009.186320

23. Imazio M, Adler Y. Management of pericardial effusion. *Eur Heart J* (2013) 34(16):1186–97. doi: 10.1093/eurheartj/ehs372

24. Karschnia P, Jordan JT, Forst DA, Arrillaga-Romany IC, Batchelor TT, Baehring JM, et al. Clinical presentation, management, and biomarkers of neurotoxicity after adoptive immunotherapy with car T cells. *Blood* (2019) 133 (20):2212–21. doi: 10.1182/blood-2018-12-893396

25. Lee DW, Gardner R, Porter DL, Louis CU, Ahmed N, Jensen M, et al. Current concepts in the diagnosis and management of cytokine release syndrome. *Blood* (2014) 124(2):188–95. doi: 10.1182/blood-2014-05-552729

26. Alvi RM, Frigault MJ, Fradley MG, Jain MD, Mahmood SS, Awadalla M, et al. Cardiovascular events among adults treated with chimeric antigen receptor T-cells (Car-T). *J Am Coll Cardiol* (2019) 74(25):3099–108. doi: 10.1016/j.jacc.2019.10.038

27. Goldman A, Maor E, Bomze D, Liu JE, Herrmann J, Fein J, et al. Adverse cardiovascular and pulmonary events associated with chimeric antigen receptor T-cell therapy. *J Am Coll Cardiol* (2021) 78(18):1800–13. doi: 10.1016/j.jacc.2021.08.044

frontiers | Frontiers in Cell and Developmental Biology

TYPE Original Research
PUBLISHED 31 March 2023
DOI 10.3389/fcell.2023.1134121

Check for updates

OPEN ACCESS

EDITED BY
Maristella Maggi,
University of Pavia, Italy

REVIEWED BY
Aashish Soni,
Essen University Hospital, Germany
Claudia Wiese,
Colorado State University, United States

*CORRESPONDENCE
Michael R. Lieber,
lieber@usc.edu
Yong Mi Kim,
ymkim@chla.usc.edu

SPECIALTY SECTION
This article was submitted to Cancer Cell Biology, a section of the journal Frontiers in Cell and Developmental Biology

RECEIVED 29 December 2022
ACCEPTED 20 March 2023
PUBLISHED 31 March 2023

CITATION
Ogana HA, Hurwitz S, Hsieh C-L, Geng H, Müschen M, Bhojwani D, Wolf MA, Larocque J, Lieber MR and Kim YM (2023), Artemis inhibition as a therapeutic strategy for acute lymphoblastic leukemia.
*Front. Cell Dev. Biol.* 11:1134121.
doi: 10.3389/fcell.2023.1134121



# Artemis inhibition as a therapeutic strategy for acute lymphoblastic leukemia

Heather A. Ogana[1], Samantha Hurwitz[1], Chih-Lin Hsieh[2], Huimin Geng[3], Markus Müschen[4], Deepa Bhojwani[1], Mark A. Wolf[5], James Larocque[5], Michael R. Lieber[6]* and Yong Mi Kim[1]*

[1]Department of Pediatrics, Children's Hospital Los Angeles, Division of Hematology and Oncology, Keck School of Medicine, University of Southern California, Los Angeles, CA, United States, [2]Department of Urology, USC Norris Comprehensive Cancer Center, Keck School of Medicine, University of Southern California, Los Angeles, CA, United States, [3]Department of Laboratory Medicine, UCSF, San Francisco, CA, United States, [4]Department of Immunobiology, Center of Molecular and Cellular Oncology, Yale University, New Haven, CT, United States, [5]Curia Global Inc, Albany, NY, United States, [6]Departments of Pathology, The Molecular and Computational Biology Section of the Department of Biological Sciences, USC Norris Comprehensive Cancer Center, Biochemistry and Molecular Biology, Molecular Microbiology and Immunology, Keck School of Medicine, University of Southern California, Los Angeles, CA, United States

As effective therapies for relapse and refractory B-cell acute lymphoblastic leukemia (B-ALL) remain problematic, novel therapeutic strategies are needed. Artemis is a key endonuclease in V(D)J recombination and nonhomologous end joining (NHEJ) of DNA double-strand break (DSB) repair. Inhibition of Artemis would cause chromosome breaks during maturation of RAG-expressing T- and B-cells. Though this would block generation of new B- and T-cells temporarily, it could be oncologically beneficial for reducing the proliferation of B-ALL and T-ALL cells by causing chromosome breaks in these RAG-expressing tumor cells. Currently, pharmacological inhibition is not available for Artemis. According to gene expression analyses from 207 children with high-risk pre-B acute lymphoblastic leukemias high Artemis expression is correlated with poor outcome. Therefore, we evaluated four compounds (827171, 827032, 826941, and 825226), previously generated from a large Artemis targeted drug screen. A biochemical assay using a purified Artemis:DNA-PKcs complex shows that the Artemis inhibitors 827171, 827032, 826941, 825226 have nanomolar IC50 values for Artemis inhibition. We compared these 4 compounds to a DNA-PK inhibitor (AZD7648) in three patient-derived B-ALL cell lines (LAX56, BLQ5 and LAX7R) and in two mature B-cell lines (3301015 and 5680001) as controls. We found that pharmacological Artemis inhibition substantially decreases proliferation of B-ALL cell lines while normal mature B-cell lines are not markedly affected. Inhibition of DNA-PKcs (which regulates Artemis) using the DNA-PK inhibitor AZD7648 had minor effects on these same primary patient-derived ALL lines, indicating that inhibition of V(D)J hairpin opening requires direct inhibition of Artemis, rather than indirect suppression of the kinase that regulates Artemis. Our data provides a basis for further evaluation of pharmacological Artemis inhibition of proliferation of B- and T-ALL.

KEYWORDS

**acute lymphoblastic leukemia, ARTEMIS, pharmacological inhibition, proliferation, V(D)J recombination, DNA hairpin, double-strand break, SNM1 nucleases**

## Highlights

- Artemis gene expression is associated with poor survival in pediatric B-cell acute lymphoblastic leukemia (B-ALL).
- Pharmacological Artemis inhibition can decrease proliferation of patient-derived primary B-ALL cell lines.

## Introduction

V(D)J recombination is the gene rearrangement process by which the variable domain exons of the antigen receptors are assembled at the DNA level (Schatz and Swanson, 2011). The process is initiated by the RAG1/2 complex to generate DNA hairpins at the termini of the V, D, or J sub-exons. The DNA hairpins must be nicked before they can be ligated together to form the complete exon of the B and T cell antigen receptor. These DNA hairpins are unique in the genome and are absent in mature B and T cells and absent in all nonlymphoid cells.

Artemis, a DNA nuclease in the metallo-β-lactamase family, is an enzyme that is specifically responsible for opening these DNA hairpins (Moshous et al., 2001; Lieber, 2010). Therefore, inhibition of Artemis to block its hairpin opening action would result in double-strand DNA (chromosome) breaks in pro-B/pre-B and pro-T/pre-T cells (Watanabe et al., 2022). Artemis is an ideal therapeutic target because it is a structure-specific nuclease which, upon inhibition, could result in the persistence of chromosome breaks. This is because the V(D)J recombination activating gene (RAG) enzyme complex generates DNA hairpins at T-cell receptor and immunoglobulin gene loci, which must be processed by Artemis to allow ligation and maintain chromosome integrity (Kurosawa and Adachi, 2010; de Villartay, 2015; Felgentreff et al., 2015; Betermier et al., 2020; Shibata and Jeggo, 2020; Fournier et al., 2022).

One strategy that we have been pursuing for targeting ALL cells takes advantage of the fact that over 90% of ALL patient cell lines express the RAG complex (Bories et al., 1991). Therefore, blocking Artemis systemically would cause chromosome breaks in ALL cells (Anne-Esguerra et al., 2022), resulting in inhibition of cell proliferation.

This rationale was supported here by examining the expression level data for Artemis in primary and relapse human ALL patients. Based on this rationale, a high throughput screen was done using a proprietary library to evaluate inhibition of the Artemis catalytic domain and its nuclease activity (to be reported elsewhere). Following hit confirmation and medicinal chemistry optimization to improve potency and selectivity, four compounds were assessed for inhibition of primary and relapse ALL cells.

## Methods

### Patient samples and cells

Bone marrow (BM) and peripheral blood (PB) samples from ALL patients were acquired in compliance with the Institutional Review Board regulations of each institution. Informed consent for cell banking was obtained from all human subjects. Leukemia cells were processed and cultured as previously described (Gang et al., 2020). Human studies were conducted in accordance with the Declaration of Helsinki.

Normal mature human B cell lines, immortalized lymphoblastoid cell lines 3301015 and 5680001, were generated using EBV-transformation of peripheral blood from patients with no hematopoietic abnormalities.

## Correlation of Artemis gene expression on leukemic blasts with clinical outcomes of pre-B ALL patients

Clinical and gene expression microarray data from 207 high-risk B-precursor ALL patients from the COG Clinical Trial P9906 were obtained from the GEO database (GSE11877) (Kang et al., 2010). The patients were treated uniformly with a modified augmented Berlin-Frankfurt-Münster Study Group (BFM) regimen, and individuals with very high-risk features (*BCR-ABL1* or hypodiploidy) were excluded from the study (Figure 1). Cryopreserved residual pretreatment leukemia specimens were available for a representative cohort of 207 patients, including 131 BM and seventy-six peripheral blood (PB) samples. Artemis expression (probeset DCLRE1C_242927) was determined by Affymetrix GeneChip analyses. The correlation of Artemis with overall survival analysis (OS) and relapse free survival (RFS) analysis was performed using the Wilcoxon test in the R package (R Development Core Team http://www.R-project.org/).

### *In vitro* drug assay

Lentivirally green fluorescence protein (GFP) labeled patient-derived B-ALL cells (LAX56, BLQ5, LAX7R) or mature B cell lines 3301015 and 5680001 were plated on irradiated murine stromal OP9 cells and treated with four compounds optimized for Artemis inhibition (827171, 827032, 826941, 825226) (provided by Curia Global Inc., as part of the NCI NExT Program). These compounds ranged in $K_D$ binding affinity to Artemis from 20 to 150 nM. The commercially available DNA-PK inhibitor (AZD7648) (obtained from a commercial source) was evaluated in parallel as a positive control. Proliferation was determined by measuring the green fluorescence intensity per image (9 images were captured per well) by Incucyte every 8 h for 3 days. Raw values were normalized to the zero-time DMSO control. On day 3, viability of the treated cells was determined by annexin V/DAPI staining *via* flow cytometry.

### Biochemical Artemis catalytic activity assay

Artemis activity assay was developed using full length Artemis with DNA-PKcs to generate a fluorescent signal from the cleavage of the 5′ 6-FAM modified end of hairpin DNA with a black-hole quencher (3-BHQ) on the 3’ end. The assay buffer used was 25 mM MOPS, pH 7.5, 10 mM MgCl2, 10 mM KCl, 10 µM ATP, 1 mM DTT, 0.05% (w/v) CHAPS with 5 nM FL-Artemis, 5 nM DNA-PKcs, and 200 nM DNA FAM hairpin

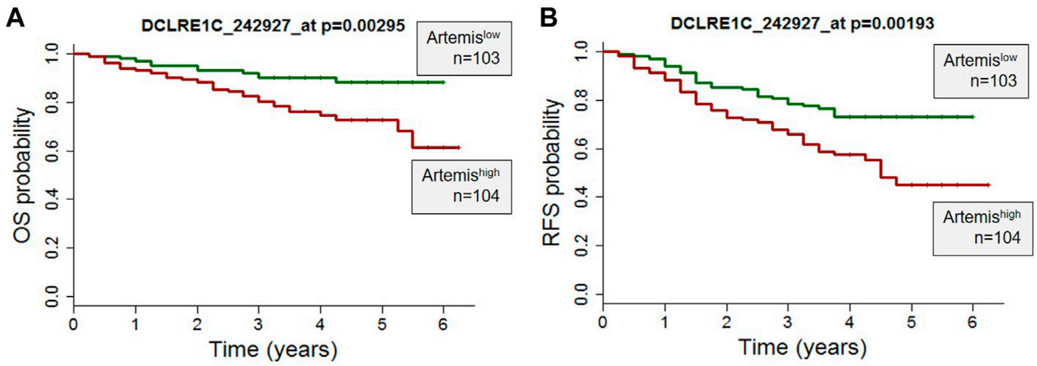


FIGURE 1
High Artemis expression is associated with poor outcome in primary B-ALL. **(A)** A probe set for Artemis in 207 pediatric ALL cases from COG study P9906 were analyzed. RNA was purified from 207 pretreatment diagnostic samples with more than 80% blasts (131 BM, 76 PB). **(A)** Overall Survival Probability (OS) and **(B)** Relapse Free Survival (RFS) of Artemis low ($n$ = 103) and Artemis high ($n$ = 104) are shown. $p$-values were obtained from the Wilcoxon test for each probe set (*$p$ = 0.00295 and *$p$=0.00193 for probe 242927_at).

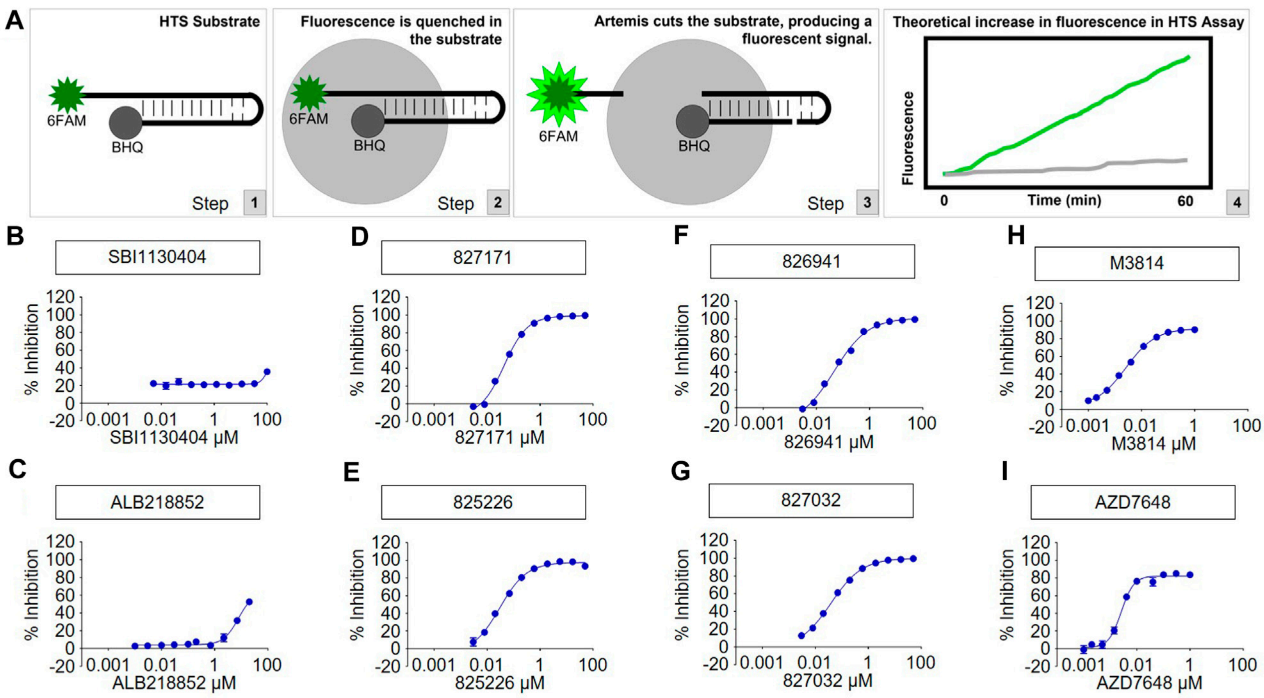


| Compound: | SBI1130404 | ALB218852 | 827171 | 827032 | 826941 | 825226 | M3814 | AZD7648 |
|---|---|---|---|---|---|---|---|---|
| $IC_{50}$ (µM) | >100 | 16.56 | 0.059 | 0.043 | 0.075 | 0.038 | 0.003 | 0.003 |
| $IC_{50}$ Error (µM) | ND | 1.2561 | 0.0045 | 0.0045 | 0.0108 | 0.0046 | 0.0002 | 0.0003 |
| %Inh at Max | 35.59 | 52.56 | 99.5 | 99.4 | 99.3 | 93.4 | 90.2 | 83.6 |
| $R^2$ | 0.9 | 0.993 | 0.998 | 0.999 | 0.997 | 0.998 | 0.999 | 0.995 |

FIGURE 2
The tested compounds are potent inhibitors of the catalytic activity of purified full-length human Artemis with DNA-PKcs. **(A)** Schematic of High-Throughput Screening (HTS) Assay. Steps 1, 2, and 3 show the fluorescence assay for cutting of the DNA hairpin substrate by Artems:DNA-Kcs. Artemis activity assay was optimized for development of a fluorescent signal from the cleavage of the 6-FAM modified end of hairpin DNA (to release it from proximity to the BHQ quenching) and monitored kinetically on a Perkin Elmer Envision microplate reader with FITC filters (excitation wavelength = 485 nm, emission wavelength = 520 nm). Compounds were tested in concentration response and the slopes of the enzyme readouts were converted to percent inhibition fit to a 4-parameter logistic curve to calculate the $IC_{50}$ of each compound. Two inactive compounds **(B)** SBI1130404 and **(C)** ALB218852, are shown for comparison. The assay was used to test compounds to aid in determining the structure activity relationship to develop through medicinal chemistry the Artemis inhibitors **(D)** 827171, **(E)** 827032, **(F)** 826941 and **(G)** 825226. The concentration responses curves and calculated results of the inhibitors are shown compared with known DNA-PK inhibitors **(H)** M3814 and **(I)** AZD7648.

substrate. The fluorescence signal was monitored kinetically on a Perkin Elmer Envision microplate reader with FITC filters ($\lambda_{ex}$ = 485 nm, $\lambda_{em}$ = 520 nm) with 1-min reads for 40 min. Compounds were tested in 10-point concentration (10 different concentrations with 3-fold dilutions) responses using the slopes of the enzyme readouts to determine percent inhibition which was fit to a 4-parameter logistic curve to calculate the $IC_{50}$ of each compound. We have previously published the purity of the protein preparations (Ma et al., 2002; 2004; Lu et al., 2008), and these will be published once again as part of the high throughput study of the large chemical libraries used.

# Results

## Artemis expression in patient B-ALL cells inversely correlate with clinical outcome

To determine the role of Artemis in ALL, expression of Artemis mRNA (DCLRE1C) in 207 ALL patients uniformly treated with the COG P9906 clinical trial (Kang et al., 2010) was correlated with outcome. Artemis expression was determined by Affymetrix GeneChip analyses on ALL tumor cells at the time of diagnosis (prior to chemotherapy). The overall survival (OS) (Figure 1A) and relapse free survival (Figure 1B) were analyzed by Artemis expression and could be separated into Artemis$^{high}$ (DCLRE1C expression ≥mean; $n$ = 104) and Artemis$^{low}$ expressing cases (DLCRE1C expression <mean, $n$ = 103). Artemis$^{high}$ leukemias were associated with inferior outcome with lower overall survival and relapse-free survival. This supported the rationale for targeting Artemis.

## Specificity of the Artemis inhibitors

A high throughput screen of Artemis active site inhibitors using a proprietary library to assess for inhibition of the Artemis catalytic domain and its nuclease activity identified four small molecule inhibitors (Figure 2A). The medicinal chemistry and high throughput screen that led to these will be described elsewhere. We determined the specificity of the four Artemis inhibiting compounds using a biochemical Artemis activity assay which generates a fluorescent signal from the cleavage of the 5′ 6-FAM modified end of hairpin DNA with a black-hole quencher (3-BHQ) on the 3’ end. For comparison, the AZD7648 and M3814 compounds were used to inhibit DNA-PKcs kinase activity. DNA-PKcs kinase activity is required for DNA-PKcs to autophosphorylate itself, and this autophosphorylation event thereby activates Artemis nuclease activity. Though Artemis activation as a nuclease predominantly requires DNA-PKcs kinase activity, direct inhibition of Artemis avoids the non-specific toxicity of generic kinase inhibitors that act at the ATP binding pocket of kinases. Two inactive compounds, SBI1130404 (Figure 2B) and ALB218852 (Figure 2C), are shown for comparison. Therefore, the compounds 827171, 827032, 826941, and 825226 (Figures 2D–G) act with nanomolar IC50 values to inhibit Artemis, and these are nearly as potent as the established commercial DNA-PKcs inhibitors, M3814 and AZD7648 (Figure 2H, I).

We have previously shown that full-length Artemis under $Mg^{2+}$ conditions is entirely inactive without DNA-PKcs (Ma et al., 2002; 2004; Lu et al., 2008). This indicates that the Artemis:DNA-PKcs complex is formed; otherwise, no FAM hairpin substrate would be cut to generate the fluorescence signal.

## Evaluation of Artemis inhibitors on viability of B-ALL and mature B cell lines

Here, we determined the effect of four Artemis inhibitors 827171 (Figures 3A–C), 827032 (Figures 3D–F), 826941 (Figures 3G–I), 825226 (Figures 3J–L) and the DNA-PK inhibitor AZD7648 (Figures 3M–O) on the viability of patient-derived B-ALL cells (BLQ5, LAX56 and LAX7R) (Table 1) after an incubation time of 3 days. Three of four Artemis inhibitors, 827171 (Figures 3A–C), 827032 (Figures 3D–F), 826941 (Figures 3G–I), showed a dose-dependent mild to moderate decrease in viability in all three tested B-ALL cells compared to DMSO controls. Of these three compounds, compound 827171 showed the smallest effect on viability. The Artemis inhibitor 827032 (Figures 3D–F) only showed a decrease in viability at 20 µM in all three B-ALL cases. The compound, 825226 (Figures 3J–L), only showed a dose-dependent decrease in viability in BLQ5 and LAX56 cells, but not in LAX7R cells, as 20 µM did not significantly affect viability. The compound 826941 affected the viability of all 3 cell lines at doses 5–20 µM. All cell lines showed a decrease in viability after exposure to the reference control DNA-PK inhibitor AZD7648 (Figures 3M–O).

Normal B cell lines 3301015 and 5680001 were treated for 3 days with Artemis inhibitors 827171 (Figures 4A, B), 827032 (Figures 4C, D), 826941 (Figures 4E, F), 825226 (Figure 4G, H). It is important to note that the viability of the normal mature B-cell lines is low in general (DMSO control). Artemis inhibitors 827171 (Figures 4A, B), 827032 (Figures 4C, D), 825226 (Figure 4G, H) do not affect viability of B cell lines 3301015 and 5680001 at 1 µM. However, 826941 (Figures 4E, F) and AZD7648 (Figures 4I, J) decrease viability of one or both B-cell lines at 1–20 µM. Similarly, AZD7648 (Figures 4I, J) decreases the viability of one or both B-cell lines at 1–20 µM. The statistical analysis of all viability differences is compared to DMSO controls.

Overall, the 827171 compound among the four has the smallest effects on B-ALL or mature B cell viability. Cells affected by 827171 may not decrease in viability but they may be arrested in S phase and therefore be slowed in the proliferation assay, as we investigated below (Wang et al., 2009; Yan et al., 2011).

## Artemis inhibitor 827171 substantially reduces proliferation of B-ALL compared to normal B-cell lines

Based on these viability studies, we next tested the compounds for their effect on proliferation. Preliminary testing indicates that the 827171 compound showed the largest effect on proliferation, and it was chosen for more detailed study. The 827171 compound and AZD7648 were evaluated in parallel. Ideally, normal B-cell lines would continue to proliferate upon Artemis inhibition and only

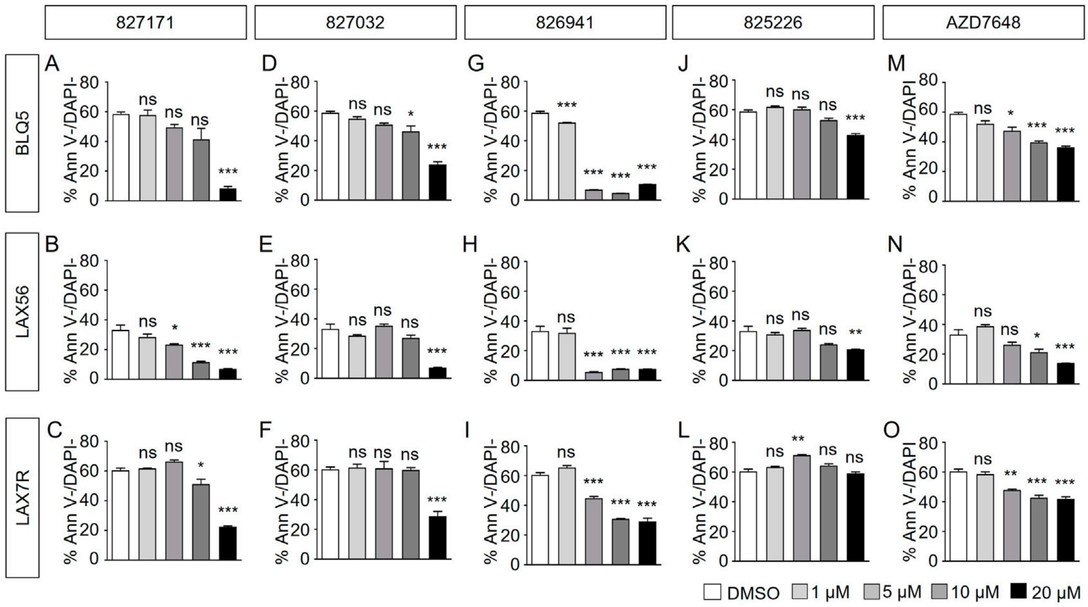


FIGURE 3
Artemis inhibitors and DNA-PK inhibitor AZD7648 effects on viability of B-ALL cells. B-ALL cells (BLQ5, LAX56 and LAX7R) were treated with Artemis inhibitor 827171 **(A–C)**, 827032 (D-F), 826941 **(G–I)**, 825226 **(J–L)** and DNA-PK inhibitor AZD7648 **(M–O)** with indicated concentrations. On day three, primary B-ALL cells were collected and used for flow cytometry analysis with PE Annexin V and DAPI to measure % viability (PE Annexin V-/DAPI-). The statistical analysis of viability differences is compared to DMSO control: ns: non-significant; $^{*}p < 0.05$; $^{**}p < 0.001$; $^{***}p < 0.0001$, one-way ANOVA.

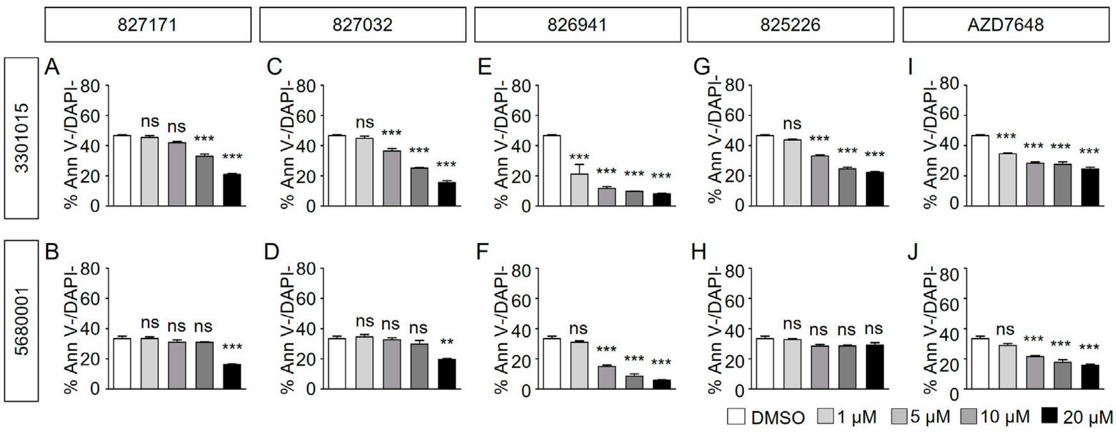


FIGURE 4
Artemis inhibitors and DNA-PK inhibitors effect on viability of normal mature B cell lines. Normal mature B cell lines 3301015 and 5680001 were treated for 3 days with 827171 **(A, B)**, 827032 **(C, D)**, 826941 **(E, F)**, 825226 **(G, H)** and DNA-PK inhibitor AZD7648 **(I, J)** with indicated concentrations. On day three, mature B cells were collected and used for flow cytometry analysis with PE Annexin V and DAPI to measure % viability (PE Annexin V-/DAPI-). The % viability (Ann V-/DAPI-) is depicted. The statistical analysis of viability differences is compared to DMSO control: ns: non-significant; $^{*}p < 0.05$; $^{**}p < 0.001$; $^{***}p < 0.0001$, one-way ANOVA.

**TABLE 1 Patient-derived B-ALL information.**

| B-ALL cells | Diagnosis | Cytogenetics |
|---|---|---|
| BLQ5 | Relapse | BCR-ABL1 |
| LAX56 | Relapse | t(Y;7)(p1.3;p13) |
| LAX7R | Relapse | KRASG12V |

B-ALL cell lines would be inhibited due to chromosome breaks. Primary patient-derived B-ALL cells (BLQ5, LAX56, and LAX7R) were transduced with GFP and 100,000 cells were plated in 24-well plates seeded with irradiated OP9 cells. Increasing green fluorescence intensity is indicative of proliferation as measured by Incucyte every 8 h. Although the GFP expression varied between cell lines (Supplementary Figure S1), the normalized

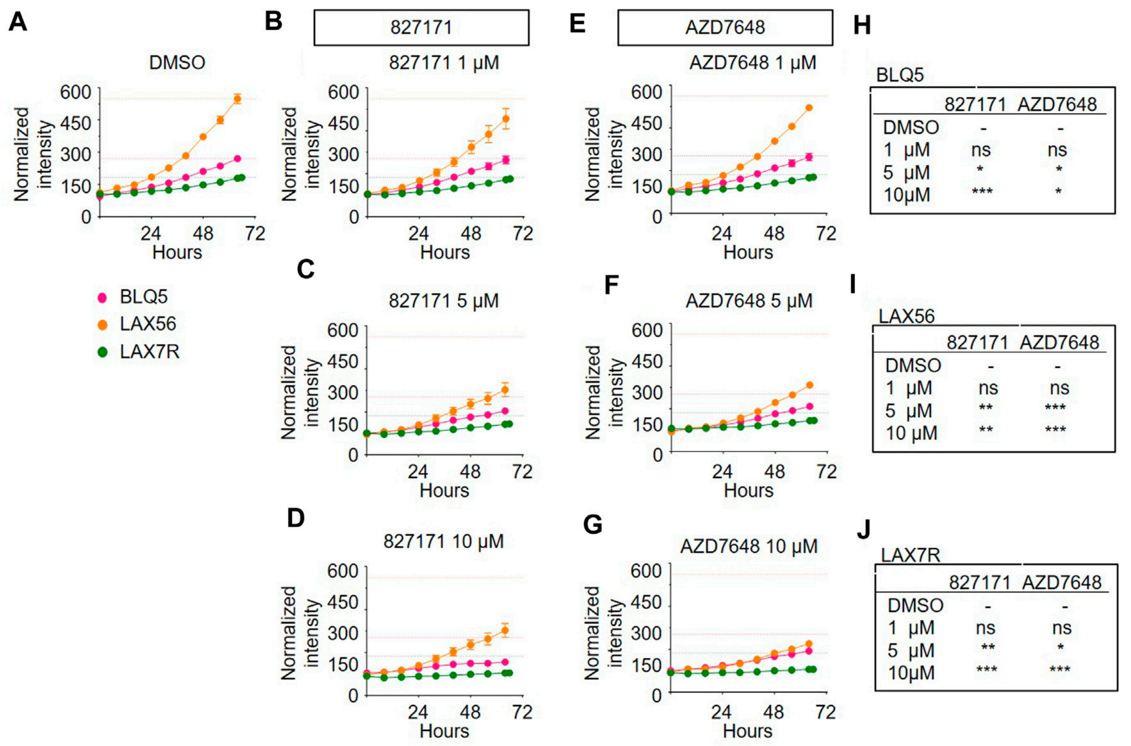


FIGURE 5
The Artemis inhibitor 827171 and DNA-PK inhibitor AZD7648 substantially inhibit proliferation of B-ALL. Primary B-ALL cells (BLQ5, LAX56, and LAX7R) were transduced with GFP, and 100,000 cells were plated in 24-well plates seeded with irradiated OP9 cells. Cells were treated with DMSO control **(A)**, Artemis inhibitor 827171 **(B–D)** or DNA-PK inhibitor AZD7648 **(E–G)** with the indicated doses. Green fluorescence intensity was measured by Incucyte every 8 h. Raw values were normalized to the 0 h DMSO control. The dashed lines indicate the mean of the final time point measurements of the DMSO control for each primary B-ALL cell. The statistical analysis of proliferation differences is shown for the final time point measurements for BLQ5 **(H)**, LAX56 **(I)**, LAX7R **(J)**, after treatment with 827171 or DNA-PK inhibitor AZD7648 at indicated doses compared to DMSO control. ns: non-significant. $^*p < 0.05$; $^{**}p < 0.001$; $^{***}p < 0.0001$, one-way ANOVA.

data show the relative changes in proliferation compared to the DMSO control, which showed continuous proliferation of B-ALL (Figure 5A). The mature B cell line proliferation is slow enough that it appears relatively flat in the proliferation assays, but the cells do increase in number (Supplementary Figure S2). Compared to B-ALL cells which grow as single cells (Supplementary Figure S3A–F), the mature B-cell lines grow in clusters and the measurement of total intensity per image is a potential caveat and may not capture this growth (Supplementary Figure S3G–J). Artemis inhibitor 827171 (Figures 5A–D) showed inhibition of B-ALL cell lines at 5 µM and 10 µM and no decrease in proliferation of normal B-cells (Figures 6A–D). The proliferation of LAX56 was also decreased, which was not observed after treatment with the other Artemis inhibitors described earlier. The DNA-PK inhibitor AZD7648 (Figures 5E–G) inhibited the proliferation of B-ALL cell lines at 5µM and 10 µM. AZD7648 also suppressed proliferation of the normal mature B cell 3301015 at 5µM and 10 µM. There were no significant decreases in proliferation for 5680001 in either 827171 or AZD7648, but rather the compounds at 1 or 5 µM may have caused a minor increase in proliferation. Statistical analysis is compared to DMSO control and is summarized in Figures 5H–J. Thus, the 827171 compound shows substantial inhibition of B-ALL cell proliferation and minimal effects on normal mature B-cells.

## Discussion

Our studies indicate that the 827171 compound substantially inhibits the proliferation of primary patient B-ALL lines, and it is comparable to the AZD7648 compound (Figure 5). The advantage of direct inhibition of the structure-specific Artemis endonuclease is that it avoids the typical complications of kinase inhibitors that block many ATP binding pockets of the >3,000 kinases in the cell.

The effects of 827171 on viability, in contrast to proliferation, are among the mildest of the compounds evaluated. This likely reflects that DSBs in nondividing cells may not cause death immediately or at all. In contrast, an unrepaired DSB in proliferating cells represents more of a challenge. This increased effect of DSBs on proliferating cells may be because of a much higher probability of losing large chromosome fragments. Such a loss is because only the portion of the chromosome with the centromere is retained at the metaphase plate during cell division, and the chromosomal fragment lacking a centromere portion is easily lost. In addition, inhibition of Artemis

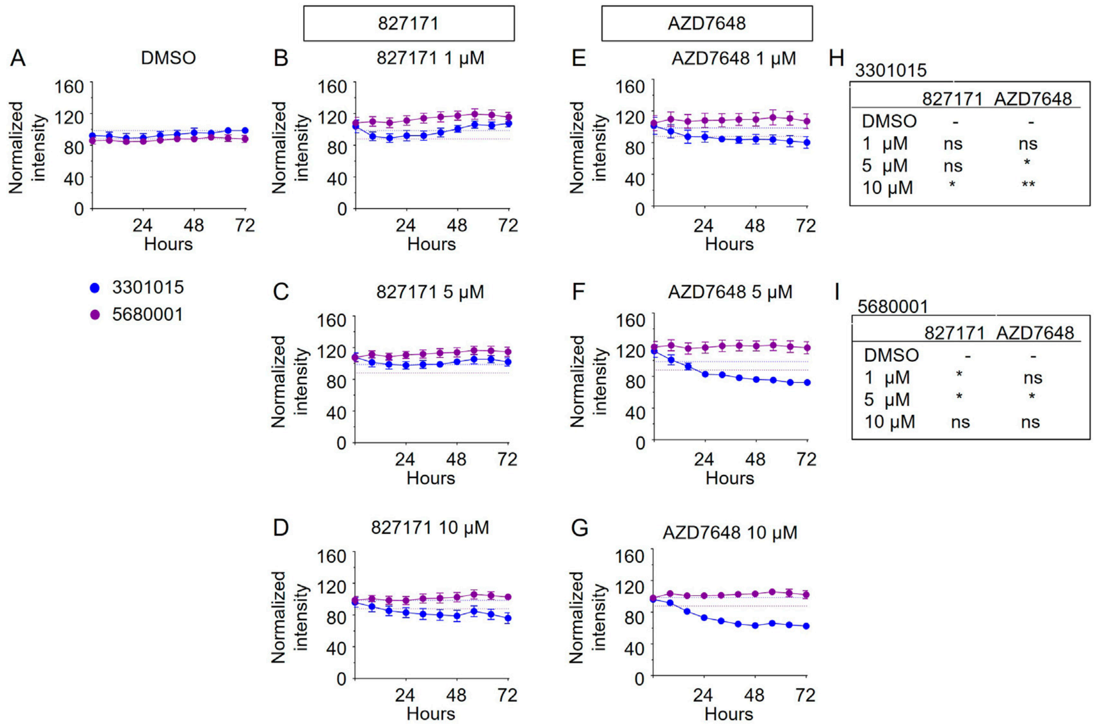


FIGURE 6
The Artemis inhibitor 827171 and DNA-PK inhibitor AZD7648 have minimal effect on mature B cells. Mature B cell lines (3301015 and 5680001) were transduced with GFP, and 100,000 cells were plated in 24-well plates seeded with irradiated OP9 cells. Cells were treated with DMSO control **(A)** or Artemis inhibitor 827171 **(B–D)** or DNA-PK inhibitor AZD7648 **(E–G)** with the indicated doses. Green fluorescence intensity was measured by Incucyte every 8 h. Raw values were normalized to the 0 h DMSO control. The dashed lines indicate the mean of the final time point measurements of the DMSO control for each mature B cell line. The statistical analysis of proliferation differences is shown for the final time point measurements for 3301015 **(H)** or 5680001 **(I)** after treatment with 827171 or DNA-PK inhibitor AZD7648 at indicated doses compared to DMSO control. ns: non-significant. *$p < 0.05$; **$p < 0.001$; ***$p < 0.0001$, for statistically significant changes in proliferation of a treatment group compared to DMSO by one-way ANOVA.

may interfere with the ability of cells to exit from S phase (Wang et al., 2009; Yan et al., 2011).

The large majority of acute lymphoblastic leukemias (ALL) produce the RAG enzyme complex encoded by the RAG genes (Bories et al., 1991). The RAG complex cuts DNA to generate a double-strand break (DSB) with a perfect DNA hairpin at the edge of each V, D, and J segment at heptamer/nonamer signal sequence sites. Off-target sites that have sequences sufficiently similar to heptamer/nonamer sites also are cut by the RAG complex at a lower, but still relevant frequency (Shimazaki et al., 2012; Papaemmanuil et al., 2014). The perfect DNA hairpins on each side of the double-strand break (DSB) must be nicked to open them before they are eligible for ligation and repair of the DSB. Artemis inhibitors would block hairpin opening, a key step in V(D)J recombination, resulting in chromosome breaks thereby killing the cells or slowing their growth. A side effect of this strategy would be the transient loss of the pro-B/pre-B and pro-T/pre-T cells in the bone marrow and thymus during the period of treatment, but the memory compartments of B and T cells would not be affected, and neither would the stem cells because none of these express the RAG complex.

Here, we evaluated four of the Artemis inhibitors generated from a high-throughput screen and medicinal chemistry effort. These were assessed in three primary human ALL samples, with human mature B cell lines used for comparison. For comparison with the Artemis inhibitors, we used a known DNA-PKcs inhibitor, AZD7648, because DNA-PKcs is a kinase which regulates Artemis activity, and this compound has been evaluated in clinical trials for utility in a variety of non-lymphoid human malignancies (Matsumoto, 2022).

We found that the 827171-compound reduced proliferation of the three B-ALL lines at 1, 5, and 10 μM without affecting the mature B-cell control lines. In contrast, the DNA-PKcs inhibitor, AZD7648, showed little inhibition of the B-ALL lines, and instead suppressed the growth of the mature B cell control lines. These findings are encouraging for future work to make derivatives of the 827171 compounds. Importantly, the DNA-PKcs inhibitor AZD7648 decreased the proliferation less than 827171 in these same lines. This suggests that inhibition of hairpin opening requires direct inhibition of Artemis, rather than indirect suppression of the kinase that regulates Artemis, namely, DNA-PKcs. This may be because Artemis can be activated by DNA ligase IV, even when DNA-PKcs is not present (Gerodimos et al., 2017). Therefore, inhibition of hairpin opening to cause chromosome breaks likely requires direct Artemis inhibition.

While the 827171 compound shows promise for inhibition of the active site of Artemis, the brief study here also raises the interest in parallel strategies for inhibiting Artemis. Future work may take advantage of the recently described cryo-EM structure for the basal state of the Artemis:DNA-PKcs complex to develop inhibitors that prevent Artemis from being activated (Watanabe and Lieber, 2022;

Watanabe et al., 2022). Combinations of strategies to block hairpin opening and thereby create chromosome breaks in B-ALL cells is a promising approach.

## Data availability statement

The original contributions presented in the study are included in the article/Supplementary Material, further inquiries can be directed to the corresponding authors.

## Ethics statement

The studies involving human participants were reviewed and approved by the IRB of CHLA. Human samples are deidentified and exempted. Written informed consent to participate in this study was provided by the participants' legal guardian/next of kin.

## Author contributions

HO, SH, HG, MM, C-LH, DB, MW, JL, ML, and YMK. designed the research and analyzed data. HO, SH, C-LH, DB, ML, and YMK. wrote the paper. C-LH and DB provided vital reagents.

## Funding

Work in the laboratory of YMK was funded by NIH R01 CA172896. Work in the laboratory of ML was funded by CA100504 and GM118009 and the USC Norris Cancer Center Core grant, 5P30CA014089. Additional work was funded in part with Federal funds from the National Cancer Institute, National Institutes of Health, under Chemical Biology Consortium Contract No. HHSN261200800001E.

## Acknowledgments

The authors thank all members of the NCI's NExT (NCI Experimental Therapeutics) CBC (Chemical Biology Consortium) Artemis Drug Discovery Team for helpful discussions. The authors also thank the Flow Cytometry Core at CHLA for their expertise and support. The content of this publication does not necessarily reflect the views or policies of the Department of Health and Human Services, nor does mention of trade names, commercial products, or organizations imply endorsement by the U.S. Government.

## Conflict of interest

Authors MW and JL were employed by Curia Global Inc.

The remaining authors declare that the research was conducted in the absence of any commercial or financial relationships that could be construed as a potential conflict of interest.

## Publisher's note



## Supplementary material

The Supplementary Material for this article can be found online at: https://www.frontiersin.org/articles/10.3389/fcell.2023.1134121/full#supplementary-material

## References

Anne-Esguerra, Z., Wu, M., Watanabe, G., Flint, A. J., and Lieber, M. R. (2022). Partial deletions of the autoregulatory C-terminal domain of Artemis and their effect on its nuclease activity. *DNA Repair (Amst)* 120, 103422. doi:10.1016/j.dnarep.2022.103422

Betermier, M., Borde, V., and De Villartay, J. P. (2020). Coupling DNA damage and repair: An essential safeguard during programmed DNA double-strand breaks? *Trends Cell Biol.* 30, 87–96. doi:10.1016/j.tcb.2019.11.005

Bories, J. C., Cayuela, J. M., Loiseau, P., and Sigaux, F. (1991). Expression of human recombination activating genes (RAG1 and RAG2) in neoplastic lymphoid cells: Correlation with cell differentiation and antigen receptor expression. *Blood* 78, 2053–2061. doi:10.1182/blood.v78.8.2053.2053

De Villartay, J. P. (2015). Congenital defects in V(D)J recombination. *Br. Med. Bull.* 114, 157–167. doi:10.1093/bmb/ldv020

Felgentreff, K., Lee, Y. N., Frugoni, F., Du, L., Van Der Burg, M., Giliani, S., et al. (2015). Functional analysis of naturally occurring DCLRE1C mutations and correlation with the clinical phenotype of ARTEMIS deficiency. *J. Allergy Clin. Immunol.* 136, 140–150 e7. doi:10.1016/j.jaci.2015.03.005

Fournier, B., Mahlaoui, N., Moshous, D., and De Villartay, J. P. (2022). Inborn errors of immunity caused by defects in the DNA damage response pathways: Importance of minimizing treatment-related genotoxicity. *Pediatr. Allergy Immunol.* 33, e13820. doi:10.1111/pai.13820

Gang, E. J., Kim, H. N., Hsieh, Y. T., Ruan, Y., Ogana, H. A., Lee, S., et al. (2020). Integrin α6 mediates the drug resistance of acute lymphoblastic B-cell leukemia. *Blood* 136, 210–223. doi:10.1182/blood.2019001417

Gerodimos, C. A., Chang, H. H. Y., Watanabe, G., and Lieber, M. R. (2017). Effects of DNA end configuration on XRCC4-DNA ligase IV and its stimulation of Artemis activity. *J. Biol. Chem.* 292, 13914–13924. doi:10.1074/jbc.M117.798850

Kang, H., Chen, I. M., Wilson, C. S., Bedrick, E. J., Harvey, R. C., Atlas, S. R., et al. (2010). Gene expression classifiers for relapse-free survival and minimal residual disease improve risk classification and outcome prediction in pediatric B-precursor acute lymphoblastic leukemia. *Blood* 115, 1394–1405. doi:10.1182/blood-2009-05-218560

Kurosawa, A., and Adachi, N. (2010). Functions and regulation of Artemis: A goddess in the maintenance of genome integrity. *J. Radiat. Res.* 51, 503–509. doi:10.1269/jrr.10017

Lieber, M. R. (2010). The mechanism of double-strand DNA break repair by the nonhomologous DNA end-joining pathway. *Annu. Rev. Biochem.* 79, 181–211. doi:10.1146/annurev.biochem.052308.093131

Lu, H., Shimazaki, N., Raval, P., Gu, J., Watanabe, G., Schwarz, K., et al. (2008). A biochemically defined system for coding joint formation in V(D)J recombination. *Mol. Cell* 31, 485–497. doi:10.1016/j.molcel.2008.05.029

Ma, Y., Lu, H., Tippin, B., Goodman, M. F., Shimazaki, N., Koiwai, O., et al. (2004). A biochemically defined system for mammalian nonhomologous DNA end joining. *Mol. Cell* 16, 701–713. doi:10.1016/j.molcel.2004.11.017

Ma, Y., Pannicke, U., Schwarz, K., and Lieber, M. R. (2002). Hairpin opening and overhang processing by an Artemis/DNA-dependent protein kinase complex in nonhomologous end joining and V(D)J recombination. *Cell* 108, 781–794. doi:10.1016/s0092-8674(02)00671-2

Matsumoto, Y. (2022). Development and evolution of DNA-dependent protein kinase inhibitors toward cancer therapy. *Int. J. Mol. Sci.* 23, 4264. doi:10.3390/ijms23084264

Moshous, D., Callebaut, I., De Chasseval, R., Corneo, B., Cavazzana-Calvo, M., Le Deist, F., et al. (2001). Artemis, a novel DNA double-strand break repair/V(D)J recombination protein, is mutated in human severe combined immune deficiency. *Cell* 105, 177–186. doi:10.1016/s0092-8674(01)00309-9

Papaemmanuil, E., Rapado, I., Li, Y., Potter, N. E., Wedge, D. C., Tubio, J., et al. (2014). RAG-mediated recombination is the predominant driver of oncogenic rearrangement in ETV6-RUNX1 acute lymphoblastic leukemia. *Nat. Genet.* 46, 116–125. doi:10.1038/ng.2874

Schatz, D. G., and Swanson, P. C. (2011). V(D)J recombination: Mechanisms of initiation. *Annu. Rev. Genet.* 45, 167–202. doi:10.1146/annurev-genet-110410-132552

Shibata, A., and Jeggo, P. A. (2020). Roles for 53BP1 in the repair of radiation-induced DNA double strand breaks. *DNA Repair (Amst)* 93, 102915. doi:10.1016/j.dnarep.2020.102915

Shimazaki, N., Askary, A., Swanson, P. C., and Lieber, M. R. (2012). Mechanistic basis for RAG discrimination between recombination sites and the off-target sites of human lymphomas. *Mol. Cell Biol.* 32, 365–375. doi:10.1128/MCB.06187-11

Wang, H., Zhang, X., Geng, L., Teng, L., and Legerski, R. J. (2009). Artemis regulates cell cycle recovery from the S phase checkpoint by promoting degradation of cyclin E. *J. Biol. Chem.* 284, 18236–18243. doi:10.1074/jbc.M109.002584

Watanabe, G., and Lieber, M. R. (2022). Dynamics of the Artemis and DNA-PKcs complex in the repair of double-strand breaks. *J. Mol. Biol.* 434, 167858. doi:10.1016/j.jmb.2022.167858

Watanabe, G., Lieber, M. R., and Williams, D. R. (2022). Structural analysis of the basal state of the Artemis:DNA-PKcs complex. *Nucleic Acids Res.* 50, 7697–7720. doi:10.1093/nar/gkac564

Yan, Y., Zhang, X., and Legerski, R. J. (2011). Artemis interacts with the Cul4A-DDB1DDB2 ubiquitin E3 ligase and regulates degradation of the CDK inhibitor p27. *Cell Cycle* 10, 4098–4109. doi:10.4161/cc.10.23.18227

TYPE Original Research
PUBLISHED 03 April 2023
DOI 10.3389/fonc.2023.1126354



OPEN ACCESS

EDITED BY
Daekyu Sun,
University of Arizona, United States

REVIEWED BY
Daniela Sanchez Bassères,
University of São Paulo, Brazil
Antonio Giovanni Solimando,
University of Bari Aldo Moro, Italy
Claudia Scotti,
University of Pavia, Italy

*CORRESPONDENCE
Mattias K. Andersson
mattias.andersson@llcr.med.gu.se

SPECIALTY SECTION
This article was submitted to Cancer Molecular Targets and Therapeutics, a section of the journal Frontiers in Oncology

RECEIVED 17 December 2022
ACCEPTED 24 March 2023
PUBLISHED 03 April 2023

CITATION
Tejera Nevado P, Tešan Tomić T, Atefyekta A, Fehr A, Stenman G and Andersson MK (2023) Synthetic oleanane triterpenoids suppress *MYB* oncogene activity and sensitize T-cell acute lymphoblastic leukemia cells to chemotherapy.
*Front. Oncol.* 13:1126354.
doi: 10.3389/fonc.2023.1126354



# Synthetic oleanane triterpenoids suppress *MYB* oncogene activity and sensitize T-cell acute lymphoblastic leukemia cells to chemotherapy

Paloma Tejera Nevado, Tajana Tešan Tomić, Ali Atefyekta, André Fehr, Göran Stenman and Mattias K. Andersson*

Sahlgrenska Center for Cancer Research, Department of Pathology, University of Gothenburg, Gothenburg, Sweden

T-cell acute lymphoblastic leukemia (T-ALL) is an aggressive hematologic malignancy with poor prognosis. The *MYB* oncogene encodes a master transcription factor that is activated in the majority of human T-ALLs. In the present study, we have performed a large-scale screening with small-molecule drugs to find clinically useful inhibitors of *MYB* gene expression in T-ALL. We identified several pharmacological agents that potentially could be used to treat MYB-driven malignancies. In particular, treatment with the synthetic oleanane triterpenoids (OTs) bardoxolone methyl and omaveloxolone decreased *MYB* gene activity and expression of MYB downstream target genes in T-ALL cells with constitutive *MYB* gene activation. Notably, treatment with bardoxolone methyl and omaveloxolone led to a dose-dependent reduction in cell viability and induction of apoptosis at low nanomolar concentrations. In contrast, normal bone marrow-derived cells were unaffected at these concentrations. Bardoxolone methyl and omaveloxolone treatment downregulated the expression of DNA repair genes and sensitized T-ALL cells to doxorubicin, a drug that is part of the standard therapy of T-ALL. OT treatment may thus potentiate DNA-damaging chemotherapy through attenuation of DNA repair. Taken together, our results indicate that synthetic OTs may be useful in the treatment of T-ALL and potentially also in other MYB-driven malignancies.

KEYWORDS
*MYB*, acute lymphoblastic leukemia, oleanane triterpenoid, bardoxolone methyl, omaveloxolone

# 1 Introduction

T-cell acute lymphoblastic leukemia (T-ALL) is an aggressive hematologic malignancy characterized by abnormal expansion of transformed lymphoid progenitor cells in the bone marrow, blood, and extramedullary sites (1, 2). It accounts for approximately 25% of ALL cases in adults and 10-15% of cases in children. Even though risk-based stratification and dose-intensification therapy have led to marked improvements in survival of pediatric patients, the prognosis for adults remains poor, particularly for older patients (2). Less than half of adults diagnosed with T-ALL survive more than five years (3). Thus, development of improved therapies for this disease is needed.

The *MYB* oncogene is activated in the majority of T-ALLs (4, 5). It encodes a pioneer master transcription factor that binds to super-enhancers and regulates chromatin accessibility and genes involved in cell division and maturation (5, 6). In T-ALL, *MYB* gene activation leads to blocked differentiation and increased proliferation of neoplastic lymphoid progenitor cells, suggesting that the gene is a potential therapeutic target in this disease (4, 7). The *MYB* gene is activated by various molecular mechanisms in T-ALL. *MYB* is activated by the TAL1 complex that is overexpressed in up to 60% of T-ALL (8) and is a downstream target of MLL-fusions (9). In 10-15% of T-ALLs, *MYB* is activated by gene duplication or gene fusion (7, 10, 11). Furthermore, potentially activating hot spot mutations in the 5´-part of *MYB* were recently described in T-ALL (11). We and others have previously shown that the MYB protein and its downstream effectors can be successfully targeted in acute myeloid leukemia (AML) (12–24). However, very few MYB inhibitors with therapeutic effects in T-ALL have been identified (25). Given that MYB is an oncogenic driver in the majority of T-ALLs and primarily regulated at the transcriptional level (26), we decided to perform a large-scale drug screening with small-molecule agents to identify inhibitors of *MYB* gene expression. We hypothesized that suppression of MYB might improve the treatment of patients with this aggressive disease that are refractory to the conventional therapies currently used. We now show that synthetic oleanane triterpenoids both inhibit MYB expression and sensitize T-ALL cells to chemotherapy.

# 2 Materials and methods

## 2.1 Cell culture

The T-ALL cell lines (27–29) MOLT-4 (ATCC no. CRL-1582), CCRF-CEM (ATCC no. CCL-119), P12-ICHIKAWA (DSMZ no. ACC-34), and RPMI-8402 (DSMZ no. ACC-290) were obtained from ATCC (Manassas, VA, USA) and DSMZ (Braunschweig, Germany). The cell lines have *MYB*-activation by gene duplication (7, 10). Cell identity was confirmed by STR-analysis and all cell lines were shown to be mycoplasma free prior to experiments. T-ALL cells were maintained in RPMI-1640 medium with GlutaMAX, 10% or 20% FBS, and 1% penicillin-streptomycin (Thermo Fisher Scientific, Waltham, MA, USA). Human mononuclear cells (Merck, Darmstadt, Germany) isolated from a healthy donor (HMCs) were maintained in Mononuclear cell medium (Merck) according to the instructions of the supplier. All cells were kept in a humidified incubator at 37°C and 5% $CO_2$.

## 2.2 Chemical library, drug screening, and validation experiments

The L1100 Inhibitor Library, bardoxolone methyl (CDDO-Me, RTA 402), omaveloxolone (RTA 408), and doxorubicin were purchased from Selleck Chemicals (Houston, TX, USA). The IKK inhibitor VII and IKK-2 inhibitor IV were obtained from Merck. The KI696 peptide (30) was a kind gift from Dr. Volkan Sayin. Drugs were kept at -80°C or -20°C in stock solutions of 10 µM in DMSO and diluted to working concentrations in growth medium prior to experiments. For drug screening, 4,000 MOLT-4 or CCRF-CEM cells were seeded in V-bottom 96-well plates (Greiner Bio-One, Kremsmünster, Austria) and after 24 h treated with 1 µM of 768 small-molecule inhibitors from the Inhibitor Library (Supplementary Table S1). Cells were incubated with drugs, or DMSO as control, for 48 h whereafter they were washed with PBS and harvested using direct lysis (31) in 100 µl of 1 mg/ml BSA (Thermo Fisher Scientific). The screening was performed three times and cell plates were stored at -80°C until further analysis. For validation experiments, 2-2.5x$10^5$ T-ALL cells were seeded in 24-well plates (RNA analysis) and 4x$10^5$ cells were seeded in 6-well plates (protein analysis) and on the next day treated for 24 h with drugs or equal volumes of DMSO.

## 2.3 RNA isolation and cDNA synthesis

Total RNA was isolated using the RNeasy Micro-kit (Qiagen, Hilden, Germany) following the protocol of the manufacturer. RNA purity and concentration was measured with the NanoDrop ND-1000 spectrophotometer (Thermo Fisher Scientific). Reverse transcription was performed with the iScript cDNA synthesis kit (Bio-Rad, Hercules, CA, USA) according to instructions of the manufacturer. For drug screening, 2 µl of cell lysate were used in 10 µl cDNA reactions.

## 2.4 Western blot

Total protein was isolated using RIPA buffer supplemented with the Halt protease and phosphatase inhibitor (Thermo Fisher Scientific). Protein concentrations were measured with the DC protein assay (Bio-Rad). Protein expression was analyzed by Western blotting using the NuPAGE system (Thermo Fisher Scientific) with monoclonal antibodies to MYB (clone 1-1; Merck Millipore) and beta-actin (ab8226, Abcam, Cambridge, UK). Bands were visualized with horseradish peroxidase-conjugated secondary antibodies and chemiluminescent detection with the Supersignal West Femto Max Sensitivity Substrate (Thermo Fisher Scientific). Blots were scanned with an Amersham ImageQuant 800 imaging system (Cytiva, Marlborough, MA, USA). MYB protein expression was quantified using ImageJ v2.0.0-rc-43 and normalized with beta-actin expression.

### 2.5 Quantitative real-time PCR (qPCR)

qPCR was done with the AB 7500 Fast Real-Time PCR system using TaqMan gene expression assays (Thermo Fisher Scientific) for *MYB* (Hs00920556_m1), *CD34* (Hs00156373_m1), *CCNB1* (Hs00259126_m1), *MCM4* (Hs00381533_m1), *CDK1* (Hs00364293_m1), and the reference genes *UBC* (Hs01871556_s1) and *18S* (Hs99999901_s1). Relative gene expression was calculated by the ddCT method (32).

### 2.6 RNA-sequencing (RNA-seq)

RNA-seq was performed at Eurofins Genomics (Luxembourg City, Luxembourg) using the INVIEW Transcriptome Discover service. Library preparation was done with poly A enrichment, random primed strand-specific cDNA synthesis, adapter ligation, and adapter-specific PCR amplification. Libraries were subjected to Illumina paired-end sequencing (2x150 bps) with at least 30 million read pairs generated. Gene counts were extracted from FastQ files on the Uppsala Multidisciplinary Center for Advanced Computational Science (UPPMAX) cluster with FastQC/0.11.5, STAR v2.5.3a, Samtools v1.5, and FeatureCounts (Subread v1.5.2). Samples were analyzed with unsupervised hierarchical clustering using the *hclust* function in R and heatmaps were generated using R or Morpheus (Broad Institute). Differential gene expression was analyzed with DESeq2 v1.22.2. Gene ontology analysis was performed with ToppGene (33) and Gene set enrichment analysis (GSEA) (34) was done with GSEA v4.2.2 (Broad Institute).

### 2.7 Cell viability, cell cycle and apoptosis assays

For cell viability assays, 2,000 T-ALL cells were seeded in black 96-well plates (BD, Franklin Lakes, NJ, USA) and after 24 h treated with single or combinations of drugs. The AlamarBlue reagent (Thermo Fisher Scientific) was added to wells after 72 h and plates were analyzed with the VICTOR3 multilabel plate reader (PerkinElmer, Waltham, MA, USA). For apoptosis assays, 2,000 cells were seeded in Corning white 96-well plates (Corning, New York, USA) and treated with drugs after 24 h. The Caspase-Glo 3/7 Assay (Promega, Madison, WI, USA) was used to estimate apoptosis and luminescent signals were quantified on the VICTOR3. For cell cycle analysis, $8x10^5$ MOLT-4 cells were seeded in 6-well plates and on the next day treated for 24 h with drugs. Cells were supplemented with 10 µM BrdU during the last 4 h and then fixed and stained using the FITC BrdU Flow kit (BD). Stained cells were analyzed with an Accuri C6 flow cytometer (BD). All experiments were performed three times.

### 2.8 siRNA experiments

*MYB* siRNA-mediated knockdown was done with the Cell Line Nucleofector Kit L on the Amaxa Nucleofector II device (Cologne, Germany) using $2x10^6$ MOLT-4 cells according to the instructions provided by the manufacturer. Cells were electroporated with 1 µM Silencer Select *MYB* (s9109, s9110) or negative control siRNAs (Thermo Fisher Scientific). Total RNA and protein were isolated from transfected cells after 48 h. All experiments were done three times.

### 2.9 Statistical analysis

Unsupervised hierarchical clustering was done with R and overlap of differentially expressed genes was visualized with BioVenn (https://www.biovenn.nl) and analyzed with chi-square tests. Drug kernel density estimation plots were generated with the *density* function of the *stats* package of R (https://www.r-project.org). Correlation of treatment effects between T-ALL cell lines was estimated by Pearson correlation. Dose-response curves were generated and analyzed by nonlinear regression in Prism 9 (GraphPad Software, San Diego, CA, USA); $IC_{25}$ and $IC_{50}$ were defined as drug concentrations that reduced cell viability by 25% and 50%, respectively. For combination treatments, the definition of drug additivity and synergy was according to Bliss (35). Differences between experimentally measured effects of drug combinations and the expected effects calculated from single drug treatments were analyzed using independent samples t-test. Bar graph values are presented as mean ± SEM. Differences between groups in qPCR, cell cycle, and apoptosis analyses were evaluated with one-way ANOVA or independent samples t-test. All statistical tests were two-sided. A *P*-value of less than 0.05 was considered statistically significant.

## 3 Results

### 3.1 Large-scale drug screening identifies synthetic oleanane triterpenoids as inhibitors of *MYB* gene expression in T-ALL cells

We performed a large-scale *in vitro* screening of two T-ALL cell lines, CCRF-CEM and MOLT-4, with *MYB*-activation using 768 small-molecule drugs from the L1100 Inhibitor Library (Figure 1, Supplementary Table S1). Cells were treated with 1 µM of inhibitors for 48 h after which relative *MYB* mRNA levels were analyzed by qPCR. Density plots of *MYB* gene expression following drug treatments showed similar distributions in three independent experiments for each cell line (Figure 1A). There was a significant ($P < 0.0001$) correlation between drug effects in the two cell lines (Figure 1B). A larger number of drugs reduced *MYB* mRNA levels in CCRF-CEM cells compared with MOLT-4 cells (Figure 1A). Further analysis showed that 46 drugs caused a greater than 50% decrease in *MYB* gene expression in both cases (Figure 1C). These

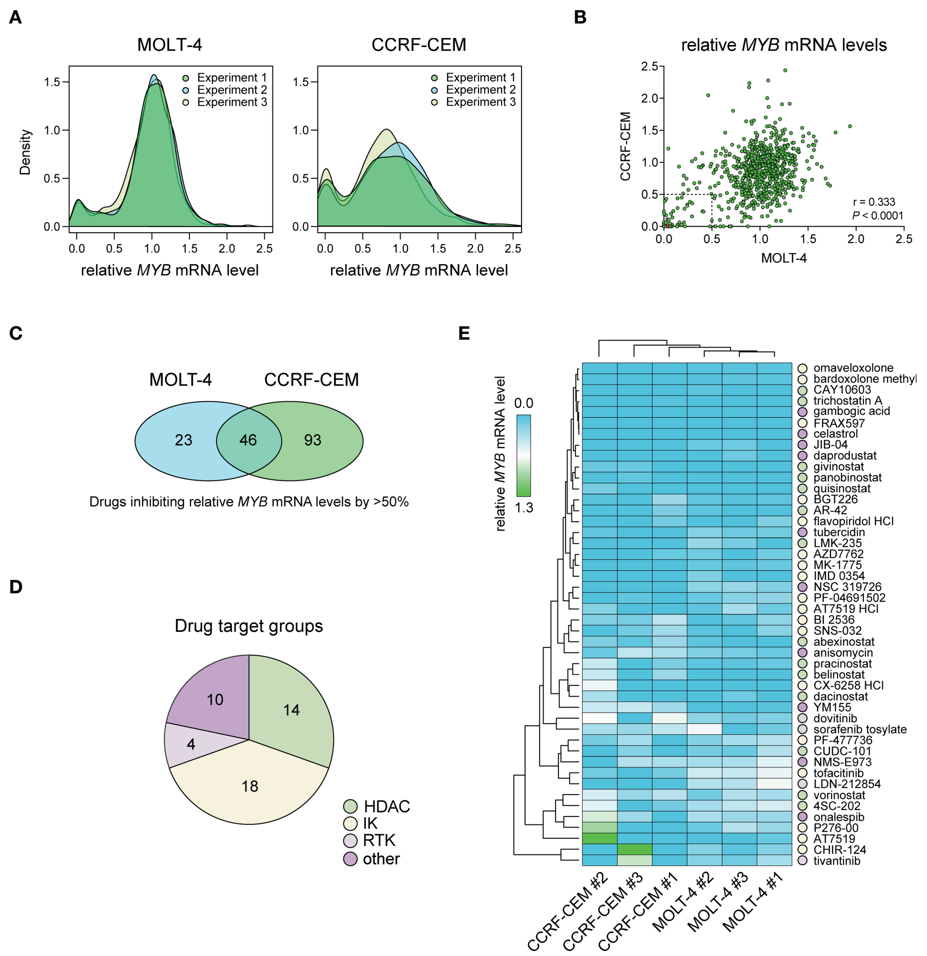

FIGURE 1
Drug screening for inhibitors of *MYB* gene expression in T-ALL cells with *MYB* gene activation. **(A)** Density plots showing treatment effects of 768 small-molecule inhibitors on *MYB* gene expression in two T-ALL cell lines. Data is derived from three independent experiments. **(B)** Pearson correlation analysis of treatment response for 768 inhibitors in two T-ALL cell lines. Dashed lines indicate thresholds for 50% *MYB* mRNA expression compared with DMSO treated control cells. The red dot shows bardoxolone methyl and omaveloxolone that had near identical effects on *MYB* expression in the screen. **(C)** Venn diagram showing the number of drugs reducing *MYB* gene expression with more than 50% in T-ALL cells. **(D)** Drug target groups of 46 inhibitors reducing *MYB* mRNA levels with more than 50% in two T-ALL cell lines. **(E)** Heat map and hierarchical clustering analyses showing the effects of 46 inhibitors on *MYB* gene expression. Drug targets with grouping as in D are indicated. IK, intracellular kinase; RTK, receptor tyrosine kinase; HDAC, histone deacetylase.

agents included histone-deacetylase inhibitors (HDACi), intracellular kinase (IK) inhibitors, receptor tyrosine kinase (RTK) inhibitors, and other drugs with diverse targets (Figure 1D, Supplementary Table S2). Among these were drugs that were previously identified as inhibitors of *MYB* gene expression (AT7519, flavopiridol, givinostat, and vorinostat) (36–39) as well as an inhibitor of MYB protein activity (celastrol) (12). To validate our drug screen, we treated MOLT-4 cells with two of the identified HDACi (givinostat and panobinostat) and two of the cyclin-dependent kinase inhibitors (CDKi) (AT7519 and SNS-032) from the screen. All tested drugs significantly decreased *MYB* mRNA levels at nanomolar concentrations (Supplementary Figure S1). We next used hierarchical clustering and heat map analysis of *MYB* mRNA levels to investigate the potency of the inhibitors of *MYB* gene expression identified in our screen (Figure 1E). These analyses identified bardoxolone methyl and omaveloxolone, two related oleanane triterpenoids (OTs), as top hits in the screen.

## 3.2 Treatment of T-ALL cells with OTs leads to downregulation of MYB expression and downstream target genes

To confirm the effects of OT treatment on *MYB* gene expression in T-ALL cells, we treated MOLT-4, CCRF-CEM, P12-ICHIKAWA, and RPMI-8402 cells with nanomolar concentrations of bardoxolone methyl or omaveloxolone for 24 h. This treatment led to a dose-dependent decrease in *MYB* mRNA levels in all T-ALL cell lines tested (Figure 2A, Supplementary Figure S2). A corresponding reduction in MYB protein levels after OT treatment was confirmed by immunoblotting (Figure 2B, Supplementary Figure S3A). To investigate the biological consequences of MYB suppression in OT treated cells, we analyzed the expression of known MYB target genes involved in cell cycle regulation and leukemic stem cell function. The expression of *CCNB1*, *CDK1*, *MCM4*, and *CD34* were

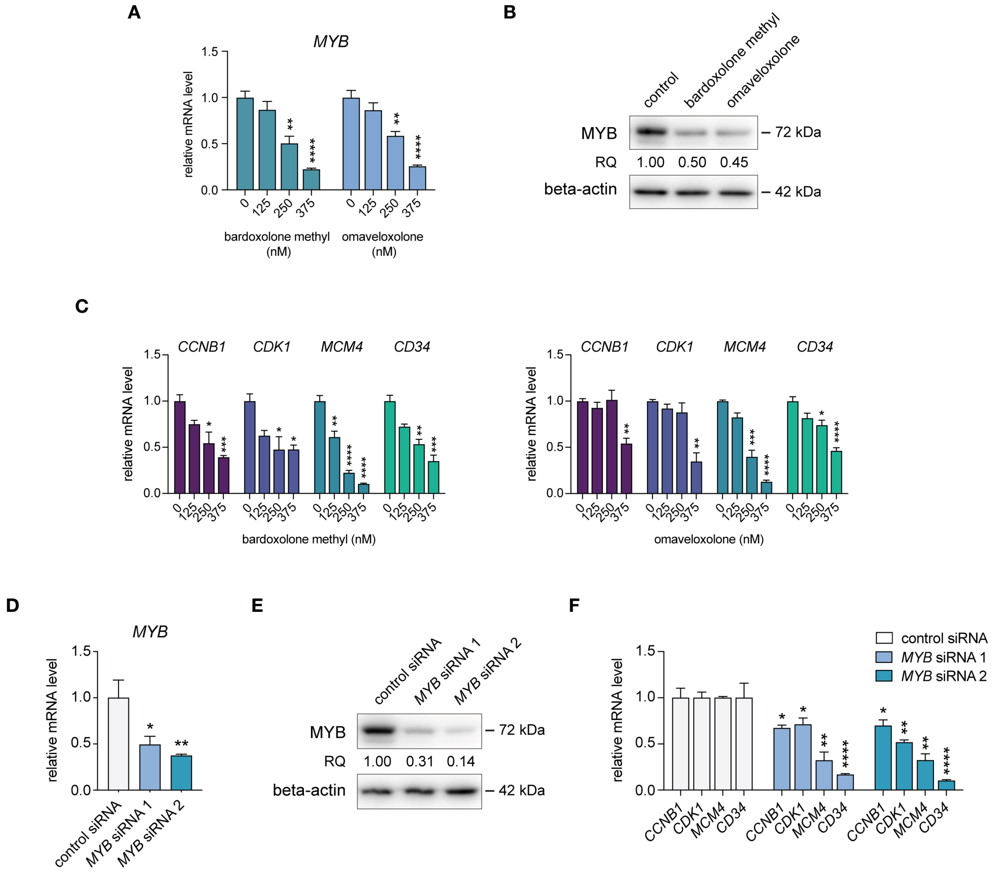


FIGURE 2
Treatment with oleanane triterpenoids (OTs) leads to decreased expression of MYB and its downstream target genes. **(A)** *MYB* mRNA expression in MOLT-4 cells treated with bardoxolone methyl and omaveloxolone for 24 h. **(B)** MYB protein expression in MOLT-4 cells treated for 24 h with 250 nM OTs. **(C)** Expression of MYB downstream target genes in MOLT-4 cells treated as in **(A, D)** Knockdown of *MYB* mRNA in MOLT-4 cells after treatment with 1 μM of *MYB* siRNAs for 48 h. **(E)** MYB protein expression in MOLT-4 cells treated with *MYB* siRNAs as in **(D, F)** Expression of MYB downstream target genes after *MYB* knockdown as in D and **(E)** Error bars indicate standard error of the mean. One-way ANOVA test (* $P < 0.05$; ** $P < 0.01$; *** $P < 0.001$; **** $P < 0.0001$). Data shown represents one of three independent experiments. RQ, relative quantification of MYB protein levels normalized with beta-actin expression.

significantly downregulated in MOLT-4 cells with OT treatment (Figure 2C). To verify that these genes are regulated by MYB in T-ALL cells, we knocked down *MYB* mRNA and protein levels in MOLT-4 cells using siRNAs (Figures 2D, E, Supplementary Figure S3B). Analogous to treatment with OTs, transfection with *MYB* siRNAs resulted in downregulation of *CCNB1*, *CDK1*, *MCM4*, and *CD34* (Figure 2F). Our results indicate that these genes are MYB targets in T-ALL that are downregulated following OT treatment.

Both bardoxolone methyl and omaveloxolone inhibit NF-κB (40, 41), a signaling pathway that has been shown to positively regulate *MYB* transcription in murine erythroleukemia cells (42, 43). To test whether NF-κB signaling is involved in *MYB* gene regulation also in human T-ALL cells, we treated MOLT-4 cells with two IKK-1 and IKK-2 inhibitors and measured *MYB* mRNA levels by qPCR (Supplementary Figure S4A). Neither of these inhibitors decreased *MYB* gene expression, which may indicate that OTs downregulate *MYB* gene activity independently of NF-κB signaling in T-ALL cells. Similarly, treatment with the cell-penetrating NRF2-activating peptide KI696 (30, 44) did not affect *MYB* gene expression in T-ALL cells (Supplementary Figure S4B), suggesting that OTs target other pathways than NF-κB and NRF2 to regulate the *MYB* gene in T-ALL cells.

## 3.3 RNA-seq reveals molecular signatures associated with a reversed MYB-driven transcriptional program and induction of apoptosis in OT treated T-ALL cells

To study the effects of OT treatment on critical cellular processes in T-ALL cells, we performed RNA-seq analysis of MOLT-4 cells treated with 375 nM bardoxolone methyl or omaveloxolone for 24 h. Global gene expression analysis showed that OT treated cells clustered separately from control cells (Figure 3A). There was a significant overlap of differentially regulated genes between the two drugs (Figures 3A–C). To

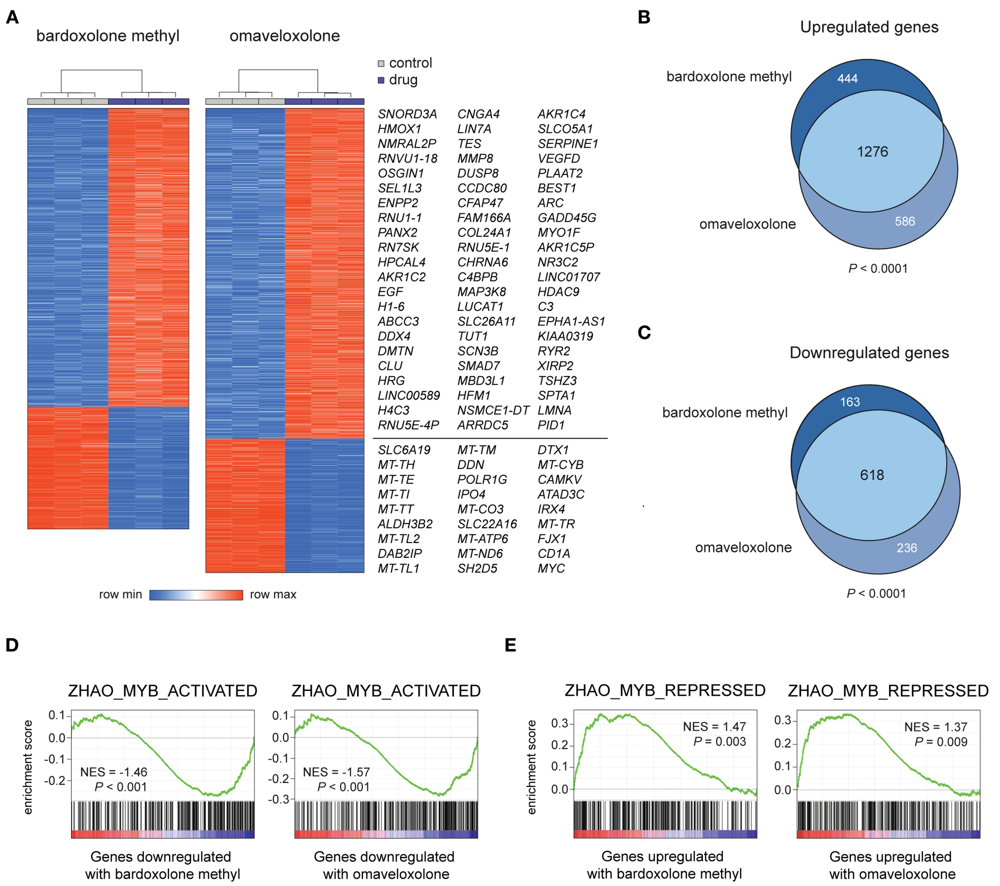


FIGURE 3
RNA-seq analysis of OT treated T-ALL cells. **(A)** Hierarchical clustering and heatmap analysis of global gene expression data from MOLT-4 cells treated for 24 h with 375 nM OTs. The most up- and downregulated genes by both drugs are shown to the right. **(B, C)** Venn diagrams of up- and downregulated genes in OT treated T-ALL cells. The significance of overlap was estimated by chi-square tests. **(D, E)** Gene set enrichment analysis of MYB-activated and repressed genes in OT treated T-ALL cells. NES, normalized enrichment score.

investigate if OT treatment affects the MYB-driven transcriptional program in T-ALL cells, we used GSEA to compare our RNA-seq data with a previously published dataset (45) of direct MYB target genes in hematopoietic progenitor cells (Figures 3D, E). OT treatment downregulated genes that are normally activated by MYB (e.g. *MYC*, *TCF7*, *MAT2A*) and upregulated known MYB-repressed genes (e.g. *CEBPB*, *IL17RA*, *BCL6*). Thus, our findings indicate that treatment with bardoxolone methyl and omaveloxolone can reverse the MYB-driven transcriptional program in T-ALL cells. GSEA also revealed activation of the p53 and apoptosis pathways in OT treated cells as well as decreased expression of genes regulating cell cycle progression, metabolism, and DNA repair (Figures 4A, B). Moreover, gene ontology analysis showed that genes upregulated by OT treatment are involved in cell differentiation and cell morphogenesis (Figure 4C) whereas genes downregulated are involved in ribosome biogenesis, RNA processing/metabolism, and nucleotide synthesis (Figure 4D). These results imply impaired synthesis of nucleic acids, RNA maturation, and translation in OT treated cells. Taken together, our RNA-seq data indicate that OT treatment reverses a MYB-driven gene expression program, inhibits cell proliferation, and induces differentiation and apoptosis in T-ALL cells.

## 3.4 Treatment of *MYB*-activated T-ALL cells with OTs results in apoptosis and decreased cell proliferation

To investigate if T-ALL cell viability is affected by treatment with OTs, we treated T-ALL cell lines derived from four cases with 50-1000 nM of bardoxolone methyl or omaveloxolone for 72 h (Figure 5A). The treatments resulted in a dose-dependent decrease in cell viability at nanomolar concentrations. There was also a significant induction of apoptosis in T-ALL cells after treatment with both drugs (Figure 5B). Importantly, HMC control cells were unaffected at low nanomolar concentrations and showed markedly less apoptosis at 500 nM compared with T-ALL cells. Cell cycle analysis showed that OT treated T-ALL cells displayed a marked G2/M arrest (Figure 5C). This was in agreement with both OT treatment and *MYB* knockdown causing a decreased expression of the G2 regulating genes *CCNB1* and *CDK1* (Figures 2C, F). OT treated cells also displayed a reduced entry into the S phase and an increased accumulation of apoptotic cells in sub G1 (Figure 5C). These results, which corroborate our findings from the global gene expression analysis (Figures 3, 4), show that T-ALL cells are sensitive to OT treatment.

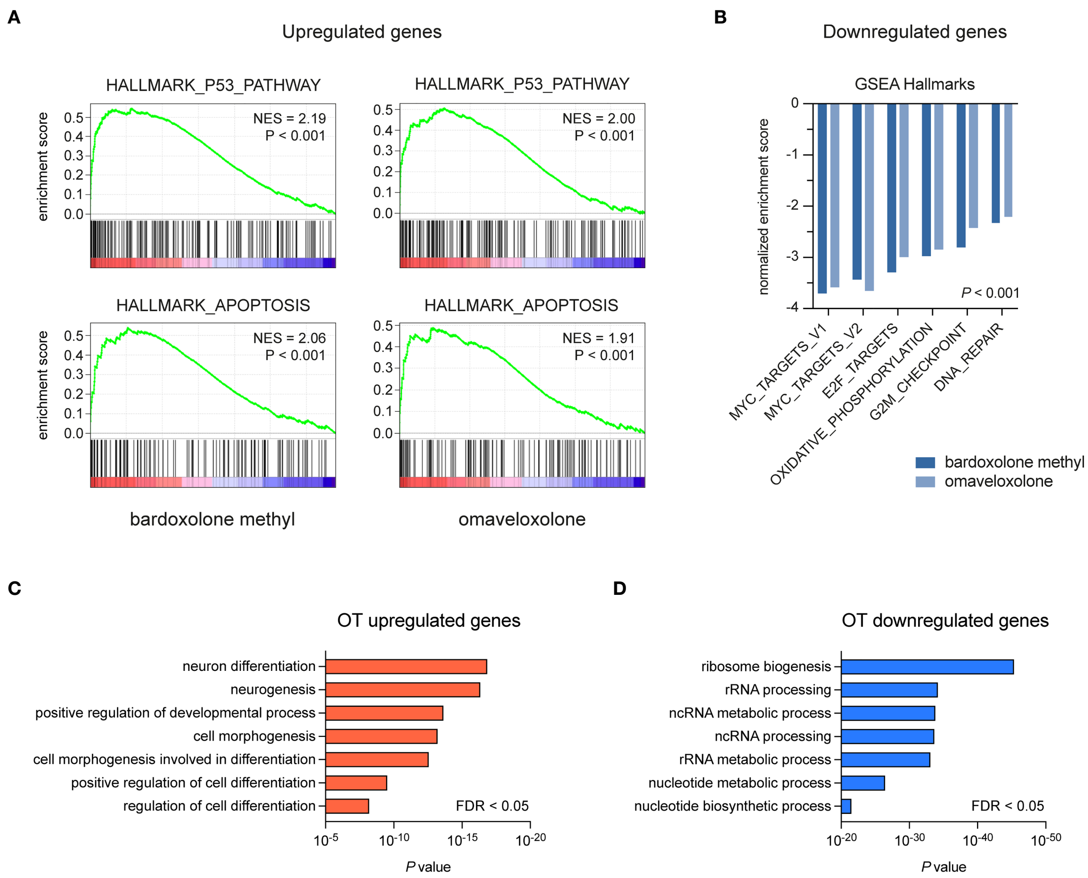


FIGURE 4
Gene set enrichment and gene ontology analysis of OT treated T-ALL cells. **(A, B)** Gene set enrichment analysis of pathways and gene sets affected by OT treatment in MOLT-4 cells. **(C, D)** Gene ontology analysis of up- and downregulated genes following OT treatment. NES, normalized enrichment score. FDR, false-discovery rate.

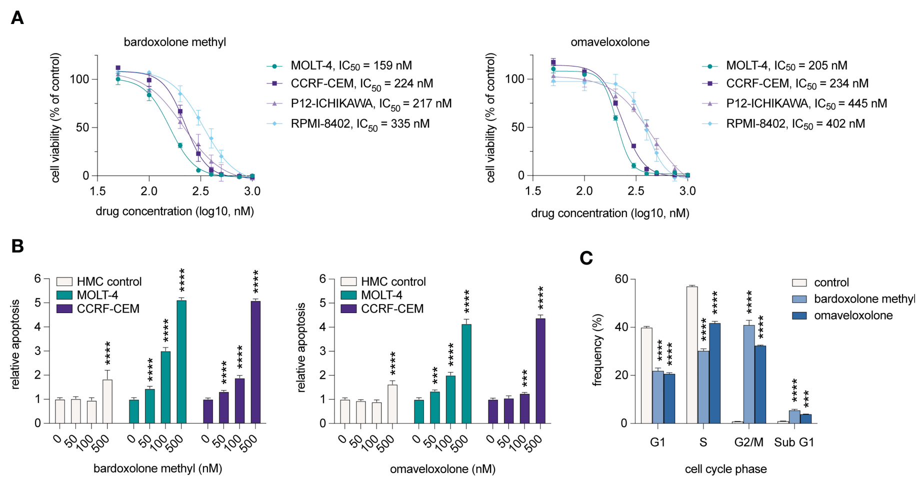


FIGURE 5
OT treatment leads to G2/M arrest, decreased cell viability, and induction of apoptosis in T-ALL cells. **(A)** Cell viability of T-ALL cells treated with OTs for 72 h. Data points represent the average of three independent experiments. Error bars indicate standard error of the mean. $IC_{50}$ is defined as the drug concentration reducing cell viability by 50%. **(B)** Apoptosis as measured by caspase 3/7 activity after 48 h of treatment with OTs. **(C)** Cell cycle distribution of MOLT-4 cells after 24 h treatment with 250 nM OTs. Error bars indicate standard error of the mean. One-way ANOVA test (*** $P < 0.001$; **** $P < 0.0001$). Data shown represents one of three independent experiments. HMC, human mononuclear cells isolated from a healthy donor.

## 3.5 OT treatment sensitizes T-ALL cells to chemotherapy

Since genes involved in DNA repair were downregulated following OT treatment (Figure 4B), we tested whether the OTs could synergize with the DNA-damaging agent doxorubicin that is part of the standard therapy of T-ALL. Treatments with bardoxolone methyl or omaveloxolone combined with doxorubicin at $IC_{25}$ and $IC_{50}$ concentrations (Figure 5A, Supplementary Figure S5) resulted in a significant synergistic decrease in cell viability at both concentrations in MOLT-4 cells (Figure 6). These results suggest that synthetic OTs may sensitize T-ALL cells to chemotherapy.

# 4 Discussion

The *MYB* oncogene is an oncogenic driver in the majority of leukemias and encodes a master transcription factor with critical roles in cell proliferation, cell survival, and leukemic stem cell maintenance (4). To find novel inhibitors of *MYB* gene expression, we have now performed a large-scale screening to identify drugs with inhibitory effects on *MYB* mRNA expression in T-ALL cells with constitutive *MYB* gene activation.

Notably, the most potent inhibitors of *MYB* gene expression in our drug screen were bardoxolone methyl and omaveloxolone, two structurally related synthetic OTs that inhibit NF-κB and activate NRF2 signaling (46, 47). Treatment with bardoxolone methyl and omaveloxolone led to downregulation of *MYB* mRNA and protein levels and decreased expression of MYB downstream target genes in a dose-dependent manner. The OTs also negatively affected cell proliferation and viability of T-ALL cells through induction of a marked G2/M arrest, apoptosis, and differentiation. Since both NF-κB pathway inhibition and NRF2 activation failed to downregulate *MYB* gene expression in T-ALL cells, this suggests that the two OT drugs act through alternative mechanisms to inhibit *MYB* activity. Our results indicate that the OTs inhibit one or more positive regulators of *MYB* gene expression in T-ALL cells, possibly independent of NF-κB and NRF2-signaling.

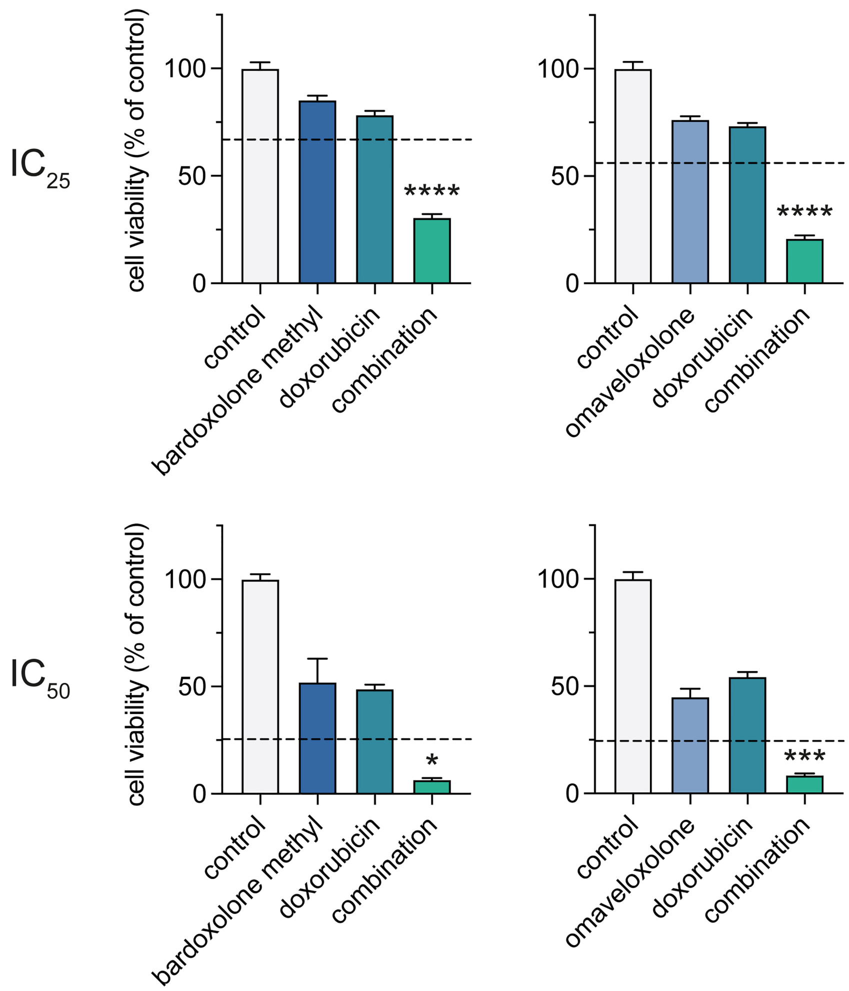


FIGURE 6
Combined treatment with OTs and doxorubicin leads to a synergistic reduction in cell viability of T-ALL cells. Cell viability of MOLT-4 cells after treatment with $IC_{25}$ and $IC_{50}$ concentrations of bardoxolone methyl or omaveloxolone combined with doxorubicin for 72 h. The expected additive effects of combination treatments, as predicated by Bliss interaction, are indicated with dashed lines. Independent samples t-test (* $P < 0.05$; *** $P < 0.001$; **** $P < 0.0001$). Error bars indicate standard error of the mean. Data shown represents one of three independent experiments.

OTs are natural compounds present in a large number of dietary and medicinal plants (48). Synthetic OTs such as bardoxolone methyl and omaveloxolone are generated by chemical modification of oleanolic acid and have anti-inflammatory and anticarcinogenic properties. We have now, for the first time, identified members of this group of compounds as potent inhibitors of *MYB* gene expression. OTs mediate their pharmacological effects in part by interaction with sulfhydryl groups of cysteine residues through Michael addition, yet do not bind non-discriminately to all cysteine-containing proteins (49). Instead, OT binding is markedly influenced by the accessibility of the drug to a specific cysteine residue and the redox potential of the cell. Thus, individual OTs are expected to have different target proteins depending on the cellular context. In addition to targeting the NF-κB and NRF2 pathways, synthetic OTs negatively affect proliferation by inhibiting specific proteins involved in the JAK/STAT and PI3K/AKT/mTOR signaling pathways (49). These pathways may regulate *MYB* expression in T-ALL cells as several JAK/STAT and PI3K/AKT/mTOR inhibitors were among the top hits in our drug screen. Moreover, mTOR signaling has previously been shown to regulate *MYB* expression in normal human T-cells (50). Previous studies have shown that OTs also may induce cell differentiation (49). Similarly, we found that genes involved in positive regulation of differentiation were upregulated in T-ALL cells following treatment with bardoxolone methyl or omaveloxolone. Since the hematopoietic progenitor marker *CD34* (51) was downregulated by both OTs and MYB knockdown, this suggests that the differentiation seen following OT treatment is, at least partly, mediated by decreased MYB expression in T-ALL cells. This conclusion is further supported by studies showing that MYB expression is high in immature and progenitor-like cells and suppress differentiation of both normal and leukemic cells (7, 26).

Bardoxolone methyl is in late clinical stage development for treatment of chronic kidney disease and omaveloxolone recently received FDA approval for treatment of Friedreich's ataxia. These drugs are currently used in several active and completed clinical trials in which they have demonstrated acceptable adverse effects (https://clinicaltrials.gov). In the present study, the two OTs were active in the low nanomolar range in T-ALL cells whereas normal bone marrow-derived cells were unaffected at these concentrations. Thus, there may be a therapeutic window for these drugs to be repurposed for use in T-ALL patients with acceptable side-effects. Notably, both bardoxolone methyl and omaveloxolone showed a synergistic negative effect on T-ALL cell viability when used in combination with the cytotoxic DNA-damaging agent doxorubicin, which is part of the standard therapy of T-ALL. Since the expression of DNA repair genes was attenuated following treatment, suppression of DNA repair may be part of the underlying mechanism that sensitizes T-ALL cells to combined treatment with OTs and doxorubicin. However, further studies are needed to determine the association between OT treatment, DNA repair, and sensitivity to chemotherapy in T-ALL. It would also be interesting to study the effects of OTs in combination with other drugs such as for example angiogenesis or NOTCH inhibitors (52, 53). Taken together, our studies suggest that bardoxolone methyl and omaveloxolone are new potential drugs for treatment of T-ALL.

Other drugs that we identified with potent inhibitory effects on *MYB* gene expression included several HDACi (e.g. givinostat, panobinostat, quisinostat) and CDKi (e.g. AT7519, SNS-032, p276-00). Previous studies have shown that HDACi (e.g. givinostat and vorinostat, also identified in our screen) downregulate *MYB* gene expression in myeloproliferative neoplasms and myeloid leukemias (36, 39). Here, we identified HDACi as potent inhibitors of *MYB* gene expression also in lymphoid leukemia cells, suggesting a conserved mechanism of *MYB* gene regulation in neoplasms of both the myeloid and lymphoid lineages. Our findings, and those of others (36, 39, 54), thus support the involvement of chromatin remodeling in the regulation of the *MYB* gene. Notably, several CDK9 inhibitors had also inhibitory effects on *MYB* gene expression in our drug screen. The inhibitory effect on *MYB* gene activity by these inhibitors is most likely a result of blocked transcription, since *MYB* gene expression is known to be positively regulated by the transcriptional elongation factor P-TEFb (which includes CDK9) and is inhibited by CDKi (e.g. AT7519 and flavopiridol, also identified in our screen) in breast cancer cells (37, 38). Notably, the plant-derived triterpenoid celastrol was one of the top hits in our screen. Celastrol was previously reported as an inhibitor of MYB transcriptional activity in AML cells (12) and, like the OTs identified here, forms covalent Michael adducts with target proteins (55). This suggests similar mechanisms of *MYB* inhibition by celastrol, bardoxolone methyl, and omaveloxolone. In contrast to the synthetic OTs identified in our screen, celastrol is a natural compound that cause severe side effects, has low bioavailability and poor water solubility, which have hindered its clinical application (56). A number of other MYB inhibitors have been identified with therapeutic effects on AML cells (13–24). It would be interesting to test if these inhibitors also have anti-leukemic effects in MYB-driven T-ALL cells. Only one of these, mebendazole, has to our knowledge been tested and shown effects in T-ALL preclinical models (25). However, many of these inhibitors, unlike the OTs found in our study, are early-stage experimental drugs that have not been tested in humans or show poor pharmacokinetics and/or toxicity. Future studies will evaluate the potential of these inhibitors as new therapies for T-ALL.

Targeting the *MYB* oncogene in a clinical setting will require information about the *MYB* activation status. Since the mechanism of activation of *MYB* varies in T-ALL, analysis of the expression of *MYB* by RT-PCR, RNA-seq or immunohistochemistry are the preferable methods to determine whether the gene is activated or not (57). T-ALL patients with overexpression of *MYB* are thus candidates for MYB inhibitory treatments, whereas those with low or undetectable *MYB* levels are not. *MYB* expression analysis will be crucial for stratification of patients in clinical trials using MYB inhibitors.

A limitation of this study is the lack of testing of bardoxolone methyl and omaveloxolone in *in vivo* T-ALL models and patient primary cells. However, we could demonstrate that normal bone marrow-derived cells are largely unaffected by the drugs compared with T-ALL cells. This is in line with the fact that the drugs show low toxicity in clinical trials (49). Furthermore, the mechanism by which the OTs negatively affect *MYB* expression is unknown. We believe that the drugs may act by similar mechanisms as celastrol, which blocks MYB activity in AML (12), but they may also regulate *MYB* expression through inhibition of for example JAK/STAT and/

or PI3K/AKT/mTOR signaling. OTs do not fit the single-target paradigm and has multiple molecular targets, yet they show low cytotoxicity in normal cells (49). This multifunctionality may be an advantage in order to potentiate treatment and to avoid drug resistance. In T-ALL, multiple driver events, in addition to MYB activation, is involved in the pathogenesis of the disease, including *NOTCH1* mutations and loss of *CDK2NA* (11). This strongly implies that inhibition of MYB must be combined with targeting of additional pathways for successful treatment.

In conclusion, we have identified several novel suppressors of *MYB* gene expression by large-scale drug screening of cultured T-ALL cells with constitutive *MYB* gene activation. In particular, the structurally related OTs bardoxolone methyl and omaveloxolone demonstrated potent inhibitory effects on *MYB* gene expression and MYB downstream targets, and induced apoptosis in *MYB* gene activated T-ALL cells. Notably, these drugs sensitized T-ALL cells in culture to DNA-damaging chemotherapy. Our results indicate that both bardoxolone methyl and omaveloxolone may synergize with the standard treatment of T-ALL but also have the potential to improve current therapies of other MYB-driven malignancies.

## Data availability statement

The datasets presented in this study can be found in online repositories. The names of the repository/repositories and accession number(s) can be found below: https://www.ncbi.nlm.nih.gov/sra/PRJNA811771.

## Author contributions

MA conceptualized, designed, and supervised the study. PN, TT, AA, AF, and MA performed experiments. PN, TT, AA, AF, GS, and MA analyzed data. GS and MA provided project resources. MA drafted the manuscript. All authors reviewed and edited the manuscript. All authors contributed to the article and approved the submitted version.

## Funding

This work was funded by the Swedish Childhood Cancer Fund (PR2020-0015), the Swedish Cancer Society (CAN 21 1773), Mary Béves Foundation for Child Cancer Research (2018-04), the Magnus Bergvall Foundation (2017-02214), and the AG-Fond (FB 17-93).

## Acknowledgments

Resources for RNA-seq analysis were provided by SNIC through Uppsala Multidisciplinary Center for Advanced Computational Science (UPPMAX) under project SNIC 2021/22-661. The authors thank Dr. Volkan Sayin for the KI696 peptide.

## Conflict of interest

The authors declare that the research was conducted in the absence of any commercial or financial relationships that could be construed as a potential conflict of interest.

## Publisher's note

All claims expressed in this article are solely those of the authors and do not necessarily represent those of their affiliated organizations, or those of the publisher, the editors and the reviewers. Any product that may be evaluated in this article, or claim that may be made by its manufacturer, is not guaranteed or endorsed by the publisher.

## Supplementary material

The Supplementary Material for this article can be found online at: https://www.frontiersin.org/articles/10.3389/fonc.2023.1126354/full#supplementary-material

## References

1. Hunger SP, Mullighan CG. Acute lymphoblastic leukemia in children. *N Engl J Med* (2015) 373(16):1541–52. doi: 10.1056/NEJMra1400972

2. Terwilliger T, Abdul-Hay M. Acute lymphoblastic leukemia: A comprehensive review and 2017 update. *Blood Cancer J* (2017) 7(6):e577. doi: 10.1038/bcj.2017.53

3. Marks DI, Rowntree C. Management of adults with T-cell lymphoblastic leukemia. *Blood* (2017) 129(9):1134–42. doi: 10.1182/blood-2016-07-692608

4. Pattabiraman DR, Gonda TJ. Role and potential for therapeutic targeting of myb in leukemia. *Leukemia* (2013) 27(2):269–77. doi: 10.1038/leu.2012.225

5. Fuglerud BM, Lemma RB, Wanichawan P, Sundaram AYM, Eskeland R, Gabrielsen OS. A c-myb mutant causes deregulated differentiation due to impaired histone binding and abrogated pioneer factor function. *Nucleic Acids Res* (2017) 45 (13):7681–96. doi: 10.1093/nar/gkx364

6. Mansour MR, Abraham BJ, Anders L, Berezovskaya A, Gutierrez A, Durbin AD, et al. Oncogene regulation. an oncogenic super-enhancer formed through somatic mutation of a noncoding intergenic element. *Science* (2014) 346(6215):1373–7. doi: 10.1126/science.1259037

7. Lahortiga I, De Keersmaecker K, Van Vlierberghe P, Graux C, Cauwelier B, Lambert F, et al. Duplication of the myb oncogene in T cell acute lymphoblastic leukemia. *Nat Genet* (2007) 39(5):593–5. doi: 10.1038/ng2025

8. Sanda T, Lawton LN, Barrasa MI, Fan ZP, Kohlhammer H, Gutierrez A, et al. Core transcriptional regulatory circuit controlled by the Tal1 complex in human T cell acute lymphoblastic leukemia. *Cancer Cell* (2012) 22(2):209–21. doi: 10.1016/j.ccr.2012.06.007

9. Zuber J, Rappaport AR, Luo W, Wang E, Chen C, Vaseva AV, et al. An integrated approach to dissecting oncogene addiction implicates a myb-coordinated self-renewal program as essential for leukemia maintenance. *Genes Dev* (2011) 25(15):1628–40. doi: 10.1101/gad.17269211

10. Clappier E, Cuccuini W, Kalota A, Crinquette A, Cayuela JM, Dik WA, et al. The c-myb locus is involved in chromosomal translocation and genomic duplications in

human T-cell acute leukemia (T-all), the translocation defining a new T-all subtype in very young children. *Blood* (2007) 110(4):1251–61. doi: 10.1182/blood-2006-12-064683

11. Liu Y, Easton J, Shao Y, Maciaszek J, Wang Z, Wilkinson MR, et al. The genomic landscape of pediatric and young adult T-lineage acute lymphoblastic leukemia. *Nat Genet* (2017) 49(8):1211–8. doi: 10.1038/ng.3909

12. Uttarkar S, Dasse E, Coulibaly A, Steinmann S, Jakobs A, Schomburg C, et al. Targeting acute myeloid leukemia with a small molecule inhibitor of the Myb/P300 interaction. *Blood* (2016) 127(9):1173–82. doi: 10.1182/blood-2015-09-668632

13. Ramaswamy K, Forbes L, Minuesa G, Gindin T, Brown F, Kharas MG, et al. Peptidomimetic blockade of myb in acute myeloid leukemia. *Nat Commun* (2018) 9 (1):110. doi: 10.1038/s41467-017-02618-6

14. Walf-Vorderwulbecke V, Pearce K, Brooks T, Hubank M, van den Heuvel-Eibrink MM, Zwaan CM, et al. Targeting acute myeloid leukemia by drug-induced c-myb degradation. *Leukemia* (2018) 32(4):882–9. doi: 10.1038/leu.2017.317

15. Xu Y, Milazzo JP, Somerville TDD, Tarumoto Y, Huang YH, Ostrander EL, et al. A tfiid-saga perturbation that targets myb and suppresses acute myeloid leukemia. *Cancer Cell* (2018) 33(1):13–28 e8. doi: 10.1016/j.ccell.2017.12.002

16. Yusenko M, Jakobs A, Klempnauer KH. A novel cell-based screening assay for small-molecule myb inhibitors identifies podophyllotoxins teniposide and etoposide as inhibitors of myb activity. *Sci Rep* (2018) 8(1):13159. doi: 10.1038/s41598-018-31620-1

17. Yusenko MV, Trentmann A, Andersson MK, Ghani LA, Jakobs A, Arteaga Paz MF, et al. Monensin, a novel potent myb inhibitor, suppresses proliferation of acute myeloid leukemia and adenoid cystic carcinoma cells. *Cancer Lett* (2020) 479:61–70. doi: 10.1016/j.canlet.2020.01.039

18. Joy ST, Henley MJ, De Salle SN, Beyersdorf MS, Vock IW, Huldin AJL, et al. A dual-site inhibitor of Cbp/P300 kix is a selective and effective modulator of myb. *J Am Chem Soc* (2021) 143(37):15056–62. doi: 10.1021/jacs.1c04432

19. Yusenko MV, Biyanee A, Andersson MK, Radetzki S, von Kries JP, Stenman G, et al. Proteasome inhibitors suppress myb oncogenic activity in a P300-dependent manner. *Cancer Lett* (2021) 520:132–42. doi: 10.1016/j.canlet.2021.07.010

20. Yusenko MV, Biyanee A, Frank D, Kohler LHF, Andersson MK, Khandanpour C, et al. Bcr-tmp, a novel nanomolar-active compound that exhibits both myb- and microtubule-inhibitory activity. *Cancers (Basel)* (2021) 14(1):43. doi: 10.3390/cancers14010043

21. Yusenko MV, Trentmann A, Casolari DA, Abdel Ghani L, Lenz M, Horn M, et al. C/Ebpbeta is a myb- and P300-cooperating pro-leukemogenic factor and promising drug target in acute myeloid leukemia. *Oncogene* (2021) 40(29):4746–58. doi: 10.1038/s41388-021-01800-x

22. Biyanee A, Yusenko MV, Klempnauer KH. Src-family protein kinase inhibitors suppress myb activity in a P300-dependent manner. *Cells* (2022) 11(7):1162. doi: 10.3390/cells11071162

23. Clesham K, Walf-Vorderwulbecke V, Gasparoli L, Virely C, Cantilena S, Tsakaneli A, et al. Identification of a c-Myb-Directed therapeutic for acute myeloid leukemia. *Leukemia* (2022) 36(6):1541–9. doi: 10.1038/s41375-022-01554-9

24. Suetaka S, Oka Y, Kunihara T, Hayashi Y, Arai M. Rational design of a helical peptide inhibitor targeting c-Myb-Kix interaction. *Sci Rep* (2022) 12(1):816. doi: 10.1038/s41598-021-04497-w

25. Smith C, Touzart A, Simonin M, Tran-Quang C, Hypolite G, Latiri M, et al. Harnessing the myb-dependent Tal1 5'super-enhancer for targeted therapy in T-all. *Mol Cancer* (2023) 22(1):12. doi: 10.1186/s12943-022-01701-x

26. Ramsay RG, Gonda TJ. Myb function in normal and cancer cells. *Nat Rev Cancer* (2008) 8(7):523–34. doi: 10.1038/nrc2439

27. Foley GE, Lazarus H, Farber S, Uzman BG, Boone BA, McCarthy RE. Continuous culture of human lymphoblasts from peripheral blood of a child with acute leukemia. *Cancer* (1965) 18:522–9. doi: 10.1002/1097-0142(196504)18:4<522::aid-cncr2820180418>3.0.co;2-j

28. Huang CC, Hou Y, Woods LK, Moore GE, Minowada J. Cytogenetic study of human lymphoid T-cell lines derived from lymphocytic leukemia. *J Natl Cancer Inst* (1974) 53(3):655–60. doi: 10.1093/jnci/53.3.655

29. Watanabe S, Shimosato Y, Kameya T, Kuroki M, Kitahara T, Minato K, et al. Leukemic distribution of a human acute lymphocytic leukemia cell line (Ichikawa strain) in nude mice conditioned with whole-body irradiation. *Cancer Res* (1978) 38 (10):3494–8.

30. Davies TG, Wixted WE, Coyle JE, Griffiths-Jones C, Hearn K, McMenamin R, et al. Monoacidic inhibitors of the kelch-like ech-associated protein 1: Nuclear factor erythroid 2-related factor 2 (Keap1:Nrf2) protein-protein interaction with high cell potency identified by fragment-based discovery. *J Med Chem* (2016) 59(8):3991–4006. doi: 10.1021/acs.jmedchem.6b00228

31. Svec D, Dolatabadi S, Thomsen C, Cordes N, Shannon M, Fitzpatrick P, et al. Identification of inhibitors regulating cell proliferation and fus-Ddit3 expression in myxoid liposarcoma using combined DNA, mrna, and protein analyses. *Lab Invest* (2018) 98(7):957–67. doi: 10.1038/s41374-018-0046-3

32. Livak KJ, Schmittgen TD. Analysis of relative gene expression data using real-time quantitative pcr and the 2(-delta delta C(T)) method. *Methods* (2001) 25(4):402–8. doi: 10.1006/meth.2001.1262

33. Chen J, Bardes EE, Aronow BJ, Jegga AG. Toppgene suite for gene list enrichment analysis and candidate gene prioritization. *Nucleic Acids Res* (2009) 37 (Web Server issue):W305–11. doi: 10.1093/nar/gkp427

34. Subramanian A, Tamayo P, Mootha VK, Mukherjee S, Ebert BL, Gillette MA, et al. Gene set enrichment analysis: A knowledge-based approach for interpreting genome-wide expression profiles. *Proc Natl Acad Sci U.S.A.* (2005) 102(43):15545–50. doi: 10.1073/pnas.0506580102

35. Bliss CI. The toxicity of poisons applied jointly. *Ann Appl Biol* (1939) 26(3):585–615. doi: 10.1111/j.1744-7348.1939.tb06990.x

36. Amaru Calzada A, Todoerti K, Donadoni L, Pellicioli A, Tuana G, Gatta R, et al. The hdac inhibitor givinostat modulates the hematopoietic transcription factors Nfe2 and c-myb in Jak2(V617f) myeloproliferative neoplasm cells. *Exp Hematol* (2012) 40 (8):634–45 e10. doi: 10.1016/j.exphem.2012.04.007

37. Mitra P, Pereira LA, Drabsch Y, Ramsay RG, Gonda TJ. Estrogen receptor-alpha recruits p-tefb to overcome transcriptional pausing in intron 1 of the myb gene. *Nucleic Acids Res* (2012) 40(13):5988–6000. doi: 10.1093/nar/gks286

38. Mitra P, Yang RM, Sutton J, Ramsay RG, Gonda TJ. Cdk9 inhibitors selectively target estrogen receptor-positive breast cancer cells through combined inhibition of myb and mcl-1 expression. *Oncotarget* (2016) 7(8):9069–83. doi: 10.18632/oncotarget.6997

39. Slaughter MJ, Shanle EK, Khan A, Chua KF, Hong T, Boxer LD, et al. Hdac inhibition results in widespread alteration of the histone acetylation landscape and Brd4 targeting to gene bodies. *Cell Rep* (2021) 34(3):108638. doi: 10.1016/j.celrep.2020.108638

40. Ahmad R, Raina D, Meyer C, Kharbanda S, Kufe D. Triterpenoid cddo-me blocks the nf-kappab pathway by direct inhibition of ikkbeta on cys-179. *J Biol Chem* (2006) 281(47):35764–9. doi: 10.1074/jbc.M607160200

41. Probst BL, Trevino I, McCauley L, Bumeister R, Dulubova I, Wigley WC, et al. Rta 408, a novel synthetic triterpenoid with broad anticancer and anti-inflammatory activity. *PloS One* (2015) 10(4):e0122942. doi: 10.1371/journal.pone.0122942

42. Suhasini M, Reddy CD, Reddy EP, DiDonato JA, Pilz RB. Camp-induced nf-kappab (P50/Relb) binding to a c-myb intronic enhancer correlates with c-myb up-regulation and inhibition of erythroleukemia cell differentiation. *Oncogene* (1997) 15 (15):1859–70. doi: 10.1038/sj.onc.1201530

43. Suhasini M, Pilz RB. Transcriptional elongation of c-myb is regulated by nf-kappab (P50/Relb). *Oncogene* (1999) 18(51):7360–9. doi: 10.1038/sj.onc.1203158

44. Sayin VI, LeBoeuf SE, Singh SX, Davidson SM, Biancur D, Guzelhan BS, et al. Activation of the Nrf2 antioxidant program generates an imbalance in central carbon metabolism in cancer. *Elife* (2017) 6:e28083 . doi: 10.7554/eLife.28083

45. Zhao L, Glazov EA, Pattabiraman DR, Al-Owaidi F, Zhang P, Brown MA, et al. Integrated genome-wide chromatin occupancy and expression analyses identify key myeloid pro-differentiation transcription factors repressed by myb. *Nucleic Acids Res* (2011) 39(11):4664–79. doi: 10.1093/nar/gkr024

46. Honda T, Rounds BV, Bore L, Favaloro FGJr., Gribble GW, Suh N, et al. Novel synthetic oleanane triterpenoids: A series of highly active inhibitors of nitric oxide production in mouse macrophages. *Bioorg Med Chem Lett* (1999) 9(24):3429–34. doi: 10.1016/s0960-894x(99)00623-x

47. Reisman SA, Lee CY, Meyer CJ, Proksch JW, Sonis ST, Ward KW. Topical application of the synthetic triterpenoid rta 408 protects mice from radiation-induced dermatitis. *Radiat Res* (2014) 181(5):512–20. doi: 10.1667/RR13578.1

48. Parikh NR, Mandal A, Bhatia D, Siveen KS, Sethi G, Bishayee A. Oleanane triterpenoids in the prevention and therapy of breast cancer: Current evidence and future perspectives. *Phytochem Rev* (2014) 13(4):793–810. doi: 10.1007/s11101-014-9337-5

49. Liby KT, Sporn MB. Synthetic oleanane triterpenoids: Multifunctional drugs with a broad range of applications for prevention and treatment of chronic disease. *Pharmacol Rev* (2012) 64(4):972–1003. doi: 10.1124/pr.111.004846

50. Rohwer F, Todd S, McGuire KL. The effect of il-2 treatment on transcriptional attenuation in proto-oncogenes pim-1 and c-myb in human thymic blast cells. *J Immunol* (1996) 157(2):643–9. doi: 10.4049/jimmunol.157.2.643

51. Civin CI, Strauss LC, Brovall C, Fackler MJ, Schwartz JF, Shaper JH. Antigenic analysis of hematopoiesis. iii. a hematopoietic progenitor cell surface antigen defined by a monoclonal antibody raised against kg-1a cells. *J Immunol* (1984) 133(1):157–65.

52. Ribatti D, Solimando AG, Pezzella F. The anti-Vegf(R) drug discovery legacy: Improving attrition rates by breaking the vicious cycle of angiogenesis in cancer. *Cancers (Basel)* (2021) 13(14):3433. doi: 10.3390/cancers13143433

53. Habets RA, de Bock CE, Serneels L, Lodewijckx I, Verbeke D, Nittner D, et al. Safe targeting of T cell acute lymphoblastic leukemia by pathology-specific notch inhibition. *Sci Transl Med* (2019) 11(494):eaau6246. doi: 10.1126/scitranslmed.aau6246

54. Stadhouders R, Thongjuea S, Andrieu-Soler C, Palstra RJ, Bryne JC, van den Heuvel A, et al. Dynamic long-range chromatin interactions control myb proto-oncogene transcription during erythroid development. *EMBO J* (2012) 31(4):986–99. doi: 10.1038/emboj.2011.450

55. Salminen A, Lehtonen M, Paimela T, Kaarniranta K. Celastrol: Molecular targets of thunder God vine. *Biochem Biophys Res Commun* (2010) 394(3):439–42. doi: 10.1016/j.bbrc.2010.03.050

56. Shi J, Li J, Xu Z, Chen L, Luo R, Zhang C, et al. Celastrol: A review of useful strategies overcoming its limitation in anticancer application. *Front Pharmacol* (2020) 11:558741. doi: 10.3389/fphar.2020.558741

57. Persson M, Andersson MK, Mitani Y, Brandwein-Weber MS, Frierson HFJr., Moskaluk C, et al. Rearrangements, expression, and clinical significance of myb and Mybl1 in adenoid cystic carcinoma: A multi-institutional study. *Cancers (Basel)* (2022) 14(15):3691. doi: 10.3390/cancers14153691

# Frontiers in
# Cell and Developmental Biology

**Explores the fundamental biological processes of life, covering intracellular and extracellular dynamics.**

The world's most cited developmental biology journal, advancing our understanding of the fundamental processes of life. It explores a wide spectrum of cell and developmental biology, covering intracellular and extracellular dynamics.

## Discover the latest Research Topics

See more →


**Frontiers**

Avenue du Tribunal-Fédéral 34
1005 Lausanne, Switzerland
frontiersin.org

**Contact us**

+41 (0)21 510 17 00
frontiersin.org/about/contact